DEGRADATION ANALYSIS AND PARAMETER EXTRACTION OF ORGANIC SEMICONDUCTOR DEVICES

INVESTIGATION BY MEANS OF COMPLEMENTARY MEASUREMENT TECHNIQUES COMBINED WITH NUMERICAL SIMULATION

SIMON DAVID ZÜFLE

I declare that, except where otherwise cited or other contribution is referenced, the work presented herein is my own.

Dissertation, Karlsruher Institut für Technologie
Elektrotechnik und Informationstechnik, 2017
Tag der mündlichen Prüfung: 20. Juli 2017
Referenten: Prof. Dr. Uli Lemmer, Prof. Dr. Sebastian Randel,
Prof. Dr. Beat Ruhstaller

Degradation Analysis and Parameter Extraction of Organic Semiconductor Devices

Investigation by means of Complementary Measurement Techniques combined with Numerical Simulation

Zur Erlangung des akademischen Grades

Doktor der Ingenieurwissenschaften

von der Fakultät für
Elektrotechnik und Informationstechnik

des Karlsruher Instituts für Technologie (KIT)

genehmigte

Dissertation

von

Dipl.-Phys. Simon David Züfle

geb. in Pforzheim

Tag der mündlichen Prüfung:	20. Juli 2017
Referent:	Prof. Dr. Uli Lemmer
Korreferenten:	Prof. Dr. Sebastian Randel
	Prof. Dr. Beat Ruhstaller

This document is licensed under a Creative Commons
Attribution-ShareAlike 4.0 International License (CC BY-SA 4.0):
https://creativecommons.org/licenses/by-sa/4.0/deed.en

ABSTRACT

The understanding of the electrical properties of organic semiconducting materials is crucial for achieving efficient and stable devices. While organic light-emitting diodes (OLEDs) already succeed as industrial consumer products in displays, organic solar cells (OSC) are still a step behind. Yet both technologies share the common potential of low-cost mass production of light-weight, flexible opto-electronic devices making them attractive for a wide range of applications.

The electrical function of both OLEDs and OSCs is governed by the physical processes of charge carrier injection/extraction, transport, recombination, light absorption and emission. The assessment of these processes requires a thorough understanding of the related material and device parameters.

Establishing reliable measurement methods and numerical models to determine these parameters is crucial for the organic semiconductor industry. 30 years after the invention of OLEDs still new active and functional materials are being developed and devices are being optimized.

In this work we present a novel synoptic approach that combines a variety of electrical characterization techniques in the steady-state, transient and ac-mode. The use of complementary techniques and analytic methods as well as the qualitative analysis of signatures in the data allows us to draw conclusions about the underlying physical processes as well as to determine specific material parameters. Hereby the various measurements are only comparable because they can be performed with the same measurement setup in a short time and under the same environmental conditions.

By marrying this combinational measurement process with numerical drift-diffusion device simulation we are for the first time able to model the whole range of electrical experiments. This enables us to evaluate the reliability of common parameter extraction routines and examine their limitations. In fact, we find that the most accurate and reliable way to determine the set of material and device parameters is a global fitting routine of the full range of measured signals with a drift-diffusion simulation.

It can be advantageous for parameter extraction to fabricate dedicated devices where only one carrier type is present, thereby avoiding recombination and other bipolar charge transport effects. Here, we demonstrate that bilayer OLEDs comprising a polar electron transport layer show a voltage regime where only holes are present in the active layer. Such devices are therefore an easy-to-fabricate alternative to metal-insulator-semiconductor (MIS) devices in order to deliberately analyse the hole injection and transport properties of the hole transport layer, or any material with suitable molecular energetic levels. By varying the device temperature we can determine the thermal activation and disentangle the charge transport from the charge injection properties.

We further apply the synoptic approach to study device degradation. A multitude of physical and chemical processes are triggered by external stress factors such as light, temperature, humidity or electrical current, and impair the performance and stability of organic electronic devices. For our investigations we perform extensive measurement routines at various points during the ageing process. Again combined with simulation as well as by analysing the specific signatures of some effects we are able to distinguish between similar processes and to identify the dominant degradation mechanisms. We also find that in many cases the full layer stack, consisting of encapsulation, various functional layers and the active materials, has to be considered in stability tests.

To conclude, the combination of various experiments and simulation allows to extract valuable information about the physics behind degradation, and represents a valid and attractive approach for further characterization of organic electronic materials and devices.

ZUSAMMENFASSUNG

Das Verständnis der elektrischen Eigenschaften von organischen Halbleiter-Materialien ist von enormer Bedeutung, um stabile und effiziente Bauelemente zu erreichen. Während organische Leuchtdioden (OLEDs) bereits industriell hergestellt werden, sind organische Solarzellen (OSCs) noch nicht so weit. Beide Technologien eint jedoch das Potential dass sie kostengünstig in grossen Massen, dabei in flexiblen und leichten Bauformen hergestellt werden könnten, was sie interessant für eine ganze Reihe von Anwendungen macht.

Die elektrische Funktionsweise von OLEDs und OSCs ist bestimmt durch die physikalischen Prozesse Ladungsträger-Injektion/Extraktion, Transport, Rekombination, Lichtabsorption und -emission. Die Untersuchung dieser Prozesse erfordert ein gutes Verständnis der damit zusammenhängenden Material- und Bauteil-Parameter.

Die Etablierung von zuverlässigen Messmethoden und numerischen Modellen zur Bestimmung dieser Parameter ist für die organische Halbleiterindustrie entscheidend, werden doch auch 30 Jahre nach der Erfindung von OLEDs stetig neue organische Halbleitermaterialien entwickelt und Bauelemente optimiert.

In dieser Arbeit präsentieren wir einen neuen synoptischen Ansatz, welcher eine Reihe von elektrischen Charakterisierungs-Methoden im stationären Zustand sowie im transienten und AC-Modus kombiniert. Die Verwendung von komplementären Messungen und analytischen Methoden sowie die qualitative Analyse von spezifischen Charakteristika in den Messungen lässt Rückschlüsse auf die zugrunde liegenden physikalischen Prozesse zu und erlaubt es einzelne Materialparameter zu bestimmen. Dabei sind die verschiedenen Messungen direkt vergleichbar weil sie mit dem selben Messaufbau in kurzer Zeit und bei konstanten Messbedingungen durchgeführt werden.

Indem wir diesen kombinatorischen Prozess mit numerischen Drift-Diffusions-Simulationen zusammenbringen, sind wir erstmalig in der Lage die gesamte Bandbreite der elektrischen Experimente zu modellieren. Dies erlaubt uns die Zuverlässigkeit von gebräuchlichen Parameter-Extraktions-Routinen zu testen und ihre Grenzen zu bestimmen. Es zeigt sich, dass der genaueste und zuverlässigste Weg zur Bestimmung des ganzen Parameter-Satzes eine globale Fit-Routine von Drift-Diffusions-Simulationen über die gesamte Reihe an Experimenten ist.

Es kann von Vorteil sein, für die Parameter-Analyse spezielle unipolare Bauteile herzustellen, womit Rekombination und andere bipolare Ladungstransport-Effekte vermieden werden. Hier zeigen wir, dass Zwei-Schicht-OLEDs, welche eine polare Elektronen-Transportschicht enthalten, in einem gewissen Spannungsbereich unipolares Verhalten aufweisen. Solche Bauelemente können daher anstelle von Metall-Isolator-Halbleiter (MIS) Bauteilen verwendet werden, um die Loch-Injektion sowie den Loch-Transport in der Loch-Transportschicht, oder in einem beliebigen Material mit passenden molekularen Energieniveaus, zu untersuchen. Durch Variation der Temperatur können wir die thermische Aktivierungsenergie bestimmen, und in Beiträge für den Transport und die Injektion zerlegen.

Wir wenden den synoptischen Ansatz weiter an, um Degradation zu untersuchen. Eine Vielzahl von physikalischen und chemischen Prozessen, ausgelöst durch Licht, Temperatur, Feuchte oder elektrischen Strom, kann die Leistung und Stabilität von organischen Halbleiter-Bauelementen beeinträchtigen. Für unsere Studien führen wir ausführliche Messroutinen zu verschiedenen Zeitpunkten während des Alterns durch. Durch die Kombination mit Simulationen sowie durch die Analyse der Signaturen spezifischer Prozesse ist es uns möglich, zwischen verschiedenen Effekten zu unterscheiden und die dominierenden Alterungsmechanismen zu identifizieren. Hierbei zeigt sich, dass in vielen Fällen der gesamte Schichtaufbau, bestehend aus Verkapselung, funktionellen Schichten und dem aktiven Material, in Stabilitäts-Untersuchungen berücksichtigt werden muss.

Zusammenfassend lässt sich sagen, dass die Kombination von verschiedenen Experimenten in Verbindung mit Simulationen es ermöglicht, wertvolle Informationen über die Physik hinter Degradationsprozessen zu erhalten. Dieser Ansatz stellt damit einen gültigen und attraktiven Weg für die weitere Charakterisierung von organischen Halbleiter-Materialien und Bauteilen dar.

PUBLICATIONS

The following peer-reviewed scientific publications have been published during the duration of this PhD project.

S. Züfle, M. T. Neukom, S. Altazin, M. Zinggeler, M. Chrapa, T. Offermans, and B. Ruhstaller. "An Effective Area Approach to Model Lateral Degradation in Organic Solar Cells". *Advanced Energy Materials* 5.20 (2015), p. 1500835. DOI: 10.1002/aenm.201500835

S. Züfle, S. Altazin, A. Hofmann, L. Jäger, M. T. Neukom, T. D. Schmidt, W. Brütting, and B. Ruhstaller. "The use of charge extraction by linearly increasing voltage in polar organic light-emitting diodes". *Journal of Applied Physics* 121 (2017), p. 175501. DOI: 10.1063/1.4982903

S. Züfle, S. Altazin, A. Hofmann, L. Jäger, M. T. Neukom, W. Brütting, and B. Ruhstaller. "Determination of charge transport activation energy and injection barrier in organic semiconductor devices". *Journal of Applied Physics* 122 (2017), p. 115502. DOI: 10.1063/1.4992041

S. Jenatsch, R. Hany, A. C. Véron, M. Neukom, S. Züfle, A. Borgschulte, B. Ruhstaller, and F. Nüesch. "Influence of Molybdenum Oxide Interface Solvent Sensitivity on Charge Trapping in Bilayer Cyanine Solar Cells". *The Journal of Physical Chemistry C* 118.30 (2014), pp. 17036–17045. DOI: 10.1021/jp5005314

M. Eck, C. V. Pham, S. Züfle, M. Neukom, M. Sessler, D. Scheunemann, E. Erdem, S. Weber, H. Borchert, B. Ruhstaller, and M. Krüger. "Improved efficiency of bulk heterojunction hybrid solar cells by utilizing CdSe quantum dot–graphene nanocomposites". *Physical Chemistry Chemical Physics* 16.24 (2014), pp. 12251–12260. DOI: 10.1039/c4cp01566e

S. A. Gevorgyan, N. Espinosa, L. Ciammaruchi, B. Roth, F. Livi, S. Tsopanidis, S. Züfle, S. Queirós, A. Gregori, G. A. dos Reis Benatto, M. Corazza, M. V. Madsen, M. Hösel, M. J. Beliatis, T. T. Larsen-Olsen, F. Pastorelli, A. Castro, A. Mingorance, V. Lenzi, D. Fluhr, R. Roesch, M. M. D. Ramos, A. Savva, H. Hoppe, L. S. A. Marques, I. Burgués, E. Georgiou, L. Serrano-Luján, and F. C. Krebs. "Baselines for Lifetime of Organic Solar Cells". *Advanced Energy Materials* 6.22 (2016), p. 1600910. DOI: 10.1002/aenm.201600910

S. Altazin, S. Züfle, E. Knapp, C. Kirsch, T. D. Schmidt, L. Jäger, Y. Noguchi, W. Brütting, and B. Ruhstaller. "Simulation of OLEDs with a polar electron transport layer". *Organic Electronics* 39 (2016), pp. 244–249. DOI: 10.1016/j.orgel.2016.10.014

S. Altazin, S. Züfle, E. Knapp, C. Kirsch, T. D. Schmidt, L. Jäger, W. Brütting, and B. Ruhstaller. "Combining Simulations and Experiments to Study the Impact of Polar OLED Materials". *SID Symposium Digest of Technical Papers* 47.1 (2016), pp. 1750–1753. DOI: 10.1002/sdtp.11059

S. Altazin, S. Züfle, E. Knapp, C. Kirsch, T. D. Schmidt, L. Jäger, W. Brütting, and B. Ruhstaller. "On the role of polar molecules and the barrier for charge injection in OLEDs". *Proceedings of SPIE* 9941 (2016). Ed. by F. So, C. Adachi, and J.-J. Kim, 99410O. DOI: 10.1117/12.2238620

M. T. Neukom, S. Züfle, E. Knapp, M. Makha, R. Hany, and B. Ruhstaller. "Why perovskite solar cells with high efficiency show small IV-curve hysteresis". *Solar Energy Materials & Solar Cells* 169 (2017), pp. 159–166. DOI: 10.1016/j.solmat.2017.05.021

Furthermore the following manuscripts are already submitted and currently under review or still in preparation.

D. Fluhr, S. Züfle, B. Muhsin, R. Öttking, M. Seeland, R. Rösch, U. Schubert, B. Ruhstaller, S. Krischok, and H. Hoppe. "Unified description of electrode corrosion dynamics in organic solar cells". *submitted* (2017)

M. Regnat, S. Züfle, K. Pernstich, and B. Ruhstaller. "The importance of changes in the emission zone for the efficiency roll-off in OLEDs". *manuscript in preparation* (2017), submitted

S. Züfle, G. Zanotti, E. A. Katz, P. Tiwana, and B. Ruhstaller. "Reversible Photodoping of Organic Solar Cells aged by Concentrated Sunlight". *manuscript in preparation* (2017)

S. Züfle, R. Hansson, E. A. Katz, E. Moons, and B. Ruhstaller. "Burn-in degradation of PCDTBT:PC70BM organic photovoltaics: underlying mechanism and interlayer effect". *manuscript in preparation* (2017)

T. Sauermann, S. Züfle, M. T. Neukom, S. Altazin, B. Ruhstaller, H. J. Egelhaaf, and C. Brabec. "Investigation of degradation induced doping in organic solar cells using complementary measurements and simulations". *manuscript in preparation* (2017)

CONTENTS

LIST OF FIGURES

LIST OF TABLES

ACRONYMS

α-NPD 4,4-bis[N-(1-naphthyl)-N-phenylamino]-biphenyl, N,N0-bis(1-naphthyl)-N,N0-diphenyl-1,10-biphenyl-4,40-diamine, N,N′-diphenyl-N,N′-bis(1-naphthyl)-1,1′-biphenyl-4,4′-diamine

Alq_3 Tris-(8-hydroxyquinoline)aluminum, Tris-(8-hydroxyquinolate) aluminum, Tris(8-hydroxyquinolato)aluminium

BHJ Bulk-heterojunction

CE Charge extraction

CELIV Charge extraction by linearly increasing voltage

C-f Capacitance-frequency

C-V Capacitance-voltage

DCM Displacement current measurement

DIT Dark/Double injection transient

DLTS Deep-level transient spectroscopy

DOS Density-of-states

DUT Device under test

EBL Electron blocking layer

EGDM Extended Gaussian disorder model

EIL Electron injection layer

EML Emission layer

EQE External quantum efficiency

ETL Electron transport layer

GDM Gaussian disorder model

HBL Hole blocking layer

HIL Hole injection layer

HOMO Highest occupied molecular orbital

HTL Hole transport layer

IMPS Intensity-modulated photocurrent spectroscopy

IMVS Intensity-modulated photovoltage spectroscopy

IQE Internal quantum efficiency

ISOS International Summit on OPV Stability

ITO Indium tin oxide

IV Current-Voltage curve

LUMO Lowest unoccupied molecular orbital

MIM Metal-insulator-metal

MIS Metal-insulator-semiconductor

MoO_3 Molybdenium oxide

OCVD Open-circuit voltage decay

OLED Organic light-emitting diode

OPV Organic photovoltaics

OSC Organic solar cell

OTFT Organic field-effect transistors

P_3HT poly(3-hexylthiophene-2,5-diyl)

$PC_{61}BM$ [6,6]-Phenyl C61 butyric acid methyl ester

$PC_{71}BM$ [6,6]-Phenyl C71 butyric acid methyl ester

PCDTBT
Poly[N-9′-heptadecanyl-2,7-carbazole-alt-5,5-(4′,7′-di-2-thienyl-2′,1′,3′-benzothiadiazole)], Poly[[9-(1-octylnonyl)-9H-carbazole-2,7-diyl]-2,5-thiophenediyl-2,1,3-benzothiadiazole-4,7-diyl-2,5-thiophenediyl]

PCE Power conversion efficiency

PEDOT:PSS Poly(3,4-ethylenedioxythiophene)-poly(styrenesulfonate)

SCLC Space-charge limited current

TADF Thermally activated delayed flourescence

TPC Transient Photocurrent

TPV Transient Photovoltage

VP Small voltage pulse

V_2O_5 Vanadium pentoxide

WOLED White OLED

USED SYMBOLS AND CONSTANTS

The used symbols for physical quantities and constants used in equations throughout this thesis are specified in the tables below.

QUANTITY:	SYMBOL	UNIT
Layer Thickness:	d	nm
Active Surface:	S	cm^2
Admittance:	Y	Ω^{-1}
Angular Frequency:	ω	Hz
Bandgap	E_g	eV
Built-in Voltage:	V_{bi}	V
Capacitance:	C	nF
CELIV Ramp-Rate:	$\mathcal{A}$	V/ms
Charge	Q	C
Charge Density	n/p	m^{-3}
Conductance:	G	Ω^{-1}
Current:	I	mA
Current-Density:	J	mA/cm^2
Density-of-states:	N_0/P_0	m^{-3}
Doping Density	N_A, N_D	m^{-3}
Electrical Permittivity:	ε_r	1
Electrical Power:	P	mW
Electric Field:	$\mathcal{E}$	V/m

QUANTITY:	SYMBOL	UNIT
Electric Potential	Φ	eV
Energy	E	eV
Fermilevel	E_F	eV
Frequency:	f	Hz
Illum. Intensity:	L	1
Impedance:	Z	Ω
Injection Barrier	E_a/E_c	eV
Luminance:	EL	cd
Mobility:	μ	cm^2/Vs
Parallel Resistance:	R_p	Ω
Position	x	nm
Series Resistance:	R_s	Ω
Temperature:	T	K
Time:	t	μs
Voltage:	V	V
Workfunction	WF	eV

PHYSICAL CONSTANT:	SYMBOL		VALUE	
Boltzmann Constant:	k_B	=	$1.381 \cdot 10^{-23}$	J/K
Pi:	π	=	3.1416	
Unit Charge	q	=	$1.602 \cdot 10^{-19}$	C
Vacuum Permittivity:	ε_0	=	$8.85 \cdot 10^{-12}$	F/m

Part I

METHODS

The first part of this thesis gives a general introduction into organic light-emitting diodes and solar cells as well as their stability. We then present the main motivation and objectives of this dissertation. Furthermore the experimental techniques and methods as well as the numerical simulation models which have been employed are introduced.

1 INTRODUCTION AND MOTIVATION

1.1 ORGANIC ELECTRONIC MATERIALS

Organic electronics are founded on the electrical conductivity of a wide class of materials known as organic semiconductors. The first organic material to show electric properties was the anthracene molecule investigated in the early 20th century [1–3]. In the 1950s the photoconductive behaviour of anthracene [4], later also of other organic materials [4, 5], as well as electroluminescent behaviour or organic crystals was reported [6, 7]. In 1977 Heeger, MacDiarmid and Shirakawa discovered semiconducting polymers, for which they were awarded the Nobel Prize in Chemistry in 2000 [8, 9]. This development led to the first bilayer organic solar cell (OSC) in 1986 [10] and the first bilayer organic light-emitting device (OLED) in 1987 [11]. Also the first organic field-effect transistors (OTFT) were demonstrated in the 1980s [12–14]. The next major steps were the invention of polymer OLEDs in 1990 [15, 16] and the bulk-heterojunction (BHJ) solar cell in 1991 [17, 18]. These potential applications raised enormous interest in the scientific community and also triggered investments from industry, empowering a huge progress throughout the last three decades. This is due to a range of advantages over conventional semiconductor electronics:

- Many properties of organic semiconductors can be tuned by chemical engineering.
- The materials themselves can be produced in large quantities by low-cost chemical processes and from abundant raw materials.
- Solution-processing enables high-throughput, large-area, roll-to-roll printing and therefore cheap production. Optimized vacuum-processing has the same potential.
- Thin-film technology allows for mechanically flexible and low-weight products.
- Non-toxic and biodegradable materials may be employed.
- New classes of products are conceivable which are not possible with other materials.
- Organic solar cells have good performance at low-intensity and indirect light and show a positive temperature coefficient.

The origin of the (semi-)conducting behaviour of organic electronic materials lies in the molecular energetics of their units, which are always small molecules or polymers with a carbon backbone. Alternating covalent carbon double-bonds lead to a delocalization of π-electrons and hence to a high microscopic electrical conductivity. The macroscopic conductivity is, however, reduced due to energetically hindered intermolecular charge transport, so-called hopping. The actual film morphology and layer crystallinity strongly influence the charge transport properties and are therefore subject to research and optimization.

The relevant energetic levels of a single molecule are the HOMO (Highest occupied molecular orbital) and the LUMO (Lowest unoccupied molecular orbital) which are separated by the optical bandgap. When many molecules form an amorphous or nanocrystalline film, the molecular levels shift and distribute according to the disorder of the film, leading to a band-like density-of-states

(DOS). Charge transport occurs in the HOMO band (corresponding to the valence band in conventional semiconductors), and the LUMO band (corresponding to the conduction band). An electron that is excited from the HOMO into the LUMO can be transported there, leaving a positively charged "hole" in the HOMO which can be imagined as a mobile charge carrier. Thus current in organic semiconductor devices is usually bipolar.

In opposition to conventional semiconductors organic electronic materials are by themselves intrinsic, undoped semiconductors, yet often favour one carrier species. However, conductivity doping leading to specific n- or p-type behaviour has been developed in order to optimize charge transport, injection or extraction [19, 20]. So today standard devices comprise multiple functional layers such as transport, injection, and blocking layers around the active layer(s).

The physical processes taking place in an organic layer are charge generation, transport and recombination. While charge generation by light absorption and subsequent charge extraction are the working process of solar cells, in light-emitting diodes charges need to be injected from the contacts, transported and to recombine radiatively, thereby emitting photons. So in principle the same physical processes as in conventional semiconductors take place. Therefore the terminology, theoretical and analytical models, as well as characterization methods for organic semiconductors are very similar and sometimes equal to those for inorganic semiconductors. In the following we will introduce the working principles of OLEDs and OSCs in more detail.

1.2 ORGANIC LIGHT-EMITTING DIODES

The most simple organic light-emitting diodes (OLEDs) consist of just one layer between two contacts, where charges are injected from both sides and recombine radiatively to emit light. These devices are however very inefficient, so more complex structures are employed. In bilayer OLEDs two materials are combined which are charge-selective (see Fig. 1.1a). Then charge transport is phase-separated and the carriers meet at the internal interface between the hole transport layer (HTL) and the electron transport layer (ETL). There they can form a charge-transfer exciton which can decay radiatively, hereby emitting light. The spectrum of the emitted light depends on the bandgap of the emitting material, is however broadened due to disorder effects and vibronic oscillations.

In order to confine the recombination to a larger region it has become common to introduce a dedicated emission layer (EML) between ETL and HTL, which can transport both electrons and holes and thereby increases the probability for radiative recombination. Furthermore, additional injection layers (HIL, EIL) which are usually highly doped and have suitable energy levels, facilitate injection from the electrodes. Finally, blocking layers (HBL, EBL) help the confinement of charges in the EML (see Fig. 1.1b) and minimize leakage currents.

Due to spin-selection rules excitons are generated in singlets (25 %) and triplets (75 %). However, only the singlet excitons can decay radiatively (fluorescence), while the triplets recombine non-radiatively [7, 21, 22]. In order to overcome this limitation, another deeper-lying energy level can be introduced that allows relaxation of the triplet excitons into singlet excitons (phosphorescence) [23–25]. This approach is usually followed in Host-Guest systems, where the fluorescent host material of the EML is doped with a phosphorescent emitter molecule, in order to harvest all the excitons. There are also other approaches like thermally activated delayed fluorescence (TADF) OLEDs that can reach internal quantum efficiencies of 100 % [26–31].

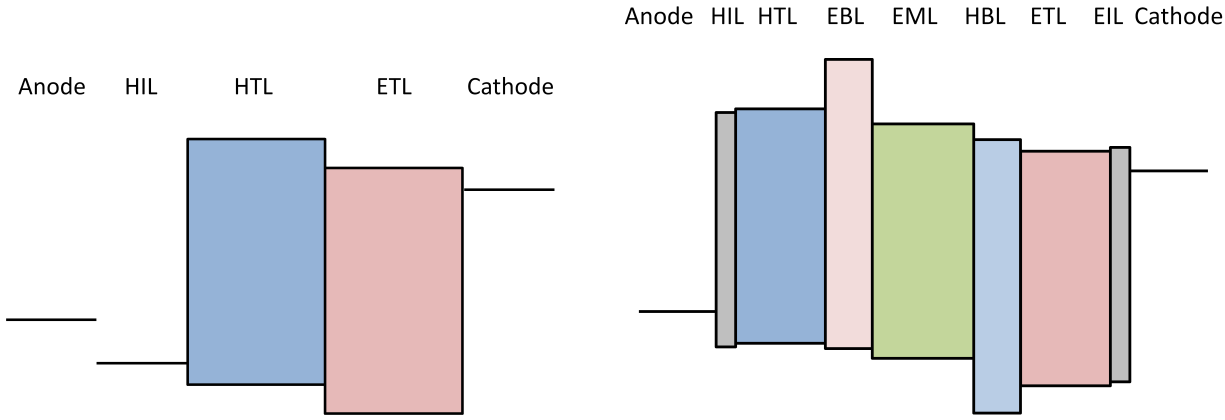

(a) Bilayer OLED stack.

(b) Multilayer OLED stack.

Figure 1.1: Different OLED layer stacks and their schematic energy profile.

The operation voltage of polymer OLEDs is in the range of $2-5$ V, while that of small-molecule based devices is in the range of $3-7$ V. Stacked tandem OLEDs comprising several emission layers allow for white light emission, but also need higher voltages. Using several phosphors or conversion layers it is, however, also possible to obtain a white OLED (WOLED) in a single configuration [32–35].

The main application for OLEDs is in display technology, where they are employed today on a large industrial scale in smartphones as well as in TVs. Compared to conventional LCD displays OLEDs offer high contrast ratio, wide viewing-angle and a thinner form-factor [36–38]. The second market is lighting. Here OLEDs compete with conventional LEDs to replace incandescent and fluorescent lamps. While both are very energy efficient, OLED lighting offers additional mechanical flexibility, large-area and homogeneous illumination, as well as variable colours [37, 39–42].

The most important figures-of-merit for OLEDs are quantum efficiency, luminous and current efficiency. The external quantum efficiency (EQE) of OLEDs is characterized as the number of photons that are outcoupled to air per injected electron. For qualification of light sources the luminous efficacy, being the luminance per driving current, and the power efficiency, being the luminous flux per electrical power, are more important. Hereby the efficiencies in monochromatic OLEDs strongly depend on the wavelength, as the same electrical power converts to different amounts of photons [43]. Today's most efficient WOLEDs reach power efficiencies of $70-120$ lm/W, in the same range as conventional LEDs, luminous efficacies of 70 cd/A, and EQEs of 26 % [41, 44–46]. Interestingly, the main reason for the low EQE are outcoupling losses, meaning that most emitted photons are internally reflected, scattered and reabsorbed. Thus, optical modelling and optimization holds a large potential for further device improvement. For example using a scattering top electrode the EQE could be enhanced to 54 % [41].

The limited OLED stability was a big issue in the beginning hindering the market entry [47–50]. The most important degradation mechanisms of the active materials are polaron-induced, meaning that they occur due to the current flowing through the device. These effects are mainly chemical degradation of the molecules, thereby leading to both loss in transport properties as well as in radiative efficiency [51–55]. Due to space-charge formation, as a result of imbalanced

transport and energetic barriers, often interfaces are affected most [53, 56–58]. In phosphorescent OLEDs the guest molecules which are recombination centres are susceptible to degradation [59–62]. These degradation pathways could however be largely mitigated by the development of chemically more stable organic materials [63, 64]. Furthermore, tuning of the recombination/emission zone by thickness optimization and the introduction of blocking layers contributed to both enhanced efficiencies and lifetimes [51, 65–67]. A second prominent degradation mechanism in OLEDs is the oxidation of the low-workfunction electrode due to oxygen and water ingress through pinholes and grain boundaries, which leads to electrode delamination and dark spot formation [68–74]. By development of good encapsulation materials and improved processing, as well as introducing thin barrier layers, this problem can be largely avoided today in high-efficiency devices [75–78]. Today lifetimes exceeding 50000 h, greater than the ones of LCDs, have been demonstrated [26, 79–81].

The OLEDs investigated in this thesis are vacuum-processed small-molecule bilayer OLEDs comprising the electron transport layer Alq_3 which is also the emitting material, and the hole transport layer α-NPD. This is actually the same device layout as used in the very first OLED by Tang and Van Slyke [11]. Since the emitter is fluorescent the internal quantum efficiency is below 25 %. Yet due to its simplicity this layer stack configuration has been proven to be very interesting and suitable for fundamental research. Our interest lies in the understanding of the charge carrier injection and transport processes as well as the polarity of the ETL, thus we focus on electrical characterization, and largely disregard the emission behaviour. In fact, the polar ETL (in our case Alq_3) leads to a voltage regime below the turn-on voltage where the device behaves as a metal-insulator-semiconductor MIS device [82, 83]. We exploit this behaviour to investigate and develop routines for the extraction of material parameters.

1.3 ORGANIC SOLAR CELLS

The second promising application for organic electronics are organic solar cells (OSCs), also called organic photovoltaics (OPV). Here the high light absorption coefficients of some organic materials are exploited, making them suitable for thin-film applications[84–87]. This bears the potential of flexible, light-weight solar cells, hereby opening a new market. Roll-to-roll processing on flexible plastic substrates enables high-throughput and large-area production of organic solar cells, making them a low-cost technology [86, 88, 89]. Further, using printing, bladecoating, but also evaporation as the deposition methods allows for free-form photovoltaic modules [90–92]. Furthermore, by tuning the thickness as well as the material properties it is possible to adjust the colour and even make semitransparent cells [93–95]. Finally it is also conceivable that sustainable and non-toxic materials can be employed, which would be a major advantage over other thin-film technologies. The main drawback for a commercialization so far have been the low power conversion efficiencies (PCEs) below 12 % and, perhaps even more, the limited stability under atmospheric conditions as well as under illumination. Eventually, OPV may find its niches in specific applications, while conventional PV will probably maintain their major role [37, 96–99].

The basic layer structures of organic solar cells are depicted in Fig. 1.2, where the active layer(s) is (are) sandwiched between two electrodes. Due to the workfunction difference of the high-workfunction contact (anode) and the low-workfunction contact (cathode) a built-in potential drops over the active layer under short-circuit condition. Organic solar cells' active layers

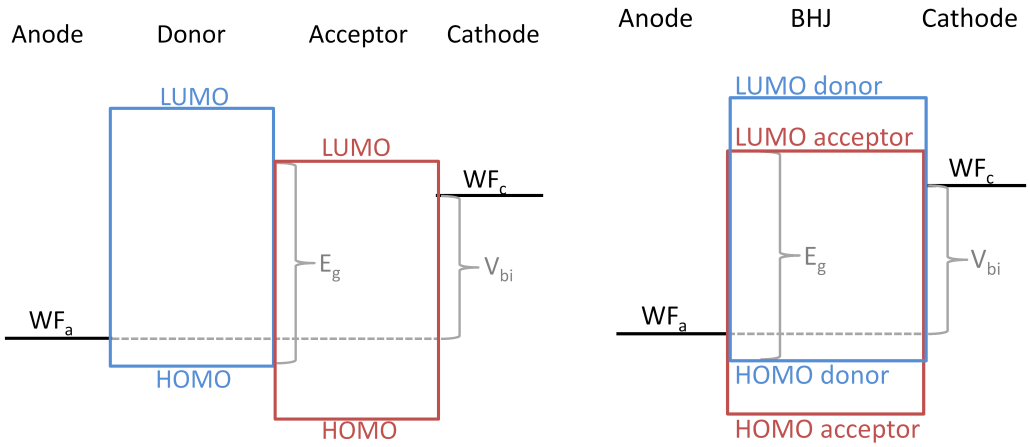

(a) Planar OSC stack.

(b) BHJ OSC stack.

Figure 1.2: Planar and bulk-heterojunction OSC stacks and their schematic energy profile. The different energy levels mentioned in the text are indicated.

are usually made up of a combination of two materials, an electron donor and an electron acceptor. They can be deposited as a bilayer (planar heterojunction) [10, 100] or intermixed as a bulk-heterojunction (BHJ) [18]. Charge generation takes place by absorption of incident photons by a material, exciting electrons from the LUMO into the HOMO, and thereby forming a bound electron-hole-pair, called exciton. In the ideal case this exciton is separated at a donor-acceptor interface, where the energetics are favourable for charge transfer of one charge carrier to the other material. The separated electron and hole can then be transported in the acceptor and donor phases, respectively [101]. Hereby the built-in field serves as a driving force for the exciton dissociation as well as for charge transport and thus is crucial to extract the photogenerated charges as an electrical current at the electrodes.

The exciton, having a binding energy of several 100 meV, can however also recombine radiatively or non-radiatively. For an efficient exciton separation it is necessary that an exciton finds a donor-acceptor interface within its diffusion length of several nm. The main advantage of an intermixed active layer - the bulk-heterojunction - compared to the planar stack is therefore the strongly increased exciton separation probability leading to an enhanced photocurrent [102].

Knowing the absorption of the material at a specific wavelength (and with a specific illumination spectrum) the maximum obtainable short-circuit current can be calculated. The actual short-circuit current I_{sc} is however smaller, as the internal quantum efficiency (IQE) is below one due to several loss mechanisms. As mentioned, not all excitons are separated, although for BHJ this can usually be assumed. Another loss mechanism is recombination of electrons with holes or trapping of charge carriers. Due to the phase-separated transport in BHJs and depending on the specific layer morphology the bimolecular recombination losses can be minimized. Finally the extraction properties (selectivity) of the contacts represent another loss factor in OSCs.

The open-circuit voltage V_{oc} - the voltage where the current is zero - is mainly limited by the effective bandgap of the materials, that is the difference between the acceptor LUMO and the donor HOMO. The open-circuit voltage is defined as the difference between the quasi-Fermilevels of electrons and holes (see also Sec. 3.1). These are dependent on the respective photogenerated charge densities. Under open-circuit condition the quasi-Fermilevels are flat and only bent at the

contacts. As the total current is zero and the device is essentially field-free, there is an equilibrium between generation, recombination and diffusion.

At short-circuit, that is without an applied voltage, the photogenerated charges can be extracted by the built-in field. The quasi-Fermilevels are slanted, and drift in the electric field constitutes the driving force for charge transport. A schematics of the bands at short-circuit and open-circuit is shown in Fig. 3.2.

For arbitrary applied voltages as well as under non-equilibrium conditions the charge carrier current is composed of a drift current in the electric field, and a diffusion current due to charge density gradients. This allows modelling these devices using the drift-diffusion approach, as described in more detail in Chapter 3.

1.3.1 *Current Status*

Figure 1.3 gives an overview of the various solar cell technologies and their current record power conversion efficiencies (PCEs) [103]. The best organic solar cells have efficiencies just above 10 %, much lower than conventional Silicon-based cells. Currently single OSCs reach record efficiencies of $10 - 12$ % [104–111], and tandem OSCs have been reported with up to 13 % [112–116]. There are calculations based on detailed balance as well as drift-diffusion models showing that the theoretical limit for OSC efficiencies is $21 - 28$ %, nearly at the Shockley-Queisser limit [117–122]. Yet, in spite of the enormous effort in the last decades OSCs have been quickly surpassed by the evolving perovskite-based solar cells which already reach 21 % in single cell and 26 % in tandem configurations with Silicon [123–125]. The unprecedented increase seen in perovskite-based devices has led many researchers to shift focus from OPV to perovskite research in the last years. Still, the rapid progress in perovskite solar cells would not have been possible without the preceding effort of the OPV community. Many scientific methods and achievements that came out of OPV research can now be transferred very usefully to other technologies. Furthermore, with perovskites showing low stability, and containing toxic materials, there may still be a chance for OSCs.

1.4 ORGANIC SOLAR CELL STABILITY

While the potential in terms of efficiency and fabrication cost are relatively clear and promising, as a third factor the stability of OSCs is of crucial importance in order for them to become commercially viable [126–129]. As Fig. 1.4 shows there has been a lot of effort in the past years leading to a significant increase in the reported device stabilities.

The degradation manifests itself in the reduction of specific characteristic parameters like short-circuit current and a consequential loss in overall device performance. The decay curves of the performance, but also of other parameters can be classified into different shapes, as shown in Fig. 1.5 [126, 130]. All these shapes have been found and reported in literature, yet the most meaningful is shape 1 , which can be further differentiated in two parts - a fast initial decay, often called burn-in, which is followed by a slower decay or even a nearly stable behaviour (see also figure part (b)) [130–134]. In this curve it is meaningful to define a characteristic lifetime T_{80}, where the parameter under investigation (E in Fig. 1.5) has dropped from an initial value E_0 to 80 % of this value E_{80}. If there is a burn-in then a T_{80} time can be defined for both phases.

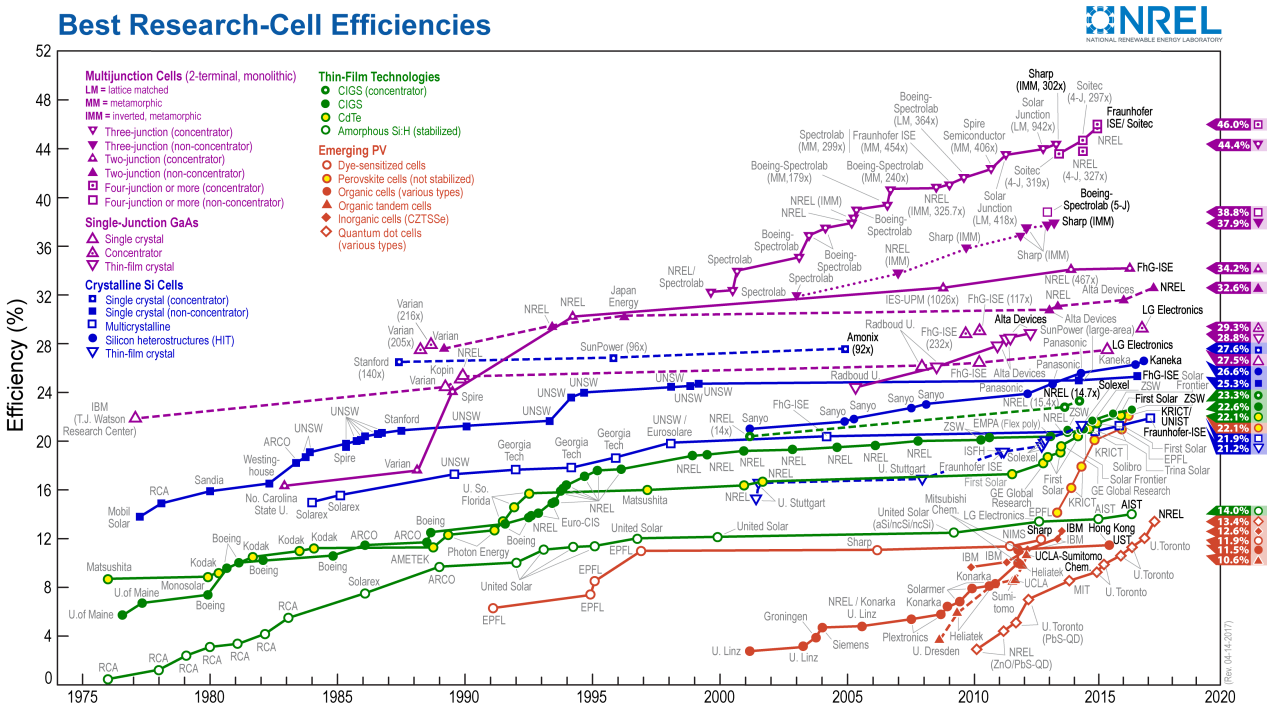

Figure 1.3: Best research solar cell efficiencies, as of 17.04.2017. Taken from www.nrel.gov [103].

1.4.1 *Degradation Mechanisms*

Figure 1.6 summarizes the various factors that influence device stability. These extrinsic factors can harm the different components of an organic solar cell or organic light-emitting diode. In the following we will focus on solar cell degradation, yet, as many materials can also be employed in OLEDs, the mechanisms there can be very similar.

The most critical effect is that the active layer itself is prone to degradation under illumination, which can occur by absorption loss (photobleaching), usually of the polymer [135–138]. This photodegradation is understood as light induced chemical reactions usually decomposing the polymer chain, making it less absorbing as well as less conductive [139–149]. If oxygen can ingress the device, photo-oxidation can take place which also leads to absorption loss [150–157]. The chemical (by-)products from these reactions can further act as traps or charged dopants and then additionally harm charge carrier transport, leading to a reduced mobility, enhanced recombination losses, and extraction problems [158–172]. Some of the photodegradation processes have been observed to be reversible, for example by thermal annealing or just by letting the device rest [171, 173–178]. Another interesting effect is light-soaking (see shape 3 in Fig. 1.5), where the device performance first improves upon illumination [179–182], which can make it difficult to characterize a stable cell efficiency.

The active layer morphology can be intrinsically unstable, even in annealed devices. This leads to a slow equilibration of the morphology, happening even in the dark and at room temperature [183, 184]. Increased temperature accelerates this process, as it enhances the molecular diffusion in the layer [185–192]. The result is a de-mixing of the two bulk-heterojunction phases (phase-segregation) leading to a less efficient exciton separation and transport [187, 191, 193–200]. It has also been shown that some fullerene acceptors tend to dimerize, thereby changing their electric properties [187, 195, 201–203].

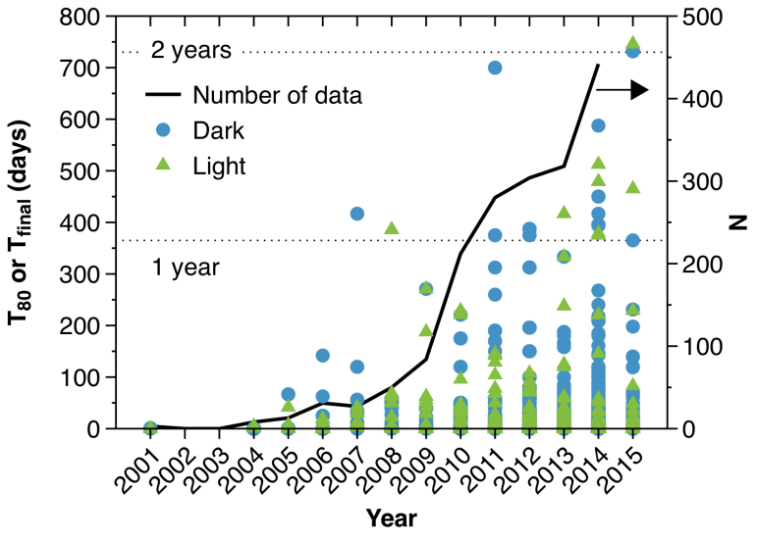

Figure 1.4: Published lifetimes of organic solar cells, and number of publications reporting lifetimes. Plot taken from [126].

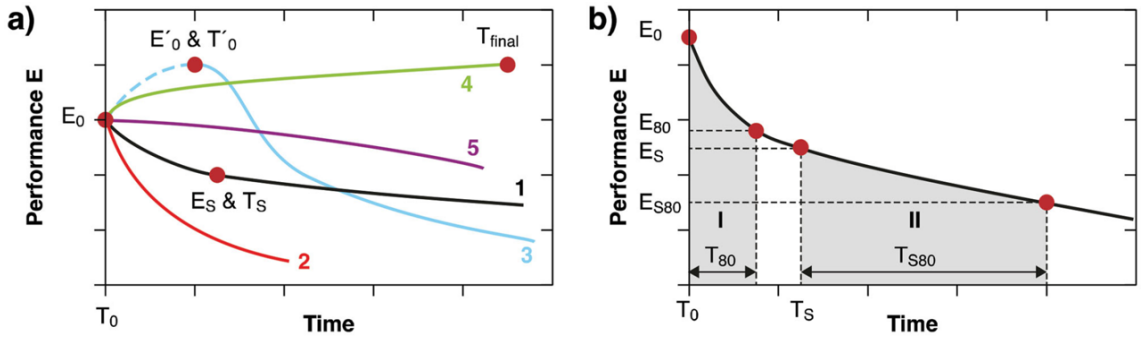

Figure 1.5: a) Overview of possible shapes of degradation curves in OSCs. b) Shape 1 showing definition of the parameters mentioned in the text. Plots taken from [126].

In order to make the active layer intrinsically more stable, the crosslinking of the polymer phase during layer deposition has been shown to help controlling and stabilizing the morphology [204–209]. Furthermore by optimizing the active materials on a molecular level their optoelectrical properties and stability can be improved [188, 210–214].

The surrounding functional layers for charge extraction are also prone to degradation. When organic materials are employed, they can suffer from the same photochemical instabilities as decribed above [215–218]. A commonly used interlayer material in polymer solar cells, serving as a hole transport layer, is the conducting polymer PEDOT:PSS. However, PEDOT:PSS is acidic and hygroscopic [127] and has been shown to induce corrosion of the low-workfunction electrode [219–222]. Furthermore the PEDOT:PSS workfunction is subject to change due to UV-illumination or water [223–225].

Hence, the device stability can be improved by replacing PEDOT:PSS with alternative HTL materials. By using metal oxides instead of PEDOT:PSS, both the stability and the performance of the devices can be improved [226–230]. The most common metal oxides employed for this purpose are MoO_3, V_2O_5 and NiO, and they can even be deposited from solution [221, 226,

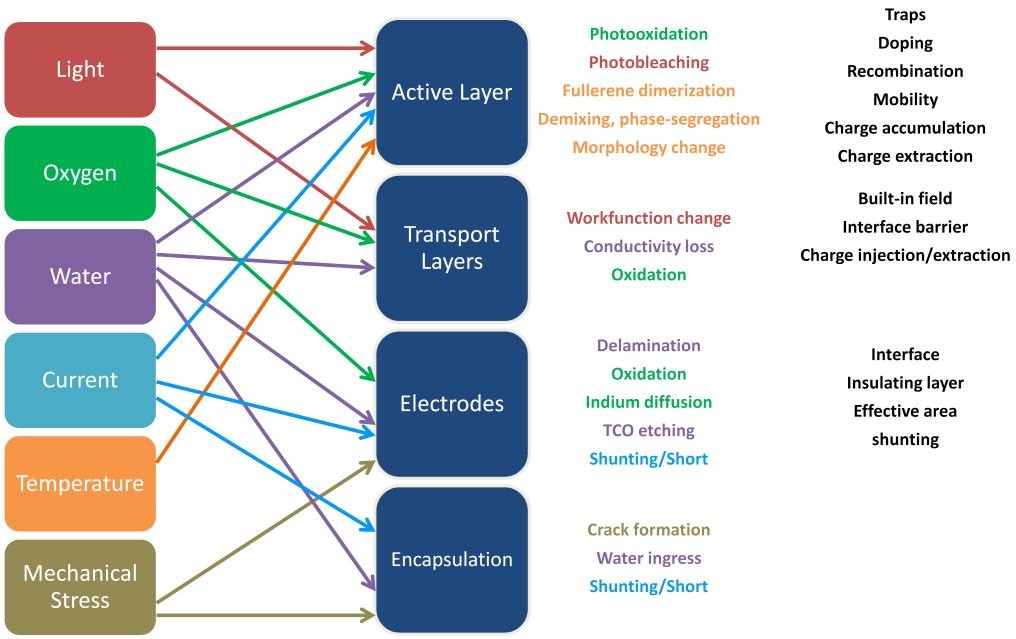

Figure 1.6: Overview of possible degradation mechanisms in organic solar cells and OLEDs.

231–240].

As mentioned, the low-workfunction electrode, usually aluminium or calcium, is sensitive to humidity and can corrode, thereby forming a thin insulating oxide layer [222, 241]. As this layer grows laterally following the humidity ingress, it leads to a loss in effective device area [242–244]. Sometimes a chemical reaction leads to the production of gas and a formation of so-called bubbles, where the electrode contact is completely lost by delamination [68, 220, 222, 245–247]. Also mechanical stress like bending can lead to electrode delamination [172, 248–250].

One approach to prevent the degradation of the low-workfunction electrode is the use of thin interlayers that are impermeable for oxygen or water [240, 251–254]. Another possibility is represented by an inverted stack design, that places the sensitive electrode at the bottom [255–257].

The high-workfunction electrode is usually transparent indium-tin-oxide (ITO). Here the diffusion of indium and tin into the active layers has been reported [258, 259]. It has further been reported that the acidic PEDOT:PSS can etch the ITO [219]. Additionally the ITO workfunction may also change with time, harming the built-in and open-circuit voltage [260].

Finally, the encapsulation material, usually a plastic barrier foil, can degrade [261–263]. Mechanical bending can lead to delamination, but also to crack formation with subsequent water ingress [243, 244, 264–271]. Even in glass-glass encapsulated devices water ingress through the edge sealing can play a role.

Thus, it is clear that a reasonable lifetime of organic solar cells can only be guaranteed when they are well-encapsulated, so that no oxygen or water are present in the active and functional layers. In research this condition is usually fulfilled by fabricating and characterizing the devices in gloveboxes in nitrogen atmosphere. This allows to focus the degradation analysis on the intrinsic and extrinsic stability of the absorber material, being the most important ingredient for an organic solar cell. Another reason for this way of working is of course that leaving out the encapsulation or some functional layers represents a smaller fabricational effort. Moreover, also in encapsulated

devices failure may happen due to insufficient or defective encapsulation, which can sometimes lead to a misinterpretation of the defect as a failure of the active layer.

1.4.2 *ISOS guidelines*

In order to understand the manifold degradation mechanisms in organic solar cells better, a useful approach is to generate ageing conditions that allow to exclude some of them. Furthermore a systematic variation of the ageing conditions and/or device parameters is the best approach to identify specific processes.

Another very important point for the understanding and improvement of organic solar cell stability is the comparison of results from different groups. Such comparison is only meaningful when the same or at least similar ageing conditions were applied [272, 273]. This factor is even more important when quantitative results like device efficiency or lifetime are compared. Several interlaboratory and round-robin studies have been performed in the past to assess the intercomparability of stability measurements [272–281].

Test type	**Dark**			**Outdoor**		
Test ID	ISOS-D-1 Shelf	ISOS-D-2 High temp. storage	ISOS-D-3 Damp heat	ISOS-O-1 Outdoor	ISOS-O-2 Outdoor	ISOS-O-3 Outdoor
Light source	None	None	None	Sunlight	Sunlight	Sunlight
Temp.[a]	Ambient	65/85 °C	65/85 °C	Ambient	Ambient	Ambient
Relative humidity (R.H.)[a]	Ambient	Ambient (low)	85%	Ambient	Ambient	Ambient
Environment[a]	Ambient	Oven	Env. chamber	Outdoor	Outdoor	Outdoor
Characterization light source	Solar simulator or sunlight	Solar simulator	Solar simulator	Solar simulator	Sunlight	Sunlight and solar simulator
Load[b]	Open circuit	Open circuit	Open circuit	MPP or open circuit	MPP or open circuit	MPP

Test type	**Laboratory weathering testing**			**Thermal cycling**		
Test ID	ISOS-L-1 Laboratory weathering	ISOS-L-2 Laboratory weathering	ISOS-L-3 Laboratory weathering	ISOS-T-1 Thermal cycling	ISOS-T-2 Thermal cycling	ISOS- T-3 Thermal cycling
Light source	Simulator	Simulator	Simulator	None	None	None
Temp.[a]	Ambient	65/85 °C	65/85 °C	Between room temp. and 65/85 °C	Between room temp. and 65/85 °C	−40 to +85 °C
Relative humidity (R.H.)[a]	Ambient	Ambient	Near 50%	Ambient	Ambient	Near 55%
Environment/setup	Light only	Light & Temp.	Light, Temp. and R.H.	Hot plate/oven	Oven/env. chamb.	Env. chamb.
Characterization light source	Solar simulator	Solar simulator	Solar simulator	Solar simulator or sunlight	Solar simulator	Solar simulator
Load[b]	MPP or open circuit	MPP or open circuit	MPP	Open circuit	Open circuit	Open circuit

Table 1.1: ISOS guidelines for stability testing of organic solar cells. Table taken from [282].

These considerations led the researcher community that is investigating OPV stability to develop a set of guidelines how to measure and report device stability [126, 272, 282]. The so-called ISOS-protocols define various ageing conditions, as summarized in Table 1.1. The four classes D, O, L and T establish conditions for ageing in the dark, outdoors with real sunlight, in the lab with artificial sunlight, and at high temperatures, respectively. The protocols further come in several gradings specifying the exact requirements and which kind of characterization and ageing equipment should be employed. Thus, while only very few groups have the equipment to execute all of the defined tests [283, 284], most laboratories have the possibility to perform at least some of them.

By following the ISOS tests it is now easier to intercompare results from different laboratories. The reported cell stabilities can then be classified according to the ISOS protocols, as has been done in a recent review by Gevorgyan et al. [126]. For that work the COST StableNextSol consortium, composed of a majority of the European research groups in the field of OPV stability, joined forces

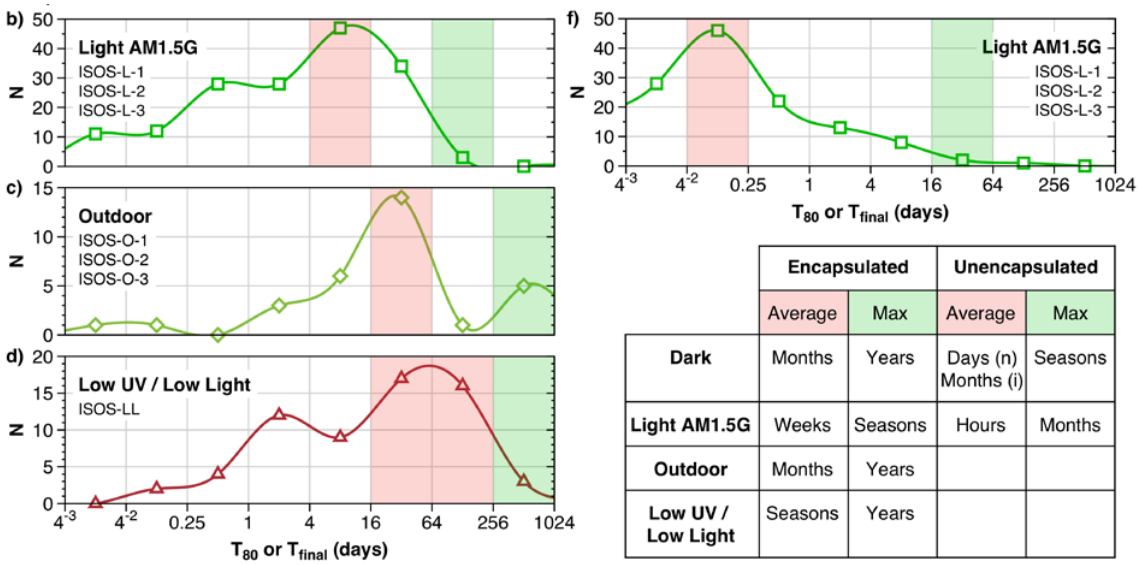

	Encapsulated		Unencapsulated	
	Average	Max	Average	Max
Dark	Months	Years	Days (n) Months (i)	Seasons
Light AM1.5G	Weeks	Seasons	Hours	Months
Outdoor	Months	Years		
Low UV / Low Light	Seasons	Years		

Figure 1.7: Distribution of lifetimes for different testing conditions and ISOS protocols. Plot taken from [126].

and data-mined all existing literature for data on OSC lifetimes. The data that could be assigned to a specific ISOS condition were then assembled, giving a total of 983 datasets, and analysed further. The results are shown in Fig. 1.7, therein classified by the specific ISOS test. The data shows that the photodegradation strongly depends on the illumination source and intensity. So, devices photodegraded with low intensity or with low UV-part of the spectrum as well as devices aged under real outdoor conditions are more stable than devices illuminated by an artificial AM1.5g spectrum. The relatively higher outdoor stability can be explained by both the lower average light intensity as well as by the daily cycling, allowing part of the performance to restore overnight [285–287]. Figure 1.7 furthermore shows that the shelf-life stability of cells in the dark already reaches up to years, being a very promising result.

1.4.3 *Architectures and Encapsulation*

Figure 1.8 compares the stability of organic solar cells with different architectures. The standard architecture has already been described above, where the layers are deposited in the order transparent anode - active layer - metal cathode. In an inverted stack design a transparent electron contact, often ZnO, is deposited first, followed by the active layer and a metallized hole contact. In this configuration the upper contact is a high-workfunction metal, while the more sensitive low-workfunction contact is buried inside [255–257].

The standard stack, having the metallic cathode on top, is much more sensitive to the surrounding air and therefore the lifetimes are on the order of days when the cells are not encapsulated. Encapsulation leads to a pronounced increase of lifetime to several months, showing that the dominant degradation mechanisms are oxygen- and water-induced (see Fig. 1.8). In inverted stacks the sensitivity to oxygen and water is strongly reduced, showing in the higher lifetimes on the order of months for unencapsulated cells. Here encapsulation only slightly improves the stability [257, 268, 288, 289].

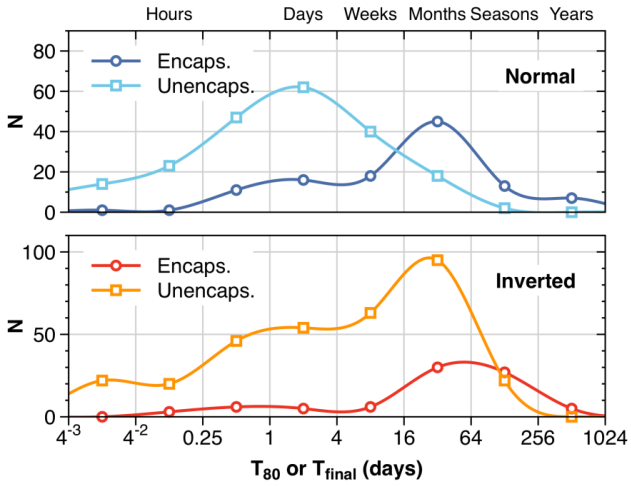

Figure 1.8: Distribution of lifetimes for standard and inverted, encapsulated and unencapsulated organic solar cells. Plot taken from [126].

1.4.4 *Status*

The stability of organic solar cells has increased a lot during the last years. As described above, two main developments have contributed to this progress - the inverted stack and encapsulation. Of course another important aspect is the development of new active layer materials and the use of alternative functional layers. The hygroscopic and acidic PEDOT:PSS has been shown to introduce several degradation mechanisms into the system. Thus, by replacing PEDOT:PSS with alternative hole transport materials like MoO_3 or V_2O_5 the stability can be enhanced [228, 229, 234, 290]. Furthermore the introduction of ultrathin interface layers at the electron contact has been demonstrated to improve both efficiency and stability [240, 251, 267]. Finally, also the active materials can be made more stable by chemical optimization [213, 214], and the layer morphology can be stabilized using crosslinking methods [204, 208, 209].

All of these efforts have led to the progress in device stability as observed in Fig. 1.4. Figure 1.9 shows the highest reported lifetimes under different conditions. Today T_{80} times of more than 2 years (17000 h) have been reported under dark and outdoor conditions [131, 276, 291–297].

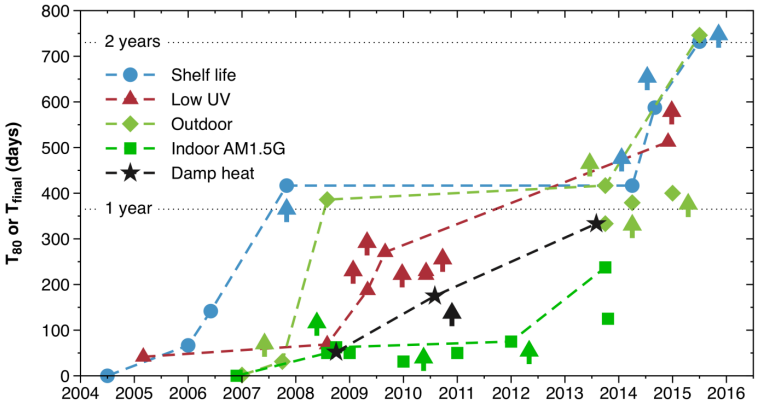

Figure 1.9: Best reported lifetimes of organic solar cells under different testing conditions. Plot taken from [126].

1.5 MOTIVATION AND CONTENTS

While organic light-emitting diodes are already an industrial-scale technology, organic solar cells are not yet at this stage. The three basic challenges efficiency, cost, and stability need to be solved in order to make organic photovoltaics a powerful product. While the cost factor is mainly governed by processing and the choice of materials, the improvement of efficiency and stability requires a fundamental understanding of the physical processes and relations. Many numerical methods and experimental techniques have been developed to address these issues, to quantify parameters, analyse correlations and to develop a deeper understanding of the macroscopic and microscopic device physics. As pointed out, OLEDs and OSCs employ the same or similar materials and their function is based on the same physics. Thus, many experimental techniques as well as modelling approaches are applicable to both OLEDs and OSCs.

The physical processes we are interested in are charge carrier injection/extraction, transport and recombination. This implies that we focus on electrical characterization techniques. The most common electrical measurement are current-voltage curves, which assess the steady-state (equilibrium) device current depending on the applied external bias (and on illumination in the case of solar cells). However, dynamic measurements can provide a lot of additional valuable information. We therefore mainly employ a range of transient techniques as well as frequency-domain experiments like impedance spectroscopy.

The novelty of our work is based on the combination of several experimental techniques in the dc, ac- and transient modes, both in measurement and simulation. This is possible only due to the development of the measurement setup *Paios* and the integration of the simulation software *Setfos* into the same graphical user interface [298, 299]. The various measurements are only comparable because they can be performed with the same equipment in a short time and without changes of the device or the measurement conditions during the measurement time. This is even more important when investigating degradation. The crucial factor governing the modelling part is that the computation times have strongly reduced in the last years due to improved algorithms, now for the first time enabling multi-mode simulations of all investigated electrical techniques. The approach of combining several experiments and adding simulation is proposed as a powerful, yet inexpensive way for device investigation and material screening.

Simulation-based analysis is expected to allow to derive new analytic formulas for material and device parameter determination, as well as to test existing formulas and their validity.

The other goal of this work is to find out how the combinatorial approach can help to investigate device degradation. One part of this goal is realized through the *Paios* setup which yields very systematic datasets during the degradation progress. The second part is the identification of the dominant degradation mechanisms with help from numerical modelling. We want to find out if, with this concept, we are able to arrive at the same conclusions as other groups, who have investigated degradation with much more expensive and complex experiments.

As we are mainly dealing with solution-processed and small-area research cells, the reproducibility of fabrication is rather low. This implies that often a qualitative understanding of the participating processes is more valuable than a full quantitative description of one specific device. This is why we put a lot of focus on qualitative behaviour and "shapes" of the different experimental curves. Especially when investigating the changes during degradation, a synoptic view

on several experiments helps to draw conclusions and understand the underlying processes. The modelling can then confirm these assumptions by demonstrating the connections and sensitivities of experiments on specific parameters. Often several physical and chemical processes happen in parallel during degradation, some of them linked, some of them independently. In these cases we concentrate on the most severe mechanism that dominates the performance loss. This comes with the side effect that we are not able to quantitatively describe the device at all times during ageing, but helps to point out the most important problems.

The following paragraph gives a short overview of the contents of this thesis. In Chapter 2 we present the automated measurement platform *Paios* which was employed for nearly all experiments in this work. We also introduce various experimental techniques that have been used and analysed a lot. Chapter 3 gives an introduction to drift-diffusion modelling, and summarizes various theoretical models that have been employed in the simulation to describe the measurements.

In Part II we investigate new methods for parameter extraction, hereby employing polar OLEDs. After an introduction to polar OLEDs in Chapter 4 we present the MIS-CELIV approach for determination of the charge carrier mobility in Chapter 5. The following Chapter 6 contains a method for extraction and discrimination of the thermal activation energies of injection and transport in polar OLEDs and MIS-devices. Finally we show some degradation measurements on polar OLEDs in Chapter 7. The part is closed with Chapter 8 by a summary and discussion of further applications of the parameter extraction methods.

Part III is the main part of this thesis containing results on organic solar cells and their degradation under different conditions. In Chapter 9 we analyse initial defects that are very common for hand-made research devices, and which not only affect device efficiencies, but also can aggravate parameter analysis.

Chapter 10 presents a degradation study on unencapsulated organic solar cells, that have been exposed to humid air leading to a loss in effective area due to oxidation of the aluminium electrode. Encapsulated cells have been subject to photodegradation in Chapters 11 & 12, where we investigate the hypothesis that the photodegradation process is independent on the illumination concentration.

The findings of this thesis are summarized in Chapter 13 and further discussed and put in a larger context in Chapter 14.

The first chapter in the Appendix (Part V) contains additional information regarding simulation parameters (Appendix A). In Appendix B we show several global fits of various measurements with one set of parameters quantitatively describing the cells. Finally, in Appendix C we perform parameter sweeps in order to better understand the sensitivities of different experiments on specific material and device parameters.

2 EXPERIMENTAL

We aim to contribute to a better understanding of the physical processes in organic electronic devices by employing a range of opto-electrical measurement techniques. So, in addition to current-voltage curves, which are the most common characterization technique for OSCs and OLEDs, we perform transient and impedance measurements. By measuring the same device with several of these techniques, it is possible to identify physical processes by their specific signatures in the different measurements. Often for this purpose much more complicated, expensive and time-consuming experiments need to be performed, which we aim to avoid with our approach. Our concept also adds the modelling of all the performed experiments to the process, thereby allowing us to validate proposed hypotheses. While we will introduce the simulation model in Chapter 3, here we present the measurement setup *Paios* that has been employed for the experimental work.

2.1 PAIOS PLATFORM

The *Paios* "All-in-one Characterization Platform for Organic Light-Emitting Diodes and Solar Cells" has been developed by the company Fluxim AG, and could be employed by the author in their lab as well as in the Organic Electronics and Photovoltaics Laboratory at the Institute of Computational Physics of ZHAW. The author has also been involved in the software development of *Paios*.

The main goal behind *Paios* is to deliver a reliable, systematic set of data from different experiments of the same device in a short time. Today many labs have dedicated measurement setups for specific experiments, for example a source-measure-unit (SMU) setup for current-voltage acquisition, a digital oscilloscope for transient measurements, and an impedance analyser. Not only is such equipment expensive, performing several experiments on the same device leads to time-consuming transfer time from one setup to the other, and to a loss of systematics and comparability. All electrical equipment comes with its own systematic measurement errors, internal resistance, eventually different contacting probes, and sometimes even a different lab. This makes it impossible to fully intercompare data acquired with different equipment, and it is highly inconvenient in order to perform systematic series of measurements, for example to investigate degradation.

Therefore the *Paios* system has been developed and is commercially available since 2012 in a Solar Cell and an OLED version. The system basically consists of two sets of function generators and digital oscilloscopes. The first set is used to drive and measure the device under test (DUT). The function generator hereby applies a transient voltage signal depending on the measurement type. For impedance measurements a small modulation voltage is added on top of a constant offset. For steady-state measurements several types are implemented, allowing different accuracy levels and acquisition times. The resulting current of the device under test is then measured over the internal resistance with the digital oscilloscope.

In the solar cell version the second function generator − digitizer pair is used to drive and measure a high-power white LED [300] employed as illumination source. This allows to perform short light pulses, but also constant-illumination measurements. It also allows to vary the illumination intensity over several orders of magnitude by controlling the LED current. In the OLED version

the second digitizer measures the signal from an amplified photodetector, and thus records the electroluminescence of the DUT.

Using a trans-impedance amplifier currents between 1 nA and 100 mA can be well resolved. This and other specifications of *Paios* are given in Table 2.1. These properties make *Paios* well-suited for the investigation of thin-film organic electronic devices.

MEASUREMENT SPECIFICATIONS		
Voltage Range	± 10	V
Minimum Current	< 1	nA
Maximum Current	± 100	mA
Voltage measurement resolution	12	Bit
Current measurement resolution	12	Bit
Maximum sampling rate	60	MS/s
Minimum time resolution	16	ns
Minimum signal length	1	μs
Maximum signal length	5	h
Impedance frequency range	$10^{-2} - 10^{7}$	Hz

Table 2.1: *Paios* measurement specifications.

2.1.1 *RC Effects and Displacement Currents*

When investigating transient electrical signals one always has to take RC-effects into account, which are the main source of displacement currents. According to Maxwell's equations a changing external or internal electric field induces a displacement current [301]:

$$J_{disp} = \left(\varepsilon_0 \varepsilon_r \frac{\partial V_{ext}(t)}{\partial t} \right) + \int_0^d \left(\varepsilon_0 \varepsilon_r \frac{\partial \mathcal{E}(x,t)}{\partial t} \right) \tag{2.1}$$

The capacitance is hereby the effective capacitance of the layer stack, thus in first approximation $C = \frac{\varepsilon_0 \varepsilon_r}{d}$. The series resistance is composed of the contact resistance between the probes and the electrodes, the lateral resistivity of the electrodes, the resistance of the cables, and the measurement resistance of the setup. While the latter can be calibrated and corrected for, the first are device-specific. The most simple equivalent circuit to describe this is shown in Figure 2.1a, where the device is described as a diode with the geometric capacitance C, and where R_s is the external series resistance.

In many devices shunts leading to leakage currents and a non-blocking behaviour in reverse complicate the situation. In this case part of the current flows through the parallel resistance R_p which is no longer high enough to be blocking. The situation is shown in Fig. 2.1b. When the

applied device voltage and the measured device current are known the signals can be corrected according to:

$$V_{dev} = R_s \cdot I_{dev} + V_c \tag{2.2}$$

$$I_{dev} = I_{meas} = I_{pure} + \frac{V_c}{R_p} + C \cdot \frac{dV_c}{dt} \tag{2.3}$$

$$I_{RC} = \frac{V_c}{R_p} + C \cdot \frac{dV_c}{dt} = f\left[V_{dev}(t), R_s, R_p, C\right] \tag{2.4}$$

$$I_{corr} = I_{pure} = I_{dev} - I_{RC} \tag{2.5}$$

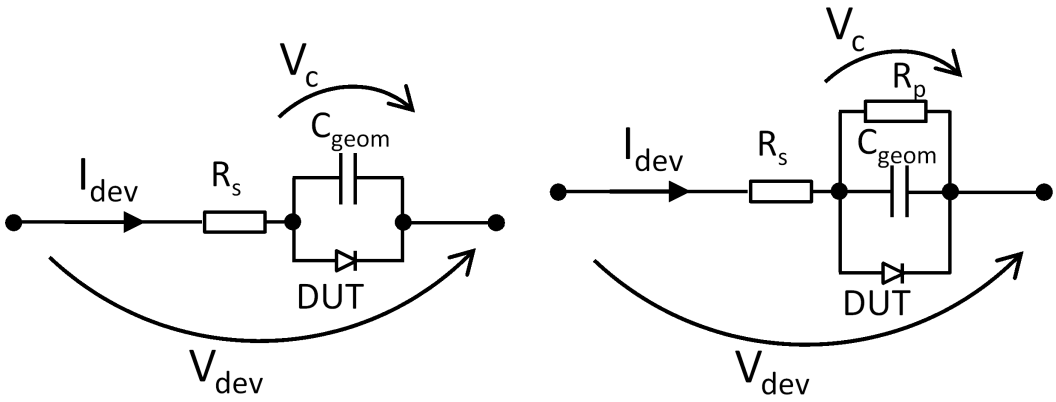

(a) Equivalent circuit with series resistance, geometric capacitance and diode.

(b) Equivalent circuit with series and parallel resistance, geometric capacitance and diode.

Figure 2.1: Equivalent circuits taking into account series and parallel resistance of the device.

The influence of the series and parallel resistance can be visualized in *Paios*. Especially in transient measurements they can affect the signal strongly, and can also distort parameter analysis or even render it impossible. So, for example CELIV currents are slowed down by a series resistance, leading to a photo-CELIV peak at later times and thereby to an underestimation of the charge carrier mobility, as seen in Fig. C.1f [302]. In case the device is non-blocking in reverse as a result of shunting (low parallel resistance), the CELIV current does not show a plateau but the parallel/parasitic current rises strongly and can completely hide the peak feature (see Fig. C.4b). But also in steady-state, both series and parallel resistance affect the performance of a solar cell. We will discuss these influences further in Sections 9.1 & 9.2, and we show simulation results with varying series and parallel resistance in the Appendix C.1 & C.2.

2.1.2 *Flex-Res*

An important feature of *Paios* is the flexible transient sampling method. This allows to resolve 6 orders of magnitude in time in a single transient measurement. Using a linear sampling would lead to a problem in storing all the measured points, therefore with a reasonable number of data points only three orders of magnitude in time are accessible. The "Flex-Res" feature makes it possible to analyse transients in log-t scale, where specific features of charge transport can be identified more easily. The function is also very valuable for perovskite devices where charge

and ion transport happen on different timescales. Figure 2.2 shows an example of the transient photocurrent rise of a perovskite solar cell upon turning on the LED. Using a linear sampling the initial rise and overshoot could not be resolved in the same measurement with the slow second rise.

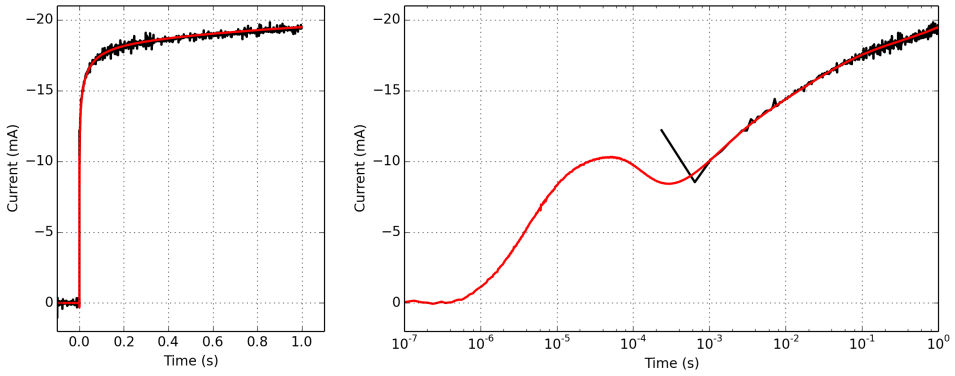

Figure 2.2: Transient photocurrent rise of a perovskite solar cell with flexible time sampling (Flex-Res). The two graphs show a linear and logarithmic representation of the time axis. The black line corresponds to a linear sampling rate, the red line shows the same measurement acquired with Flex-Res. Plot taken from [303].

2.1.3 *Series Measurements*

Another functionality of *Paios* that has been used extensively in this work is the "Series Measurement Module". It allows to repeat a measurement routine automatically after a specified condition is fulfilled. So it is perfectly suited for stress-tests and accelerated ageing. Devices may be stressed by applying a voltage, current and/or illumination. The module can also be coupled with the "Temperature Module" of *Paios* in order to investigate low-temperature behaviour or to perform thermal stress tests. Due to the automation the resulting set of data is highly systematic and consistent, which can be crucial when ruling out other effects.

2.2 MEASUREMENT TYPES

In the following we will introduce the various measurement types that *Paios* offers and which have been extensively used in this work. Many experimental techniques employed in organic electronics research have their origins in the inorganic semiconductor field and have been transferred to OSCs and OLEDs. However, in some cases the analytic framework to describe these measurements is then no longer valid and needs adaptation. By simulating the experiments we are able to examine the analytic routines for parameter determination and find out the limitations of their validity. The following overview introduces the different experimental techniques and informs about correlations with specific parameters. For simulated parameter sweeps of the various experiments we refer to the Appendix C.

- **Current-Voltage Curve (IV)**

  The current-voltage curve is the default characterization technique for solar cells. The standard solar cell parameters short-circuit current (I_{sc}), open-circuit voltage (V_{oc}), fillfactor (FF), maximum power point (V_{mpp}, I_{mpp}) and power conversion efficiency (η) are determined from it. The efficiency can be calculated knowing the incident illumination intensity P_{light} :

$$\eta = \frac{V_{mpp} \cdot I_{mpp}}{P_{light}} = \frac{V_{oc} \cdot I_{sc} \cdot FF}{P_{light}} \tag{2.6}$$

  where the fillfactor is defined as $FF = \frac{V_{mpp} \cdot I_{mpp}}{V_{oc} \cdot I_{sc}}$.

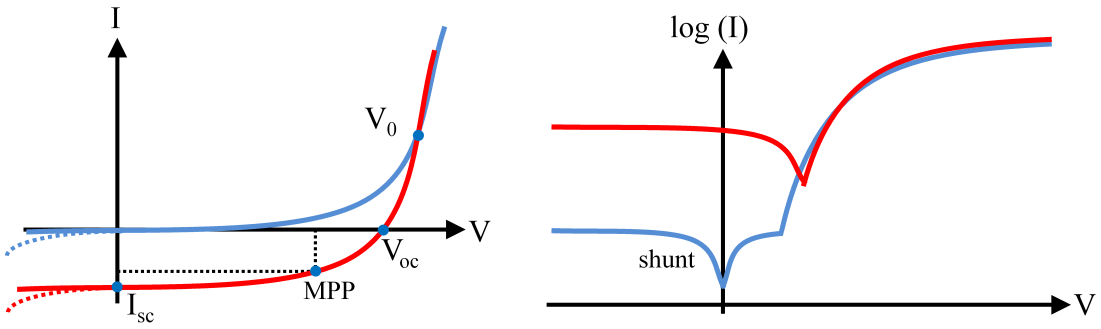

(a) Linear scale.

(b) Logarithmic scale.

Figure 2.3: Schematics of the dark and light current-voltage curve in linear and logarithmic representation. The parameters mentioned in the text are indicated.

  By analysing the slope of the open-circuit voltage versus the light intensity L in a log-lin plot information about the recombination mechanism (geminate or non-geminate recombination) can be obtained [304–309]. Furthermore the light ideality factor is calculated as [310]:

$$n_{id} = \frac{q}{k_B T} \cdot \frac{dV_{oc}}{dln(L)} \tag{2.7}$$

  At low light intensities the slope of the short-circuit current versus the light intensity is proportional to the photon-to-charge conversion efficiency, which can be related to the exciton dissociation efficiency. Furthermore the saturation of the photocurrent at high light intensities can be observed [304, 311].

  The fillfactor is affected by the series and parallel resistance of the device as well as the recombination losses (see Appendix C) [312].

  Furthermore the voltage V_0 where the photocurrent (difference between light and dark IV-curve) becomes zero, can be interesting to study, as it allows conclusions about the contact selectivity.

  In the high-voltage regime of the dark IV-curve, unipolar and sometimes also bipolar devices exhibit a space-charge limited current (SCLC) which can be used to determine the mobility. In the unipolar case the current follows the Mott-Gurney relation [313–317]:

$$I_{SCLC} = \frac{9}{8} \epsilon_0 \epsilon_r \cdot S \cdot \mu \cdot \frac{V_{eff}^2}{d^3} \tag{2.8}$$

where the effective voltage is reduced by the built-in voltage and the series resistance:

$$V_{eff} = V_{app} - V_{bi} - I \cdot R_s \tag{2.9}$$

An extension of this model includes the Poole-Frenkel effect which describes the field dependence of the mobility: $\mu = \mu_0 \cdot exp\left(\gamma\sqrt{\frac{V_{eff}}{d}}\right)$, giving [318]:

$$I_{SCLC_{field}} = \frac{9}{8}\epsilon_0\epsilon_r \cdot S \cdot \mu_0 \cdot \frac{V_{eff}^2}{d^3} \cdot exp\left(\gamma\sqrt{\frac{V_{eff}}{d}}\right) \tag{2.10}$$

Another approach to analyse IV-curves is the use of equivalent circuit models as in Fig. 2.1. The most common one is the 1-diode-model using the Shockley equation (see Eq. 3.1). In order to describe real devices, the series and shunt resistance have to be taken into account. As shown in Sections C.1 & C.2 these can strongly influence the solar cell parameters.

- **Capacitance-Frequency (C-f)**

  The impedance of a device is measured by applying a small sinusoidal voltage and measuring the current response (see also Eqs. 3.25 & 3.26). The impedance is then defined by:

$$Z = \frac{V(t)}{I(t)} = Re(Z) + iIm(Z) = |Z| \cdot e^{i\phi} \tag{2.11}$$

  If the amplitude of the voltage modulation is small enough the device acts linear in the specified working point (offset voltage, offset illumination), and the measured current signal has the same frequency as the applied voltage sinus. By using a large range of frequencies $f = \omega/2\pi$ different physical effects in the device can be distinguished due to their different characteristic timescales. Traps can for example show an effect in the low frequency range, while the series resistance leads to a cutoff at high frequencies [319–321].

  Impedance-frequency measurements are often plotted showing the real and imaginary parts of the impedance or the admittance in a Cole-Cole-plot [175, 319–329]. These plots are usually analysed by equivalent circuit models. Here one half-circle is related with one RC-circuit, and by combining several resistances and capacitances in series and parallel, many shapes of the Cole-Cole-plot can be reproduced. A major task is then the interpretation of the equivalent circuit and the assignment of the different elements to physical processes and device parameters [327–329]. For this purpose the impedance-frequency is measured at varied offset voltage or light intensity, and the behaviour of the equivalent circuit fit parameters versus the varied parameter is analysed.

  Further the admittance, capacitance and conductance of the device can be calculated according to Eqs. 3.26. The geometric capacitance is usually extracted as the limit in the dark and at reverse bias, however traps or doping can complicate the analysis. The capacitance-frequency plot is often used to study traps because the capacitance in the low frequency range increases with trap density [330–332].

- **Capacitance-Voltage (C-V)**

  For the Capacitance-Voltage analysis, the impedance of the device is measured versus varied offset voltage at a constant frequency, and the calculated capacitance is analysed [177, 325,

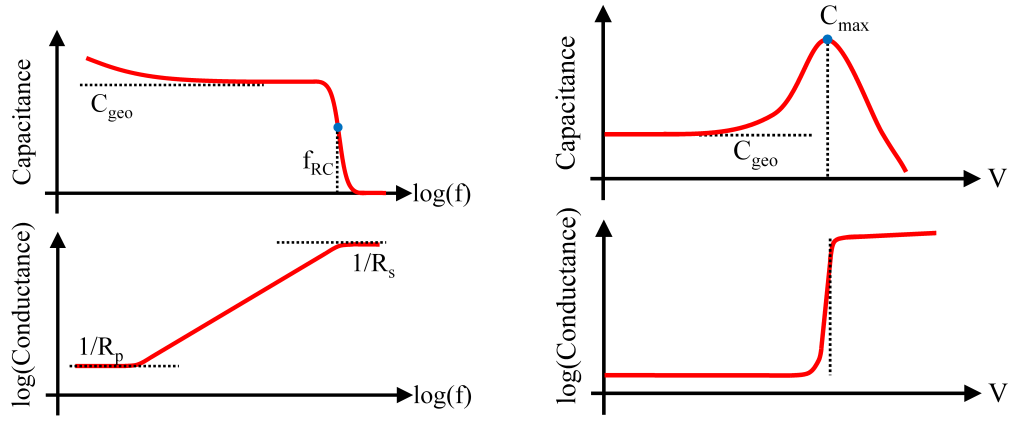

(a) Capacitance-frequency / Conductance-frequency.

(b) Capacitance-voltage / Conductance-voltage.

Figure 2.4: Schematics of the capacitance and conductance measured a) versus frequency and b) versus voltage.

333–336]. Again, the capacitance limit for negative bias is identified as the geometric value. Further a peak around the built-in voltage is often observed, which however also depends on various other parameters.

A Mott-Schottky analysis can be employed in order to extract doping densities and the built-in potential. For this purpose the inverse of the squared capacitance is plotted (see also Eq. 11.1), and in case the device shows the build-up of a space-charge region, the plot is linear. However, it has been shown that the extracted doping density is only valid for thick and highly doped devices [337–339]. Under some conditions a Mott-Schottky behaviour is also observed for illuminated C-V measurements (see Fig. 11.2b).

- **Transient Photocurrent (TPC)**

  For this measurement technique the device is flashed with a light pulse, charges are generated and the transient photocurrent is measured at short-circuit or with an offset voltage applied [340–345].

  The dynamics of the TPC rise and decay are directly linked to the charge carrier mobilities. It is, however, not yet clear if a quantitative model to determine the mobilities can be found.

  In some cases where charges accumulate due to an energy barrier or due to trapping an overshoot in the TPC rise can be observed, and sometimes even an undershoot after turning the light off again appears.

  The TPC can also be performed as a small-signal technique where at a given working point defined by offset light and voltage a small light pulse is added. The decay of the photocurrent is then integrated as a measure of the amount of extracted charge. This experiment is usually combined with the small-signal transient photovoltage decay, in order to calculate the differential capacitance.

- **Transient Photovoltage (TPV/OCVD)**

  For the transient photovoltage measurement the device is forced into the open-circuit condition by using a high load resistance, so that no current can flow. The TPV signal is the

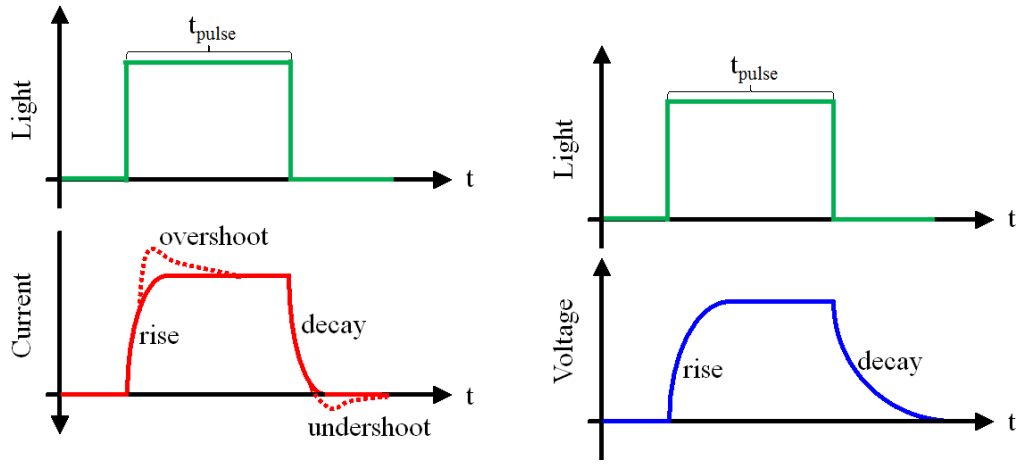

(a) Transient photocurrent.

(b) Transient photovoltage.

Figure 2.5: Schematics of the transient photocurrent and photovoltage experiments.

voltage response to a light pulse, and usually the decay of the signal after turning off the light is analysed. The assumption is that the open-circuit voltage can only decay by charge recombination, therefore the decay kinetics can give information about the recombination mechanism.

This method can be performed as a large-signal technique (OCVD) but also using a small light pulse on top of an offset illumination [306, 346].

The TPV decay is then fitted with a mono- or biexponential law, in order to analyse the recombination lifetimes. Often the extracted lifetime for varied offset light intensity is plotted versus the charge density that is obtained from the corresponding small-signal TPC decay [306, 346–350]. The use of TPV in organic solar cells is still under debate, as this technique was originally developed for inorganic devices with minority carriers. In contrast to this, in OSCs the recombination law is not easy to determine and the measurement can be influenced by the used measurement resistor as well as by a nonideal parallel resistance (see Section C.2).

- **Charge Extraction by Linearly Increasing Voltage (CELIV)**

  Charge extraction by linearly increasing voltage measures the current response to a negative voltage ramp. According to Maxwell's law a linearly changing external field induces a constant displacement current I_0 in the organic layer [351]:

  $$I_0 = \frac{\varepsilon_0 \varepsilon_r \cdot S \cdot \mathcal{A}}{d} = C_{geo} \cdot \mathcal{A} \ , \tag{2.12}$$

  where $\mathcal{A} = \frac{dV}{dt}$ is the negative voltage ramp rate. The displacement current plateau can thus be used to determine the geometric capacitance.

  I_0 can be superimposed by a current peak, if charges are in the layer prior to the ramp that can be extracted by the negative field. This peak contains information about the charge carrier mobilities, the number of charges, and furthermore about disorder.

  Various modifications of the CELIV technique exist:

  – In Dark-CELIV the ramp is applied in the dark and without an offset voltage. Usually then only the constant displacement current is expected. In the special case of doping,

however, mobile equilibrium carriers are extracted, leading to an overshoot [175, 302, 352].

- For Injection-CELIV a positive offset voltage is applied, so that an injection current flows before the ramp. During the ramp the current reverses and shows a peak before reaching the displacement plateau [353–355].
- In Photo-CELIV the device is illuminated and an offset voltage around V_{oc} is applied prior to the ramp, so that no current flows. The ramp then extracts the photogenerated carriers showing in a peak on top of the displacement current plateau [302, 356–360]. While we wait for steady-state before starting the ramp, other groups are working with short laser pulses generating many charges instantaneously, before the ramp starts. We find, however, that deviations from zero of the current before the ramp can influence the extracted parameters strongly [352, 356].
- MIS-CELIV is basically an Injection-CELIV experiment performed on a MIS-device. The difference is that charges are injected by a positive pre-bias, but no equilibrium current can flow, so the CELIV current starts at zero, making it easier to interpret [353, 354, 361–363].
- In Delaytime-CELIV the Photo-CELIV measurement is performed several times with a varying delaytime between the light pulse and the voltage ramp. During the delaytime charges can recombine and less charges are extracted. The technique can therefore be used to study the recombination kinetics [364–368]. Keeping the voltage at a constant value during the delaytime, however, can lead to counter-injection. OTRACE therefore adapts the voltage according to the TPV decay during the delaytime, such that the current is always zero prior to the ramp [369, 370].
- In Reverse-CELIV a positive voltage ramp is applied, starting at a negative bias. The current then rises to the displacement current plateau, and when injection sets in, increases rapidly. This technique is only interesting in MIS-devices or strongly degraded cells [228].

The CELIV technique was originally developed to investigate the charge carrier mobility. In a simple picture charges inside the active layer drift in the external, changing electric field towards their respective electrodes. A basic analytical model assuming a homogeneous carrier distribution as well as a position-independent field was deduced, relating the transient position of the current peak with the carrier transit time and therefore with the mobility [351, 352]:

$$\mu_{CELIV} = \frac{2d^2}{3\mathcal{A} \cdot t_{max}^2 \cdot \left(1 + 0.36 \frac{I_{max} - I_0}{I_0}\right)} \tag{2.13}$$

Due to the simplification made in the derivation of this formula, its application is very limited and usually gives only the order of magnitude of the mobility. Several adaptations and improvements have been attempted [302, 368, 371, 372], one of which is the approach by Lorrmann et al. [360]:

$$\mu_{CELIV} = \frac{d^2}{2\mathcal{A} \cdot t_{max}^2} \cdot \left[\frac{1}{6.2 + 0.0124 \frac{I_{max} - I_0}{I_0}} + \frac{1}{1 + 0.12 \frac{I_{max} - I_0}{I_0}}\right]^2 \tag{2.14}$$

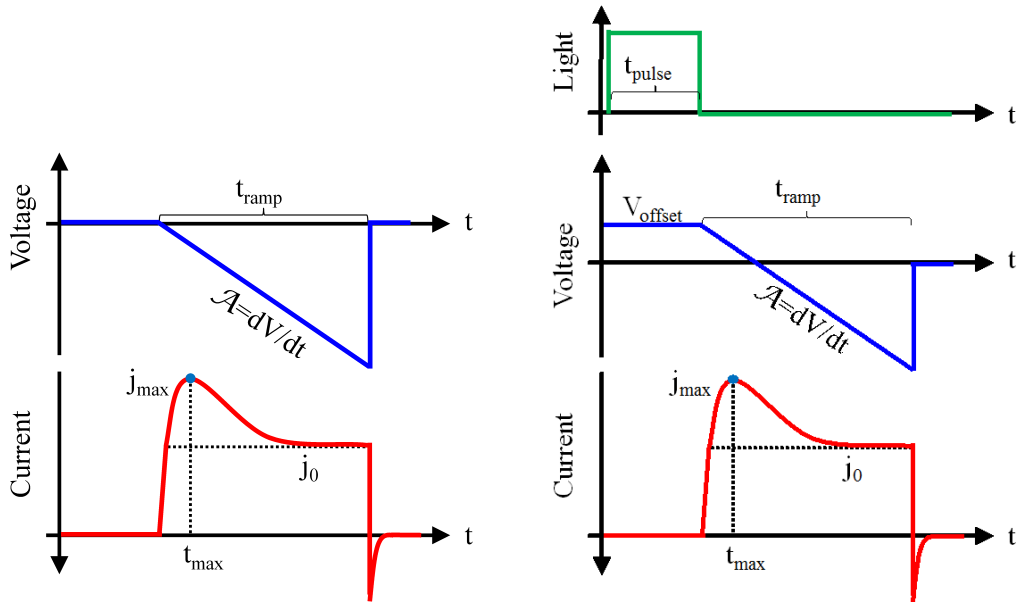

(a) Dark-CELIV / MIS-CELIV. (b) Photo-CELIV.

Figure 2.6: Schematics of the dark-CELIV/MIS-CELIV and photo-CELIV experiments, indicating the parameters mentioned in the text.

By integration of the current peak the number of extracted charges is calculated. Due to recombination losses, and due to the finite ramp time, only part of the charges can be extracted [352, 356]. In principle with a faster ramp more charges are extracted.

$$N_{CELIV} = \frac{1}{q \cdot d \cdot S} \int \left(I(t) - I_{disp}(t) \right) dt \tag{2.15}$$

In OTRACE the number of extracted charges decays with the delaytime due to recombination:

$$\frac{dn}{dt} = -R = -k_1 n - k_2 n^2 \tag{2.16}$$

The equation takes into account recombination losses by bimolecular recombination (second order) as well as first-order recombination losses (Shockley-Read-Hall, trap-assisted recombination). The general solution to this Ricatti equation is

$$n(t) = \frac{-k_1 \cdot exp\left(k_1 c_1\right)}{k_2 \cdot exp\left(k_1 c_1\right) - exp\left(k_1 t\right)} \tag{2.17}$$

With the initial charge density $n(t = 0) = n_s$ as the boundary condition we obtain

$$n(t) = \frac{k_1}{\left(\frac{k_1}{n_s} + k_2\right) \cdot exp\left(k_1 t\right) - k_2} \quad \text{for } k_1 > 0 \tag{2.18}$$

If first-order recombination can be neglected, that is $k_1 = 0$, the solution to Eq. 2.16 becomes

$$n(t) = \frac{n_s}{k_2 n_s t + 1} \quad \text{for } k_1 = 0 \tag{2.19}$$

Herein the recombination constant k_2 is often called β in literature [373]. When the recombination is Langevin-type, the bimolecular recombination constant is related to the charge carrier mobility: $\beta_L = \frac{e\mu}{\epsilon_0 \epsilon_r}$.

- **Charge Extraction (CE)**

  In the charge extraction experiment a reverse extraction voltage is applied after the illumination is turned off. During the light pulse the applied voltage is adapted such that no current flows. The extraction current is then integrated to give a measure of the photogenerated charge density at open-circuit [374–376].

  Like in OTRACE the recombination dynamics can be studied with delaytime charge extraction, where during the delaytime the TPV decay signal is applied, ensuring no current is flowing [377].

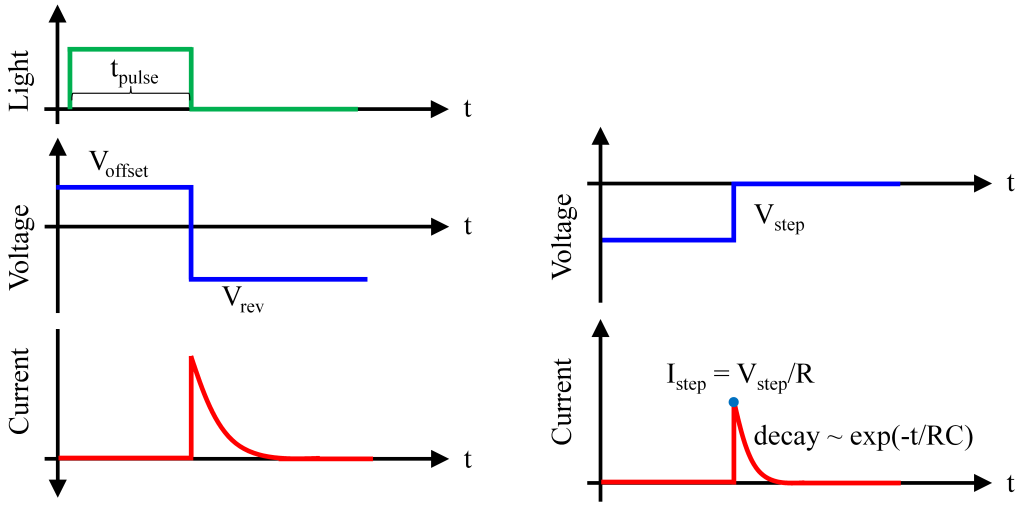

(a) Charge extraction.

(b) Voltage step.

Figure 2.7: Schematics of the charge extraction and the small voltage step experiments.

- **Small Voltage Step (VP)**

  The small voltage step experiment is used to investigate the RC-time. Assuming the device is empty of charges and a small voltage step around 0 V or in reverse is applied, only displacement current is measured. For an ideal voltage step the current peak response is inversely proportional to the series resistance, $Istep = V_{step}/R_S$, and the decay constant is the RC-time. So from this simple experiment both series resistance and geometric capacitance of the device can be determined [302].

- **Dark/Double Injection Transient (DIT)**

  The dark injection transient current is a technique to determine the mobility in thick unipolar layers. Here, when a forward voltage pulse is applied, charges are injected. The injection current is superimposed to the RC current peak and decay. In the unipolar and trap-free case, and under space-charge limited injection, a current peak can be observed. From the transient position of the peak the charge carrier mobility can be determined [331, 378–384]:

$$\mu_{DIT} = \frac{0.787 d^2}{t_{max}(V - V_{bi})} \tag{2.20}$$

The technique can also be performed in bipolar devices as double injection transient. Here a peak can occur as well, and the dynamics of the rise of the injection current can be analysed. There is, however, no analytic model for this case, and the measurement needs to be compared to simulation.

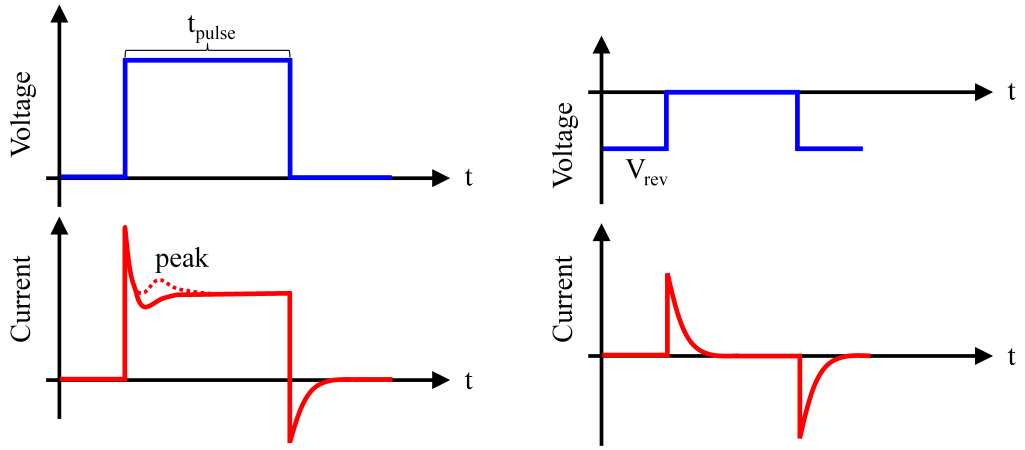

(a) Dark / double injection transient.

(b) Deep-level transient spectroscopy

Figure 2.8: Schematics of the DIT and DLTS experiments.

- **Deep-Level Transient Spectroscopy (DLTS)**

  Deep-level transient spectroscopy is a technique to study trap effects. A negative prebias is applied for several milliseconds during which all trapped charges should be released and extracted. Then the voltage is switched to zero, allowing the traps to be filled. This leads to a small current superimposed to the large displacement current due to the voltage step. After a long enough waiting time, the voltage is switched back to reverse, and the detrapping current is measured. The trap release and filling processes are strongly temperature dependent, and this measurement is usually performed in a cryostat at various temperatures [385–387]. From a sophisticated analysis it may be able to determine the trap density-of-states as well as the trapping rates. For this analysis usually the second voltage step is used, however, in case of a device with a shunt there will be a high offset current under reverse bias, so in this case the first voltage step can be analysed.

- **Intensity-Modulated Photocurrent/Photovoltage Spectroscopy (IMPS/IMVS)**

  Similar to the impedance measurement, this is a modulation technique, whereas here the illumination is modulated. For IMPS the voltage is kept constant (or zero) and the current response is measured. For IMVS the device is forced to open-circuit using a high-load measurement resistor and the voltage is analysed [388–393].

  IMPS is employed to investigate charge transport, while IMVS contains information about recombination. The peak frequency of the imaginary part of the IMPS signal is related to the charge carrier collection time τ_{sc}, and depends on transport and recombination at short-circuit [388, 394, 395]:

$$\tau_{sc} = \frac{1}{2\pi \cdot f_{max}} = \left(\frac{1}{\tau_{rec}} + \frac{1}{\tau_{cc}} \right)^{-1} \tag{2.21}$$

The peak frequency of the imaginary part of the IMVS signal is related to the recombination time at open-circuit τ_{oc} [388, 394]:

$$\tau_{oc} = \frac{1}{2\pi \cdot f_{min}} = \tau_{rec} \tag{2.22}$$

The IMPS and IMVS time constant are further related by the charge collection efficiency [394]:

$$\eta_{cc} = \frac{J_{sc}}{J_{inj}} = \frac{J_{sc}}{J_{sc} + J_{rec}} = \frac{1/\tau_{cc}}{1/\tau_{cc} + 1/\tau_{oc}} = 1 - \frac{\tau_{sc}}{\tau_{oc}} \tag{2.23}$$

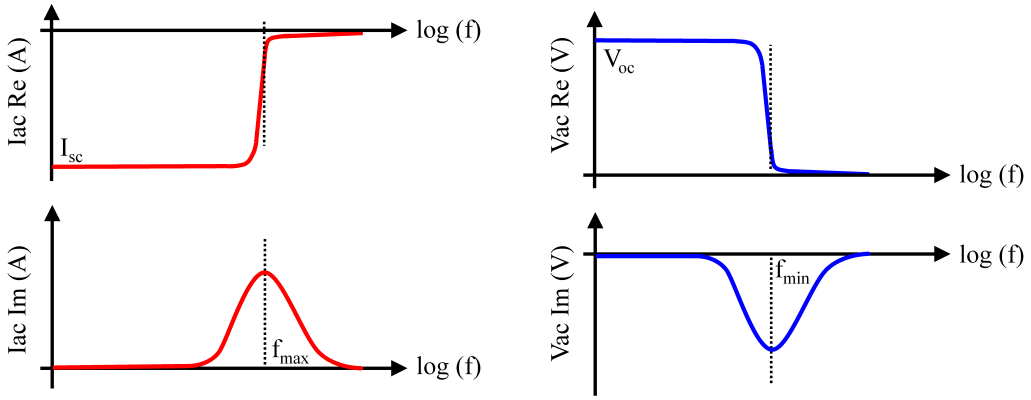

(a) IMPS real and imaginary part.

(b) IMVS real and imaginary part.

Figure 2.9: Schematics of the IMPS and IMVS experiment.

These techniques promise to hold a lot of interesting information on charge transport and recombination. Also traps may be observed by specific signatures at lower frequencies. However, a thorough simulation-based understanding of these techniques was not possible until now.

While in the main part of this thesis often only a few of the presented techniques are shown and discussed, for most studies we have performed a larger range of techniques. All of these experiments can be simulated with *Setfos* and most of them are presented in the global fits and parameter sweeps shown in Appendix B & C.

3 SIMULATION

There exist several approaches for the modelling of organic semiconductor devices [396–398]. Many of them have been originally transferred from inorganic semiconductor modelling and then adapted to the special requirements of organics. In order to simulate charge transport there are three basic routes: microscopic modelling of transport between molecules, macroscopic modelling of the transport in an effective medium, and full-device modelling. The microscopic simulations are usually employing Monte Carlo [399–401], finite elements [402] or Master equation models [403, 404], and simulate the charge transfer between molecules by hopping rates [405, 406] and based on random walk. By statistical averaging empirical models for the charge carrier mobility, for example the Gaussian disorder model (GDM) [407–409], can be found. These models parametrize the mobility dependence on temperature, electric field, charge density and the density-of-states distribution.

Situated on the other end of the model range are equivalent circuit models, that allow to analytically describe the device current depending on different parameters such as voltage or temperature. The best known of these models is the Shockley equation, that describes the IV-curve of an ideal diode [305, 410]:

$$I(V) = I_S \cdot \left[\exp\left(\frac{qV}{k_B T}\right) - 1\right] - I_{ph} \tag{3.1}$$

where I_S is the saturation dark current and I_{ph} is the (voltage-independent) photocurrent. As this equation is too simplified for use in OSCs some additions are commonly made:

$$I(V) = I_S \cdot \left[\exp q\left(\frac{V - IR_s}{n\, k_B T}\right) - 1\right] + \frac{V - IR_s}{R_p} - I_{ph}(V) \tag{3.2}$$

where the series and parallel resistance and an ideality factor n different from unity as well as a voltage-dependent photocurrent are accounted for.

A combination of several diodes, resistance, capacitance and inductance elements defines an equivalent circuit, which can describe a single cell (see Fig. 2.1), a tandem cell or even a full solar cell module. These models are mainly employed to analyse impedance data, where the different physical processes like transport or interface effects are related to the various elements of the equivalent circuit, which are characterized by their frequency-dependent resistance, conductance or capacitance [411, 412].

The intermediate class of models, which we will employ here, focuses on the description of the charge carrier generation, transport and recombination in a single device. The microscopic hopping between molecules is not taken into account, instead the outcome of the microscopic models, namely the empirical mobility relation, is employed and describes an effective mobility inside a material. The model treats each layer as an effective medium with homogeneous properties. Furthermore, when applicable, the outer functional layers (HTL, ETL) are simulated as perfect conductors presenting no limitation to charge transport, thus acting as metallic. The most common way to model charge transport in organic electronic devices is therefore the MIM-model (metal-insulator-metal) [398], where the electrodes, injection and transport layers are subsummized as metallic, and the organic semiconductor is treated as a nearly insulating,

low-conductive layer. This approach is also justified regarding the device geometric capacitance, where only the "insulating" layer contributes.

We aim to model the various experiments with a fully coupled 1D opto-electrical drift-diffusion simulation in order to understand the charge generation, transport, recombination, injection and extraction better. For this purpose we employ the commercial software *Setfos* 4 by Fluxim AG [299]. In the following the implemented physical models, which have been used, are introduced. The basic model to describe electrical charge transport is the drift-diffusion model [413–424]. As mentioned above, usually only the active layers with low conductivity are simulated, while the outer well-conducting electrodes and doped transport layers are usually treated as ideal.

Still, concerning the optical simulation, which describes the light incoupling and absorption in solar cells, respectively the outcoupling of emitted photons in OLEDs, all layers need to be taken into account. For this purpose a 1D Transfer Matrix approach is employed [413]. It calculates the absorption inside the layers, and reflection and transmission at all layer interfaces, thereby considering wavelength-dependent interference. In organic solar cells the actual optical field profile leads to a strongly thickness-dependent absorption and inhomogeneous charge carrier generation profile in the active layer. For simulating the *Paios* measurements the spectrum of the white LED light source as shown in Fig. A.2b is used for the simulation.

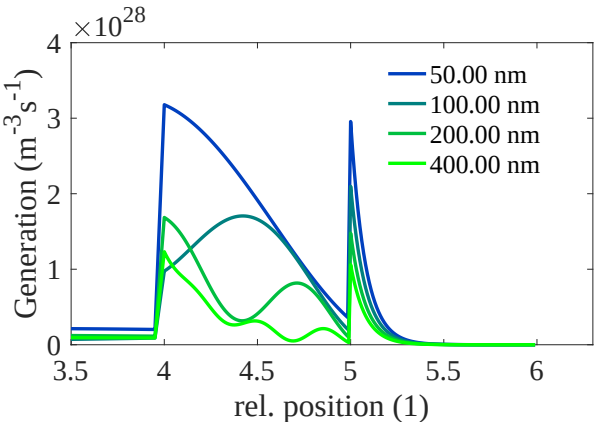

Figure 3.1: Simulated charge generation profiles for a solar cell with different active layer thicknesses. The standard layer stack (see Fig. A.1) is used, the active layer position is between 4 and 5, and the reflecting metal electrode is between 5 and 6.

As mentioned in the introduction, excitons can play an important role in organic semiconductors. In this work, however, we did not assume any exciton processes to be relevant on the investigated timescales. We choose a constant effective photon-to-charge conversion efficiency in solar cells hereby neglecting a possible field- or temperature-dependent exciton dissociation and charge generation. With this simplification the optical simulation directly gives a charge carrier generation profile $G(x)$. Figure 3.1 shows the generation profiles for various active layer thicknesses, emphasizing the wavelength-dependent interference effects and absorption profiles.

While the optical simulation is always performed, the exact generation profile has only a small influence on the transient measurements. The strongest sensitivity towards thickness and therefore on the generation profile has the spectral EQE measurement, where the actual shape is largely influenced by the various layer thicknesses and their spectral absorption coefficients.

3.1 DRIFT-DIFFUSION MODEL

Our main focus is on the electrical part of the simulation, which describes the charge carrier transport and the electrical currents.

The first equation to consider is the continuity equation:

$$\begin{aligned} \frac{dn}{dt} &= g_{opt_{np}} G_n - R_{Lang} - R_{nt} + \frac{1}{q}\frac{\partial J_n}{\partial x} \\ \frac{dp}{dt} &= g_{opt_{np}} G_p - R_{Lang} - R_{pt} - \frac{1}{q}\frac{\partial J_p}{\partial x} \end{aligned} \tag{3.3}$$

which relates the change of mobile carrier concentration at a point x due to charge generation, recombination, or a change in current. This relation ensures the conservation of charge. The generation rate results from the generation/absorption profile G times the photon-to-charge conversion rate g_{opt}, which is assumed constant here, but could include exciton dissociation models. Equation 3.3 contains two recombination terms - bimolecular, Langevin-type recombination and monomolecular, trap-assisted recombination. Note that all quantities depend on the position x in the layer.

The electric field profile is given by the Poisson equation through the mobile and immobile charge densities:

$$\frac{\partial \mathcal{E}}{\partial x} = -\frac{q}{\varepsilon_0 \varepsilon_r} \cdot (n - p + n_t - p_t + N_A - N_D) = -\frac{\partial^2 \Phi}{\partial x^2} \quad . \tag{3.4}$$

Herein $\mathcal{E}$ is the electric field, Φ is the electrostatic potential, n/p are mobile electrons/holes, n_t/p_t are trapped charges and N_A/N_D denote immobile charged species (acceptor/donor doping). The boundary conditions for the electrostatic potential at an applied voltage V are:

$$\Phi(x = d) = \int_0^d \mathcal{E}\, dx = V - V_{bi} \qquad \Phi(x = 0) = 0 \tag{3.5}$$

with the built-in potential being the electrode workfunction difference:

$$V_{bi} = \frac{1}{q}\left(WF_a - WF_c\right) \quad . \tag{3.6}$$

The charge current is driven by drift in the electric field and diffusion due to a density gradient:

$$\begin{aligned} J_n &= qn\mu_n\mathcal{E} + qD_n\frac{\partial n}{\partial x} = qn\mu_n\mathcal{E} + \mu_n k_B T\frac{\partial n}{\partial x} \\ J_p &= qp\mu_p\mathcal{E} - qD_p\frac{\partial p}{\partial x} = qp\mu_p\mathcal{E} - \mu_p k_B T\frac{\partial p}{\partial x} \end{aligned} \tag{3.7}$$

, where the Einstein relation for the diffusion $\frac{D}{\mu} = \frac{k_B T}{q}$ was used. The combination with Eq. 3.3 yields:

$$\begin{aligned} \frac{dn}{dt} &= g_{opt_{np}} G_n - R_{Lang} - R_{nt} + \frac{\partial}{\partial x}\left[n\mu_n\mathcal{E} + \frac{\mu_n k_B T}{q}\frac{\partial n}{\partial x}\right] \\ \frac{dp}{dt} &= g_{opt_{np}} G_p - R_{Lang} - R_{pt} - \frac{\partial}{\partial x}\left[p\mu_p\mathcal{E} - \frac{\mu_p k_B T}{q}\frac{\partial p}{\partial x}\right] \end{aligned} \tag{3.8}$$

The intrinsic carrier concentration is defined by:

$$n_i = N_0 \cdot \exp\left(\frac{-E_g}{k_B T}\right) \tag{3.9}$$

with the density of states N_0 and the bandgap E_g. The carrier densities are then given by

$$n = n_i \cdot \exp\left(\frac{V - E_{Fn}}{k_B T}\right) \qquad p = n_i \cdot \exp\left(\frac{E_{Fp} - V}{k_B T}\right) \tag{3.10}$$

These equations introduce the quasi-Fermilevels, which describe the filling of the density-of-states:

$$E_{Fn} = E_{LUMO} - k_B T \cdot \ln\left(\frac{N_0}{n}\right) \qquad E_{Fp} = E_{HOMO} + k_B T \cdot \ln\left(\frac{P_0}{p}\right) \tag{3.11}$$

At equilibrium in the dark $n \cdot p = n_i^2$ is always fulfilled (mass-action law), and the quasi-Fermilevels are the same, $E_{Fn} = E_{Fp}$, and lie in the middle of the band gap [425].

Under illumination this no longer holds and the quasi-Fermilevels split:

$$n \cdot p = N_0 \exp\left(-\frac{E_{LUMO} - E_{Fn}}{k_B T}\right) \cdot P_0 \exp\left(-\frac{E_{Fp} - E_{HOMO}}{k_B T}\right) = n_i^2 \exp\left(\frac{E_{Fn} - E_{Fp}}{k_B T}\right) \tag{3.12}$$

The splitting of the quasi-Fermilevels defines the open-circuit voltage:

$$qV_{oc} = E_{Fn} - E_{Fp} = E_g - k_B T \cdot \ln\left[\frac{N_0 \cdot P_0}{n \cdot p}\right] \tag{3.13}$$

Figure 3.2 depicts the steady-state solution of the combined set of differential equations for an organic solar cell under short-circuit and open-circuit conditions. The graphs show the potential distribution, the charge densities and the electric field profiles. For this simulation the default device and material parameters as summarized in Appendix A were used.

Under short-circuit condition the built-in potential leads to a nearly constant negative electric field, serving as a driving force for photocurrent extraction. Conversely, at open-circuit the electric field is zero in the main part of the device and the bands are flat. This leads to higher charge carrier densities under open-circuit condition compared to the short-circuit. Also at voltages around the open-circuit voltage diffusion currents dominate the total current, whereas otherwise drift dominates.

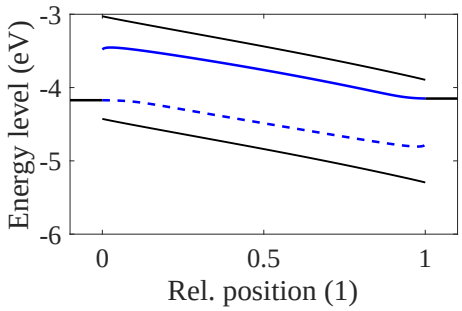

(a) Bands at short-circuit. HOMO, LUMO, electrodes (black lines), electron (solid) and hole (dashed) quasi-Fermilevels (blue lines).

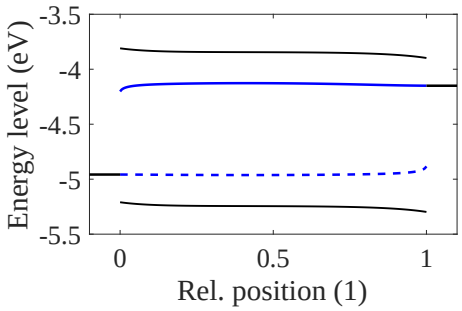

(b) Bands at open-circuit. HOMO, LUMO, electrodes (black lines), electron (solid) and hole (dashed) quasi-Fermilevels (blue lines).

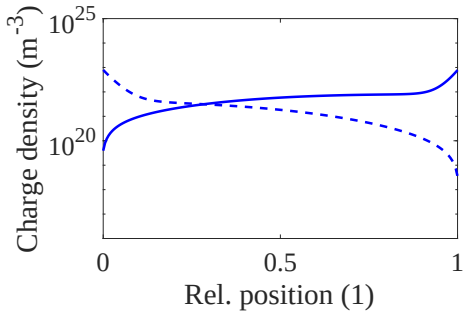

(c) Electron density (solid line) and hole density (dashed line) at short-circuit.

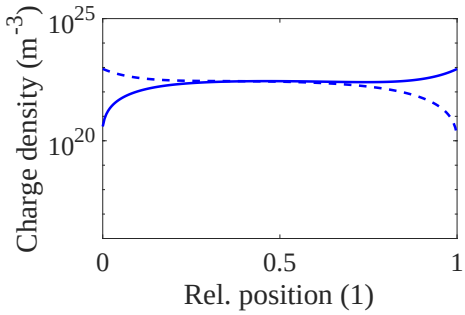

(d) Electron density (solid line) and hole density (dashed line) at open-circuit.

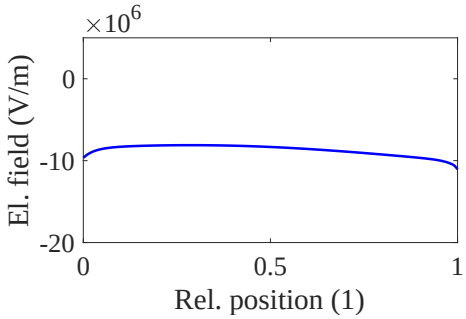

(e) Electric field distribution at short-circuit.

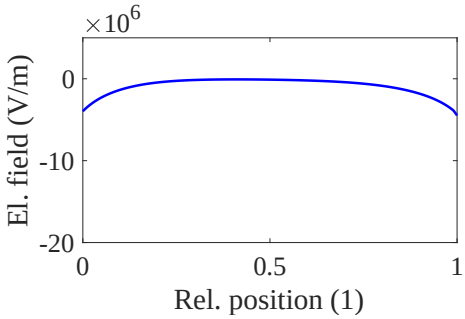

(f) Electric field distribution at open-circuit.

Figure 3.2: Simulated band, charge density and electric field profiles at short-circuit (left) and open-circuit (right) conditions. The x-axis goes from 0 (anode) to 1 (cathode).

We employ the "ohmic" injection / Schottky diffusion contact model [425–427], where the Fermilevel continuity/alignment at the electrode interfaces is prescribed. The charge densities at the interfaces to the electrodes are given by

$$n_{electrode} = N_0 \cdot \exp\left[-\frac{E_{LUMO} - WF_c}{k_B T}\right] = N_0 \cdot \exp\left[-\frac{E_c}{k_B T}\right] \tag{3.14}$$
$$p_{electrode} = P_0 \cdot \exp\left[-\frac{WF_a - E_{HOMO}}{k_B T}\right] = P_0 \cdot \exp\left[-\frac{E_a}{k_B T}\right]$$

where $E_c = E_{LUMO} - WF_c$ is the electron injection barrier and $E_a = WF_a - E_{HOMO}$ is the hole injection barrier.

The bimolecular recombination rate in Eq. 3.3 depends on both carrier densities and their mobilities [428, 429]:

$$R_{Lang} = \beta \cdot n \cdot p \qquad \beta_L = \gamma \frac{q}{\varepsilon_0 \varepsilon_r} \cdot (\mu_n + \mu_p) \tag{3.15}$$

Hereby $\gamma < 1$ is a morphology-dependent reduction factor accounting for the reduced recombination efficiency observed in many bulk-heterojunctions [430–432].

Simulations in this work including traps use single trap levels for electrons or holes, where the trapping is described by a capture-and-release model [331, 420]:

$$\frac{dn_t}{dt} = R_{nt} = c_n \cdot n \cdot (N_t - n_t) - e_n \cdot n_t \tag{3.16}$$
$$\frac{dp_t}{dt} = R_{pt} = c_p \cdot p \cdot (P_t - p_t) - e_p \cdot p_t$$

, with the release or detrapping rate $e_{n/p}$ being thermally activated and depending on the capture rate $c_{n/p}$:

$$e_n = c_n N_0 \cdot \exp\left[\frac{E_t - E_{LUMO}}{k_B T}\right] \tag{3.17}$$
$$e_p = c_p P_0 \cdot \exp\left[\frac{E_{HOMO} - E_t}{k_B T}\right]$$

In case Shockley-Read-Hall (also called trap-assisted or monomolecular) recombination [433, 434] is taken into account, holes can also be captured by electron traps and vice versa, and the change in the densities of trapped electrons and holes is:

$$\frac{dn_t}{dt} = R_{nt} - R_{pt} = c_n \cdot n \cdot (N_t - n_t) - e_n \cdot n_t + e_p \cdot (N_t - n_t) - c_n \cdot p \cdot n_t \tag{3.18}$$
$$\frac{dp_t}{dt} = R_{pt} - R_{nt} = c_p \cdot p \cdot (N_t - p_t) - e_p \cdot p_t + e_n \cdot (N_t - p_t) - c_p \cdot n \cdot p_t$$

So far we have considered only single transport levels E_{HOMO} and E_{LUMO}, which is sufficient for most purposes. In Chapter 12 we discuss the influence of disordered bands and transport. In this case the density-of-states (DOS) for electrons (so far denoted by N_0) becomes:

$$N(E) = \frac{N_0}{\sqrt{2\pi\sigma^2}} \cdot \exp\left[-\left(\frac{E - E_0}{\sqrt{2}\sigma}\right)\right] \tag{3.19}$$

where E is the energy, N_0 the total number of states, distributed around the mean energy E_0 and σ is the disorder parameter. The electron density is then obtained by the Fermi-Dirac distribution:

$$n(x, E_{fn}) = \int_{-\infty}^{\infty} N(x, E) \cdot f_{FD}(E, E_{Fn})\, dE \tag{3.20}$$

$$f_{FD}(E, E_F) = \frac{1}{\exp\left(\frac{E-E_F}{k_B T}\right) + 1} \tag{3.21}$$

The mobility can be described by the Extended Gaussian Disorder Model (EGDM), which is implemented in *Setfos* as [408, 416, 435]:

$$\begin{aligned} \mu(T, n, E) &= \mu_0(T) \cdot g_1(T, n) \cdot g_2(E) \\ \mu_0(T) &= \mu_* \cdot \exp\left[-c_2 \hat{\sigma}\right] \\ g1(T, n) &= \exp\left[0.5(\hat{\sigma}^2 - \hat{\sigma})\left(2\frac{n}{N_0}\right)^{\delta}\right] \\ g_2(T, E) &= \exp\left[0.44(\hat{\sigma}^{1.5} - 2.2)\right] \cdot \left(\sqrt{1 + 0.8\left(\frac{E \cdot qa}{\sigma}\right)} - 1\right) \end{aligned} \tag{3.22}$$

where $\hat{\sigma} = \frac{\sigma}{k_B T}$ describes the energetic width of the density-of-states.

Furthermore *Setfos* can consider an external series resistance, which is of crucial importance for direct comparison with measurements. The resistance affects the applied voltage according to:

$$V_{source} = V_{dev} + R_s \cdot I \tag{3.23}$$

The most recent *Setfos* version 4.5 also allows to include a nonideal parallel resistance (shunt) in the circuit, as shown in Fig. 2.1b. Then the total current only partly flows through the device:

$$I_{tot} = I_{dev} + I_p = I_{dev} + \frac{V_{dev}}{R_p} \tag{3.24}$$

Setfos further is able to calculate modulated signals like impedance or IMPS. Here a small modulation is introduced into the voltage (or illumination) and the charge density and current responses are calculated:

$$\begin{aligned} V(t) &= V_{eq} + V_{ac} \cdot e^{i\omega t} \\ n(t) &= n_{eq} + n_{ac} \cdot e^{i\omega t} \\ p(t) &= p_{eq} + p_{ac} \cdot e^{i\omega t} \\ I(t) &= I_{eq} + I_{ac} \cdot e^{i\omega t - \varphi} \end{aligned} \tag{3.25}$$

Assuming a linear behaviour in the small-signal regime, the complex impedance Z and admittance Y as well as the conductance G and capacitance C at the specific working point V_{ac}, n_{ac}, p_{ac} and frequency $w = 2\pi f$ can then be calculated as:

$$\begin{aligned} Z &= \frac{V(t)}{I(t)} = \frac{V_{ac}}{I_{ac}} \\ Y &= \frac{I(t)}{V(t)} = \frac{I_{ac}}{V_{ac}} = G + i\omega C \end{aligned} \tag{3.26}$$

For IMPS/IMVS the imaginary and real parts of Z are usually analysed.

3.1.1 *Setfos*

The simulation software *Setfos* 4 allows to model steady-state, transient and modulated experiments. In fact, currently all the techniques implemented in *Paios* except for IMVS can be simulated, using dedicated algorithms and solvers for the different modes. The algorithms have been optimized for the specific modes, enabling unparalleled simulation speed.

The "Setfos-Paios-Integration" Module allows to perform the simulation from within the *Paios* GUI. This is very advantageous, as it facilitates the direct comparison of measurement and simulation data, as well as postprocessed plots. Additionally the user does not need to care about the specific settings of the experiment, which reduces human error.

3.1.2 *Fitting*

The functionality of simulating all experiments from within *Paios* consequently gives way to parameter extraction by fitting. It is possible to choose various material or device parameters, various experiments and devices and to perform a global fit. It should be noted, however, that this process still needs some manual adjustment, and can only be performed by experienced users, therefore it is far from being fully automated. It is advisable to follow a specific order for parameter extraction. In the Appendix B we show various examples where such a global fitting procedure was successfully performed.

In order to achieve a global fit, it is useful to follow some routine. The first parameters to be determined are the series resistance and the capacitance from which the active layer thickness can be deduced. The RC are best extracted from capacitance-frequency plots or dark-CELIV curves. The next step could be the extraction of the built-in voltage from IV and CV curves, where, however, the injection barriers and the density-of-states already play a role. Now one can start to fit several transient experiments like TPC and CELIV together, in order to estimate the mobility and recombination prefactor. The Setfos-Paios-Integration also calculates the correlation matrix of the fit parameters, which is a measure of how reliably parameters can be determined independent from each other. By adding more experiments the correlation can be minimized [340].

3.1.3 *Default Device Stack and Parameters*

The standard layer stacks for simulation of organic solar cells and OLEDs can be found in the Appendix A. There we also summarize the default parameters that have been used for qualitative simulations like in Fig. 3.2.

Our basic approach for defining a stack and the appropriate models is to simplify as far as possible. For example, in most cases the injection and transport layers can be assumed as highly-conductive and are therefore not playing a role in the electrical transport, which allows us to model them only optically, and incorporating them into the electrode for electrical simulations. Furthermore, if it is not absolutely necessary to use other models, we employ the ohmic (Fermilevel alignment) injection model, constant mobilities, and single trap levels. In order to demonstrate trends which happen during degradation and to investigate parameter sensitivity, this reduction of complexity is very helpful. Furthermore, as one usually does not know a lot about the investigated material, we find it a more scientific approach to limit number of unknown model parameters to as few as possible.

Part II

ANALYSIS OF POLAR OLEDS

This part deals with bilayer organic light-emitting diodes. We show that this device type can be more generally employed as a prototypical layer stack for parameter extraction. Validated by modeling we propose several experiments to determine material parameters. Furthermore we also investigate degradation phenomena of bilayer OLEDs.

4 POLAR OLEDS

4.1 INTRODUCTION

Organic light-emitting diodes (OLEDs) rely on the use of functional materials in order to facilitate charge carrier injection and transport, as well as to confine the recombination/emission zone. In standard bilayer OLEDs this functionality is used to ensure a selective charge transport, by stacking a hole transport layer (HTL) and an electron transport layer (ETL), where one or both also serve as the emitting material. The different materials have suitable energy levels for injection of one carrier type (see Figs. 1.1a & 4.1), and usually also comprise high charge carrier mobilities for this carrier type. This approach allows for efficient charge injection and transport. The radiative recombination (emission) is then confined to the interface of HTL and ETL, and the layer thicknesses can be tuned in order to optimize the optical outcoupling. The first OLED demonstrated by Tang and van Slyke in 1987 [11] had in fact such a bilayer structure. While today there are more efficient stack architectures as mentioned in Section 1.2, this bilayer heterojunction is still employed for research. The main reasons for this are the simplicity of the stack allowing to distinguish and investigate specific physical processes, but also the easy fabrication by sequentially depositing all layers. While most reported bilayer OLEDs are based on small-molecule materials which are usually vacuum-processed, there have been efforts to also employ polymers [436, 437] as well as to use solution-processing [438]. Furthermore this stack layout is well-suited to analyse new HTL and ETL materials in depth, which can then later be employed in multilayer architectures.

In this work we are investigating "**polar**" bilayer OLEDs. This expression stems from the fact that many electron transport materials exhibit a permanent polarization upon deposition. The molecules do not arrange fully randomly, but have a slight preference for orientation, so that a small permanent molecular dipole moment leads to a macroscopic orientation polarization of the thin film [82, 439]. This polarization can be physically described as two surface charge densities with opposite sign on both sides of the layer, and is therefore effectively an interface effect.

The polarization effect has been first discovered experimentally at PTCDA/Alq_3 and α-NPD/Alq_3 interfaces using photoelectron spectroscopy, however interpreted as an interface dipole [440, 441]. Later Berleb and Brütting found a signature of an interfacial electric field jump in capacitance-voltage measurements which they also initially attributed to an interface dipole [82, 442]. Ito et al. discovered a giant surface potential (GSP) in Kelvin probe force microscopy measurements on Alq_3 films [443]. They explained it by a preferential orientation of the Alq_3 molecules during deposition, which, as the molecules have a permanent dipole moment, leads to a macroscopic surface charge density. They could further confirm this picture using second harmonic generation, which is an optical technique and also sensitive to molecular dipoles. It was found that only a very small portion of the molecular dipoles are oriented [443, 444]. Furthermore the orientation polarization in Alq_3, which is still the most investigated ETL, has been shown to depend on the fabrication conditions, and to decay with time [443, 445–447].

With the years it became clear that many commonly used electron transport materials show the orientation polarization effect, and the polar sheet charge density Q_S is always in the range

of $0.1 - 5\,\mathrm{mC/m^2}$. Some values reported for Alq_3 are $0.44\,\mathrm{mC/m^2}$ [443] and $1.1\mathrm{mC/m}^2$ [439], obtained from Kelvin probe measurements, and $-1.1\,\mathrm{mC/m^2}$ [56, 82, 448], $-1.7\,\mathrm{mC/m^2}$ [444] from capacitance-voltage and displacement current measurements. Other polar ETLs are TPBi ($-1.1\,\mathrm{mC/m^2}$), BCP ($-0.51\,\mathrm{mC/m^2}$) and OXD-7 ($-2.3\,\mathrm{mC/m^2}$) [439, 449]. Hereby the positive values from Kelvin probe refer to the top surface of the layer, while the CV measurements address the buried interface, giving negative values [450]. All of these materials have the same macroscopic orientation. Only one material - $Al(7\text{-}Prq)_3$ - has been demonstrated so far to exhibit an "inverted" polarity with a sheet charge density of $+3.1\,\mathrm{mC/m^2}$ [451, 452].

Up to now no hole transport layers with a relevant macroscopic polarity have been reported. Yet, such materials can in principle be obtained using dipolar doping, for example by mixing Alq_3 into an α-NPD matrix [444].

4.2 MODELLING APPROACH

Figure 4.1 schematically shows the bilayer band structure at short-circuit without and with a polar ETL. In fact there is a huge difference due to the strong field jump at the interface. While in the non-polar device neither holes nor electrons can be injected below the built-in voltage, in the polar OLED a voltage range below V_{bi} exists where holes are already injected into the HTL.

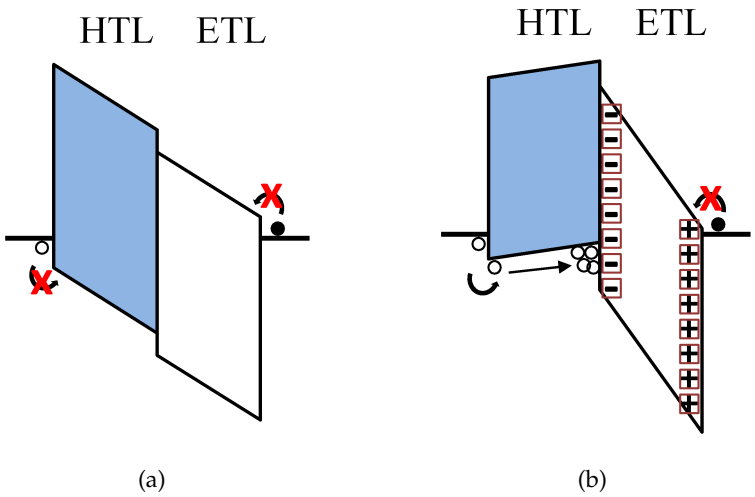

Figure 4.1: Schematics of the energy profile of a bilayer OLED (a) without and (b) with a polar ETL. The sheet charge densities are denoted by squares, and mobile electrons and holes by filled and open circles, respectively.

As in the IV-curve only bipolar currents are observed, this technique shows no signatures of the polar ETL. Yet this property can be investigated by other electrical techniques such as impedance spectroscopy or displacement current measurements. Figure 4.2 shows the original capacitance-voltage measurements from Berleb et al. [442] of bilayer OLEDs, where the thickness of the ETL (Alq_3) was varied. A second plateau starting at the transition voltage V_t is identified as a clear signature of the polar effect. This transition voltage is the voltage where holes start to be injected, and shifts to smaller, even to negative values when increasing the ETL thickness. The following

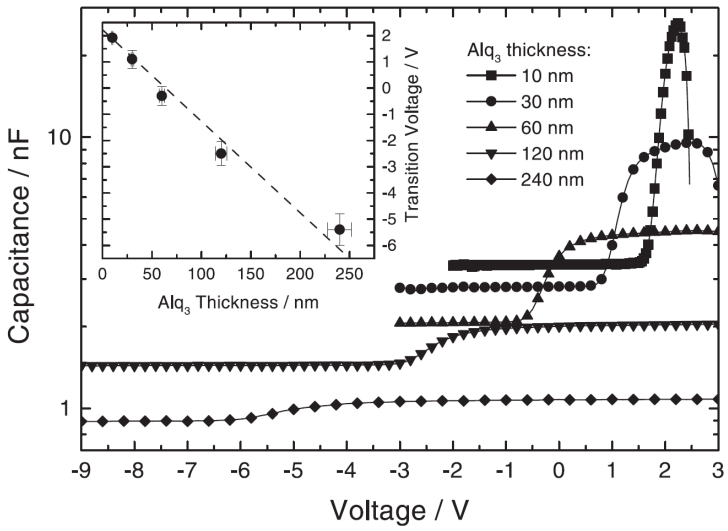

Figure 4.2: CV measurements of α-NPD/Alq_3 polar OLEDs with varied ETL thickness. The inset shows the correlation of the hole injection voltage with the ETL thickness. Plot taken from [442].

relation was established between the ETL thickness and the transition/hole injection voltage [82, 442] :

$$V_t = V_{bi} + \frac{Q_S d_{ETL}}{\varepsilon_0 \varepsilon_r} = V_{bi} + \frac{Q_S}{C_{ETL}} \tag{4.1}$$

where Q_S is the effective sheet charge density, which is negative in most cases, as mentioned above.

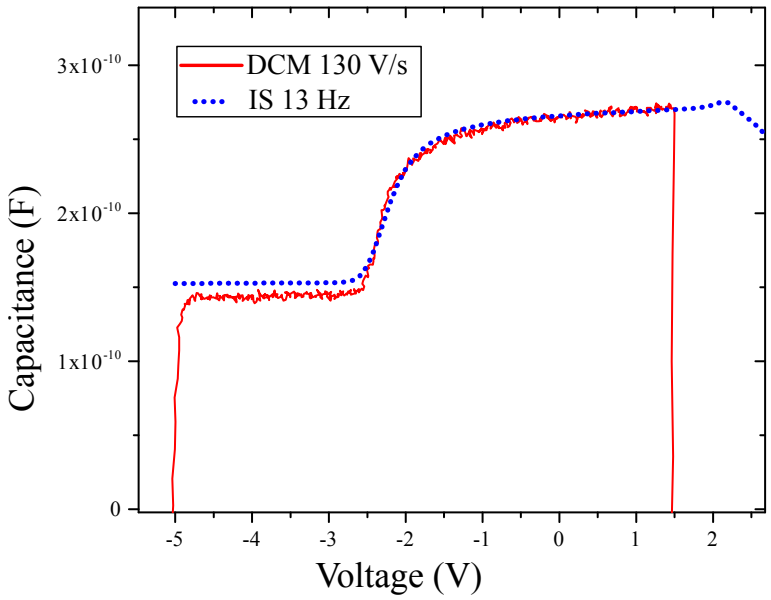

Figure 4.3: Displacement current measurement of an α-NPD/Alq_3 device (full red line) using a ramp rate of 130 V/s corresponding to frequency 13 Hz and the capacitance-voltage curve of the same device (dotted blue line) at 13 Hz.

The displacement current measurement (DCM) technique consists of two cycles of forward and reverse voltage ramps [453]. The forward voltage ramp probes charge injection, while the reverse

ramp probes extraction, being basically a very slow injection-CELIV measurement. Capacitance-voltage curves measured at low frequency are equivalent to the forward ramp measurements in DCM. The measured displacement current can be converted into a capacitance by dividing through the ramp rate $\mathcal{A}$:

$$I = \frac{\varepsilon_0 \varepsilon_r \mathcal{A} \cdot S}{d} \quad \text{and} \quad C = \frac{\varepsilon_0 \varepsilon_r S}{d} \quad : \quad C = \frac{I}{\mathcal{A}}$$

The characteristic frequency corresponding to the transient measurement is the repetition rate of the ramp cycles, $f = 1/T = \mathcal{A}/(2 \cdot V_{amp})$. Under the condition of low enough frequency, then the DCM capacitance and the capacitance-voltage curve are identical below the built-in voltage, as depicted in Fig. 4.3, therefore allowing to determine the hole injection voltage also from DCM.

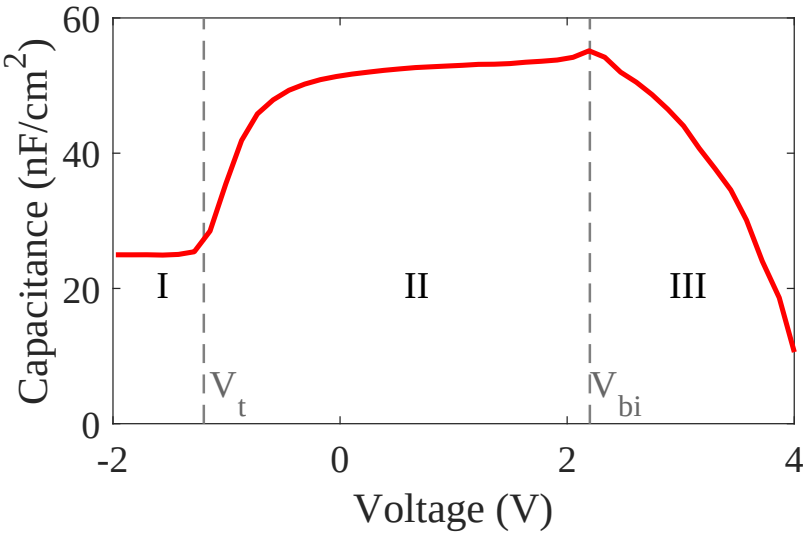

Figure 4.4: Capacitance-voltage plot of an α-NPD(80 nm)/Alq$_3$(60 nm) OLED measured at 100 Hz. The MIS-regime (II) between $V_t = -1.2$ V and $V_{bi} = +2.2$ V is indicated by the vertical dashed lines.

In order to model the polarity effect in the drift-diffusion software *Setfos*, the two sheet charge densities can be introduced as very thin additional layers on both sides of the ETL, where the sheet charge is modelled as a high electrical doping (being a fixed charge density). In the standard polar devices a negatively doped layer is added at the HTL/ETL interface, and a positively doped layer is added at the ETL/Cathode interface. Altazin et al. have shown that this approach allows to simulate polar layers within the drift-diffusion model [83]. Figure 4.4 shows a typical CV curve of a bilayer polar OLED, where three voltage regimes are indicated. At high reverse bias (regime I) the bilayer device is insulating and the measured capacitance is the geometric capacitance of the complete stack:

$$C_{geo} = \left(\frac{d_{HTL}}{\varepsilon_0 \varepsilon_{HTL}} + \frac{d_{ETL}}{\varepsilon_0 \varepsilon_{ETL}} \right)^{-1} = \frac{\varepsilon_0 \cdot \varepsilon_{HTL} \cdot \varepsilon_{ETL}}{\varepsilon_{ETL} \cdot d_{ETL} + \varepsilon_{HTL} \cdot d_{ETL}} \tag{4.2}$$

At the transition/hole injection voltage V_t (in this case -1.2 V) the capacitance rises to a second plateau corresponding to the capacitance of the ETL $C_{ETL} = \frac{\varepsilon_0 \varepsilon_{ETL}}{d_{ETL}}$. When holes are injected into the HTL, it does no longer act as an insulating dielectric and therefore does not contribute to the capacitance any more. This second regime can be described by a MIS (metal-insulator-semiconductor) structure, where the HTL is semiconducting and the polar ETL acts as an insulator. The third

regime is above the built-in voltage (in this case 2.2 V), where bipolar charge injection and radiative recombination set in so that the capacitance drops and can even become negative [454, 455].

The simulation of the polar OLED can be used to investigate the charge carrier and field profiles in more detail. As we have already shown in the schematics of Fig. 4.1 we expect a field jump at the HTL/ETL interface. Figure 4.5 shows typical charge density, electric field and potential profiles for the three voltage regimes defined in the capacitance-voltage curve. The schematics above are confirmed by the simulation. We find that in the second regime between V_t and V_{bi} holes are already injected and accumulate at the HTL/ETL interface, while the ETL is still empty. The effect of the polar sheet charge is the strong bending of the potential in the ETL related to the field jump.

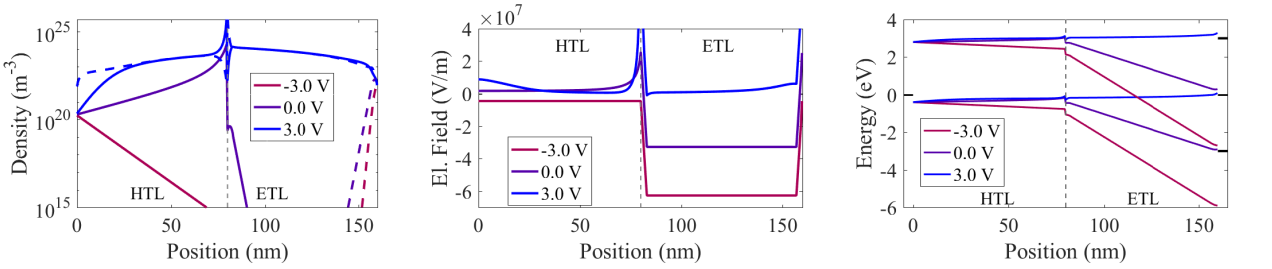

(a) Hole densities (solid lines) and electron densities (dashed lines).

(b) Electric field distribution.

(c) HOMO and LUMO bands and contact potentials (black).

Figure 4.5: Simulated profiles in a polar OLED for regime I (-3 V), regime II (0 V) and regime III (3 V). Simulation parameters as in Table A.2, except for ETL thickness: $d_{ETL} = 80$ nm.

Figure 4.6 depicts several representations of simulated impedance-voltage data with varied ETL thickness. The hole injection voltage can be clearly identified in the capacitance, conductance and amplitude data. It is, however, concealed in the phase data, where a change only happens with bipolar injection above 2.5 V.

In the following Chapters 5 & 6 we will discuss in detail several possible applications for polar layers for parameter determination. Yet the polar layers also are of practical importance, as they have a direct influence on the device performance. This is difficult to measure by itself, but it becomes clear in Fig. 4.7, where we have simulated the IV-curves of a device without, with and with an inverted polar ETL. It turns out that the standard polar ETL has a (small) beneficial effect on the injection, as the positive sheet charge induces a high electron density at the ETL/cathode interface. Oppositely, employing an inversely oriented ETL such as Al(7-Prq)$_3$, the electron injection is hindered, leading to a strongly impaired IV-curve and a less efficient device.

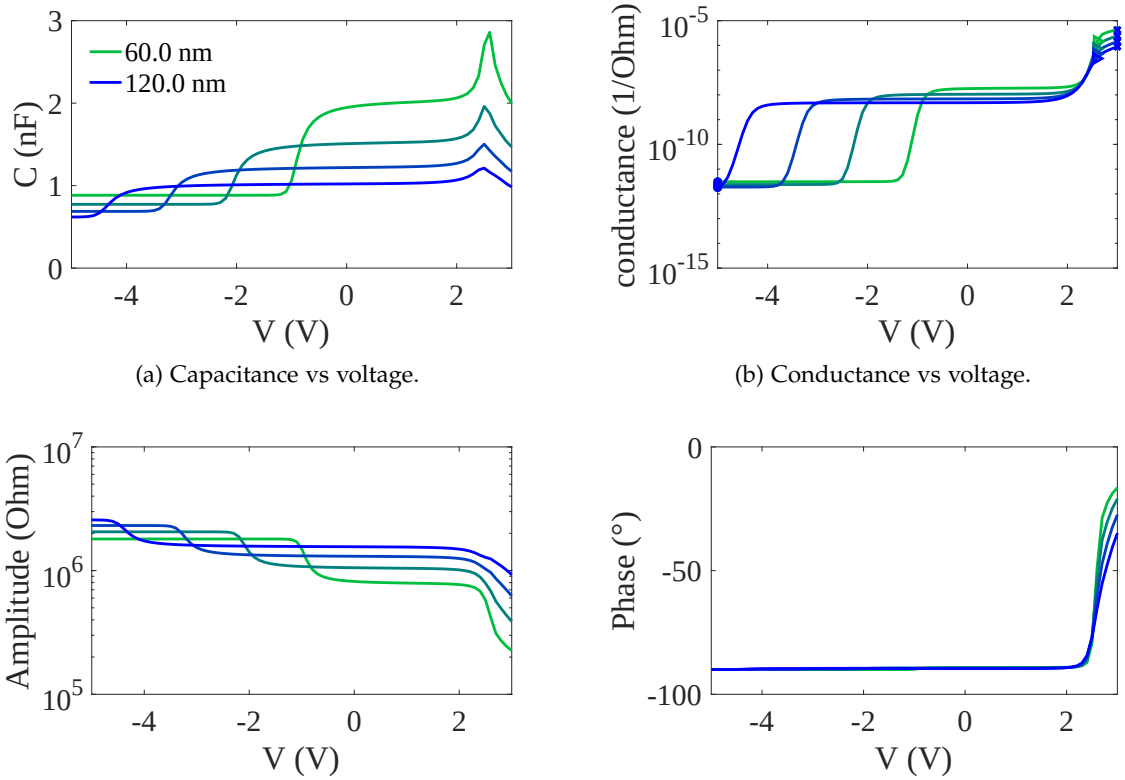

(a) Capacitance vs voltage.

(b) Conductance vs voltage.

(c) Amplitude vs voltage.

(d) Phase vs voltage.

Figure 4.6: Simulations of impedance versus voltage at 100 Hz for ETL thickness varied between 60 and 120 nm and an HTL thickness of 80 nm. The hole injection voltage can be determined from several representations of the impedance data. Simulation parameters as in Table A.2.

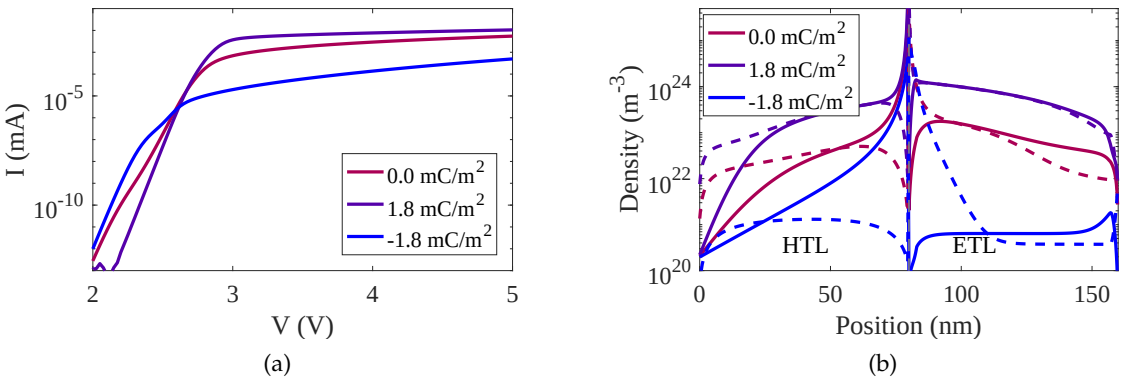

(a)

(b)

Figure 4.7: (a) Simulated IV-curves for a non-polar OLED, a polar OLED, and a polar OLED with inverted polarity. (b) Hole (solid lines) and electron (dashed lines) densities at 3 V for the three different values of the sheet charge density. Simulation parameters as in Table A.2, except ETL thickness is 80 nm.

5 MIS-CELIV IN POLAR OLEDS

The charge carrier mobility is one of the most important material parameters in organic electronics. In OLEDs of the key factors determining the (current-to-luminance) efficiency is the charge balance factor [21, 417, 456]. This factor can be maximized by the stack design, e.g. using blocking layers, as well as optimizing the carrier mobilities in the charge transport layers. Bimolecular carrier recombination is directly proportional to carrier mobility (see Eq. 3.15) [457], thus a high carrier mobility translates into a high recombination efficiency which in turn is linked to a high charge balance factor, too.

In organic solar cells, conversely, a high current collection efficiency is based on high carrier mobilities and ensures maximum photocurrent, and low bimolecular recombination losses allow for a high fill factor. As a rule-of-thumb, higher and balanced electron and hole mobilities are favourable for good organic solar cells (see also Appendix C.5) [121, 458–460]. It has however been shown that there is a trade-off discouraging too high mobilities, and furthermore monomolecular recombination can play a role as well [362, 461, 462].

In any case the charge carrier mobility of the majority charge carriers in an organic semiconductor material is one of the most relevant parameters for further optimization of organic electronic devices. Various experimental techniques such as space-charge limited current-voltage curves [463], time-of-flight [464, 465], admittance spectroscopy [466, 467], dark injection transients [468, 469], field-effect mobility [14] and charge extraction by linearly increasing voltage (CELIV) [351, 470] are in principle available to assess this parameter. Most of these techniques come with the need to fabricate dedicated devices with especially thick layers, or with different contact materials than in the final device geometry, to ensure unipolar transport. The only one that can be performed on fully operating devices is photo-CELIV in organic solar cells, where the identification of the sign of the majority charge carrier is a non-obvious task, however.

The CELIV technique was originally developed by Juška et al. [351] to extract the charge carrier drift mobility in thin-film silicon, and has been subsequently applied to doped organic layers [352, 471] and to organic photovoltaic cells [343]. The technique can in principle be applied to any kind of device that behaves as a diode, meaning that it needs to be non-injecting under reverse bias condition. Applying a negative voltage ramp induces a constant displacement current due to the electric field changing linearly with time. In case mobile charges are already present in the device under the conditions prior to the voltage ramp, these charges are extracted by the reverse field, and the transit time and number of carriers are linked to an additional current peak on top of the displacement current plateau. The charges being extracted can be equilibrium carriers (induced by electrical dopants), photo-generated carriers or previously injected carriers. We can thus distinguish among dark-CELIV, photo-CELIV and injection-CELIV (see also Section 2.2). To clarify the experimental details we schematically show the voltage and current transients in Fig. 2.6.

The transient position of the CELIV current peak is related to the charge carrier transit time and therefore to the mobility. The first analytical model to calculate the mobility μ was given by Juška et al. with Eq. 5.1 [351]:

$$\mu = \frac{2d^2}{3\mathcal{A} \cdot t_{max}^2} \tag{5.1}$$

where the layer thickness is denoted by d, the voltage ramp is $\mathcal{A} = dV/dt$ and the position of the current maximum is t_{max}.

The application of this formula is, however, very limited, as the underlying assumptions (drift only, uniform charge carrier distribution, no RC-effects) are usually not justified [302]. Several other approaches have therefore been pursued to describe the full transient current, and specifically to quantify the mobility [360, 368, 371, 372]. In bipolar devices the peak consists of both electrons and holes, and it is not possible to unambiguously assign the extracted mobility to one specific charge carrier type. Also, depending on the ratio of the electron and hole mobility as well as the ratio of electron and hole density the extracted mobility can be the faster one, the slower one or an average of the two species. Finally, the peak position and thereby the extracted mobility depend on the relation of the peak height j_{max} to the displacement current plateau j_0, the employed voltage ramp rate, (bipolar) recombination and the external series resistance [302, 360] which further complicates the analysis and can render simple analytic formulas inaccurate. There have been adaptions and extensions to the initial equation, but also these are approximations and valid only in specific cases [343, 352, 371]. A planar heterojunction organic solar cell represents such a special case, where the identification of the carrier species was supported by a thickness variation of either of the two layers [472]. The most general modelling approach for the bipolar case still is the dual-carrier drift-diffusion model, ideally coupled with a fitting routine, which in the end allows for a real quantitative extraction of both charge carrier mobilities [228, 302, 415].

5.1 APPROACH

So far, it seemed impossible to use fully operating bipolar devices for a valid CELIV analysis. However, recently several groups have developed a new approach by fabricating metal-insulator-semiconductor (MIS) devices to determine both mobilities of the semiconductor [353, 362, 473]. Here the extraction current shows signatures of only one charge carrier type, which was injected in the first place and for which the electrode on the semiconductor is selective. The main advantage of MIS-CELIV is that it is a quite general approach which can be followed for a large range of materials. Furthermore the active layer to be investigated can be deposited with the same parameters (thickness, morphology) as in the full stack, so the mobilities in a "real" device can be inferred to be very similar. Yet, the fabrication of well-controlled thin and dense insulating layers can be challenging. The deposition of metal-oxide insulators can harm the underlying organic layer, furthermore the use of specific insulators like MgF_2, can lead to undesired side effects such as contamination of the evaporation chamber. Finally interface states between the insulator and organic layer may lead to band-bending and trapping effects and therefore complicate the analysis. These shortcomings make the use of inorganic insulators not suitable for all research groups and every material of interest.

Due to their diode behaviour, OLEDs are also suitable for CELIV experiments, but a pre-bias above the built-in potential needs to be applied for injecting carriers in the first place. Like in bulk-heterojunction OSCs, the CELIV peak, however, cannot unambiguously be assigned to one carrier type alone as both of them are injected above the built-in voltage. In this work we present the application of the CELIV technique in OLEDs with clear identification of the carrier type, namely holes. For this endeavour, we take advantage of the concept of polar layers that was introduced in the previous Chapter.

5.2 RESULTS

In order to demonstrate the approach proposed here, we investigate a prototypical OLED stack consisting of ITO (160 nm)/PEDOT:PSS (30 nm)/α-NPD (80 nm)/Alq_3 (60 nm)/Ca (15 nm)/Al (100 nm). The devices have been fabricated at Augsburg University using standard procedures that have already been described elsewhere [447]. The electrical transient and impedance measurements reported here have been performed with *Paios*. Drift-diffusion simulations to calculate the CELIV currents and charge density profiles have been generated using *Setfos*. Hereby the macroscopic polarization was taken into account by two thin, doped layers, as described in the previous Chapter [83]. The model parameters are summarized in Table A.2.

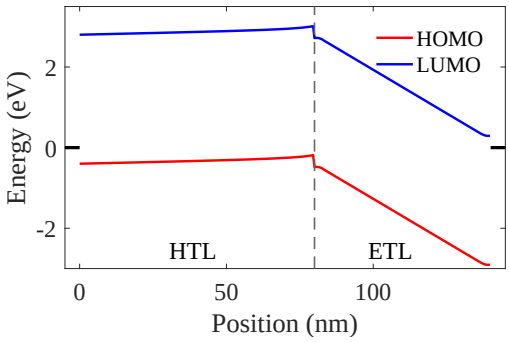

(a) Band diagram for a polar OLED at an offset voltage of 0 V

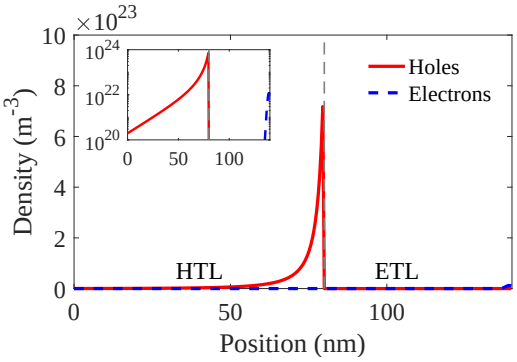

(b) Equilibrium charge carrier densities of holes (red full line) and electrons (blue dashed line) at an offset voltage of 0 V. The inset shows a logarithmic representation.

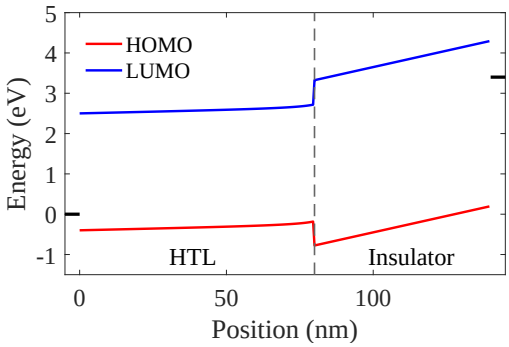

(c) Band diagram for a MIS-device at an offset voltage of 3.4 V

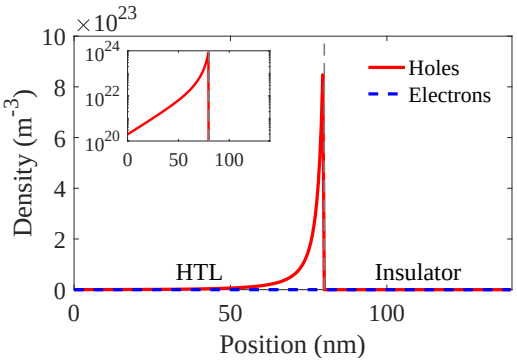

(d) Equilibrium charge carrier densities of holes (red full line) and electrons (blue dashed line) at an offset voltage of 3.4 V. The inset shows a logarithmic representation.

Figure 5.1: Simulated potential and charge density profiles of a polar OLED and a MIS-device. See Table A.2 for the simulation parameters.

Figures 5.1a & 5.1b depict the simulated potential and charge density profiles of a polar OLED at zero volt, that is between V_t and V_{bi}. The energy levels show a large potential drop over the ETL, leading to a strong negative field in this layer caused by the polar sheet charge densities, in line with Fig. 4.5. Conversely there is a weak positive electric field in the HTL, however, giving rise to hole injection into the HTL. The injected holes accumulate at the internal interface with

the polar ETL, since both the interfacial energy barrier and the opposite electric field in the ETL prevent the holes from entering the ETL.

For comparison Figs. 5.1c & 5.1d show the corresponding situation in a standard MIS device. Here, a forward bias above the built-in potential is applied. The resulting small positive electric field enables hole injection into the HTL. The injected holes accumulate at the HTL/insulator interface, as they cannot overcome the large energetic barrier towards the insulator. Even though the field inside the polar ETL is strongly negative compared to the constant positive field in the insulator, the charge density and potential profiles inside the HTL are nearly identical for the two layer stacks. This proves that a polar OLED in hole accumulation regime does behave like a standard MIS device under forward bias. Therefore a CELIV measurement will extract the equilibrium hole density, resulting in the typical extraction peak. In this case there is no doubt about the type of extracted carriers - holes - and the extracted mobility is neither perturbed by the opposite charge carrier nor by recombination losses.

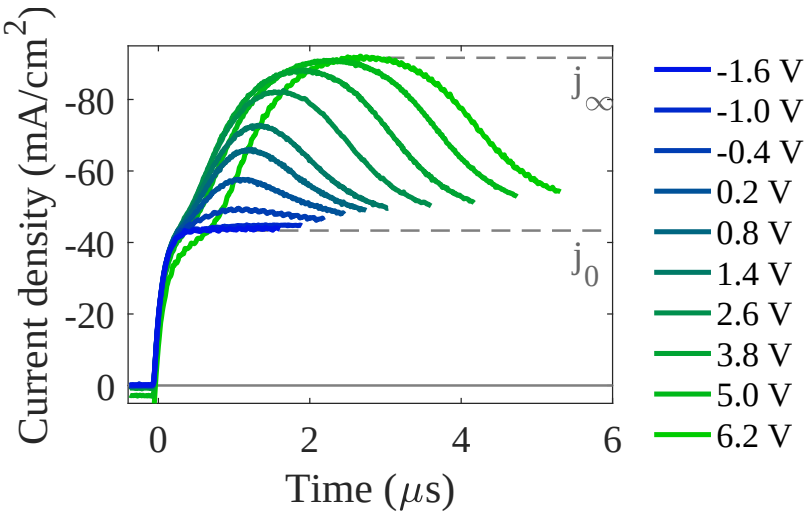

Figure 5.2: MIS-CELIV measurement on an α-NPD(80 nm)/Alq_3(60 nm) device at varied offset voltages from -1.6 V to 6.2 V. For offset voltages below the hole injection voltage $V_t = -1.2$ V only the displacement current plateau is observed. The displacement current j_0 and the saturation current j_∞ are denoted by dashed lines.

For the MIS-CELIV measurement, an offset voltage with a value between the hole injection voltage V_t and the built-in voltage V_{bi} is applied prior to the CELIV voltage ramp. The closer the offset voltage is to V_{bi}, the more holes will be present in the active layer prior to the extraction ramp. Figure 5.2 shows the measured CELIV currents using a ramp rate $\mathcal{A} = -2$ V/μs at varied offset voltages. For offset voltages below the hole injection voltage $V_t = -1.2$ V both HTL and ETL are empty and therefore insulating; then the current density consists only of the displacement current $j_0 = C_{geo} \cdot \mathcal{A}$. For voltages above V_t holes are present prior to the ramp and are extracted by it, leading to the characteristic current peak. We observe a saturation of this peak at a value corresponding to the capacitive current density of the ETL $j_\infty = C_{ETL} \cdot \mathcal{A}$. The appearance of this saturation corresponds to the space-charge limited current, as pointed out by Juška et al. [353]. The reason is that during a time step not more than the charge on the capacitor plates $C_{ETL} \cdot V$ can be displaced. The ratio of the current levels corresponds to the simple layer thickness ratio $\frac{j_\infty}{j_0} = \frac{d_{ETL}+d_{HTL}}{d_{ETL}}$ of about 2.2 in our case if we neglect differences in dielectric permittivity.

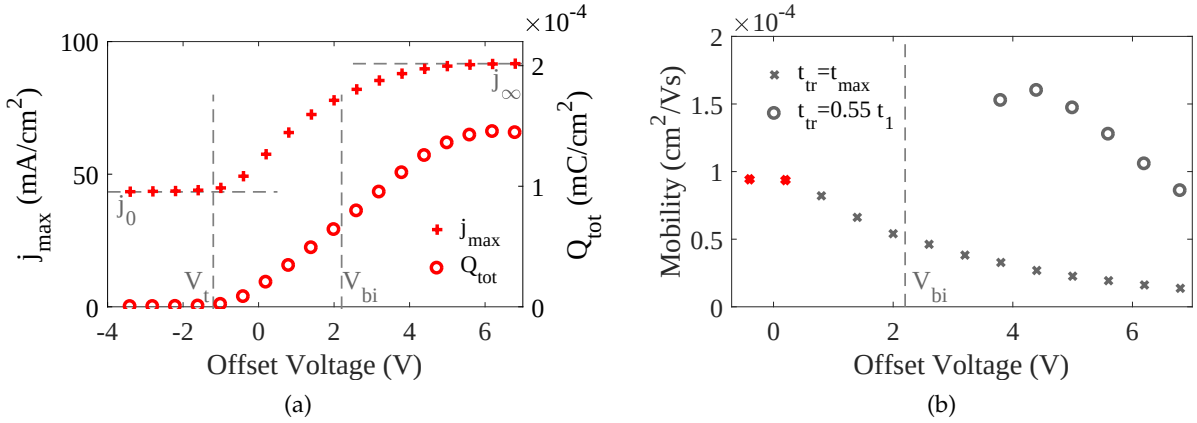

Figure 5.3: Extracted parameters from the MIS-CELIV measurements shown in Fig. 5.2 with offset voltage variation. (a) Current maximum and integrated charge. For clarification some variables used in the text are also denoted in grey. (b) Calculated mobility using Eq. 5.2 with two different estimates of the transit time.

Figure 5.3 shows various parameters extracted from the data of Fig. 5.2. The current maximum and the extracted charge, which is the time-integrated current $Q_{tot} = \int_0^{t_{ramp}} (j(t) - j_0)\, dt$, are plotted in Fig. 5.3a. Below the hole injection voltage no charges are extracted, and the current is just the constant displacement current. Above V_t holes are extracted, showing up in the linearly rising current maximum and extracted charge. For high voltages above the built-in voltage both quantities saturate due to the space-charge limitation.

In order to determine the hole mobility the conventional CELIV formula (Eq. 5.1) cannot be used as it assumes a bulk charge distribution, and does not account for the redistribution of the electric field by the insulating layer. There is, however, the analytic framework for MIS-CELIV, which was originally proposed by Juška et al. This is based on the assumption that all the equilibrium charges accumulate at the internal interface in an infinitesimally narrow distribution [353, 362, 474]:

$$\mu = \frac{2d_{HTL}^2}{\mathcal{A} \cdot t_{tr}^2} \cdot \left(1 + \frac{\varepsilon_{HTL} d_{ETL}}{\varepsilon_{ETL} d_{HTL}}\right) = \frac{2d_{HTL}^2}{\mathcal{A} \cdot t_{tr}^2} \cdot \left(1 + \frac{j_0}{j_\infty - j_0}\right) \tag{5.2}$$

In Eq. 5.2 t_{tr} is the transit time, $\mathcal{A}$ is the voltage ramp, d denotes the layer thicknesses and ε is the respective relative permittivity of the layers. If the permittivity is not known and the saturation current j_∞ is observed in the measurement, using the second part of Eq. 5.2 can help to reduce uncertainties.

In standard MIS devices the ratio j_∞ / j_0 is large due to the typically thin insulator layers and their high permittivities. Under this condition the transit time can be estimated from the time t_1 when the current reaches twice the plateau value, $j(t_1) = 2 \cdot j_0$ [353]. The two times are then related by $t_{tr} = \frac{4}{\pi}\, t_1$ [353, 474]. In case the proportions of the layer thicknesses are nonideal, Važgėla et al. provide a correction factor in Figure 2 of their publication [474]. For our device the ratio j_∞ / j_0 is approximately 2.2, so we take the relation between t_1 and t_{tr} to be approximately: $t_{tr} \approx 0.55\ t_1$. The problem is that t_1 can be determined only for high offset voltages above V_{bi}, and hence the mobility analysis may be disturbed by electron contributions.

Therefore we focus on the low-conductivity regime by investigating the small peaks that occur for offset voltages just above the hole injection voltage. Here only a small charge density is present and the extraction current is unperturbed by space-charge effects. In accordance with conventional

CELIV theory, Juška et al. state that in the small-charge limit the transit time is identical with the transient position of the current peak [353].

Figure 5.3b shows the extracted mobility values for the measurements of Fig. 5.2 using Eq. 5.2. Thereby we have estimated the transit time by either the peak position $t_{tr} = t_{max}$, or, if possible, using the time t_1 via $t_{tr} = 0.55\ t_1$. The first method gives values around $9 \cdot 10^{-5}$ cm^2/Vs just above V_t, while for higher offset voltages the extracted mobility is lower, due to the starting saturation and space-charge effects. The values estimated using t_1 are higher (up to $1.6 \cdot 10^{-4}$ cm^2/Vs), however they are not reliable as t_1 is only observed in the bipolar regime above V_{bi}. We therefore conclude that for bilayer OLEDs the most convenient and reliable way to determine the mobility is from the small-charge regime, that is using offset voltages just above the hole injection voltage.

Obviously the field dependence can be further investigated, where in the CELIV theory usually the extraction field at the peak time $\mathcal{E}_{ext} = \frac{V(t_{tr})-V_{bi}}{d_{tot}}$ is taken. The consistency with mobility values determined by the alternative methods confirms the new CELIV method with standard devices to be reliable in practice.

However, as a side remark we want to note that, instead of using CELIV formulas, we can also resort to drift-diffusion simulations as we have already demonstrated in the context of OSCs [228, 340]. Since in the MIS-regime of the polar device only holes are present, the CELIV transients may be fitted with the hole mobility as the only fitting parameter. Using the drift-diffusion simulation software *Setfos* we obtain a value of $1.2 \cdot 10^{-4}$ cm^2/Vs, in very good agreement with the measurement. A global fit of several measurements of a polar OLED can be found in the Appendix B.4.

5.3 DISCUSSION

In principle the presented approach can also be used in order to analyse the electron mobility of an active layer. In this case a polar hole transport material is needed, on top of which the active layer is deposited, followed by the electron injecting contact (see Fig. 5.4b). While so far no hole transport materials leading to films with a permanent dipole moment have been reported, such materials can be obtained using dipolar doping. Jäger et al. have shown that by mixing Alq_3 into an α-NPD matrix the polarity of the HTL can be controlled [444].

The electron transport material Al(7-Prq)$_3$ has been demonstrated to exhibit an inverted polarization with a sheet charge density of $+3.1$ mC/m^2 [451]. In a bilayer configuration as shown in Fig. 5.4c, it would thus be possible to determine the electron mobility in this material. It would then also be feasible that by dipolar doping of Al(7-Prq)$_3$ into an HTL the hole mobility of the HTL host could be determined (Fig. 5.4d).

Of the different configurations depicted in Fig. 5.4 the first two seem the most relevant, as they allow to selectively determine the hole and electron mobility of an active layer by fabricating two devices where the material under investigation once is deposited onto the hole-injecting contact, and once an electron-selective contact is deposited onto this layer. Obviously this also allows to selectively investigate charge carrier transport in general bipolar and bulk-heterojunction semiconductor layers.

There are two key advantages of the presented approach compared to other measurement techniques. Firstly, the active layers to investigate can be prepared and deposited in the same way and especially with the same thickness as in a regular OLED or solar cell stack, thus the extracted mobility values can be assumed to be the same in the regular device.

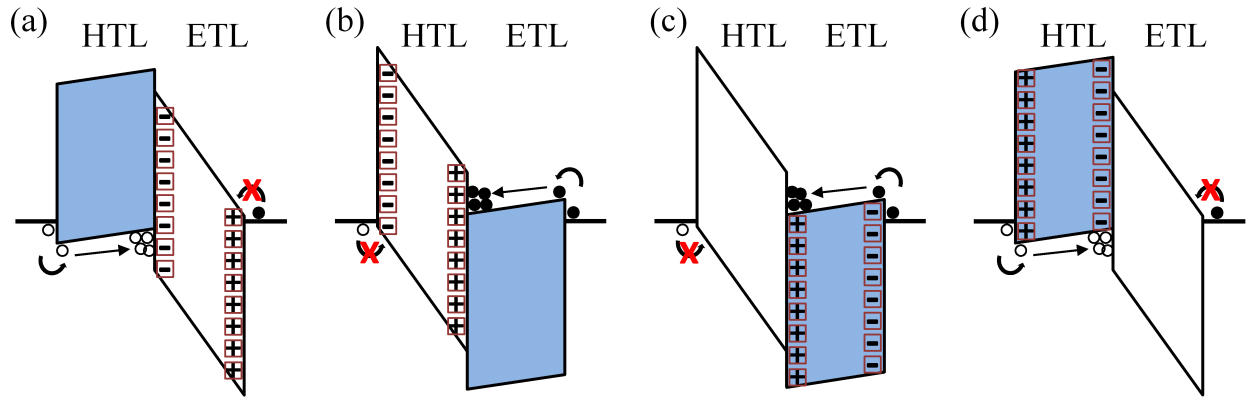

Figure 5.4: Schematic energy levels of standard and alternative bilayer configurations of HTL and ETL where one of the layers shows a permanent polar moment, and the layer under investigation is highlighted in blue. The sheet charge densities are denoted by the squares, and mobile electrons and holes by filled and open circles, respectively. (a) Standard polar OLED configuration as discussed in the main text. The ETL is polar with a negative sheet density at the interface, the hole mobility in the HTL is determined. (b) The HTL is polar with a positive sheet density at the interface. This can be fabricated by dipolar doping of the HTL with a polar material, and can be used to determine the electron mobility in the ETL. (c) The ETL is polar with an inverted polarity. This allows to determine the electron mobility of the ETL. (d) The HTL is polar with a negative sheet density at the interface. This would allow to determine the hole mobility of the HTL, however no such material is reported so far.

The second key advantage is that the employed organic polar electron transport layers are very easy to handle and deposit, and furthermore less harmful to the underlying materials than oxide insulators. Basically every group working in the OLED field can fabricate Alq_3 layers by thermal evaporation, and could thus employ the new CELIV technique.

6 ACTIVATION ENERGIES

There is great interest in the knowledge of the temperature-dependent behaviour of organic semiconductor devices such as organic light-emitting diodes (OLEDs) and organic solar cells (OSCs). The reason for this is the operation temperature of such devices which is usually higher than room temperature. In OLEDs Joule heating by the charge current leads to selfheating effects and an increase of the device temperature up to 70 °C [454, 475–477]. Conversely, in OSCs, parasitic absorption as well as non-radiative recombination also lead to operation temperatures in a similar range. However, many materials for these devices are usually still investigated under standard test conditions, which is 25 °C. Furthermore for OSCs a standard illumination intensity and spectrum of 1 sun (AM1.5g) is employed for efficiency measurements [478]. In contrast to this during real outdoor operation solar cells will experience strongly changing temperatures due to daily cycling, sunlight incidence angle, and weather conditions like clouds or wind [479]. In OLEDs used in display applications the stack temperature may also change quickly, furthermore different driving currents in different pixels can lead to inhomogeneous two-dimensional temperature distributions. All these arguments show that it is indispensable to investigate the temperature dependence of charge transport in organic materials and devices.

In OLEDs good charge carrier injection is important to achieve high efficiencies. However, in standard devices it is challenging to distinguish effects of injection and transport, which in turn makes it difficult to characterize the energetic barrier for charge injection. Furthermore the bipolar current depends on both electron and hole injection barriers as well as their mobilities, making the analysis rather challenging.

For the study presented here we concentrate on the temperature dependence of bilayer OLEDs with the stack configuration ITO/HIL/HTL/Alq_3/Ag as depicted in Fig. 6.2a. The findings of this work are however not restricted to OLEDs alone, but can easily be transferred to other device stacks and materials, as discussed in the final section.

6.1 ANALYTICAL MODEL

In polar bilayer OLEDs hole injection from the hole injection layer into the hole transport layer occurs already below the built-in voltage V_{bi} due to the permanent polarization of the electron transport layer Alq_3 [82, 439, 442]. Depending on the ETL thickness the hole injection voltage V_t can be shifted even to reverse bias. In these devices the HTL is already flooded with holes at voltages below V_{bi}, which can be witnessed in the capacitance of the device. The capacitance is no longer the geometric value, $C_{geo} = \left(\frac{d_{HTL}}{\varepsilon_0 \varepsilon_{HTL}} + \frac{d_{ETL}}{\varepsilon_0 \varepsilon_{ETL}}\right)^{-1}$, but, as the HTL no longer contributes to it, is enhanced to the value of the ETL alone, $C_{ETL} = \frac{\varepsilon_0 \varepsilon_{ETL}}{d_{ETL}}$. The hole injection voltage V_t giving the transition from the geometric to the ETL capacitance can be obtained from capacitance-voltage experiments, or displacement current measurements [82, 83, 480].

If the capacitance is measured versus frequency at a bias $V_t < V < V_{bi}$, the transition from the geometric to the ETL capacitance occurs at a characteristic frequency f_t, as can be seen in the measurement of Fig. 6.1. If the temperature is lowered this transition occurs at lower frequency. The temperature dependent behaviour of the capacitance-frequency experiment (C-f-T), especially

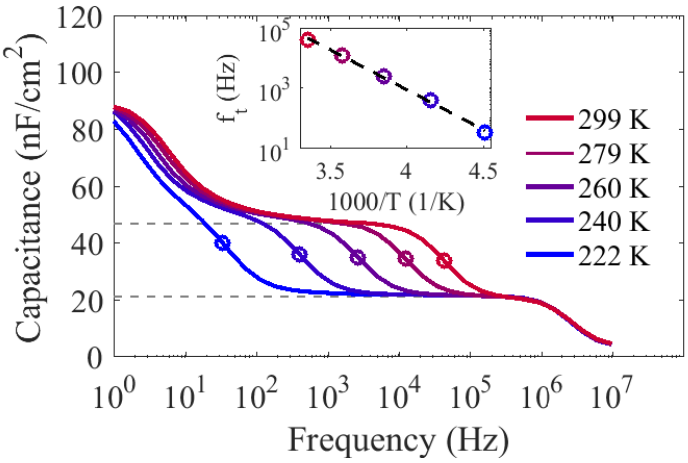

Figure 6.1: Capacitance-frequency measurement at varied temperature for an α-NPD/Alq$_3$ bilayer OLED at zero volts. The inset shows an Arrhenius plot of the temperature-dependent transition frequency which is marked by the symbol, giving an activation energy of 0.53 eV. The geometric capacitance and the increased ETL capacitance plateaus are also highlighted by the dashed grey lines.

the one of this transition frequency, can be used to analyse the thermal activation of the hole current[319, 481–485]. The activation energy is obtained from an Arrhenius analysis, as shown in the inset of Fig. 6.1, by employing:

$$f_t(T) = f_0 \cdot \exp\left(\frac{-E_{act}}{k_B T}\right) \tag{6.1}$$

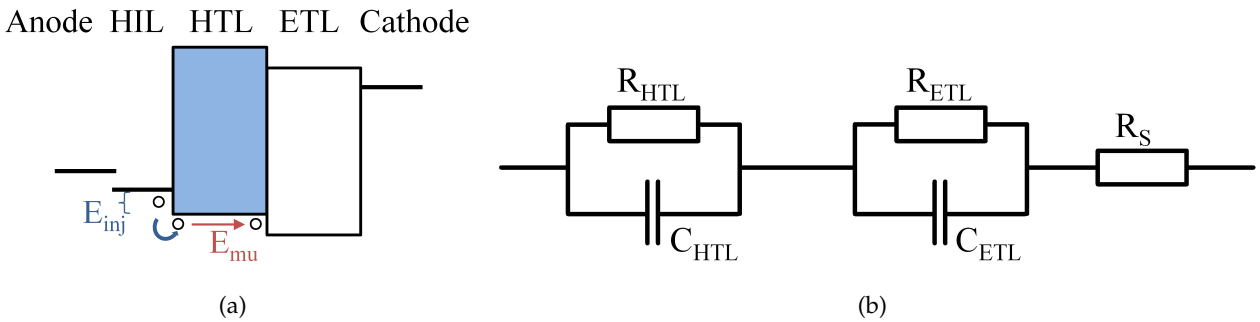

Figure 6.2: a) Schematics of the bilayer stack layout, and definition of the activation energies for hole injection and transport. b) Equivalent circuit representation of the bilayer stack as a series of two RC-circuits and a series resistance.

The behaviour of the transition frequency can be understood from a simple equivalent circuit model of the bilayer OLED, where the two layers are represented by RC elements (see Fig. 6.2b) [82, 485–487]. When the conductance of the HTL increases with temperature, its resistance decreases. The transition frequency for the case that the HTL is significantly less resistive than the ETL is given by [326] :

$$f_t = \frac{1}{R_{HTL} \cdot (C_{HTL} + C_{ETL})} \tag{6.2}$$

Thus a HTL conductance increasing exponentially with temperature corresponds to a resistance decreasing like $R_{HTL}(T) = R_0 \cdot \exp\left(\frac{E_{act}}{k_B T}\right)$. Then the transition frequency, being proportional to the HTL resistance, is Arrhenius-activated as Eq. 6.1.

As a side remark we would like to note that the observed capacitance increase at very low frequencies in Fig. 6.1 is an effect of the lateral conductivity of the PEDOT:PSS layer [326]. This parasitic capacitance is not accounted for in the simple equivalent circuit model. Furthermore the influence of an external series resistance produces the capacitance decay at high frequencies above 1 MHz.

However, this simple model conceals that the activation energy of f_t contains contributions of both the hole injection barrier (E_{inj}) at the interface with the HIL and the thermal activation of the hole mobility inside the HTL (E_μ). To account for this increased complexity we move to a microscopic description of the conductivity of the HTL layer, which allows us to describe and investigate the two processes independently. In a first approximation, we will assume that the hole concentration in the HTL is constant and equal to the concentration at the HIL contact interface. Ensuring Fermi-level alignment at the HIL/HTL interface, the hole density in the HTL is given by $p_{HTL} = P_0 \cdot \exp\left(\frac{-E_{inj}}{k_B T}\right)$, where P_0 is the density-of-states of the HTL. The conductivity of the HTL is defined by $G_{HTL} = q \cdot p_{HTL} \cdot \mu_{HTL}$, with q being the unit charge and μ the hole mobility. If the mobility is thermally activated by E_μ we obtain:

$$G(T) = q \cdot P_0 \cdot \exp\left(\frac{-E_{inj}}{k_B T}\right) \cdot \mu_0 \cdot \exp\left(\frac{-E_\mu}{k_B T}\right) = G_0 \cdot \exp\left(-\frac{E_{inj} + E_\mu}{k_B T}\right) \tag{6.3}$$

The consequent assumption is that the observed temperature-dependence of the G-f-T and therefore of the transition frequency is determined by the sum:

$$E_{act} = E_{inj} + E_\mu \tag{6.4}$$

These thoughts make it clear that the two parameters cannot be decoupled easily. As we noted in a previous publication, measured C-f-T data could be fitted with a high injection barrier and temperature-independent mobility, thereby however leading to unrealistically high mobility values [83]. Obviously a good fit would also be obtained by setting the injection barrier E_{inj} zero and putting all thermal activation into the mobility.

In summary, assuming that the hole concentration and therefore the conductivity in the HTL is constant already gives a qualitative understanding of the temperature dependence of the transition frequency. We will later see that it is, however, a too simplified model to quantitatively determine the activation energies.

In order to decouple the two activation energies, we propose to add a second, independent experiment which is performed at different temperatures, namely MIS-CELIV. In this experiment a negative voltage ramp is applied to the device in order to extract the charge density present at the working point prior to the ramp. The CELIV technique is mostly employed to determine the charge carrier mobility from the characteristic drift time leading to a peak in the measured current [351, 353, 362]. In our previous publication we have demonstrated that this technique can be employed for mobility determination in the context of polar OLEDs [480], which behave like MIS-diodes in accumulation regime for applied bias voltages between the hole injection voltage V_t and the built-in voltage V_{bi}. Under this condition the CELIV current shows a peak on top of a

constant displacement current and allows to determine the charge transit time, which is related to the charge-carrier mobility by [353, 474, 480]:

$$\mu = \frac{2d_{HTL}^2}{\mathcal{A} \cdot {t_{tr}}^2} \cdot \left(1 + \frac{\varepsilon_{HTL} d_{ETL}}{\varepsilon_{ETL} d_{HTL}}\right) \tag{6.5}$$

where ε denotes the relative dielectric permittivity and d the thickness of the respective layers, $\mathcal{A} = -dV/dt$ is the applied voltage ramp, and t_{tr} is the transit time.

We have shown that this technique is best employed using offset voltages just above the hole injection voltage, thereby avoiding space-charge effects [480]. In this limit the transit time is equal to the transient position of the current peak [353]. Figure 6.3 shows the temperature-dependence of such a measurement, together with the Arrhenius plot of the extracted mobility from measurements at different offset voltages, thereby assuming a thermally activated mobility, in line with Eq. 6.3 [463, 488–490]:

$$\mu(T) = \mu_0 \cdot \exp\left(\frac{-E_\mu}{k_B T}\right) \tag{6.6}$$

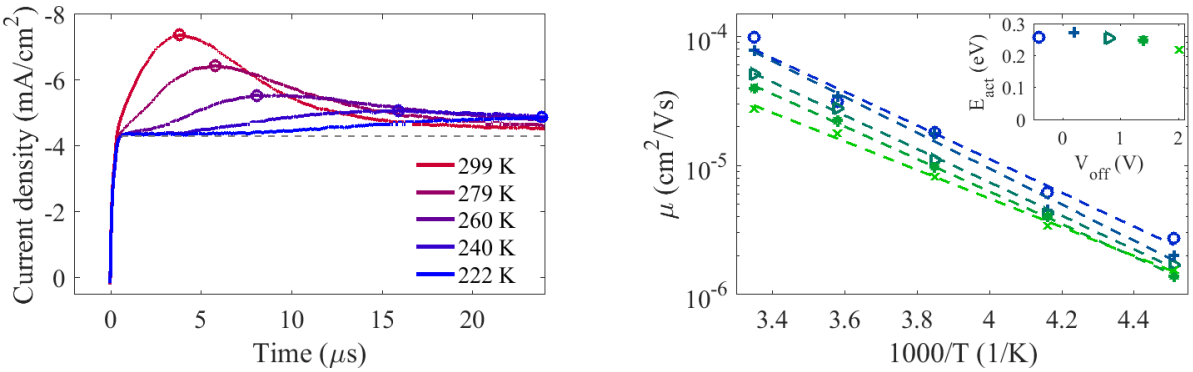

(a) The offset voltage prior to the ramp is 0.2 V, the ramp rate is 0.2V/μs. The grey dashed line denotes the displacement current, the symbols show the current maximum which is used to calculate the mobility.

(b) Arrhenius plot and linear fits for the measurements in (a) (offset voltage 0.2 V) and additional offset voltages from -0.4 to 2.0 V, denoted by their different symbols. The determined activation energies lie between 0.22 eV and 0.28 eV.

Figure 6.3: MIS-CELIV measurement of an α-NPD/Alq_3 bilayer OLED for varied temperature.

For simplicity we assume that the non-uniform electric field that may be present in the HTL does not affect the analysis and that the observed MIS-CELIV mobility is mainly influenced by the thermal activation and not the field-dependence. Since the MIS-CELIV experiments are carried out for the same electrical driving conditions (i.e. ramp rate), this seems a safe assumption.

As there is no energy barrier for charge extraction the determined activation energy from the MIS-CELIV experiment is only the thermal activation of the hole mobility E_μ. Thus, by combination of this experiment with the C-f-T technique we believe to be able to individually determine the two activation energies E_{inj} and E_μ. In the next section we are going to examine this hypothesis by means of numerical drift-diffusion simulation which allows us to investigate the accuracy of the extracted parameters. We will then apply this combination of methods to the already presented experimental data. In the last section we discuss the broader application of the proposed method in the context of OLED and OSC devices and materials.

6.2 DRIFT-DIFFUSION MODELLING

We aim to validate the proposed method by using a two-step approach. In the first "forward" simulation we calculate the two device characterization signals, namely C-f-T and MIS-CELIV current transients at various temperatures. In the second step, the above analytic approach is applied to the two kind of signals. The extracted parameters for temperature-dependent charge mobility and injection are compared to the model input parameters used in the "forward" simulations. This allows us to determine the self-consistency and how reliably we can obtain the activation energies by the combined experiments using basic analytic formulas. For this purpose we employ the commercial tool *Setfos* which is able to simulate both the (large-signal) transient CELIV experiment as well as the (small-signal) capacitance-frequency method with the same set of model parameters [299]. In previous publications we have already demonstrated the possibility of modelling polar ETLs in bilayer OLEDs in the steady-state and frequency domain with *Setfos* [83, 480].

The boundary condition in the injection model is that the Fermi-level at the contact is conserved (Fermi-level alignment). Then an injection barrier between HIL and HTL leads to a thermally activated exponential increase of the boundary charge density with temperature as:

$$p(x=0) = P_0 \cdot \exp\left(\frac{-E_{inj}}{k_B T}\right) \tag{6.7}$$

This is the same boundary condition as stated above in the simplified model. However, we do no longer assume a constant charge density throughout the HTL, but the density profile is calculated self-consistently in the drift-diffusion approach. Here we do not take barrier lowering due to image charge effect into account.

For the hole mobility in α-NPD we use the above-mentioned temperature dependent model, Eq. 6.6, where we set the mobility at 300 K to a value of 10^{-4} cm^2/Vs, which we determined from our CELIV measurements. Other model parameters have been chosen in accordance with measurements as well, and are summarized in Table A.2. We then systematically varied the hole injection barrier E_{inj} and the mobility activation energy E_μ, in order to find out about their influence on the validity of the analysis method.

Table A.2 summarizes the standard simulation parameters that have been used in the drift-diffusion part of this study. For the parameter sensitivity study a temperature-dependent hole mobility was employed, setting μ_h(T=300 K) = $1 \cdot 10^{-4}$ cm^2/Vs, and the barrier between the PEDOT:PSS (HIL) workfunction and the HTL HOMO was varied.

Figure 6.4 shows two exemplary simulations (E_{inj} = 0.4 eV, E_μ = 0.2 eV) of the C-f-T and temperature-dependent MIS-CELIV. We also mark the relevant transition frequencies and CELIV peaks, respectively, and show the Arrhenius-plots with the fits in the insets. The mobility in the CELIV simulations is determined using Eq. 6.5, as we perform simulations in the small-charge regime with offset voltages just above V_t. The transition frequency in impedance-frequency measurements can be deduced as the inflection point of the C-f plot, which is best derived as the minimum of the numerically computed first derivative.

For the C-f-T data we expect that the extracted activation energy is the sum of both the injection barrier and hole mobility activation, while for the CELIV experiment we expect to find only the mobility activation. From the simulation data of Fig. 6.4 we extract a total activation energy of 0.51 eV from C-f-T and an activation energy of 0.18 eV from MIS-CELIV, compared to the expected values of 0.6 eV and 0.2 eV, respectively. Thus, for the example in Fig. 6.4, the error for determination of E_μ by the analytic method is only 0.02 eV, and the error of the total activation

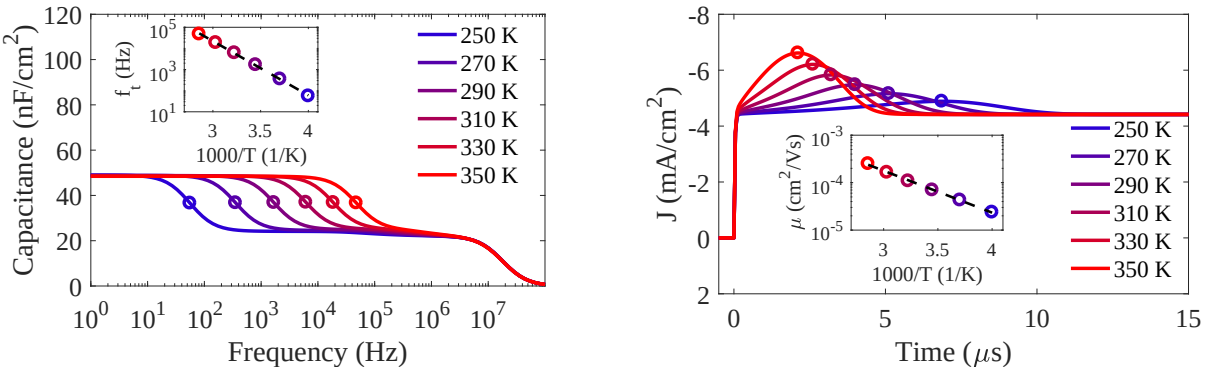

(a) Capacitance-frequency simulations at zero applied bias. The inset shows an Arrhenius plot of the transition frequency, resulting in an activation energy of 0.51 eV.

(b) MIS-CELIV simulations for an offset voltage of -0.7 V and a ramp rate of 0.2 V/us. The inset shows an Arrhenius plot of the mobility determined by Eq. 6.5, resulting in an activation energy of 0.18 eV.

Figure 6.4: Simulation of an α-NPD (80 nm)/Alq_3 (60 nm) bilayer device at varied temperature. The hole injection voltage is -2.2 V, injection barrier is 0.4 eV, and the mobility activation is 0.2 eV.

energy determined from C-f-T is 0.09 eV, leading to a total combined error for the injection barrier of 0.11 eV. We calculated this kind of systematic error for a large series of simulations performed by systematically varying both the hole injection barrier and the hole mobility activation energy. The analysed activation energies and the deviation from the expected values are shown in Fig. 6.5 and demonstrate the uncertainty of the analysis method based on Eqs. 6.1, 6.3 & 6.6.

For the MIS-CELIV simulations analysed in Figs. 6.5a & 6.5c we find nearly constant deviations < 0.07 eV for injection barriers below 0.25 eV. Here our assumption that this experiment is insensitive to the injection barrier holds. Indeed, for good contacts with low injection barriers the mobility activation energy may be determined reliably from the CELIV experiment. However, for larger injection barriers there is an influence and the deviation increases up to 0.15 eV.

Figures 6.5b & 6.5d show that for C-f-T the error in determining the activation energy is imposed by the injection barrier alone, while varying the mobility activation energy does not influence it. We find that the maximum deviation for determining the combined activation energy is 0.20 eV, at an injection barriers of 0.25 eV. Below this value, the error is on the same order of E_{act}, meaning that the experiment shows only the temperature dependence of the mobility, when the device is not contact-limited. This actually indicates that the mobility activation energy may also be obtained from C-f-T in the case of ideal ohmic contacts, with a very small systematic error below 100 meV. It is noteworthy, that for injection barriers higher than 0.25 eV the error decreases and the uncertainty of the extracted parameter will become as low as $0.05 - 0.10$ eV emphasizing that this is a powerful method to simultaneously estimate both activation energies.

Furthermore, as the deviation from the real value is always positive, the extracted parameters always underestimate the true values and thus give a quantitative lower limit.

We conclude that indeed the MIS-CELIV experiment is largely determined by the mobility activation energy. For small extracted E_{act} values the mobility activation can then be reliably determined. This is good news as the mobility activation energy in organic materials usually lies in the range of $0.1 - 0.3$ eV. Thus from the MIS-CELIV alone this parameter can be determined.

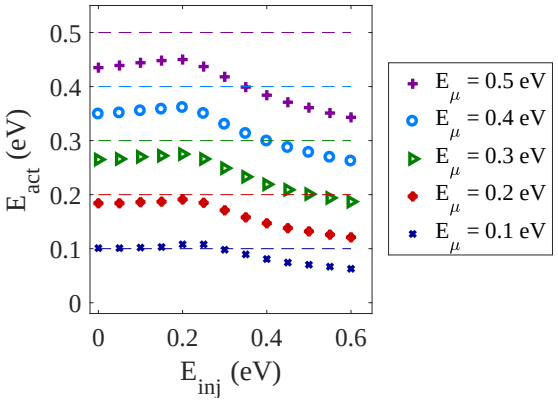

(a) MIS-CELIV with a ramp of 0.2V/us and an offset voltage of −1.5 V, the theoretical value is E_{act}=E_μ.

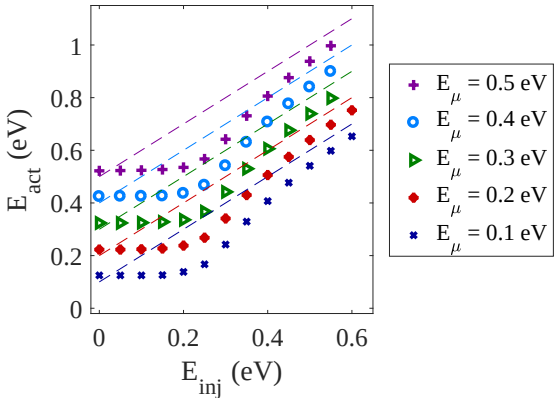

(b) Capacitance-frequency at 0 V, the theoretical value is E_{act}=E_{inj}+E_μ.

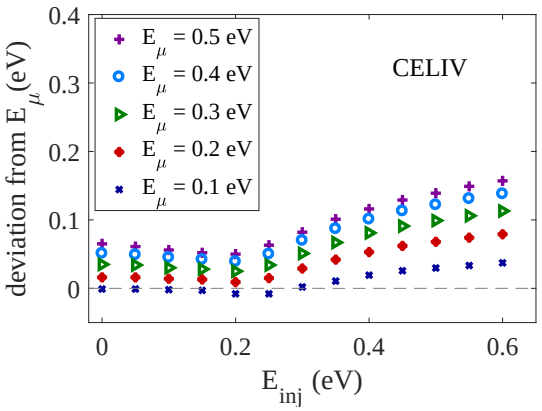

(c) MIS-CELIV with a ramp of 0.2V/us and an offset voltage of −1.5 V, the theoretical value is E_{act}=E_μ.

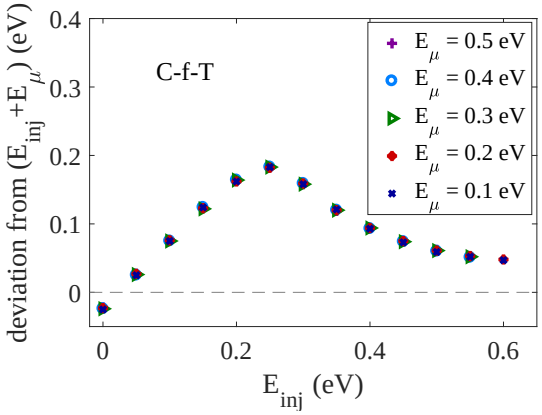

(d) Capacitance-frequency at 0 V, the theoretical value is E_{act}=E_{inj}+E_μ.

Figure 6.5: Analysis of the extracted activation energies from the simulated experiments. The upper plots show the determined values and the dashed lines depict the expexted parameters, the lower plots show the deviation between the expected (=input parameter) and the analysed value of the activation energy, for varied injection barrier E_{inj} and at different values of mobility activation E_μ. Simulation parameters as in Table A.2, except for $d_{ETL} = 80$ nm.

For a better understanding of the systematic error on parameter extraction, we show the simulated equilibrium charge carrier density and electric field profiles for varied injection barriers in Fig. 6.6. These profiles do not depend on the choice of mobility or mobility activation, as they depict the thermodynamic equilibrium. This is also the reason why the mobility activation does not influence the error in Fig. 6.5d.

As shown in Fig. 6.6b, for high injection barriers the holes accumulate only at the internal interface with the ETL, while for low barriers there is a considerable amount of charge also at the interface with the HIL, and in the bulk. Therefore, the analytic approach of Eq. 6.3 assuming position-independent density and field turns out to be too simplified. It seems that for non-limiting contacts the assumption of a homogeneous conductivity is best fulfilled, leading to the small errors in parameter determination.

In order to trust a maximum error of 0.25 eV we performed further simulations where other modelling parameters were varied. For these simulations we set E_{inj} = 0.4 eV, E_{μ} = 0.2 eV, so we would expect activation energies to lie at 0.6 eV and 0.2 eV for C-f-T and CELIV, respectively. We observe that the parameter extraction is completely unaffected by the model parameters electron mobility in the ETL, electron injection barrier, density-of-states in the HTL, internal energy barrier for holes between HTL and ETL, and the mobility prefactor μ_0 for holes. This shows the robustness of the method and allows us to specify 0.25 eV as an upper limit of the systematic error. It also confirms our initial assumption that the combination of the two experiments is indeed suited to disentangle the two activation energies, as no other parameters play a role.

We further find that for C-f-T the offset voltage plays only a minor role, so the working point (between V_t and V_{bi}, naturally) does not matter. Concerning the activation energy of the mobility using the MIS-CELIV experiment, it turns out that an offset voltage just above the hole injection voltage (-2 V in our case) leads to the most accurate results (0.18 eV), while the extracted mobility activation for an offset voltage of $+1$ V, for example, would be 0.1 eV instead of 0.2 eV. Part of this error probably stems from the evaluation of the mobility by Eq. 6.5, where for larger peaks the transit time has to be defined differently [353, 474]. Finally, also the voltage ramp was varied, and we find the smallest deviation from the input model parameter for high voltage ramps in the range of $0.1 - 1$ V/μs. Thus, by using appropriate measurement conditions the uncertainty of the extracted parameters can be narrowed further.

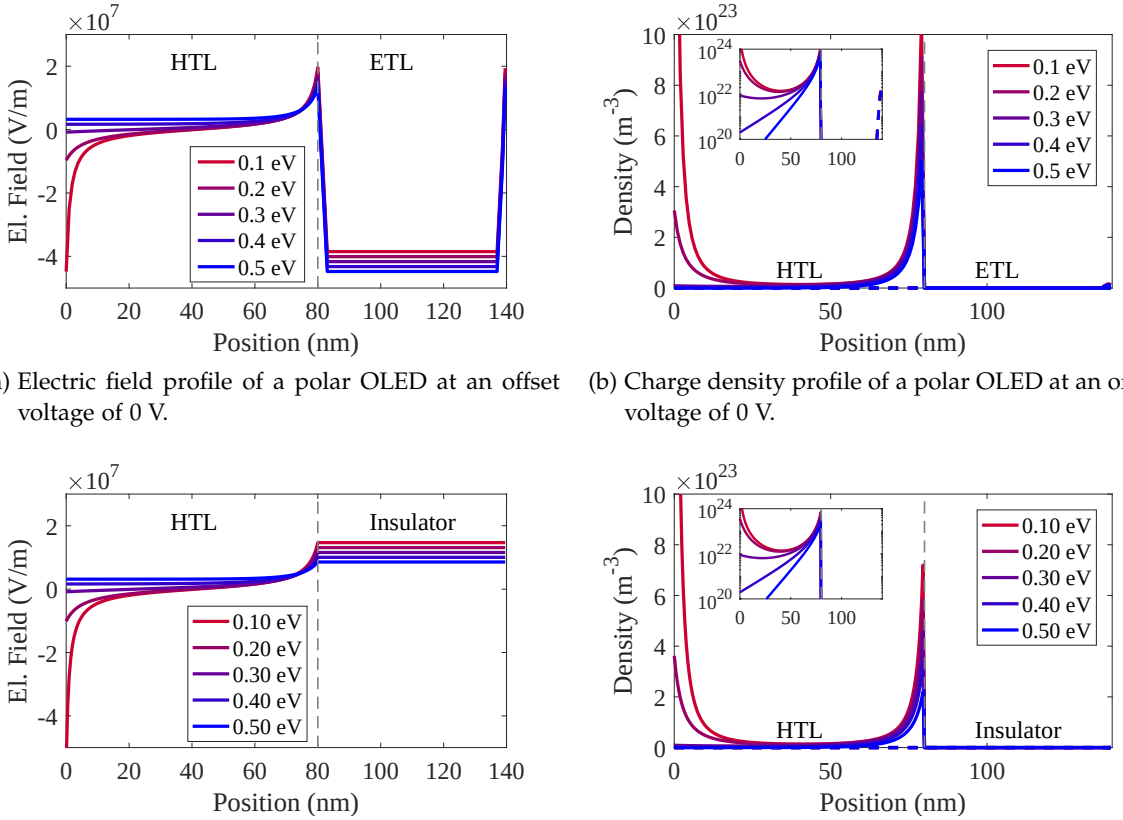

(a) Electric field profile of a polar OLED at an offset voltage of 0 V.

(b) Charge density profile of a polar OLED at an offset voltage of 0 V.

(c) Electric field profile of a MIS device at an offset voltage of 3.4 V.

(d) Charge density profile of a MIS device at an offset voltage of 3.4 V.

Figure 6.6: Simulation of the field and density profiles of a polar OLED and a MIS-device for varied injection barrier. See Table A.2 for the simulation parameters.

6.3 EXPERIMENT

In order to compare our approach with experimental characterizations, bilayer OLEDs were fabricated at Augsburg University. The layer stack was ITO (160 nm)/PEDOT:PSS (30 nm)/α-NPD (77 nm)/Alq_3 (66 nm)/Ca (15 nm)/Al (100 nm). The devices were encapsulated with a cover glass using epoxy. The active layer thicknesses are obtained from capacitance measurements. The capacitance-frequency and MIS-CELIV experiments were performed with *Paios*. For cooling we employed the low-temperature module of *Paios*, which uses a cryostat chamber cooled by liquid nitrogen. The whole temperature sweep with intermittent C-f-T and MIS-CELIV acquisition is automated in the Paios software and can be performed within 2 h, preventing accidental degradation of the device. The device temperature is logged using a PT100 temperature sensor which is placed on the glass substrate of the sample, therefore being a more relevant temperature probe than the sensor inside the cryostat cooling stage. For enhanced signal quality the CELIV measurements were performed 5 times and then averaged.

The C-f-T measurements and the temperature-dependent MIS-CELIV curves have already been shown in Figs. 6.1 & 6.3, respectively. From the CELIV measurement we determine a mobility activation energy of $0.22 - 0.28$ eV, where the highest value is obtained for offset voltages just above the hole injection voltage and therefore the most reliable one. Taking the systematic deviation as found from the simulations into account, we can give the result: E_μ = 0.28 [+0.1; -0.0] eV. The fit further allows us to estimate the high-temperature limit of the hole mobility in α-NPD to be μ_0= 3.5 cm^2/Vs.

As for the C-f-T measurements, a total activation energy of 0.53 eV is obtained at an offset voltage of 0 V. Subtracting the hole mobility activation yields the apparent injection barrier. As there is already an error on E_μ the accuracy for the injection barrier is smaller. We find E_{inj} = 0.25 [+0.2; -0.1] eV. The determined value for the injection barrier between PEDOT:PSS and α-NPD seems a bit low, as from the difference between the nominal PEDOT:PSS workfunction (5.1 eV) and the α-NPD HOMO (5.5 eV) one would assume a higher value. Such a high barrier would, however, not allow for efficient OLEDs. Our analysis suggests that the effective injection barrier is lowered at the interface. Thus, we are able to distinguish and estimate the lower limit for both activation energies relevant for the hole injection and transport, albeit with some uncertainty.

6.4 DISCUSSION

As we have seen, the implicit assumption of constant charge and field profiles throughout the layer employed in the analytic model gives rise to the systematic errors in parameter determination. A first improvement of this situation would be the use of a more complex analytic model taking the inhomogeneous density into account [491]. In order to further narrow down the confidence interval of the parameters, a full drift-diffusion modelling and global fitting of the measurement data is conceivable, and we have already demonstrated such a procedure before [228, 340]. However, even though the analytic description is not powerful enough to get a very accurate value of the injection barrier, we believe that this method still can be useful to compare different devices or to monitor the degradation of one device.

Overall, it seems that we can determine E_μ very well, while we systematically underestimate E_{act} from C-f-T, because the "effective" injection barrier is about $0.1 - 0.2$ eV smaller than the nominal value.

This approach is not limited to bilayer OLEDs, as we have only exploited their behaviour as MIS-diodes here. Conventional MIS-devices comprising an insulating layer will obviously also work. For comparison we show an exemplary simulation of the field and density profiles of a MIS-device in Figs. 6.6c & 6.6d. The profiles are qualitatively identical, thus the analytic procedure is as valid as in the polar OLED case. As a side note we want to mention that the thickness ratios in standard MIS-devices are usually different from the bilayer OLEDs, and therefore the CELIV mobility is often analysed in saturation regime, demanding a correction factor for the determination of t_{tr} in Eq. 6.5 [353, 474, 480].

Thus the method presented may be applied generally to new organic materials. In different bilayer stack layouts comprising a polar layer [444, 480], or in dedicated MIS devices it would then also be possible to gain information on the electron mobility and its thermal activation.

The value obtained for the mobility activation in α-NPD is 0.28 eV. In organic materials exhibiting disordered transport this effective activation energy depends on the shape of the density-of-states. In the context of the field- and temperature-dependent extended Gaussian disorder and correlated Gaussian disorder models (EGDM and ECDM) the width of the density-of-states σ can be related to the transport activation by $E_\mu = \frac{4}{9}\frac{\sigma^2}{k_B T}$ [492, 493]. With this formula and the activation energy of E_μ=0.28 eV we obtain a DOS width of σ = 125 meV at 300 K, in good agreement with values reported earlier for α-NPD [494–496].

Concerning the temperature activation itself, the disorder models usually note a $1/T^2$ dependence instead of the observed and discussed $1/T$ behaviour [407, 497, 498]. In fact, at high temperatures (>200 K) the two dependencies can not unambiguously be distinguished, and the disorder models are fully consistent with Arrhenius activation [499–501].

The energetic barrier for charge injection is most relevant for efficient OLEDs with a low turn-on voltage. The experimental finding that small injection barriers (<0.2 eV) are not "seen" by the charges, is confirmed by the simulation, without special care for the interface modelling. Thus if the device is not contact-limited the mobility activation energy will be the only factor contributing to E_{act} determined from C-f-T. For such small barriers the chosen contact model assuming Fermi-level alignment is physically more meaningful than the thermionic emission or tunnelling models, which are valid rather for high energetic barriers [502, 503]. Including barrier lowering effects has not been in the scope of this work, but we encourage to investigate this refinement further.

Even though there are several formulations for injection models and mobility models, it remains an experimental challenge to discriminate one from the other. Therefore we try to concentrate on the determination of effective material parameters. Concerning the mobility temperature activation, this has been most often investigated in unipolar devices by experimental techniques such as space-charge limited current [494, 504], time-of-flight [505] or negative differential susceptance [506]. However, as we have shown above, the injected current is always dependent on both the mobility activation and the injection barrier. So good care must be taken when fabricating unipolar devices and analysing these measurements. Alternatively, as proposed here, extraction experiments like CELIV are much less sensitive to the injection barrier, and therefore better suited.

Concerning the injection barrier between two organic semiconducting materials, that is the energy level offset between their conduction bands, its experimental assessment is even more problematic. The most common techniques to analyse the valence and conduction bands of organic materials are photoelectron spectroscopy and Kelvin probe force microscopy [507–509]. In order

to determine the energy offset between two materials a series of devices needs to be fabricated and measured, where the second layer is deposited onto the first with varied thickness, therefore allowing to probe the position-dependent energetics (bandbending) [440, 510–512]. While these techniques have proven valid and reproducible, they are expensive and time-consuming, and multiple devices are needed. Furthermore, these techniques also have their systematic errors for parameter determination; for UPS errors in the range of $0.1 - 0.35$ eV have been reported for organic materials [440, 513–516].

Another approach seen in literature is the use of IV-curves and capacitance-voltage measurements for the extraction of injection barriers [333, 492, 517]. However, as mentioned before, injection currents always depend on both the barrier and the mobility, so in these cases probably an effective total activation is observed. Furthermore usually simplified layer stacks have to be used.

We believe that temperature-dependent electrical measurements on MIS-devices or complete polar OLEDs can be more practical and relevant. The method presented in this work can be performed on complete layer stacks, and results are obtained more quickly and with less consumption of resources. And apart from the parameters discussed in this text, the temperature-dependence of OLEDs and OSCs is by itself an important experiment on the way of device optimization.

7 OLED DEGRADATION

The degradation of OLEDs is usually investigated under operating conditions. Hereby the device is stressed at a constant forward current, and after specified time intervals a measurement (usually IV-curve acquisition) is performed. With progressing degradation a higher driving voltage has to be applied to achieve the specified current. Furthermore, if the current efficiency degrades, the light output at this current decreases. Thus, the constant current driving condition directly allows to distinguish between degradation effects that are related to injection and transport, and those related to radiative recombination and excitonics.

Here we present a degradation study of a bilayer OLED consisting of the stack ITO (140 nm)/PEDOT:PSS (30 nm)/α-NPD (130 nm)/Alq_3 (45 nm)/Ca (15 nm)/Al (100 nm). The device was stressed at 1 mA for 2 h and at 2 mA for another 2 h. For this purpose we employed the Stress-Test Module of *Paios*, which applies and controls the constant current, and performs automated measurement routines periodically in between the stressing, in this case every 20 min. Figure 7.1 shows various measurements during the degradation. The current-voltage as well as the luminance-voltage curves decrease. While the current at 6 V decreased by 60 %, the luminance decreases by a factor of 4. The first observation is consistent with the observed increase in driving voltage needed for a current of 1 mA (see Fig. 7.1c). The injection becomes less efficient during degradation, also showing in the change of the IV-curve slope. Secondly, the strong loss in luminance relates to an additional loss in current efficiency, witnessed by a decrease of 60% of luminance at 1 mA (see Fig. 7.1d). The luminance and voltage have been plotted versus the stress, that is the stress current times the stress time. Here the luminance decrease is approximately exponential to the stress, as observed by the linear behaviour in log-x scale. Interestingly, however, the slopes change at the point where the stress current was increased from 1 to 2 mA, meaning that a two times higher current accelerates the degradation by a factor higher than two.

We further performed MIS-CELIV measurements as shown in Fig. 7.1e. Here the MIS-CELIV taken at an offset voltage of 1 V shows a strong decline of the peak. At 1 V, due to the polar ETL, the device is in the MIS-regime, thus the CELIV peak consists only of holes. So, the decreasing peak is either a sign of a weaker hole injection at 1 V or of an extraction problem. When looking at the reverse CELIV (fast DCM) (see Fig. 7.1f), we follow the injection behaviour, which shows that the hole injection voltage shifts and also the electron injection (related to the second increase after 30 μs) is impaired. The shift of the hole injection voltage becomes more clear by analysing the impedance measurements. The capacitance-frequency at 1.5 V as well as the capacitance-voltage at 1000 Hz clearly show the transition from a polar device into a non-polar device. Therefore we conclude that the polar sheet charge decays during degradation. In fact, the decrease of the polar sheet charge in Alq_3 has been reported many times [443, 445–448, 518–521], due to illumination, temperature, and current stress. The decrease of the polarity effect can be related to a decrease in conductivity of the HTL, leading to the lower relaxation frequencies, which is in line with the lower currents (compare to Fig. 4.7).

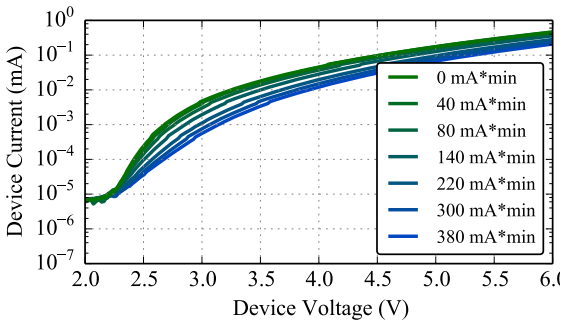

(a) Current-voltage curve

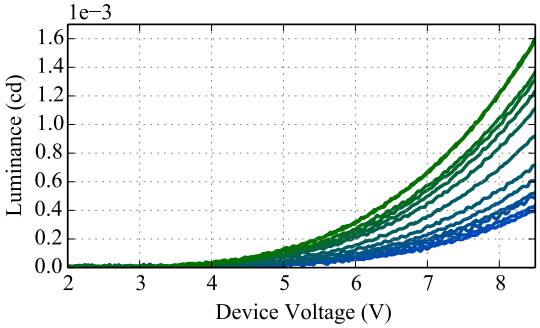

(b) Luminance-voltage curve

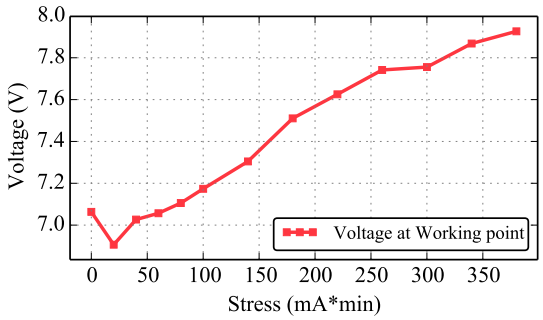

(c) Voltage at 1 mA

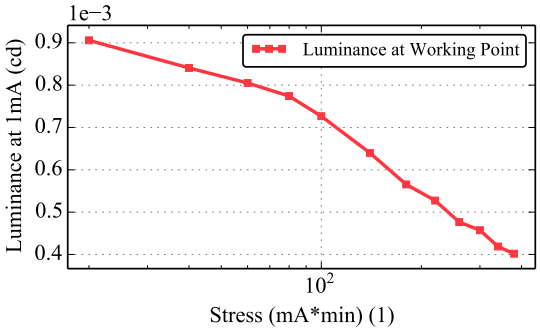

(d) Luminance at 1 mA

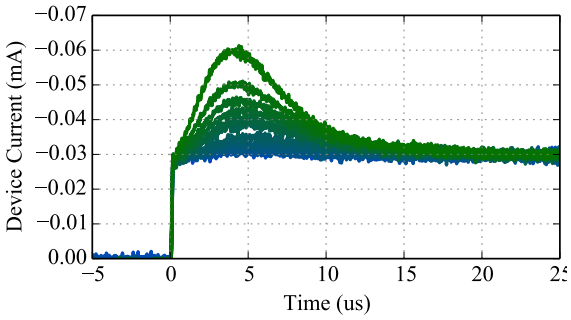

(e) MIS-CELIV at an offset voltage of 1.5 V and using a ramp rate of 200 V/ms

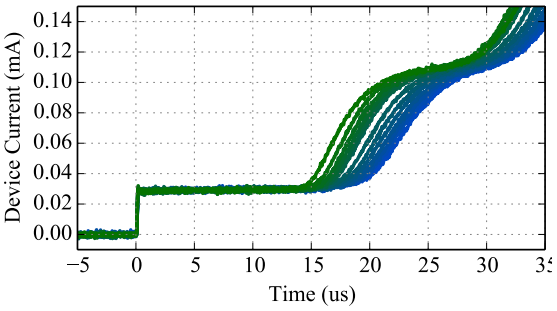

(f) Reverse CELIV at an offset voltage of −2 V and using a ramp rate of 200 V/ms

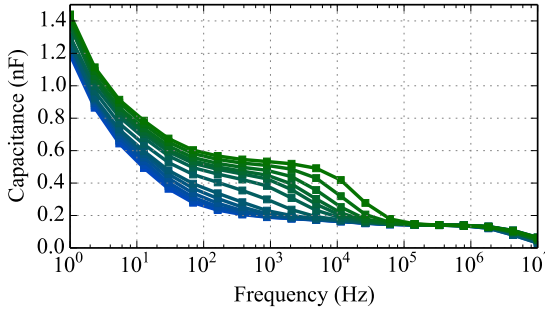

(g) Capacitance-frequency at an offset voltage of 1.5 V

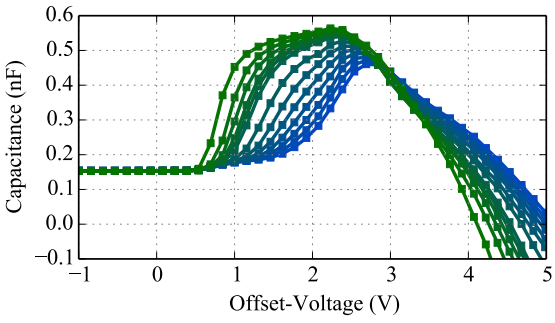

(h) Capacitance-voltage at 1 kHz

Figure 7.1: Measurements of a polar OLED degraded by constant current stressing for 380 mA*min. Legend from green (fresh) to blue (degraded) is shown in subplot (a).

The change in the hole (and electron) injection properties can explain only part of the measurements, as it does not relate to a loss in luminous efficiency. Therefore a second mechanism needs to be present to account for the exponential decrease in luminance. One possible explanation is the current (polaron) induced generation of traps as a product of chemical degradation. In fact, we can speculate that the loss in sheet charge density goes along with the generation of mid-gap states. Traps can affect the forward current, but also act as non-radiative recombination centres. Indeed, traps have been reported in literature to represent an important degradation mechanism in OLEDs [56, 447, 522–527].

Here we can only speculate where the traps are formed. Both the Alq_3 [526, 527] and the α-NPD [523–525] have been shown to be prone to current induced trap formation. On the one hand the HTL conductivity is decreased, which could be explained by a lower effective hole mobility due to trapping. On the other hand, however, the CELIV peak position is unchanged. Still, the CELIV peak time is related to the fastest carriers, and trapped holes would not contribute here, while they would affect the overall mobility and conductivity and hence the forward current.

But also electron traps in the ETL are feasible to explain the lower current. They could further be responsible for a partial compensation of the polar sheet density.

In any case traps influence the effective mobility and can decrease the charge balance factor and therefore the luminous efficiency. Trap-assisted (non-radiative) recombination will additionally decrease the light emission. Thus, trap generation and a reorientation of the Alq_3 molecular dipoles are suggested as the two dominant degradation mechanisms in this case.

8 SUMMARY

The macroscopic polarization of many electron transport layers in OLEDs has been known for 15 years [442]. Yet, only now it has become possible to quantitatively simulate this effect within the drift-diffusion modelling approach. This possibility holds many opportunities for device characterization.

The polarity effect describes the non-random orientation of the molecular dipole moments of a material during deposition, leading to an effective sheet charge density on both sides of the layer. This induces a large potential drop over the polar ETL, such that the bands in the HTL are more favourable for hole injection. In a bilayer OLED this leads to the observed three voltage regimes: (I) in reverse, where both ETL and HTL are insulating, (II) a MIS regime, where the ETL is still insulating, but holes are already injected into the HTL, and (III) the bipolar regime above V_{bi} where a steady-state current and emission set in. The most direct influence of the polar ETL is on the forward current in the IV-curve. Here the polarity which leads to a positive sheet charge at the ETL/cathode interface induces electrons into the ETL and hereby facilitates injection. This leads to a higher forward current and also a slightly lower turn-on voltage. Oppositely, with an inverted polarity (which is however not common) the forward current will be strongly impaired.

In our work we focus on the MIS regime, where only holes are present in the device. Depending on the ETL thickness the hole injection voltage can be shifted even to negative bias. As there is no steady-state current, IV-curves are not interesting in the voltage range below V_{bi}. Instead transient and impedance techniques can give valuable information.

We presented two new approaches for parameter determination in polar bilayer devices. The first one is the application of the CELIV technique. We take advantage of the fact that between the hole injection voltage and the built-in voltage the device behaves like a MIS-device. Under these conditions the MIS-CELIV experiment can be performed and the hole mobility of the active layer under investigation can be determined. This method therefore has the potential to be applied rather generally to new thin film semiconducting materials for organic solar cells and OLEDs. In combination with dipolar doping both hole and electron mobility of a material can be assessed.

The second analysis we demonstrated is the determination of activation energies. We have presented an approach how the different activation energies for hole transport and injection in polar bilayer devices can be decoupled. For this purpose we combine C-f-T data with temperature-dependent MIS-CELIV measurements. From a first simple analytical model it becomes clear that the C-f-T data contains contributions of both the temperature dependent charge injection and hole mobility. Using a self-consistency analysis enabled by numerical drift-diffusion simulation we determine the accuracy of the extracted parameters depending on the model input values of injection barrier and mobility activation energy. In this analysis we find that the extracted values are always lower than the true model parameters by up to 0.2 eV. The main reason for the deviation is the highly inhomogeneous charge profile in the hole transport layer leading to a non-constant conductivity, which is not taken into account in the analytical expression.

Employing this approach with an α-NPD/Alq_3 device comprising the hole injection layer PEDOT:PSS, we deduced the hole mobility activation energy in α-NPD to be 0.28 [+0.1;-0.0] eV, which can be translated into a width of the Gaussian density-of-states of 125 meV, in good accordance with previous reports in literature. The injection barrier from PEDOT:PSS into α-NPD is found to be 0.25 [+0.2;-0.0] eV.

We have shown that the polarity effect leads to a regime where the device behaves as a MIS-device in accumulation. This behaviour can be exploited for parameter determination. Techniques that have been developed for MIS-diodes may be applied, and our findings are directly transferable to "real" MIS-devices. This layer architecture, being either a bilayer with a polar material or comprising a fully insulating layer, therefore represents a highly valuable design for parameter determination and investigation of new materials.

Parts of the preceding Chapters presenting modelling and analysis of bilayer polar OLEDs have been published in peer-reviewed journals. The basic modelling of polar layers within the drift-diffusion approach has been presented in: S. Altazin, S. Züfle, E. Knapp, C. Kirsch, T. D. Schmidt, L. Jäger, Y. Noguchi, W. Brütting, and B. Ruhstaller. "Simulation of OLEDs with a polar electron transport layer". *Organic Electronics* 39 (2016), pp. 244–249. DOI: 10.1016/j.orgel.2016.10.014 [83].

We have further demonstrated the possibility to determine the charge carrier mobility in polar OLEDs in the MIS-regime: S. Züfle, S. Altazin, A. Hofmann, L. Jäger, M. T. Neukom, T. D. Schmidt, W. Brütting, and B. Ruhstaller. "The use of charge extraction by linearly increasing voltage in polar organic light-emitting diodes". *Journal of Applied Physics* 121 (2017), p. 175501. DOI: 10.1063/1.4982903 [480].

Another publication discussing the use of bilayer OLEDs for determining activation energies has been submitted and is currently under review: S. Züfle, S. Altazin, A. Hofmann, L. Jäger, M. T. Neukom, W. Brütting, and B. Ruhstaller. "Determination of charge transport activation energy and injection barrier in organic semiconductor devices". *Journal of Applied Physics* 122 (2017), p. 115502. DOI: 10.1063/1.4992041 [528].

Part III

DEGRADATION OF ORGANIC SOLAR CELLS

This part contains the results obtained on organic solar cell degradation. The experimental findings of several stability studies using different ageing conditions are presented. The measurements are analysed and proposed degradation mechanisms are discussed. The assumptions are then examined by numerical simulations.

9 INITIAL DEFECTS AND REPRODUCIBILITY

When investigating organic solar cell degradation, one usually analyses how the device performance decreases with time. In theory this implicates that at time 0 the device was ideal. However, in reality this is not the case, and most devices do not achieve the performance that their materials potentially allow. Some of the loss mechanisms that prevent the device from achieving its full potential are consequences of the electrodes and functional layers as well as the device layout. Some are due to the active material itself. Furthermore the actual fabrication conditions can have a detrimental effect.

In the following we will show several effects that can harm the performance already in the fresh state.

9.1 SERIES RESISTANCE

The series resistance of the device is of crucial importance for transient measurements. Here a high resistance distorts the measured currents and can render parameter extraction inaccurate. But also the device efficiency can be harmed if the resistance is too high [529, 530].

The main contribution to the series resistance comes from the contacts and the sheet resistance of the electrode fingers. In organic solar cells this is mainly the sheet resistance of the ITO. In the IV-curve the series resistance affects the short-circuit current and the fillfactor.

For dynamic measurements the RC-time is relevant:

$$\tau_{RC} = R_S \cdot C \sim (w \cdot l) \cdot S \tag{9.1}$$

As the capacitance of the device $C = \frac{\varepsilon_0 \varepsilon_r S}{d}$ increases with the active area, small pixel sizes are better for transient and impedance experiments.

When the ITO contact is metallized a big part of the series resistance can be mitigated. The contact resistance can be minimized using silver conducting paste. An optimized geometry of the electrode fingers can further help to decrease the series resistance.

The influence of the series resistance various experiments is shown in the Appendix C.1.

9.2 SHUNTS

As already described in the introduction (Section 2.1.1) a non-blocking behaviour of the device needs to be taken into account. When the parallel resistance is too low a part of the total current can flow as a parasitic current. These effects often arise from too thin layers leading to shunts where the top metal electrode touches the bottom ITO. As ITO is relatively rough and has needles the functional layers should be deposited thick enough to planarize and avoid these shorts. Another class of shunts is caused by incomplete etching and structuring leading to parasitic currents at the edges of the sample or device.

Ohmic shunts contribute a linear current-voltage characteristic adding to the diode current-voltage curve. There is, however, also the possibility of reverse injection, for example when the contact material is not fully selective for one carrier and the injection barrier is small enough, or

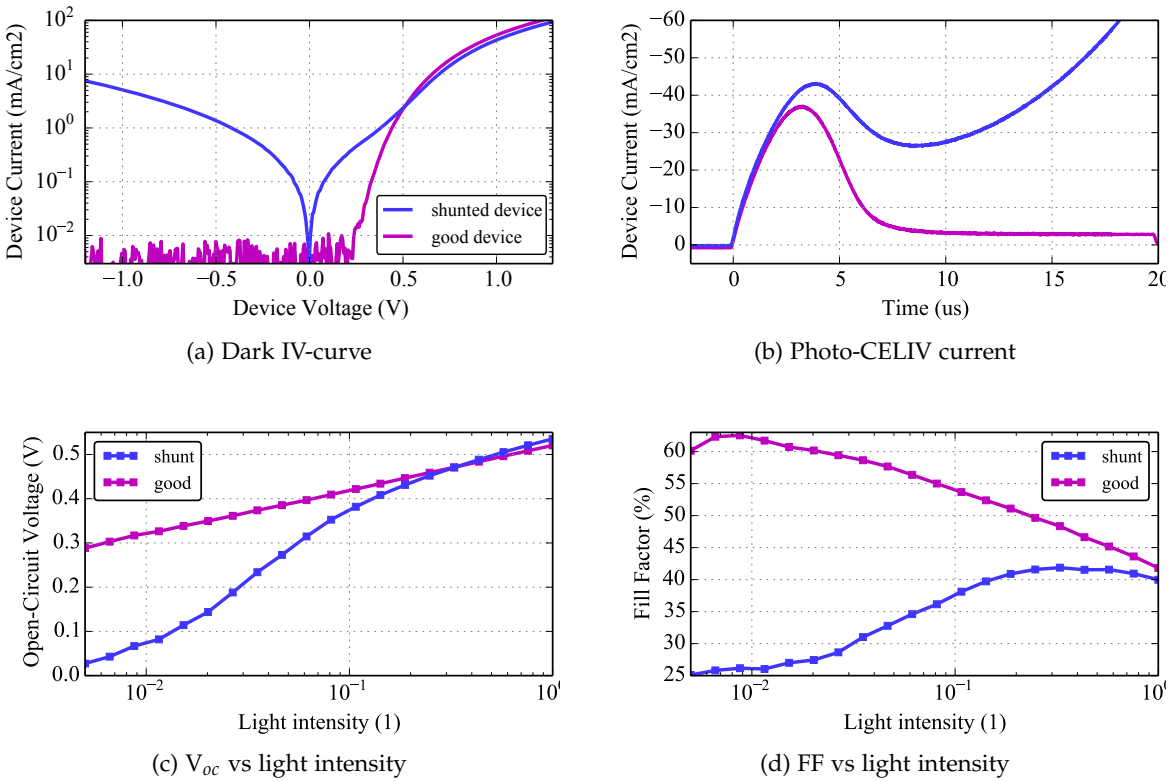

(a) Dark IV-curve

(b) Photo-CELIV current

(c) V_{oc} vs light intensity

(d) FF vs light intensity

Figure 9.1: Influence of a shunt on different measurements. The plots show data from two devices on the same P3HT:PCBM sample.

when the layer is so thin that tunnelling between the electrodes can occur. In these cases the observed reverse current is nonlinear and may be described similarly to a forward injection current.

In the IV-curve a low parallel resistance affects the open-circuit voltage and fillfactor. This is observed in the example measurement in Fig. 9.1 where the values for low intensities are affected most. Figure 9.1b also demonstrates the influence on the CELIV peak position.

The effect of the parallel resistance on this and other experiments is shown in the Appendix C.2.

Figure 9.2a shows a photoinduced shunting effect that can occur in devices employing ZnO as an electron transport layer. This material changes its conductance when subject to light and oxygen. In order to trace down the reason for the sudden shunting behaviour observed during a previous measurement routine we stressed an unencapsulated device under different conditions: At first in the glovebox by current and light stress, showing no shunting. The device was then exposed to air in the dark and stressed with current, still showing no change. Only when the device was illuminated in air the shunting effect appeared quickly. This effect has been shown before and is supposed to be (partly) reversible by an annealing step [178, 531]. Another way to avoid it is, however, the use of a different ETL, as shown in Fig. 9.2b [180].

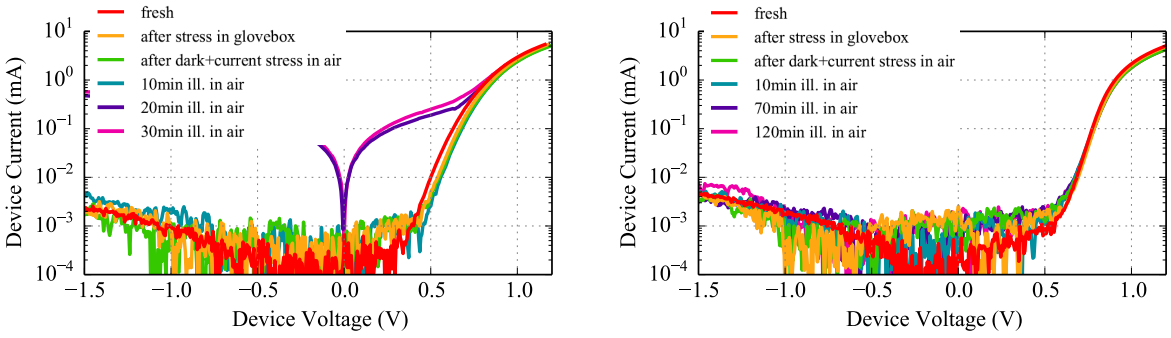

(a) ZnO device

(b) PV-E002

Figure 9.2: (a) Photo-shunting effect in a device with ZnO as ETL exposed to light and air. Different stresses are performed to identify the cause of the shunt. (b) Device with PV-E002 as ETL, showing stability for all stress conditions, and being insensitive to photo-shunting.

9.3 EQUILIBRIUM CARRIERS (DOPING)

As explained in the introduction, the active layers can usually be described as intrinsic, that is undoped, layers. However, some materials such as P3HT show "doping" under specific fabrication conditions. Intrinsic charged immobile species lead to the injection of counter-balancing charges with opposite sign in equilibrium. Similar to doped inorganic semiconductors a space-charge zone forms from where photogenerated charge cannot easily be extracted, hereby impairing the short-circuit current. The influence of doping on various experiments is shown in the Appendix C.6. Furthermore degradation-induced doping plays an important role in Chapter 11.

The doping effect is usually removed by special treatment, for example thermal annealing. This is demonstrated in Fig. 9.3 where the dark-CELIV peak nearly disappeared after annealing the cell for 20 min at 100 °C. In the IV-curve the fillfactor and short-circuit current are strongly improved by this annealing step, and the S-shape disappears.

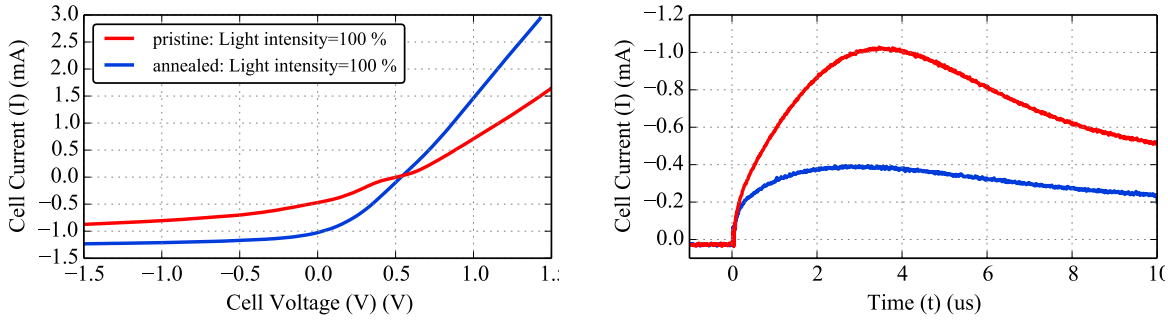

(a) IV-curve of pristine (red) and annealed (blue) device

(b) Dark-CELIV measurement of pristine (red) and annealed (blue) device

Figure 9.3: Influence of annealing for 20 min at 100 °C on the characteristics of a P3HT:PCBM device.

9.4 S-SHAPE

Another sign of a non-ideal device, be it due to fabrication conditions, choice of functional layers, or the active material itself, is the characteristic of a kink, the so-called S-shape, in the current-voltage curve. This S-shape almost always decreases the fillfactor, and therefore represents an important loss mechanism. The position of the S-shape can be determined visually as the inflection point of the IV-curve, but is easier visualized as a peak in the differential resistance plot ($R_{diff} = \frac{dV}{dI}$). The two examples in Fig. 9.4 show the position of the S-shape at forward and at reverse bias, respectively. The first one is probably due to an injection problem, while the second is related to an extraction barrier and shows a degraded device. Some S-shapes are correlated with an overshoot in the transient photocurrent, however, such an overshoot can also be observed without having an S-shape, and vice versa.

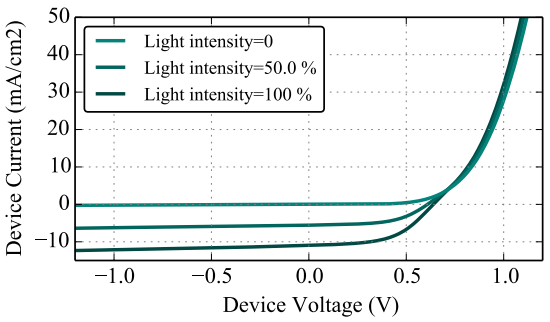

(a) IV-curves of a P3HT:PCBM cell with a slight S-shape

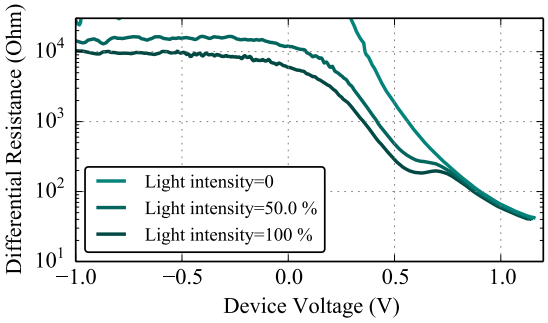

(b) Differential Resistance plots of the same data showing the S-shape more clearly

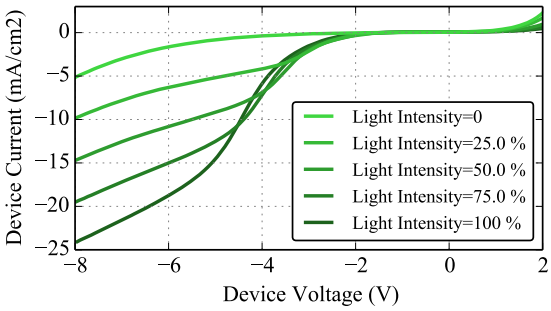

(c) IV-curves of a degraded OSC showing S-shape in reverse

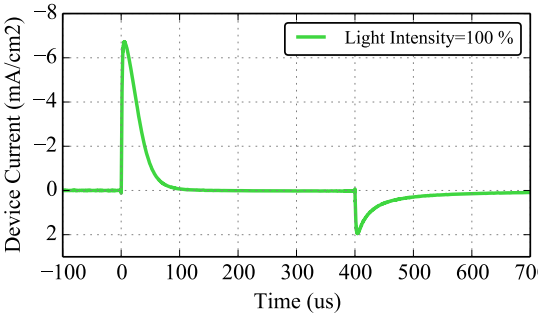

(d) Transient photocurrent at 0 V for the same device showing overshoot and undershoot

Figure 9.4: Different occurrences of S-shapes in the IV curve, and correlated signatures in other measurements.

An S-shape can have various reasons, but all have in common that one charge species accumulates, leading to a local screening of the electric field and therefore an impaired current. The accumulation can happen due to an interface barrier for injection or extraction, but also due to imbalanced electron and hole mobilities. Another cause can be traps, effectively also slowing down one carrier type. Some reasons for an S-shape are demonstrated qualitatively by the simulations in Fig. 9.5.

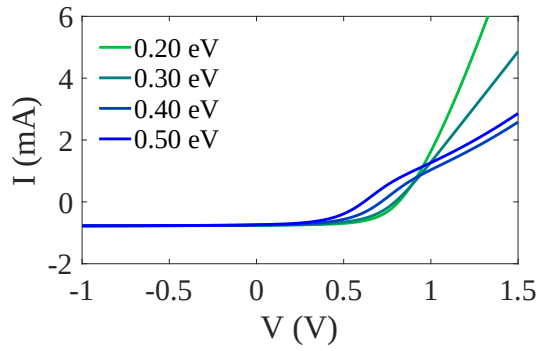

(a) Variation of the injection barrier for holes

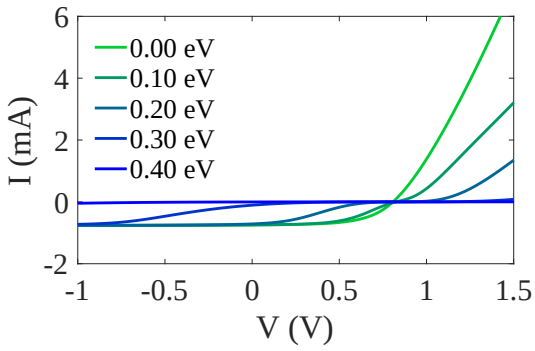

(b) Variation of a 10 nm thick extraction barrier for electrons close to the cathode

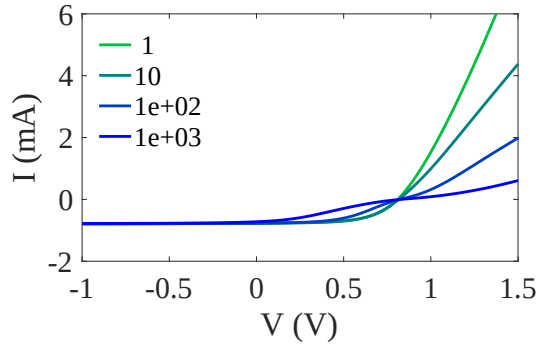

(c) Variation of the mobility in a 10 nm thick region close to the anode by a ratio to the bulk mobility

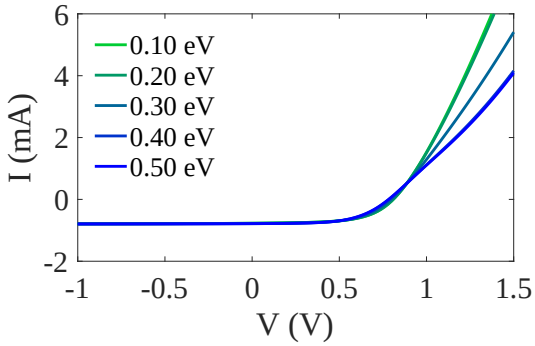

(d) Variation of the interface trap depth in a 10 nm thick region close to the anode

Figure 9.5: Simulations demonstrating several reasons for S-shapes in IV-curves.

9.5 REPRODUCIBILITY

Another big issue is the low reproducibility of device fabrication. As research OSCs are mainly fabricated in small batches and involving manual steps, this "human factor" leads to the problem that no two samples are identical. Automation where possible and thorough care on the manufacturing process can strongly reduce the cell-to-cell variation. However, also on one sample (glass substrate) containing several devices one can often observe slight differences. These are mainly due to inhomogeneous layer thicknesses from spin-coating as well as non-ideal metal evaporation leading to slightly different active areas.

Figure 9.6 shows IV-curves of several nominally identical devices on the same substrate, for two samples from different producers. While the first producer can guarantee identical current densities, even for devices with different active areas, the second case shows lower reproducibility as well as one device which shows a strong shunt from the beginning.

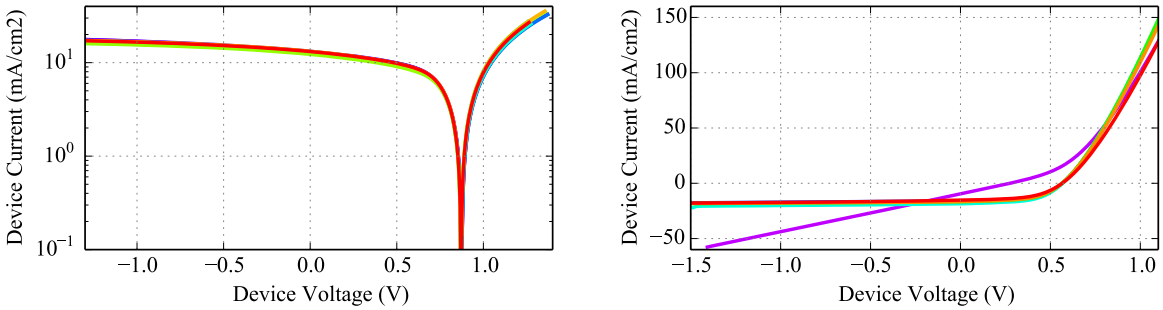

(a) HBG1:PCBM substrate with 4 small and 4 big nominally identical devices

(b) P3HT:PCBM substrate with 6 nominally identical devices

Figure 9.6: IV-curves of all devices on one substrate.

Another example featuring PCDTBT:PCBM solar cells from the COST StableNextSol Experiment [532] is given in Fig. 9.7. Here the participating producers fabricated five nominally identical samples (glass substrates). The plot shows the variation between samples and devices from one producer. While it is obvious that different producers, who all use different recipes, geometries and functional layers lead to strongly varying parameters, also the cell-to-cell variations for nominally identical devices and substrates can be quite large. Here the capacitance variation is shown as a sign of inhomogeneous layer thicknesses over the sample area.

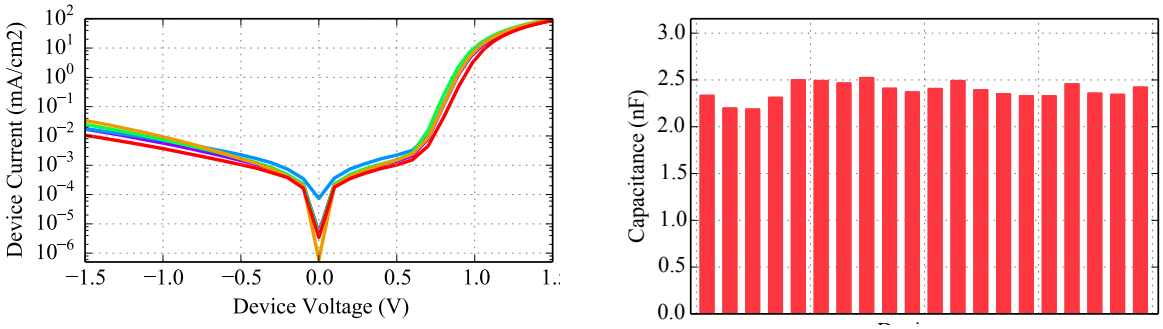

(a) Dark IV-curves of the best devices of 5 nominally identical PCDTBT:PCBM samples

(b) Analysed capacitance for 20 nominally identical devices within 5 PCDTBT:PCBM samples

Figure 9.7: Variations between different nominally identical samples.

The preceding analysis makes it clear that one should be careful already when measuring fresh devices. The first step should be measuring all devices on a substrate to find out about the variations. Then we suggest to choose the best device for further analysis and degradation studies.

It is obvious that for the reporting of efficiency values a more statistical approach involving ideally many samples is necessary.

On the other hand, for stability studies often qualitative changes during degradation are the most interesting result. Here it can still be valid to concentrate on single devices and their ageing behaviour. As a matter of fact, for the complementary measurements shown in this work a systematic measurement process, reliable ageing conditions, and measuring always the same device gives a much higher reproducibility. Involving several devices or samples in the ageing study would make it less systematic.

Another question is whether global fits of experimental data with simulation, as the ones shown in Appendix B, are still useful considering the large sample-to-sample variation. While the exact parameter values may indeed differ for another, nominally identical device, the range and magnitude of the various parameters is still valuable information. Furthermore, the fits shown here also serve to demonstrate that the simulation model is indeed appropriate to describe the full set of measurements.

10 HUMIDITY INDUCED DEGRADATION

Unencapsulated organic solar cells show only very limited stability due to chemical reactions with in-diffusing oxygen and water. In the conventional architecture, which employs low-workfunction metals as top electrode, this layer is prone to oxidation leading to a fast decay of the solar cell parameters [222]. When the device comprises PEDOT:PSS as the hole transport layer (HTL), this material's hygroscopic behaviour can accelerate water ingress and thereby the cathode oxidation [533]. One approach to enhance the stability is thus the replacement of PEDOT:PSS by other hole transport materials. For this study we employ metal-oxide based, solution-processed hole transport layers, allowing for a fully printable solar cell stack.

10.1 EXPERIMENTAL

The device stack has a standard architecture and consists of: ITO (130 nm)/HTL (20 nm)/P_3HT:$PC_{61}BM$ (85 nm)/Al (100 nm). For the comparison we use PEDOT:PSS AI4083, MoO_3, and V_2O_5 from two different precursors (V_2O_5 Xerogel and V_2O_5 Oxopolymer). The synthetisation as well as the device fabrication took place at CSEM in Basel [534].

The ageing conditions were varied also:

- Room temperature (25 °C) in the dark, with ambient humidity (45% RH), corresponding to shelf life degradation in compliance with ISOS-D-1. Ageing time was 1200 h.
- Room temperature (25 °C) in the dark, with enhanced humidity (75 % RH). Ageing time was 600 h.
- Enhanced temperature (45 °C) in the dark, with high humidity (85 % RH), in a climate chamber (ESPEC SH-641). Ageing time was around 200 min.

For the experiments at room temperature the IV-curve of the devices was repeatedly measured with a Keithley 2400 SMU under a solar simulator with an AM1.5g spectrum. These measurements were performed by Marc Zinggeler at CSEM. The cells aged in the climate chamber were characterized with the *Paios* system. Therefore the *Paios* measurement table was placed inside the climate chamber with the solar cell and the illumination source (LED) [535] contacted, and a complete measurement routine was performed periodically after a defined ageing time interval.

For drift-diffusion modelling *Setfos* 4.1 was used employing ohmic contacts, constant mobilities, series resistance, single trap levels, Langevin recombination, and doping. The insulating interface layer was implemented as a thin layer with very low mobility and a much higher LUMO level (+0.5 eV) than the active layer. The modelling parameters can be found in Table B.1. The simulations were launched from a Matlab script, that also did the parallel summation of the currents and the plotting. The diffusion modelling was carried out using Mathematica.

10.2 RESULTS

The different measurements that were performed with *Paios* are shown exemplarily for the PEDOT:PSS device in Fig. 10.2. In the following we will demonstrate that the same mechanism is present under all ageing conditions and for all devices. Later on we will focus on the PEDOT:PSS device due to its rapid degradation, that allows us to study the whole device lifetime.

The current-voltage curves in Fig. 10.2a show a rapid, homogeneous decrease in both forward and reverse current, while the open-circuit voltage remains stable [240–242, 262, 536]. When we plot the short-circuit current versus ageing time we find a good agreement with a square-root power law for all devices, that is under the three different ageing conditions and using four different hole transport materials (see Fig. 10.1). The decay kinetics are strongly slowed down when using the alternative HTLs, and the T_{80} time is increased by factors of up to 380. The T_{80} time was calculated using the fit with a square-root decay

$$I_{sc}(t) = I_{sc}(0) \cdot (1 - k\sqrt{t}) \tag{10.1}$$

and interpolating to $I_{sc}(T_{80}) = 0.8 \cdot I_{sc}(0)$ [244]. The resulting T_{80} times and the increase in lifetime are summarized in Table 10.1. V_2O_5 Oxopolymer leads to the most stable devices with T_{80} times up to 300 h, which is a 190-fold increase in stability compared to the PEDOT:PSS device under the same condition. We further notice a reduced lifetime under enhanced temperature as well as increased humidity, being a first confirmation that water ingress is the dominant degradation mechanism [537].

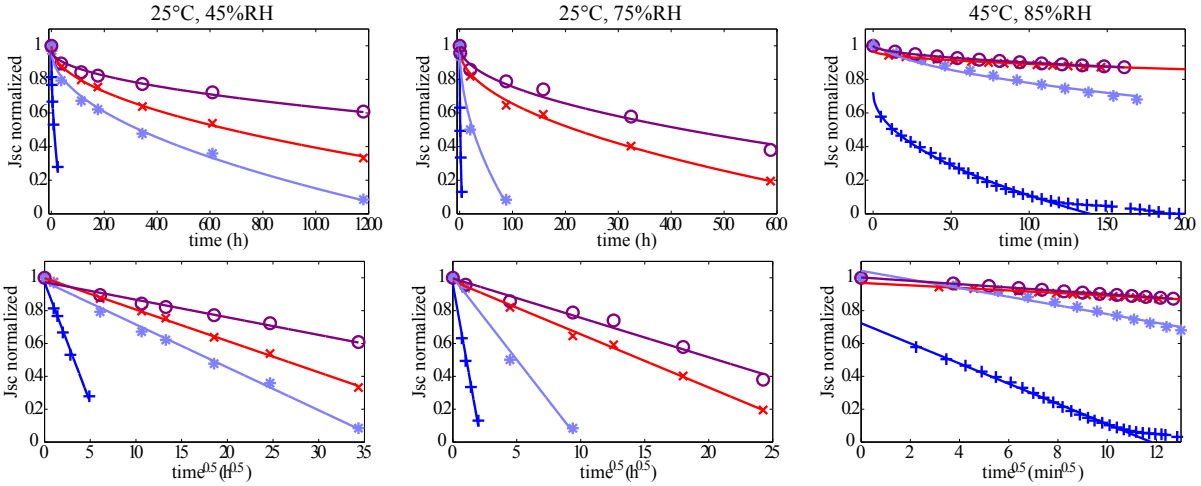

Figure 10.1: Decay of the short-circuit current for the three different ageing conditions. The hole transport materials and used symbols are PEDOT:PSS (+), MoO_3 (x), V_2O_5 Xerogel (∗), V_2O_5 Oxopolymer (o). The lines show fits to a square-root time dependence. The same plots are shown with a linear time scale (a-c) and versus the square-root of time (d-f).

T_{80} (h)	PEDOT:PSS	MoO_3	V_2O_5 Xerogel	V_2O_5 Oxopolymer
25°C, 45 % RH	1.67 (1 x)	108.5 (65 x)	53.4 (32 x)	313.1 (187 x)
25°C, 75 % RH	0.18 (1 x)	35.2 (196 x)	4.02 (22 x)	68.4 (380 x)
45°C, 85 % RH	0.05 (1 x)	10.3 (206 x)	0.98 (19 x)	6.27 (125 x)

Table 10.1: T_{80}-times of the short-circuit current for cells with different HTLs and under different ageing conditions. In parenthesis the increase in lifetime compared to the respective PEDOT:PSS device is shown.

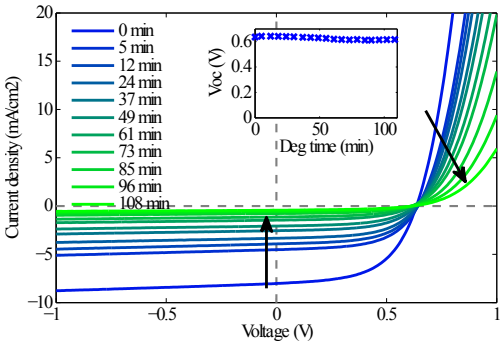

(a) Light IV-curve. The inset shows the open-circuit voltage.

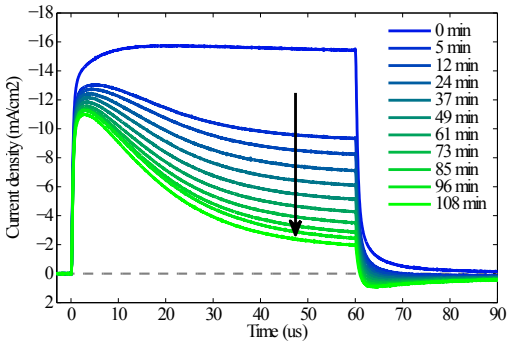

(b) Transient photocurrent response to a 60 μs light pulse.

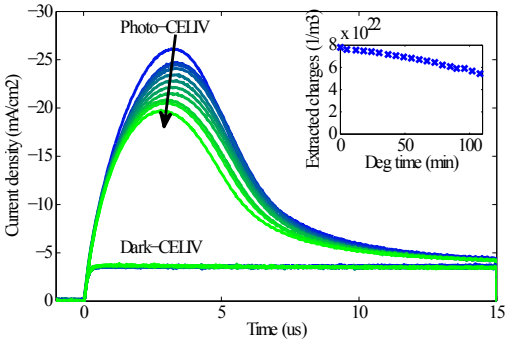

(c) Dark- and Photo-CELIV current.

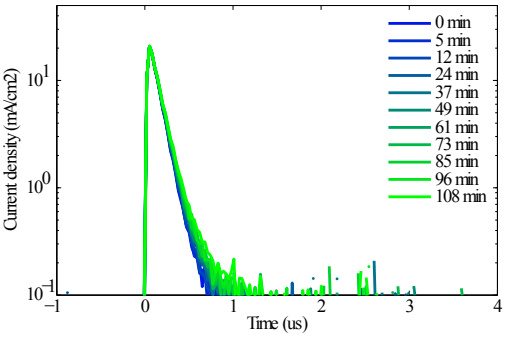

(d) Current response to a small voltage step.

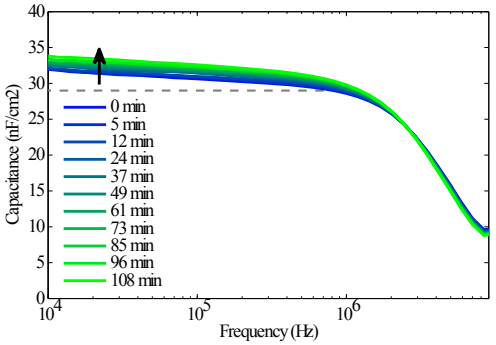

(e) Capacitance-frequency without offset voltage.

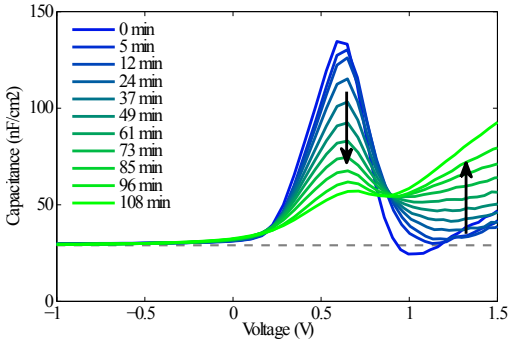

(f) Capacitance-voltage at 20 kHz.

Figure 10.2: Measurements of the PEDOT:PSS device performed repeatedly during the first two hours of degradation in the climate chamber at 45°C, 85% RH.

In the following we will discuss the various measurement results shown in Fig. 10.2, thereby trying to interpret the qualitative changes.
Concerning the transient photocurrent (Fig. 10.2b), only the fresh device shows a "normal" shape with a steady increase to the equilibrium short-circuit current, while for the degraded cell a strong overshoot is observed, and later even an undershoot after light turn-off appears. The overshoot is generally related to charge accumulation resulting in a local screening of the electric field and a reduction of the photocurrent. The undershoot, however, is a sign for a current flowing in the "wrong" direction. This is quite counter-intuitive and will be explained later in Section 10.3.

The dark-CELIV measurement shown in Fig. 10.2c does not change during ageing which is a sign that no intrinsic charge (doping) builds up. The Photo-CELIV experiment shows a loss of the extracted charge which is however much smaller than the loss of the extracted steady-state photocurrent. Therefore we can conclude that a conceivable loss in absorption, while it might explain the Photo-CELIV decrease, cannot explain the full reduction of the short-circuit current, as well as the shape change of the TPC. Furthermore absorption losses (photobleaching) are generally a photodegradation pathway, whereas here we investigate ageing in the dark. Increased recombination could also be the reason for a smaller CELIV peak, would however further affect the fillfactor of the IV-curve. And the stability of the peak position tells us that the charge carrier mobilities are unperturbed.

The small voltage step experiment (Fig. 10.2d) shows no changes, in accordance with the capacitance-frequency plot (Fig. 10.2e), where only a slight increase of the capacitance is observed. This means that neither the series or shunt resistance of the device nor the geometric capacitance and the layer thickness have changed.

Finally the capacitance-voltage plot (Fig. 10.2f) contains important information. The peak position is related to the built-in field, while its height depends on the injection and recombination properties. We find that the peak strongly decreases which could be a hint for reduced injection efficiency. At the same time it stays at the same voltage, thus the built-in voltage, defined by the difference in electrode workfunctions, does not change. This is in line with the constant open-circuit voltage observed in the IV-curves. Furthermore there is a second plateau evolving in forward bias above built-in, which shows even better at later times (Fig. 10.9f). This is a hint for an insulating interface layer that leads to a MIS-device with harmed injection and extraction properties [538, 539].

The various conclusions we can draw already by observing the qualitative changes in the different experimental techniques are summarized in Table 10.2. The only remaining mechanisms that might explain the dominant changes in all experiments are related to the interface with an electrode. Here the build-up of a thin insulating interface layer or a complete electrode delamination are conceivable.

10.3 MODELLING APPROACH

The most reasonable modelling approach is the introduction of a thin insulating layer between the active layer and an electrode. As we believe all devices show the same degradation behaviour we assume that the aluminium contact is the relevant one. This assumption is encouraged by literature describing the low-workfunction contact as the most sensitive in general, and showing that the aluminium layer is prone to oxidation when in contact with (humid) air [222, 241, 262, 540]. The oxidation will lead to the formation of a thin Al_2O_3 layer that is insulating.

MECHANISM	EXPECTED CONSEQUENCE	CONCEIVABLE?
Absorption↓	J_{sc}↓, V_{oc}↓, injection unchanged	minor
Doping↑	J_{sc}↓, dark-CELIV peak↑, capacitance↑	no
Mobility↓	J_{sc}↓, TPC rise and CELIV slower	no
Layer swelling	field↓, extraction↓, capacitance↓	no
Resistance↑	FF↓, CELIV slower	no
Trapping↑	J_{sc}↓, FF↓, Cf at low f ↑	no
Recombination↑	FF↓, photo-CELIV ↓	minor
Built-in field↓	V_{oc}↓, CV peak position ↓	no
Injection barriers↑	V_{oc}↓, CV peak position↓	no
Disorder↑	perhaps current↓, V_{oc}↓, FF↓	no
Interface barrier	current↓, field unchanged	possible
Electrode delamination	current↓, field unchanged, complete contact loss	possible

Table 10.2: List of possible degradation mechanisms and if they are conceivable here. The expected tendency is indicated with the arrows.

The different degradation kinetics can then be explained as the water ingress into the device is enhanced by the hygroscopic HTL PEDOT:PSS, while the alternative HTLs are not or much less hygroscopic, leading to longer lifetimes. This is also the reason why we choose the PEDOT:PSS device as modelling target, as for this device the most extensive dataset has been measured.

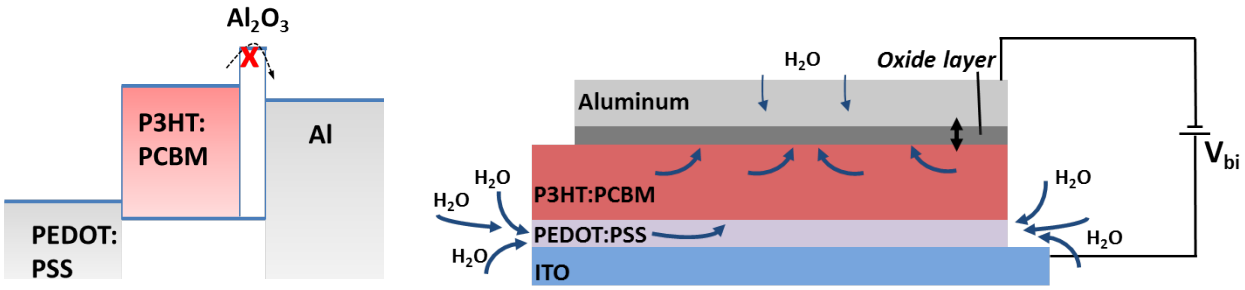

(a) Schematic energy diagram of the modelled cell. The growing Al_2O_3 layer acts as an electron extraction and injection barrier.

(b) Scheme of a homogeneous growth of the aluminium oxide layer due to water ingress.

Figure 10.3: Schematics of the degraded device comprising a homogeneous insulating interface layer.

For the modelling we start with a global fit of the various experiments with one set of parameters. This fit and the simulation parameters are found in Appendix B.1. We then aim to qualitatively reproduce the observed experimental behaviour by introducing a thin layer at the organic/cathode interface, where we simulate the insulating property by assigning very low charge carrier mobilities and a very large bandgap, as shown in Fig. 10.3a. We can now either increase the thickness of this layer to mimic the degradation progress, or increase the energetic barrier for electron injection and extraction. These two cases are modelled in Fig. 10.4.

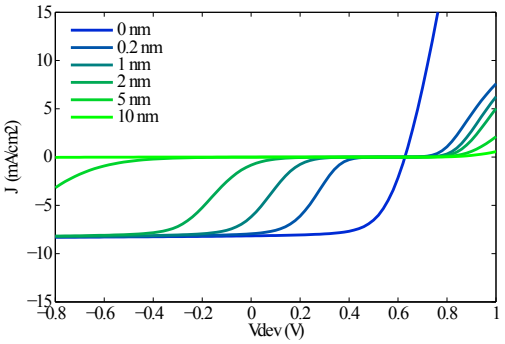

(a) Variation of the thickness of the insulating layer. Barrier height is 0.5 eV.

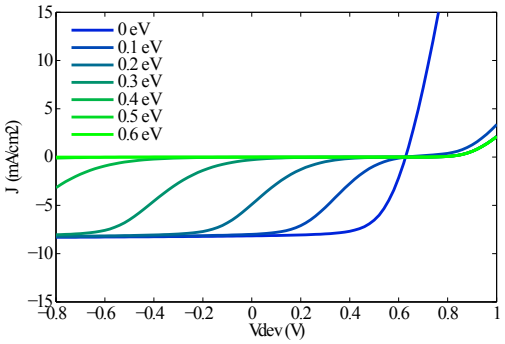

(b) Variation of the energy barrier height. Thickness of the insulating layer is 5 nm.

Figure 10.4: Simulated IV-curves assuming a homogeneous insulating interface layer as illustrated in Fig. 10.3b.

Using the modelling approach described above with a homogeneous insulating layer always leads to a pronounced S-shaped IV-curve. This is in contrast to the observed behaviour where no S-shape was seen (see Fig. 10.2a). We therefore postulate a different process, namely the lateral growth of the insulating layer from the edges of the device and through pinholes in the cathode. This would lead to a local formation of the interface resulting in a local complete loss of steady-state current, while other regions of the device are still unaffected and show their initial performance. This means that the observed decay of the short-circuit current is directly proportional to the remaining effective area of the device, which decreases with progressing water in-diffusion. When a certain concentration of water vapour is reached at a point, the insulator is considered as grown and the point no longer contributes to steady-state current generation.

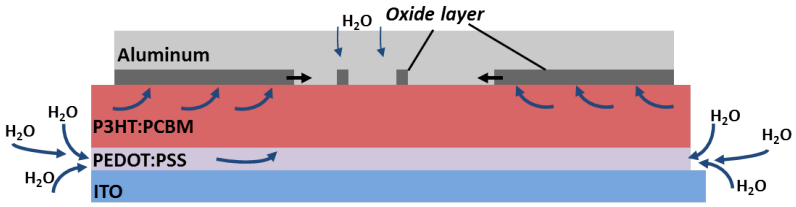

(a) Scheme of the lateral progress of aluminum oxidation due to water ingress from the sides and through pinholes.

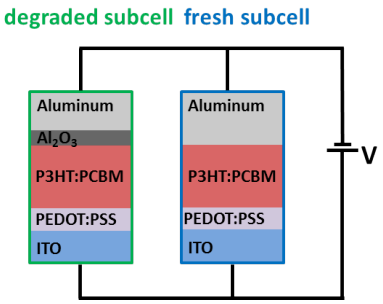

(b) Representation of the partly degraded device as a virtual parallel circuit of fresh and fully degraded subcell.

Figure 10.5: Schematics of the effective area model accounting for lateral degradation. The solar cell can be modelled by two subcells representing the fresh and the fully degraded state of the device.

We can realize this model by simulating a "fresh" device without insulating layer, and a "degraded" device with a full-grown insulating layer, and adding the currents up relative to the remaining effective area. The schematics for this "effective area approach" is shown in Fig. 10.5b. The summation of the two currents corresponds to a parallel circuit of the two virtual subcells.

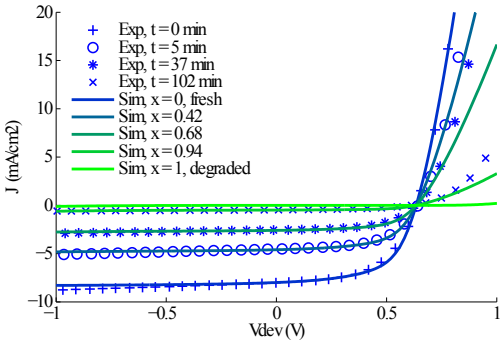

(a) Light IV-curve. Symbols denote measurements at 4 different ageing times.

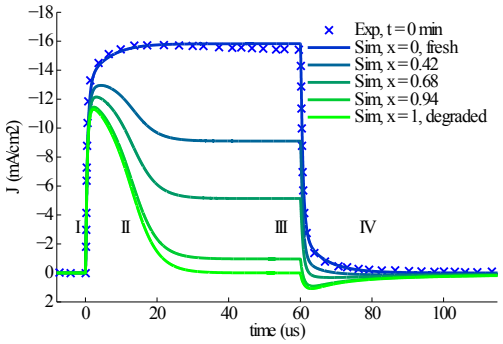

(b) Transient photocurrent response to a 60 μs light pulse.

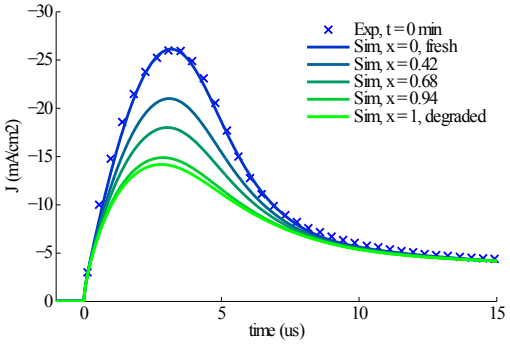

(c) Photo-CELIV current.

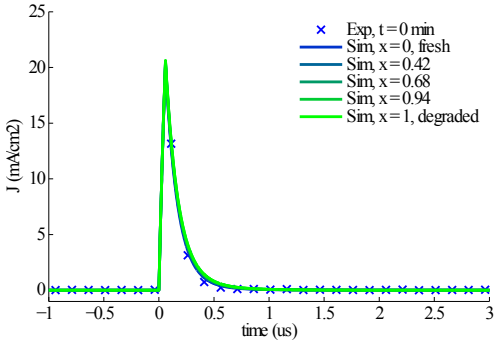

(d) Current response to a small voltage step

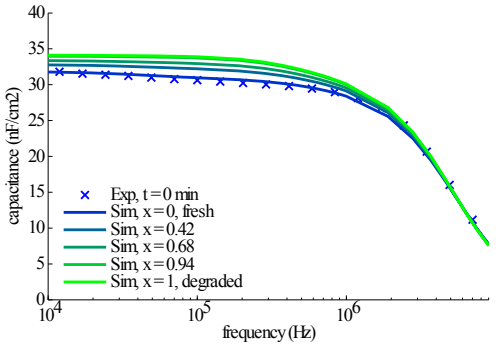

(e) Capacitance-frequency without offset voltage.

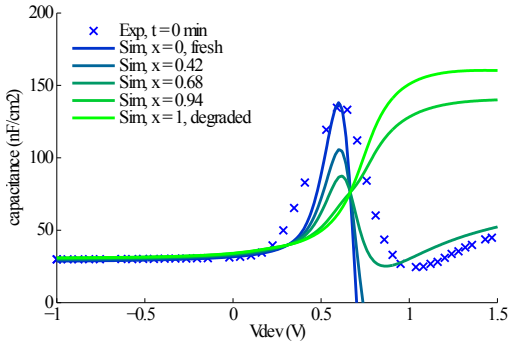

(f) Capacitance-voltage at 20 kHz.

Figure 10.6: Simulation of the degradation behaviour of the various experiments by the effective area approach. The crosses denote the measurements of the fresh PEDOT:PSS device. The modelling parameters are given in Table B.1.

Therefore we introduce a unitless parameter x describing the degraded portion of the device, thus going from 0 to 1. The effective area and the total device current are then calculated as:

$$\begin{aligned} A_{fresh} &= (1-x) \cdot A_{tot} \\ A_{deg} &= x \cdot A_{tot} \\ J_{tot} &= (1-x) \cdot J_{fresh} + x \cdot J_{deg} \end{aligned} \tag{10.2}$$

where A_{tot} is the initial active device area of 4 mm^2. The variable x then represents the dynamic decay of the short-circuit current relative to its initial value. Equation 10.2 is however not only

valid in the steady-state, but can also be employed for transient and capacitance simulations.

Figure 10.6 shows the resulting simulations together with the initial measurement, where we used the global fit as a starting point and then introduced the insulating layer as just described. We find a very good agreement for all experiments that reflects all qualitative changes observed and described in Section 10.2.

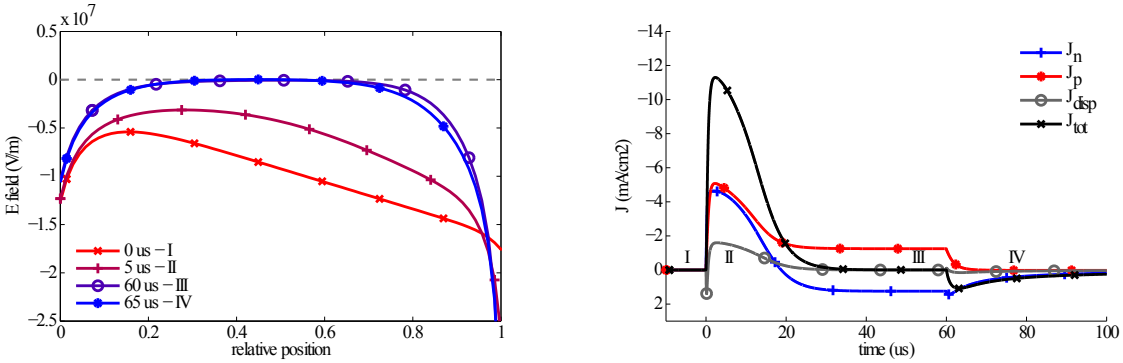

(a) Electric field profiles at various times. Position 0 denotes the PEDOT:PSS interface and position 1 denotes the interface to the aluminium oxide.

(b) Electron (blue) and hole (red) particle currents, displacement current (grey), and total current (black).

Figure 10.7: Electric field profiles and current contributions of the transient photocurrent simulation for the degraded device. The numbers denote the four transient regimes discussed in the text.

As we have found a suitable model to explain the observed behaviour we can now look a bit deeper into the device by means of simulation and understand better the transient photocurrent overshoot and undershoot observed in the degraded cell. Figure 10.7 shows the electric field profile for various times during the experiment and the separate transient current contributions of electrons and holes. At time t=0 (region I) the device is in the dark at equilibrium. The built-in field is negative and furthermore inhomogeneous due to asymmetric contacts and mobilities. When the light it turned on (region II) charges are photogenerated and move in the electric field towards their respective contacts, leading to a negative photocurrent rise. This movement also induces a small displacement current. The electrons, however, are not able to be extracted when they reach the cathode, due to the interface barrier with the aluminium oxide. This leads to their accumulation at the interface resulting in a screening of the electric field in a large part of the active layer (region III). During this process the current peaks and decreases again as the electron movement is slowed down and the driving force is cancelled. The movement of the holes is also slowed down but they can still be extracted on their side. While the electron drift current is stopped, due to their large concentration gradient the electrons start to move in the opposite direction by diffusion, generating a negative current contribution. In equilibrium the electron diffusion current cancels out the hole current, resulting in a net zero steady-state current (end of region III). When the light is turned off again (region IV), no new charges are generated and the remaining holes are quickly extracted at the anode. The bulk is however still field-free due to a remaining electron space charge, and many electrons are still diffusing in the wrong direction. The decay of the electron concentration by the diffusion current is slow, leading to a net positive current, which is observed in the experiment as undershoot.

The simulation results show that the postulated model of a laterally growing insulating layer can describe all experiments qualitatively. For a full quantitative description, however, other minor degradation mechanisms such as trapping or changes in mobility would also need to be included. Here we concentrated on the dominant effect - the water ingress induced cathode oxidation - that is responsible for the very low lifetimes of the devices.

One other possible process is the full delamination of the electrode. In such a case no conduction current at all can flow through the delaminated parts of the device. There would however still be an electric field due to the contacts, and displacement currents would also still persist. Yet by some additional measurements on a fully degraded device we can rule out that delamination takes place in our case. While the capacitance-voltage already showed signs of an evolving insulating layer (Fig. 10.2f), this can also be probed by a reverse CELIV measurement as shown in Fig. 10.8a. Here, two displacement current plateaus corresponding to the geometric capacitance of the device and the capacitance of the insulating layer alone, are observed. This behaviour is due to holes being injected and flooding the active layer, so that in forward bias only the insulating layer contributes to the measured capacitance.

Furthermore we measured illuminated IV-curves with high reverse bias (Fig. 10.8b). It turns out that at -10 V the full original photocurrent can be extracted, as the large extraction barrier for electrons can be overcome or tunnelled. This is another proof that no delamination occurred.

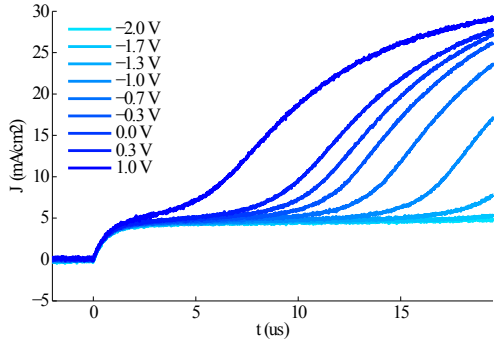

(a) Reverse-CELIV currents with varied offset voltage, measured for a degraded device. The two plateaus correspond to the capacitance of both layers and the capacitance of the insulator only, respectively.

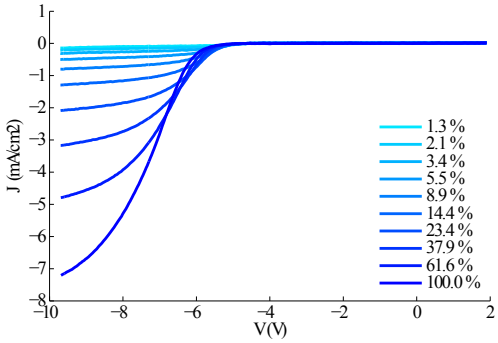

(b) IV-curves with varied light intensity, measured for a degraded device. At high reverse bias the full photocurrent can be extracted, as the interface barrier can be overcome.

Figure 10.8: Measurements on the fully degraded device showing the behaviour as a MIS-diode due to the Al_2O_3 interface layer.

Figure 10.9 shows measurements of the discussed device at later times. After two hours there is hardly any photocurrent left, yet other degradation mechanisms set in. In the IV-curve a loss of open-circuit voltage and fillfactor is observed, which may be related to recombination (Fig. 10.9a).

The main mechanism observed at later times is a charging process, showing in the dark-CELIV peak (Fig. 10.9b). However, as no constant second plateau is observed in the C-f (Fig. 10.9e), but a steady capacitance increase towards lower frequencies, we may attribute the observed behaviour to traps rather than doping. There may be deep traps that give a signature in the dark-CELIV, or a more complex trap density-of-states forms that includes both shallow and deep traps. As the dark-CELIV peak position shifts to longer times, the effective mobility is strongly reduced by the

trapping. A second reason for the slower signal may be an increased series resistance, for example because the PEDOT:PSS becomes less conductive when saturated with water.

The TPC also shows an interesting behaviour where the overshoot and undershoot discussed above disappear again (Fig. 10.9d). In the charged device the space charge can screen the built-in field completely, so that already from the start of the light pulse only diffusion currents are possible.

Finally, the capacitance-voltage reaches the MIS-device like shape at around 150 min, which would correspond to the time when the full aluminium electrode is oxidized (Fig. 10.9f). Later, however, the CV loses all features and becomes completely flat for the last measurement. The increased value compared to the geometric value might correspond to the depletion zone, and the flatness in forward bias is explained by a non-functional hole injection due to PEDOT:PSS degradation or even decomposition.

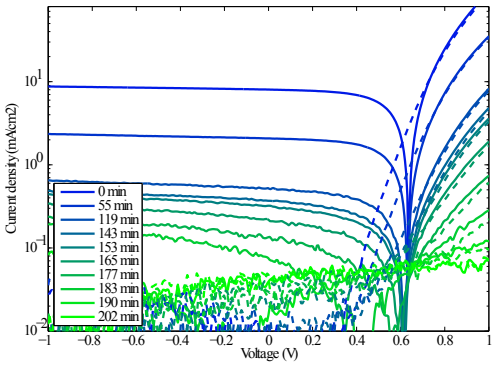

(a) Light IV-curve

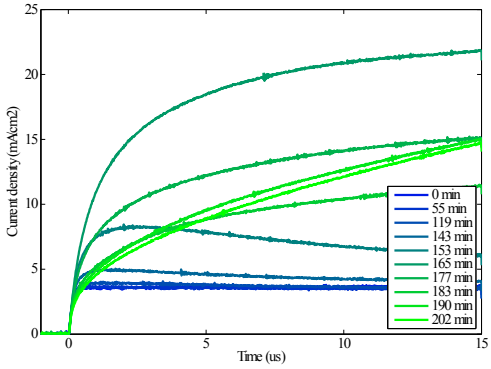

(b) Dark-CELIV current.

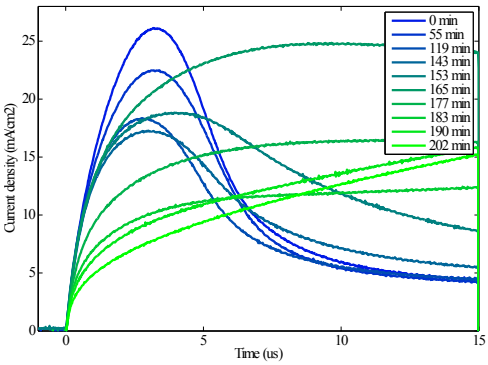

(c) Photo-CELIV current.

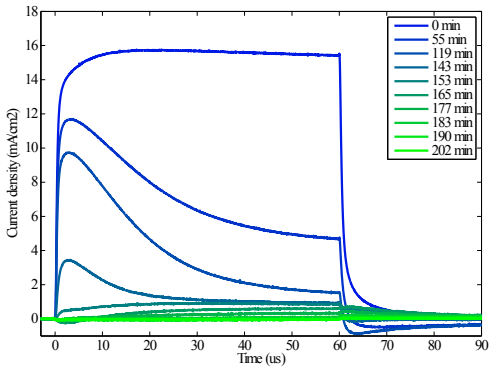

(d) Transient photocurrent response to a 60 μs light pulse.

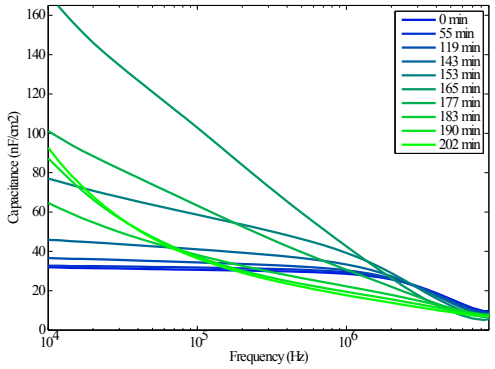

(e) Capacitance-frequency without offset voltage.

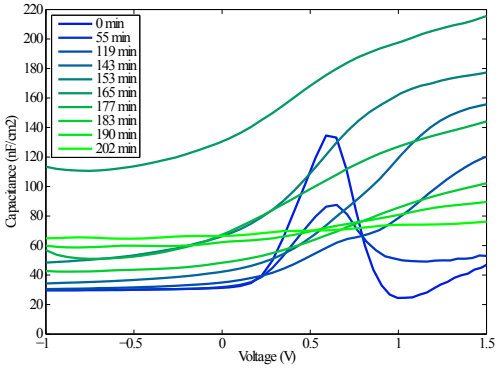

(f) Capacitance-voltage at 20 kHz.

Figure 10.9: Measurements of the PEDOT:PSS device for later times of the degradation in the climate chamber at 45 °C, 85 % RH.

10.4 WATER VAPOUR DIFFUSION MODEL

In the previous section we have shown that the loss of short-circuit current is caused by lateral diffusion of water into the cell, leading to the oxidation of the aluminium cathode and forming an insulating aluminium oxide layer. As found experimentally, the short-circuit current decay is approximately proportional to the square-root of ageing time. In this section we aim to analytically model the water vapour diffusion into the device in order to investigate the degradation kinetics further. As the aspect ratio of the lateral dimensions (usually some millimetres to centimetres) to the thickness of the layer stack (several 100 nanometres) is very high, the 3D problem can be approximated by a 2D simulation, and the whole diffusion process is governed by the in-plane lateral diffusion. In the following two different boundary conditions - pinholes and edge ingress - are investigated as possible sources of the observed decay kinetics.

The diffusion process is caused by a lateral gradient in the concentration C of water vapour [541, 542]. The transient change of concentration is hereby related to its lateral gradient, according to 1. Fick's law:

$$\frac{\partial C(x,y,t)}{\partial t} = -D\left(\frac{\partial^2 C(x,y,t)}{\partial x^2} + \frac{\partial^2 C(x,y,t)}{\partial y^2}\right) \tag{10.3}$$

where D is the diffusion coefficient. For random boundary conditions there is no simple solution to this differential equation and it needs to be solved iteratively. However, for specific geometries analytic solutions can be found in literature [543–545]. Here two relevant geometries are investigated: the constant-concentration point-source, and an iso-concentration surface. These two geometries may describe diffusion through pinholes and from the edges, respectively.

$$C(x,y,t) = C_{ext} \cdot \texttt{Erfc}\left(\frac{\sqrt{(x-x_0)^2+(y-y_0)^2}}{2\sqrt{Dt}}\right) \tag{10.4}$$

$$C(x,y,t) = C_{ext} \cdot \texttt{Erfc}\left(\frac{x}{2\sqrt{Dt}}\right) \tag{10.5}$$

$$\begin{aligned} C(x,y,t) = C_{ext} - \frac{16}{\pi^2} C_{ext} \cdot \sum_{l=0}^{\infty}\left[\frac{(-1)^l}{2l+1} \cdot \texttt{exp}\left(\frac{-D\cdot(2l+1)^2\pi^2\cdot t}{A_0}\right) \cdot \texttt{cos}\left(\frac{(2l+1)\pi(\frac{L}{2}-x)}{L}\right)\right] \\ \cdot \sum_{l=0}^{\infty}\left[\frac{(-1)^l}{2l+1} \cdot \texttt{exp}\left(\frac{-D\cdot(2l+1)^2\pi^2\cdot t}{A_0}\right) \cdot \texttt{cos}\left(\frac{(2l+1)\pi(\frac{L}{2}-y)}{L}\right)\right] \end{aligned} \tag{10.6}$$

with the diffusion constant D in mm^2/s, and the constant boundary concentration C_{ext} corresponding to the absolute humidity of the surrounding air [266, 543]. For the calculations we consider a square-shaped cell with $0 < x < L$, $0 < y < L$ and the device area $A_0 = L^2 = 4\ \mathrm{mm}^2$. Further, as the relations always depend on both time and diffusion constant in the same way, we use the generalized unitless coordinate Dt/A_0 as the parameter describing the diffusion progress. In Eq. 10.4 the pinhole position is at (x_0, y_0), in Eq. 10.5 we consider only 1D diffusion from an iso-concentration surface at $x = 0$, and by Eq. 10.6 2D diffusion from all four edges $x, y = 0$, $x, y = L$ is described. We assume that the interior of the device is water-free at time zero: $C(x, y, t = 0) = 0$. The diffusion models were numerically evaluated in Mathematica.

An evaluation of the three diffusion models allows to visualize the water concentration profile inside the device at different times (see Fig. 10.10). Figure 10.11a shows the profiles for a pinhole source at different times, while Fig. 10.11b shows the transient evolution of the concentration

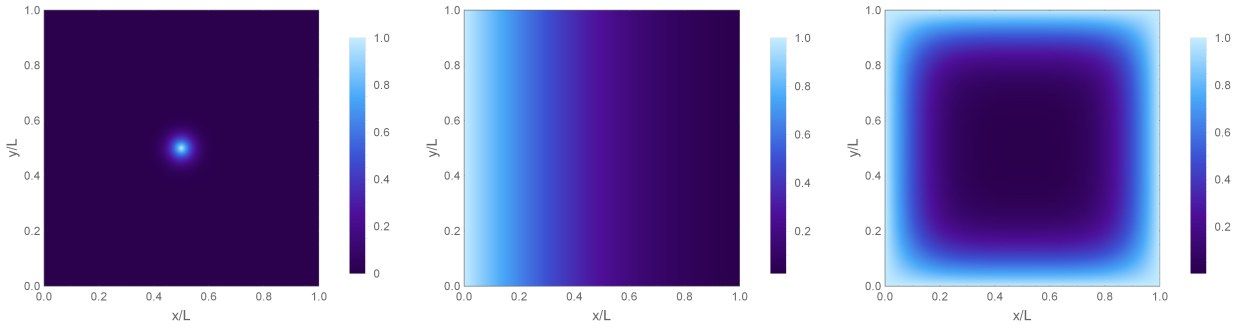

(a) Concentration profile at $Dt/A_0 = 0.01$ for a pinhole at $(0.5, 0.5)$.

(b) Concentration profile at $Dt/A_0 = 0.1$ for 1-edge diffusion from $x = 0$.

(c) Concentration profile at $Dt/A_0 = 0.01$ for 4-edge ingress.

Figure 10.10: Simulated 2D water vapour concentration for the three models.

at different distances from the surface. Figure 10.11c shows the concentration profile for edge diffusion with varied diffusion progress.

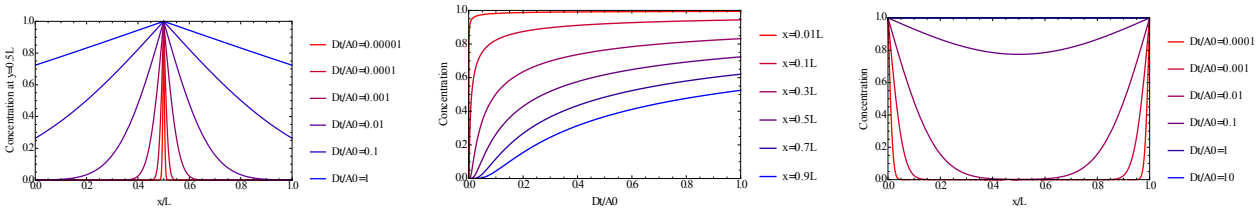

(a) Concentration profile at $y = 0.5L$ for a pinhole at $(0.5, 0.5)$ for different values of diffusion progress Dt/A_0.

(b) Concentration for 1-edge diffusion versus Dt/A_0 for different values of x.

(c) Concentration profile at $y = 0.5L$ for 4-edge ingress for different values of diffusion progress Dt/A_0.

Figure 10.11: Simulated water vapour concentration profiles for the three models.

In order to calculate the area degraded by water ingress, we assume that a point of the device becomes fully degraded when a certain threshold concentration C_{thr} is reached. The motivation for this assumption is that LBIC and EL pictures always show sharp edges and no intermediate, grey regions. We therefore numerically integrate all points with $C(x, y, t) < C_{thr}$, giving the remaining effective area $A(t)$.

Figure 10.12 shows the integrated effective area with different chosen threshold concentrations for the three models, using an external concentration of $C_{ext} = 1$, versus diffusion progress. The calculated area is then fitted using a power law dependence:

$$A(t) = A_0 \cdot (1 - k \cdot t^n) \tag{10.7}$$

For the pinhole degradation we obtain an exact linear decrease of the remaining effective area ($n = 1$), for any chosen threshold concentration. This is in agreement with measured behaviour of pinhole growth by several other studies [71, 77, 244, 546, 547].

Furthermore, for the degradation from one surface the loss in effective area is proportional to the square-root of time ($n = 0.5$) for all chosen threshold concentrations [244] .

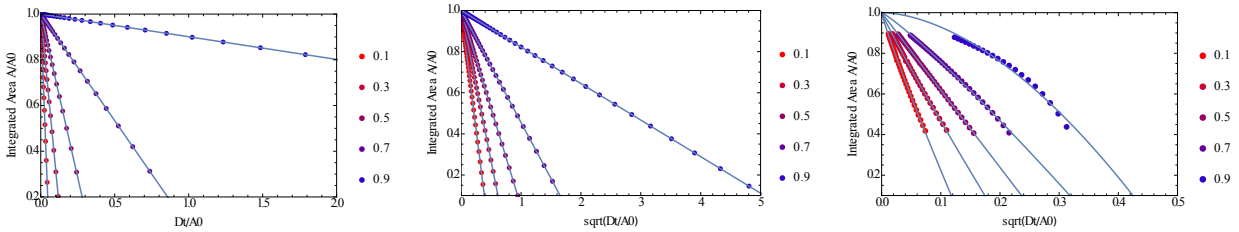

(a) Integrated effective area for pinhole diffusion.

(b) Integrated effective area for diffusion from one surface. Data is plotted versus the square-root of Dt/A_0.

(c) Integrated effective area for diffusion from four edges. Data is plotted versus the square-root of Dt/A_0.

Figure 10.12: Simulated decay of the effective area for the three diffusion models with varied threshold concentrations. Dots are simulated data, lines are fits to Eq. 10.7.

The case of 2D diffusion from four edges is more complicated, as the obtained power law depends on the threshold concentration ($n = 0.3 - 0.7$). However, for low threshold concentrations a big part of the decay curve fits well to a square-root law ($n = 0.5$).

This behaviour coincides with our own experimental observation shown in Fig. 10.1. It therefore allows us to conclude that in our case the edge ingress is the dominant degradation mechanism, and pinhole effects are negligible.

As we experimentally found a loss of the short-circuit current proportional to the square-root of time, which is a signature of edge ingress, we can now try to estimate the diffusion rate of water vapour in the different HTLs. For this we first calculate the absolute humidity corresponding to the fixed outer water vapour concentration C_{ext} for the three conditions. Using the Clausius-Clapeyron equation we obtain:

$$m = \frac{R_L}{R_d} \cdot RH \cdot E_S = \frac{R_L}{R_d} \cdot RH \cdot 6.112 \cdot \exp\left(\frac{17.67T}{T + 243.5}\right) \tag{10.8}$$

$$AH = \frac{1000 \cdot m}{1000 + m}$$

where RH is the relative and AH the absolute humidity, R_L is the specific gas constant for dry air, R_d the specific gas constant for water vapour, E_S is the saturation vapour pressure, and T is the temperature in °C. The resulting values are given in Table 10.3.

We then relate the decay constant k from Eq. 10.7 to the diffusion constant D.

$$A(T_{80}) = 0.8A_0 = A_0 - k\sqrt{D \cdot T_{80}} \qquad \rightarrow \quad D = \frac{A_0}{k^2 \cdot T_{80}} \tag{10.9}$$

Hereby T_{80} is the estimated lifetime from Table 10.1, and k is the decay fitting constant according to Eq. 10.7, where $n = 0.5$ was fixed. As can be inferred from Fig. 10.12 this decay constant depends strongly on the threshold concentration, therefore a real quantitative determination of the diffusion constant seems not feasible. Yet, to obtain an order of magnitude we will assume a threshold concentration. As degradation proceeds already for low absolute humidity values below 10 g/m^3, we used a threshold concentration of $C_{thr} = 1$ g/m^3 for the calculations. The external concentration was set to the absolute humidity values given in Table 10.3. In the table we show the resulting diffusion constants for evaluation of the 1-edge and the 4-edge model. We would like to mention, however, that these values may be not very accurate, due to the made assumptions.

D (mm^2/s)	AH (g/m^3)	Model	PEDOT:PSS	MoO_3	V_2O_5 Xerogel	V_2O_5 Oxopolymer
25°C, 45 % RH	8.8	1 edge	1.3 e-6	2.1 e-8	4.2 e-8	7.1 e-9
25°C, 75 % RH	14.6	1 edge	9.9 e-6	4.8 e-8	4.2 e-7	2.5 e-8
45°C, 85 % RH	48.4	1 edge	2.1 e-5	1.0 e-7	1.1 e-6	1.7 e-7
25°C, 45 % RH	8.8	4 edges	1.0 e-7	1.6 e-9	3.3 e-9	5.6 e-10
25°C, 75 % RH	14.6	4 edges	7.4 e-7	3.8 e-9	3.3 e-8	2.0 e-9
45°C, 85 % RH	48.4	4 edges	1.7 e-6	8.2 e-9	8.6 e-8	1.3 e-9

Table 10.3: Estimated diffusion constants of water vapour in the different hole transport layers.

10.5 CONCLUSIONS

In this study we investigated the degradation of organic solar cells under different atmospheric conditions. We find that in unencapsulated OSCs subject to ambient humidity the ingress of water and subsequent oxidation of the cathode is the dominant degradation mechanism. The decay of the short-circuit current follows the remaining effective area of the solar cell which is decreased due to the lateral growth of insulating regions in the aluminium cathode. For this conclusion we conducted a complementary analysis of various measurements that were repeatedly performed during the ageing process. We further employed numerical drift-diffusion simulations to qualitatively describe the influence of the forming insulating layer, and furthermore to prove that the degradation is a lateral and not a homogeneous process. All these conclusions, which are in perfect agreement with literature [222], could thus be made by nondestructive methods performed on a single device.

We have further shown that by replacing PEDOT:PSS with other, solution-processed metal oxide layers can strongly slow down the degradation process. We found an up to 380-fold increase in T_{80} time using V_2O_5.

By 2D diffusion modelling we could further distinguish between degradation due to pinhole growth and from edge ingress by their different decay dynamics (linear vs. square-root). Therefore we find that in our case the lateral in-diffusion of water vapour from the edges, accelerated by the hygroscopic PEDOT:PSS HTL is the main failure mechanism.

The main results of this study have been published in: S. Züfle, M. T. Neukom, S. Altazin, M. Zinggeler, M. Chrapa, T. Offermans, and B. Ruhstaller. "An Effective Area Approach to Model Lateral Degradation in Organic Solar Cells". *Advanced Energy Materials* 5.20 (2015), p. 1500835. DOI: 10.1002/aenm.201500835 [228].

The part on diffusion modelling will also be published as a joint paper in: D. Fluhr, S. Züfle, B. Muhsin, R. Öttking, M. Seeland, R. Rösch, U. Schubert, B. Ruhstaller, S. Krischok, and H. Hoppe. "Unified description of electrode corrosion dynamics in organic solar cells". *submitted* (2017) [548].

11 LIGHT INDUCED DEGRADATION: PHOTODOPING

11.1 INTRODUCTION

In this and the next chapter we investigate photodegradation of encapsulated organic solar cells that are subject to different illumination concentrations. We want to find out whether the use of concentrated sunlight is a valid tool to accelerate stability testing [176, 549–551]. Thus the question is if the same degradation mechanisms take place under one sun and under 100 suns illumination intensity. Furthermore we aim to quantify the acceleration factors for the different conditions.

Here we investigate a solar cell stack with an inverted architecture based on the polymer-fullerene bulk-heterojunction HBG1:$PC_{61}BM$. Hereby the high-bandgap polymer HBG1 is used, and PV-E002 is employed as a highly conductive electron transport material. The layer stack and nominal thicknesses are ITO (150 nm)/PV-E002 (5 nm)/HBG1:$PC_{61}BM$ (200 nm)/PEDOT:PSS AI4083 (50 nm)/Ag (100 nm) and each glass substrate comprises 4 devices with 15 mm^2 and 4 devices with 7.5 mm^2 active area. The encapsulation glass is glued on top at the edges, leaving a nitrogen-filled cavity inside. The devices have been fabricated at Merck Chemicals Ltd., Chilworth, United Kingdom in February 2016. The measurements were performed in March and April 2016.

The studies took place at Ben-Gurion University of the Negev in Israel, where we could employ a fiber-coupled concentrator setup, as shown in Fig. 11.1 [549, 552]. At this place in Sede Boker in the Negev desert the natural sun spectrum is very close to the standard ASTM AM1.5g spectrum [478, 553, 554], which allows us to work with real sunlight instead of artificial light sources. In the concentrator a mirror optic focusses the sunlight into a fiber which is then guided into the lab building and on the solar cell. The solar cell is lying on a water-cooled metal stage, and at the exit of the fiber the light is homogenized using different sized kaleidoscopes. The kaleidoscope cross section and the opening of the pizza-iris determine the total illumination intensity, which is calibrated using a precision Silicon photodiode. Furthermore the concentrator tracks the sun automatically during the day, and on clear days the diurnal change of the spectrum can be neglected [555].

Apart from using the concentrated sunlight for device degradation, we also tried to combine the concentrator setup with the *Paios* setup. Figure 11.2 shows measurements of a HBG1:PCBM cell performed with *Paios* under different sunlight concentrations. This demonstrates the general light intensity dependence of an organic solar cell IV-curve, which shows an optimum device efficiency at significantly below one sun. Furthermore we observe that for high illumination intensities around 20 suns the IV-curve becomes linear, as the series resistance becomes dominant, leading to a fillfactor of only 25 %. Interestingly the open-circuit voltage shows a peak around 10 suns, which we cannot explain so far.

The capacitance-voltage curves measured under strong illumination exhibit a Mott-Schottky behaviour, which indicates the formation of a space-charge zone. This behaviour is only possible when the photogenerated charges show inhomogeneous profiles or imbalanced transport, as otherwise they should counterbalance each other. We further find that under very high intensities a

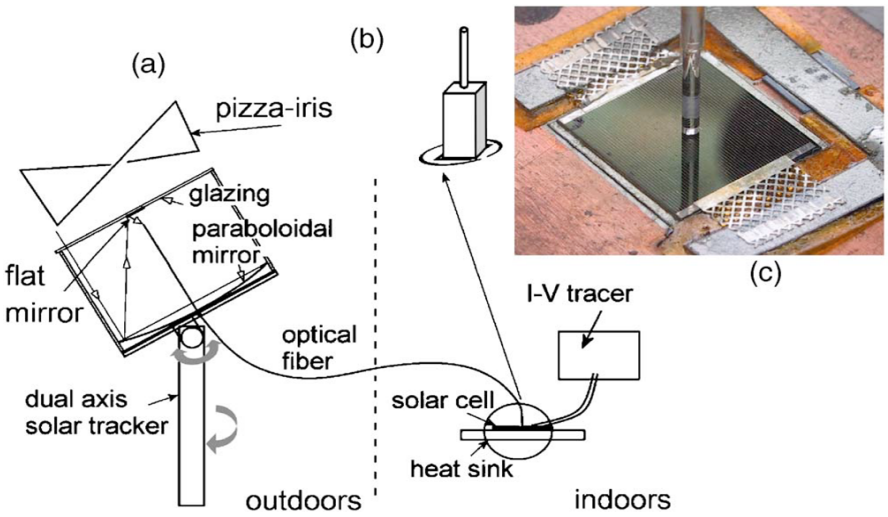

Figure 11.1: Concentrator setup at Ben-Gurion University, which has been employed in this study. Image taken from [552].

change is observed in the capacitance-voltage curve, showing the peak to shift to lower voltage, which is then also observed in the Mott-Schottky plot.

In the Appendix C.3 we simulate the effect of the illumination intensity on various experiment types. We obtain a maximum efficiency at around 0.1 suns, however the peak in open-circuit voltage is not reproduced when employing the most simple models (constant mobility, no traps, no doping) in the simulation. It seems worthwhile to investigate the light intensity dependence further, both in order to explain the behaviour at very high intensities and in order to find out the optimum illumination intensity for a specific solar cell [178, 531]. In the end organic solar cells will probably only rarely "see" a full 1-sun spectrum, while most of the time the intensity will be lower.

11.2 MEASUREMENT RESULTS

For photodegradation we illuminated the samples with different light intensities, ranging from 1 to 100 suns. Hereby the 1-sun experiment was performed outdoors, and 50-sun and 100-sun illumination was performed using the concentrator setup. After comparable light doses (illumination duration times illumination intensity) the cells were characterized with an extensive *Paios* measurement routine, and then degraded further. The goal of 100 sun*h in total could however not be achieved for all devices due to the limited time and some cloudy days. We also took EQE spectra of the fresh and degraded cells.

Figures 11.4 & 11.5 show the experimental results of two devices that were photo-degraded with 1 sun and 50 suns, respectively. The left graph always shows the 1-sun case, and the right graph the 50-sun case, and the degradation steps are chosen to be after comparable illumination doses. The last, red line shows a measurement of the same device taken a month later after storage in the dark. In the following we will discuss the various experiments and their changes during photodegradation.

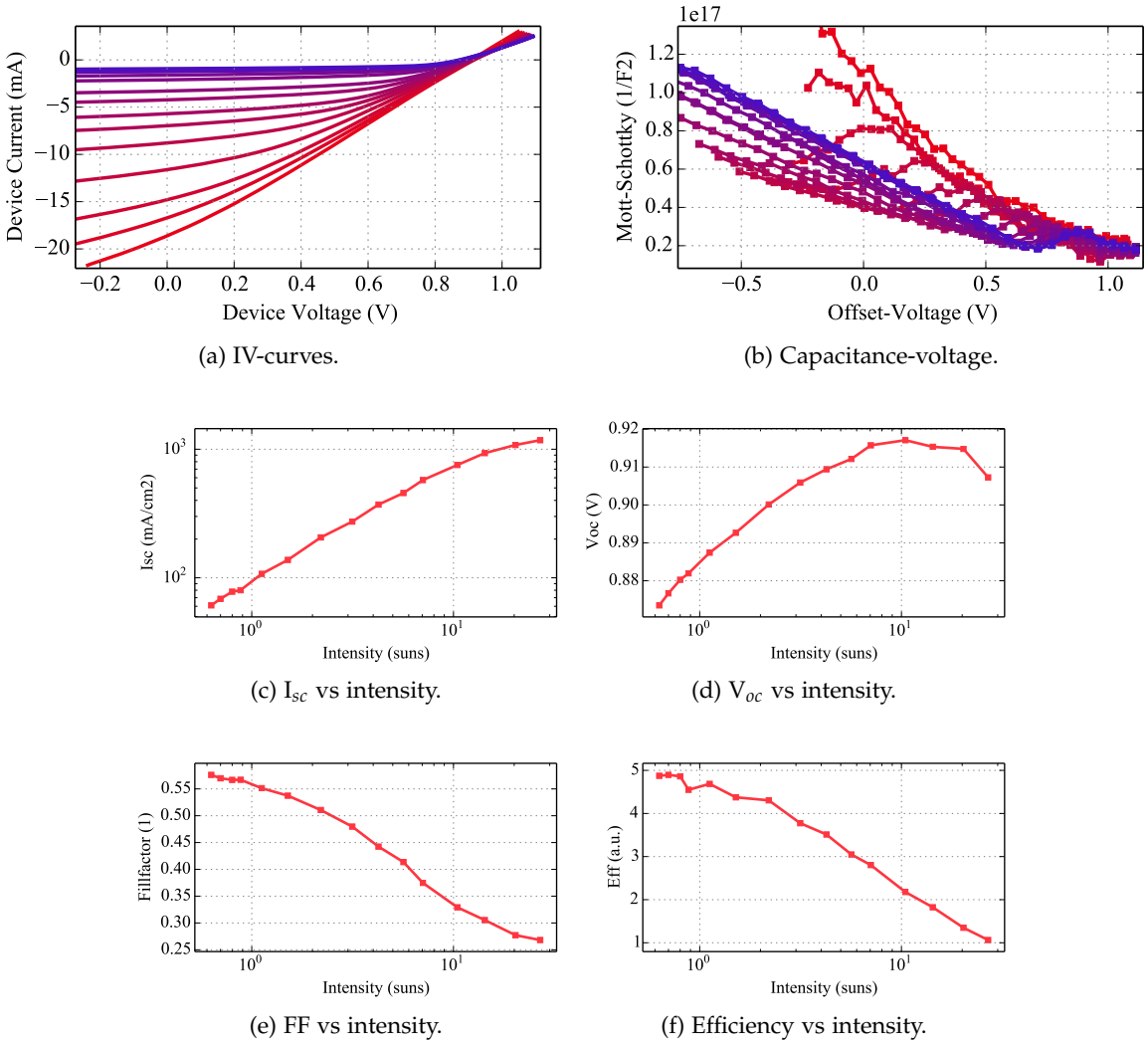

(a) IV-curves.

(b) Capacitance-voltage.

(c) I_{sc} vs intensity.

(d) V_{oc} vs intensity.

(e) FF vs intensity.

(f) Efficiency vs intensity.

Figure 11.2: I-V and C-V measurements performed under concentrated sunlight with intensities between 0.5 suns (blue) and 30 suns (red).

In the current-voltage curves (Figs. 11.4a & 11.4b) a strong loss of short-circuit current and fillfactor dominate the degradation process. The solar cell parameters measured with the *Paios* white LED are summarized for the different ageing conditions in Fig. 11.3.

The short-circuit current drops more strongly for the high-illumination case to 40 % of its initial value and then stays stable. The loss in fillfactor occurs after an initial short increase and with a slower rate than for the short-circuit current, and is also stronger for the 100-sun experiment. Furthermore we observe a slight increase in open-circuit voltage in all cases, which is also found as a slight shift of the dark and light IV-curves to higher voltages (see Figs. 11.4c & 11.4d).

The device stability can be assessed by comparing the doses necessary to degrade a parameter to a specific percentage (e.g. 80 %) of its initial value. Assuming that all occurring degradation mechanisms are linearly accelerated by concentrated sunlight, and that the same mechanisms occur, these values should be the same under all conditions. As shown in Table 11.1 this is not the case. The different solar cell parameters reach 80/90/50 % of their initial values after a smaller dose when concentrated sunlight is used. The main reason for this is believed to be heating of

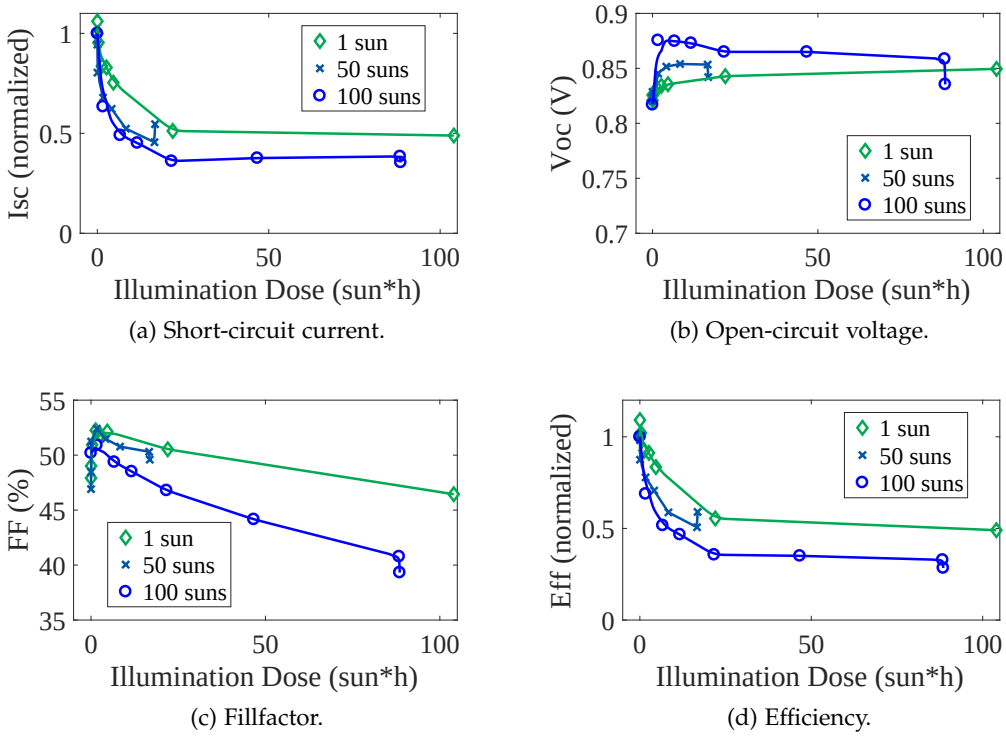

(a) Short-circuit current.

(b) Open-circuit voltage.

(c) Fillfactor.

(d) Efficiency.

Figure 11.3: Solar cell parameters during photodegradation under three different illumination intensities. The last point corresponds to the measurement of the partly recovered device after 30 days of dark storage.

the device under high illumination intensities [479, 553]. A higher temperature will accelerate basically any physical or chemical process going on in the device. We expect the cell temperature to be around $60 - 70$ °C under high intensities, even though the measurement stage was actively cooled. Using a thermocouple inside the encapsulation cavity this temperature might be measured, which could then allow us to calculate the thermal activation of the degradation process. Such an investigation of the device temperature is projected, but has not yet been done.

CONDITION	V_{oc} (D80)	I_{sc} (D80)	FF (D90)	Eff (D50)	TOTAL DOSE
1 sun	Not reached	8 sun*h	8 sun*h	30 sun*h	104 sun*h
50 suns	Not reached	4 sun*h	4 sun*h	20 sun*h	17 sun*h
100 suns	Not reached	1 sun*h	2 sun*h	7 sun*h	88 sun*h

Table 11.1: Interpolated illumination doses to reach 80/90/50 % of initial values. In general the acceleration factor is larger than 1, so for higher intensity less dose is necessary for the same degradation. The last column summarizes the total illumination dose reached for the different ageing conditions.

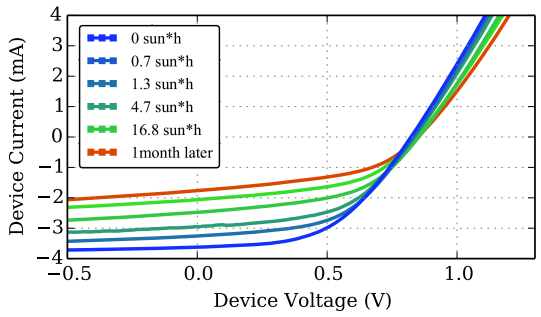

(a) Light IV-curve, degraded under 1 sun.

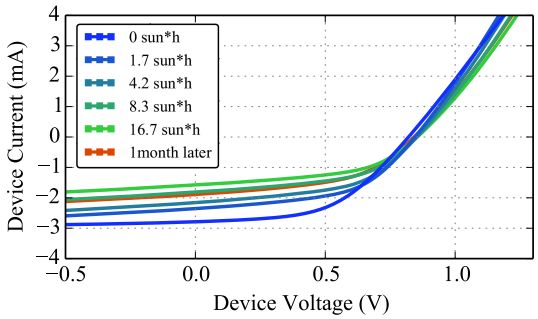

(b) Light IV-curve, degraded under 50 suns.

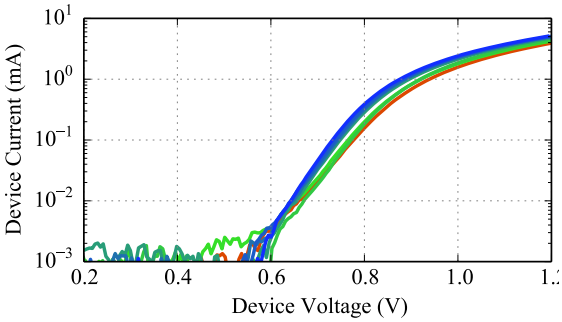

(c) Dark IV-curve, degraded under 1 sun.

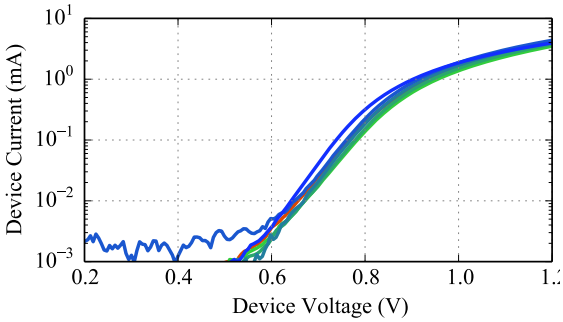

(d) Dark IV-curve, degraded under 50 suns.

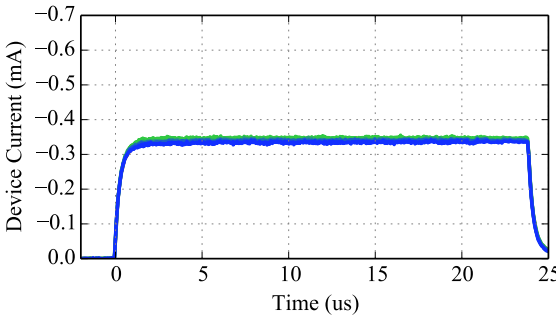

(e) Dark-CELIV current, degraded under 1 sun.

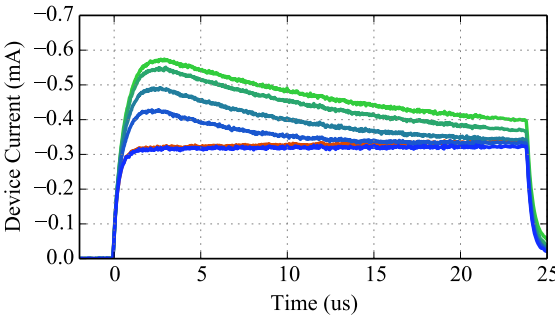

(f) Dark-CELIV current, degraded under 50 suns.

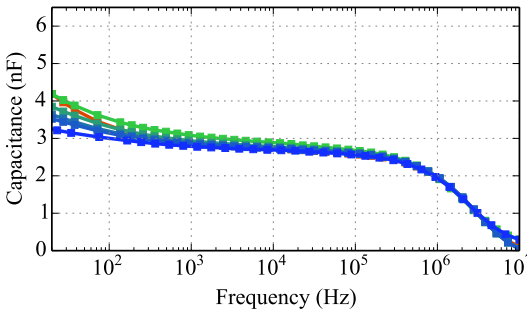

(g) Capacitance-frequency, degraded under 1 sun.

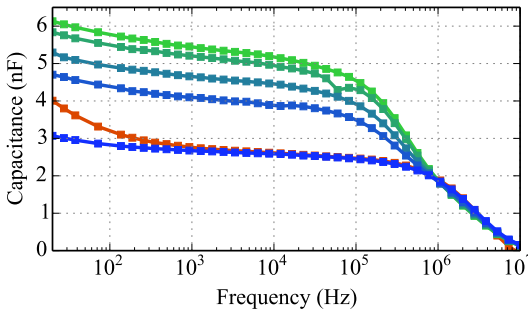

(h) Capacitance-frequency, degraded under 50 suns.

Figure 11.4: Photodegradation under 1 sun (left column) and 50 suns (right column) - Measurements at different illumination doses (from blue to green), and after one month of dark storage (red curve). Legend can be found in Figs. 11.4a & 11.4b.

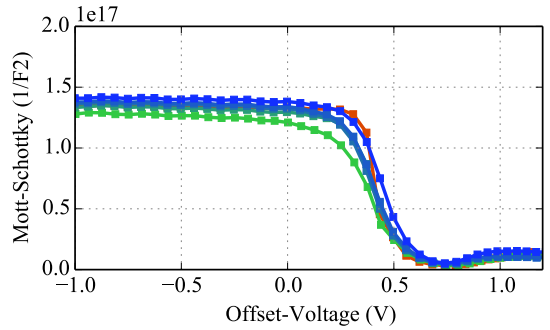

(a) Mott-Schottky plot, degraded under 1 sun.

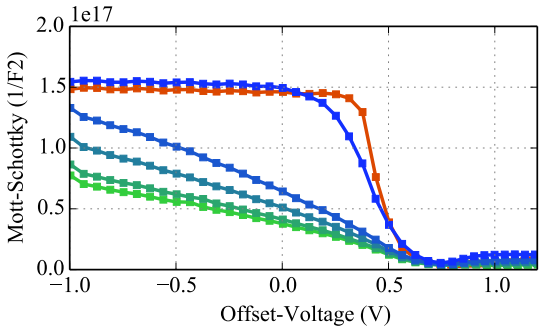

(b) Mott-Schottky plot, degraded under 50 suns.

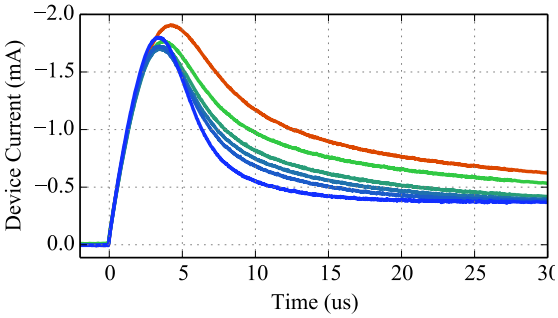

(c) Photo-CELIV current, degraded under 1 sun.

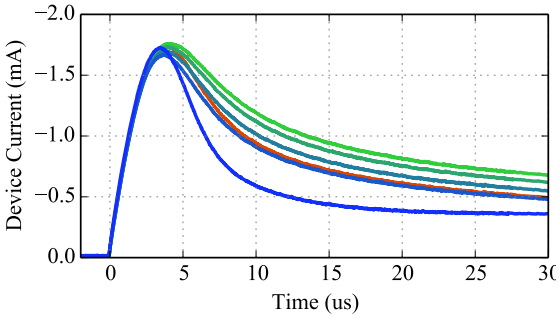

(d) Photo-CELIV current, degraded under 50 suns.

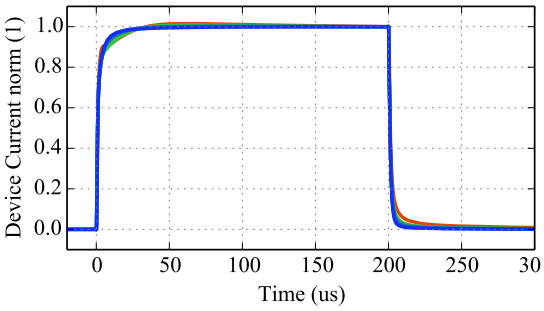

(e) TPC , degraded under 1 sun.

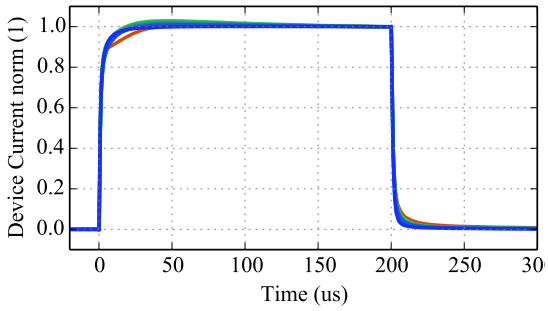

(f) TPC , degraded under 50 suns.

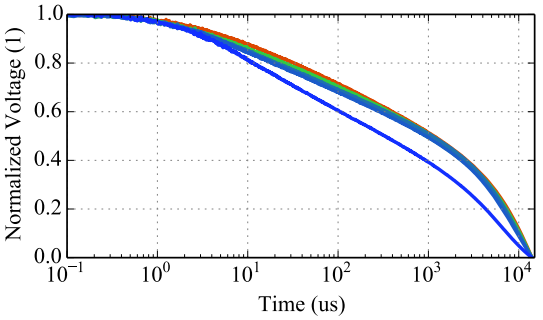

(g) OCVD decay, degraded under 1 sun.

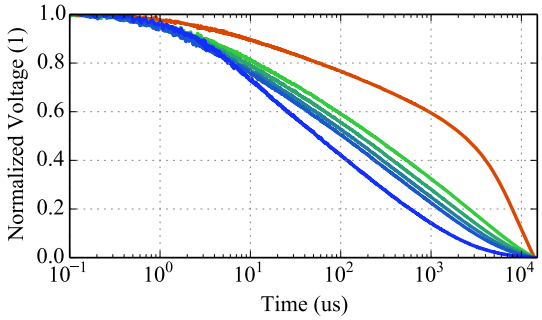

(h) OCVD decay, degraded under 50 suns.

Figure 11.5: Photodegradation under 1 sun (left column) and 50 suns (right column) - Measurements at different illumination doses (from blue to green), and after one month of dark storage (red curve). Legend can be found in Figs. 11.4a & 11.4b.

The degraded light IV-curves (Figs. 11.4a & 11.4b) show a nearly linearly field-dependent photocurrent, which is a sign of an extraction problem. Several possible causes are conceivable to lead to a field-dependent photocurrent: doping, traps, imbalanced mobilities, or field-dependent exciton separation. The latter two seem improbable to change so strongly upon photodegradation, thus trapping or doping effects will be a suitable hypothesis.

The next experiment we analyse is the dark-CELIV measurement (Figs. 11.4f & 11.4b). Here the device degraded under concentrated sunlight shows a clear peak rapidly occurring upon ageing. This peak is a strong indication of doping, that is the formation of equilibrium immobile charge carriers in the active layer. The extraction peak then stems from oppositely charged mobile species that were previously injected to counterbalance the immobile space charge of the doping thereby ensuring thermal equilibrium.

We also observe a strong rise of the capacitance plateau in the capacitance-frequency plot for the 50-sun device (Fig. 11.4h), which is again a signature of doping. As the space-charge region is highly doped and conductive it does not contribute to the capacitance any more, so that the effective thickness decreases and the measured capacitance rises.

Finally we also measured the capacitance-voltage, and show the Mott-Schottky plot in Fig. 11.5b. A linear fit is possible for the device degraded at 50 suns, giving a quantitative value for the doping. Figure 11.6 compares the doping densities extracted from the Mott-Schottky analysis to the integrated dark-CELIV extraction peak. The doping increases rapidly upon ageing and seems to saturate at higher doses. The doping density obtained from CELIV is around a factor of 4 smaller than the one from Mott-Schottky. This is usually the case as the CELIV ramp can not extract all the equilibrium charges and therefore this technique underestimates the real value.

Interestingly, the device aged under the 1-sun condition shows no signatures of doping in dark-CELIV, capacitance-frequency or capacitance-voltage (Figs. 11.4e, 11.4g & 11.5a). Instead these dark measurements seem not to change at all. So from the observed behaviour it seems that the photodegradation processes under 1 sun and at high intensities are different, as the photodoping appears only for high intensities.

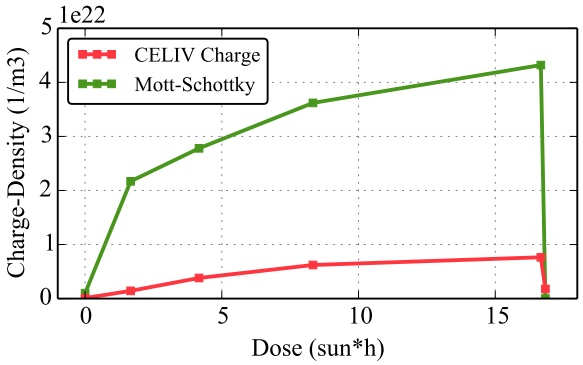

Figure 11.6: Extracted doping density versus illumination dose for the device degraded under 50 suns. The doping density was extracted from the dark-CELIV peak and by Mott-Schottky analysis.

However, the measurements performed one month of dark storage after the main experiment, might give a different view. Very interestingly we find all the effects just described as signatures of doping, have disappeared in the cells aged at 50 and 100 suns. This is shown as the red line in the plots of Figs. 11.4 & 11.5. The dark-CELIV signal shows the initial constant displacement current, and the Mott-Schottky and capacitance-frequency plots look nearly identical as for the

fresh cell. And yet, the IV-curve is still strongly degraded and has only very slightly recovered. This can also be seen in the IV-parameters in Fig. 11.3. So perhaps at least part of the degradation process is independent of the illumination intensity. At this point we want to note that it is, however, not independent of illumination, and reference devices kept in the dark the whole time do not show any relevant degradation.

When we analyse the photo-CELIV measurement (Figs. 11.5c & 11.5d), we observe the same behaviour independent of the ageing condition. In all cases the decay of the CELIV peak becomes more dispersive, which is often a signature of trap-controlled transport. In the 50-sun device the effect is superimposed to the doping, and therefore partly reversible.

The transient photocurrent rise shows only slight changes (Figs. 11.5e & 11.5f). While the doping in the 50-sun cell makes it temporarily slower, the last measurements look again very similar, having a slight shoulder and a small peak before steady-state. Again this could be related to trapping effects. If we now consider the slight change in the capacitance-frequency plot at low frequencies, it also hints to slow processes that increase with degradation, independent of the illumination intensity (Figs. 11.4g & 11.4h).

The last measurement we want to discuss is the transient photovoltage decay, as shown in Figs. 11.5g & 11.5h. For both cells we find an initial change slowing down the main part of the decay, which corresponds to a more dispersive transport, as witnessed in the photo-CELIV curve. The decay kinetics beyond 1 ms should not be compared, as they are linked to the specific parallel resistance of the two devices. We find however a further slow-down of the main decay in the 50-sun cell after the 30-day dark storage, which is not seen in the 1-sun device. The findings from these large-signal TPV (or OCVD) measurements are in line with small-perturbation TPV, which are normally used to determine the recombination lifetime. Here as well we find an increase of the lifetime with degradation in both cases, which would usually be explained as a lower recombination efficiency. This would however lead to a much higher photo-CELIV peak. Thus, also the increased lifetime can be interpreted in terms of deep traps which are released slowly and lead to the delayed extraction in photo-CELIV and slower recombination in TPV.

11.3 MODEL

Using drift-diffusion simulation we now aim to model various experiments and to confirm the hypotheses made so far. For this we start with a global fit of various experiments for the fresh device. This fit is shown in the Appendix B.2. Starting from there we can now investigate the influence of doping on the device performance.

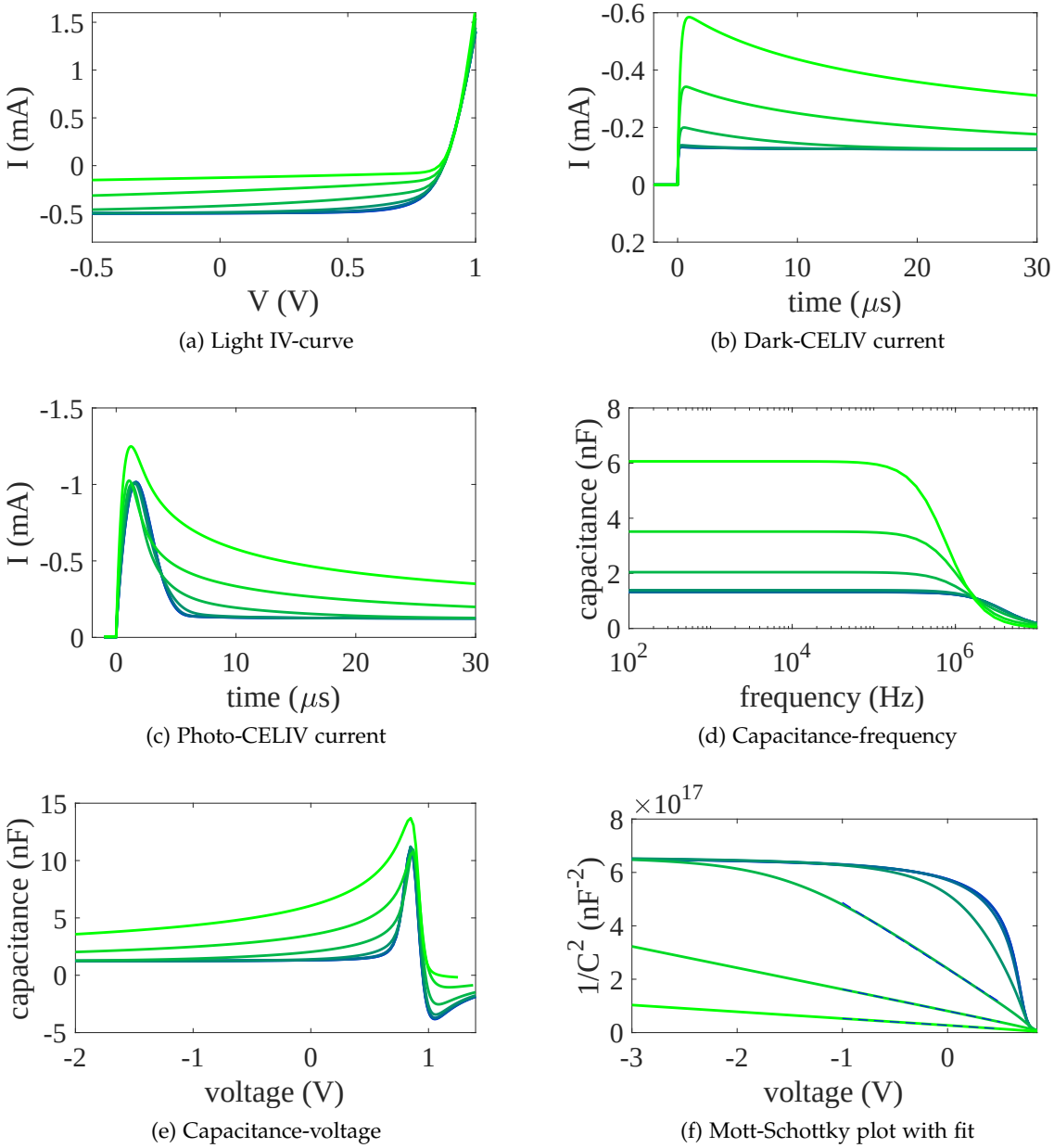

(a) Light IV-curve

(b) Dark-CELIV current

(c) Photo-CELIV current

(d) Capacitance-frequency

(e) Capacitance-voltage

(f) Mott-Schottky plot with fit

Figure 11.7: Simulations of various experiments with varied doping density. The doping density was varied from 10^{21} m^{-3} (blue curve) to 10^{24} m^{-3} (green curve).

Figure 11.7 shows modelled experiments with varied doping density. The main features as observed in the measurements of the 50-sun device are reproduced, confirming our initial as-

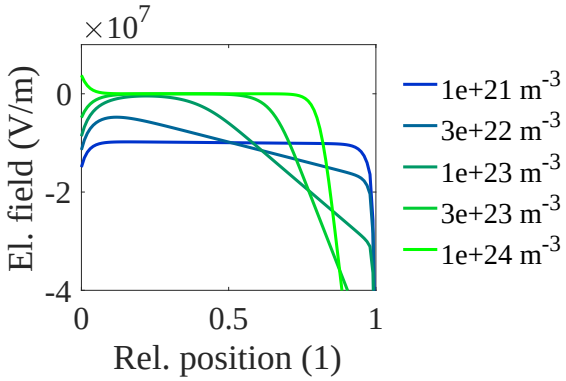

(a) Electric field profile in the dark at 0 V.

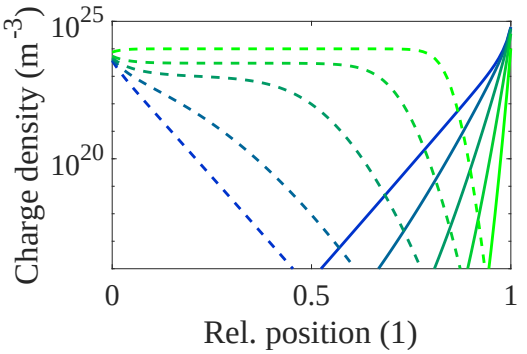

(b) Charge density profiles in the dark at 0 V.

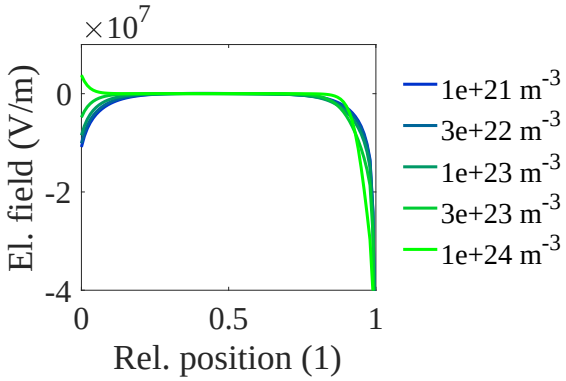

(c) Electric field profile under illumination at open-circuit.

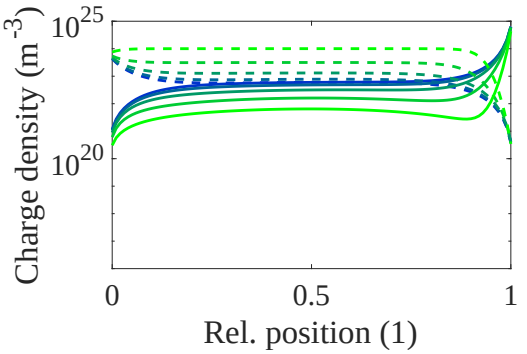

(d) Charge density profiles under illumination at open-circuit.

Figure 11.8: Simulated field and charge density profiles with varied doping density. The lines in the right graphs show electron (solid lines) and hole (dashed lines) densities. The x-axis position 0 corresponds to the anode, position 1 to the cathode.

sumption. The doping leads to a strong loss of short-circuit current in the IV-curve, as charges generated inside the field-free space-charge zone cannot efficiently be extracted.

The field profiles in the dark are shown in Fig. 11.8a and confirm that the field drops over a thin depletion zone. Fig. 11.8b shows the charge carrier densities in the active layer in the dark at zero volt. The doping itself does not show in the graph, as it is modelled as an immobile negative homogeneous space charge. What is seen in Fig. 11.8b are the oppositely charged free holes that are induced to be injected and to counterbalance the space charge in thermal equilibrium. The layer is therefore neutral in the steady-state, yet due to the built-in potential and recombination the distribution is not homogeneous. Instead a zone with low hole density is observed near the cathode, becoming thinner with increasing doping.

The acceptor doping leads to a **pi**-device, with the depleted intrinsic zone W_{dep} near the cathode, and a field-free, positive space-charge region $(d - W_{dep})$ near the anode. As the depletion zone is smaller than the active layer, the probed capacitance in C-f and C-V becomes higher with increasing doping (see Fig. 11.7d). By applying a negative external bias the depletion region can

be enhanced and the capacitance decreases quadratically to the geometric value (see Fig. 11.7e). This is represented in the Mott-Schottky formalism:

$$W_{dep}(V) = \sqrt{\frac{2\varepsilon_0\varepsilon_r}{qN_A}(V - V_{bi})} < d \tag{11.1}$$

$$C(V) = \frac{\varepsilon_0\varepsilon_r S}{W_{dep}(V)} > C_{geo} \tag{11.2}$$

$$C^{-2}(V) = \frac{2(V - V_{bi})}{q\varepsilon_0\varepsilon_r S^2 N_A} \tag{11.3}$$

where N_A is the doping density. From a linear fit this quantity can be extracted, in case the layer is thick enough [337] (see Fig. 11.6).

The equilibrium electron density is strongly reduced with increasing doping, mainly at the cathode side. This is because at thermal equilibrium in the dark the condition $n \cdot p = n_i^2 = const$ must hold [425] (see Section 3.1).

The comparison with the illuminated case (Fig. 11.8d) shows that the hole density in doped devices is hardly perturbed by illumination. The main difference to the dark case is that much more electrons are present and distribute rather homogeneously in the bulk. For highly doped layers the photogenerated holes are negligible compared to the equilibrium carriers. Again the total electron density is reduced due to ensure thermal equilibrium.

At high doping densities the device acts as a minority carrier device, which are often found in inorganic semiconductor theory [425]. Here the equilibrium holes are the majority carriers, whose density can be regarded as approximately constant, and the electrons are the minority carriers. Under this condition the transient photovoltage decay would be governed only by the electron lifetime, and have a mono-exponential shape. As seen in Fig. 11.5h this is however not the case, being a hint that additional recombination pathways like trap-assisted recombination as well as diffusion play an important role. Another reason for the non-exponential decay of the open-circuit voltage is the inhomogeneous charge distribution.

Another experiment which was performed before and after degradation is EQE. The measurements are shown in Fig. 11.9. Along with the loss in short-circuit current we observe a general drop in EQE. Additionally, we also find spectral changes, raising the question whether there could be any loss in absorption. This so called photobleaching happens in many polymers and would then affect only part of the spectrum. Previous data from Merck however do not confirm this, but to be sure the study should be repeated on thin films with the same blend, which should be characterized for transmission and absorption.

One hint that the absorption does not decay strongly, is the photo-CELIV peak, where we find hardly any change during degradation. The extracted charges should be a direct measure of the photogenerated charges, so we can rule out that absorption loss is an effective mechanism here, even for degradation under high intensities.

Furthermore there is again a difference between the 1-sun and the 50-sun devices. The spectral changes are relatively small in the device aged under 1 sun, while for the device degraded at 50 suns the region between $600 - 700$ nm is strongly affected, which is a region where mainly the polymer HBG1 absorbs. This could indicate that the photodoping can be related to certain chromophores of the polymer.

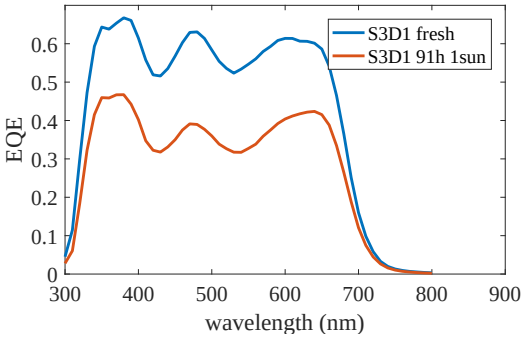

(a) EQE of the device aged under 1 sun for 91 sun*h.

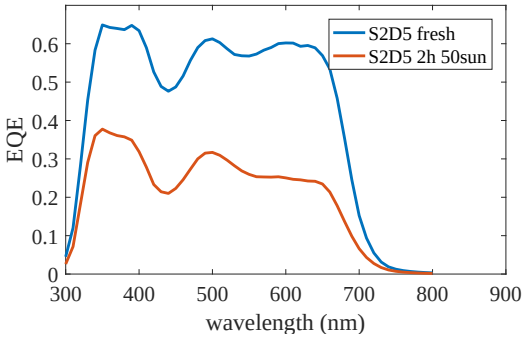

(b) EQE of the device aged under 50 suns for 100 sun*h.

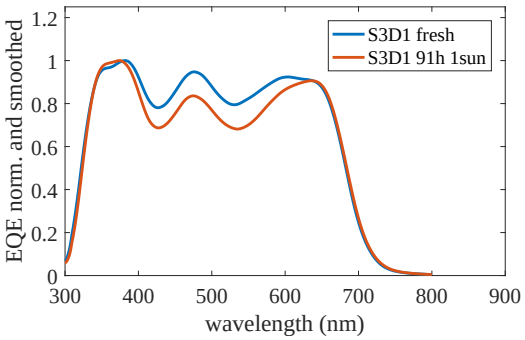

(c) Normalized EQE of the device aged under 1 sun for 91 sun*h.

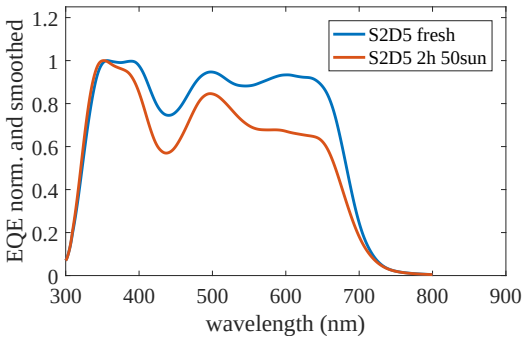

(d) Normalized EQE of the device aged under 50 suns for 100 sun*h.

Figure 11.9: EQE measurements comparing the fresh and photodegraded devices aged under 1 sun and under 50 suns. The normalized EQE emphasizes the spectral changes.

Using simulation we can still reproduce the spectral changes in EQE very well without the need for additional explanations. The EQE measurements were done directly after photodegradation, so in the 1-sun device we assume traps, and in the 50-sun device we assume traps and the doping which has not yet reversibly disappeared.

The qualitative EQE simulation in Fig. 11.10 shows strong changes in the spectral and absolute shape by only increasing the doping density. The reason is that the space-charge of the doping leads to a field-free region in the device, as explained above. Charges created within that region cannot be extracted without an applied bias. As the generation profile for each wavelength depends on the interference effects in the thin-film layer stack, some wavelengths are affected more than others [556]. We can reproduce the effect on the EQE nicely, but only qualitatively, as the exact layer thicknesses and absorption coefficients are not known.

As for the 1-sun device, the spectral changes in EQE are much less pronounced. First of all we would like to note that the manual positioning of the sample inside the EQE setup may lead to some changes in the beam positioning and illumination angle, which can already give an error of around $5 - 10$ %. Furthermore, a part of the spectral changes can also be explained by deep traps, that, when filled, act as charged, immobile species, thereby locally screening the electric field, and leading to a similar effect as dopants.

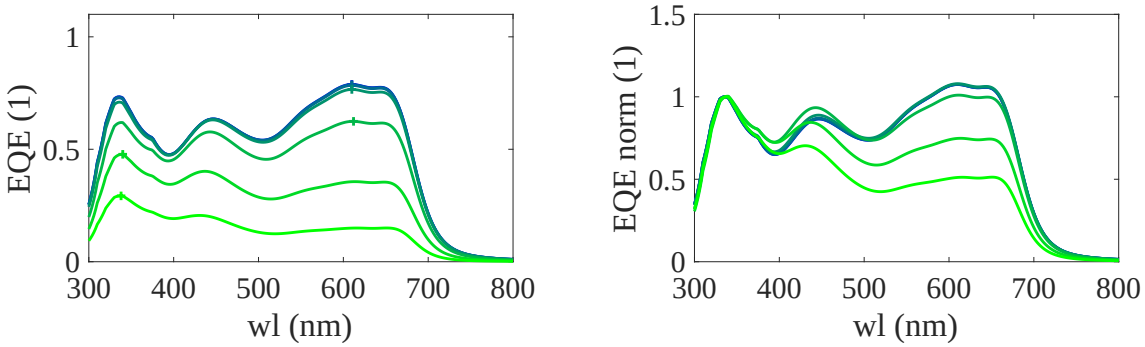

(a) (b)

Figure 11.10: EQE simulation with varied doping density, showing the change in absolute values (a) as well as spectrally (b). The doping density was varied from 10^{21} m^{-3} (blue curve) to 10^{24} m^{-3} (green curve).

11.4 DISCUSSION

The previous considerations have shown that there are at least two distinct mechanisms contributing to the photodegradation - a reversible photodoping and the generation of (deep) traps. In the device aged at 1 sun the reversible photodoping did not occur. The cell was usually aged during daylight for maximum 8 h a day, and measured directly afterwards - no doping signatures were observed. This device does however still show strong photodegradation in the IV-curves, which we attribute to the formation of (deep) traps. The traps give slow contributions to transport and recombination behaviour, which have both been observed. The question remains how they can so strongly affect the IV-curve without clear signatures in other experiments.

The devices aged at 50 and 100 suns also show the signatures of the traps, yet additionally they show the occurrence of intrinsic charges (doping), which has been verified by several techniques. We further found this doping effect to be fully reversible after 30 days in the dark.

As the doping is not observed under 1 sun, even when measuring directly after a degradation step, it is probable that the doping effect only occurs under high illumination. It may thus be thermally activated.

The disappearance of the doping during storage in the dark allows for speculations. It may be possible that by a chemical reaction the doped species become neutral, and therefore have no longer an effect on the electrical properties. Another option could be that the equilibrium charges are in fact very deep traps, which by changing/lowering their energetic depth could "relax" into traps that can take part in the transport process again, as they can be dynamically filled and released. In this case the doping would be a pre-state of the (deep) traps which are also observed in the 1-sun experiment. The question remains why and how this change of energy level should happen.

The assumption that the charging of the layer under high illuminations is a chemical and unstable by-product of photodegradation of the polymer, seems the most plausible.

Temperature-dependent measurements might give further insight into the nature of the photodegradation species and possible thermally activated processes. We performed experiments in the temperature range $150 - 320$ K on devices aged at 1 sun, 50 suns, and not degraded at all, after the dark storage for 30 days. The two degraded devices show very similar behaviour. The DLTS shows temperature-dependent decay kinetics, which could be related to trapping/detrapping processes. Also a low-frequency plateau in C-f is observed upon cooling. Furthermore at low temperatures slight signatures of intrinsic charges are again found in the dark-CELIV, while they are not observed at room temperature. These preliminary results need further analysis before a clear statement can be made. They already hint to the presence of thermally activated processes, and therefore also confirm - though only qualitatively - the assumption of deep traps.

The solar cells investigated in this study show two distinct photodegradation mechanisms. So far it is not yet clear whether these two are directly linked or fully independent processes. However, we should conclude that in this case accelerated ageing by concentrated sunlight does lead to a different degradation behaviour and can therefore not be used to predict the lifetime of the same cell under 1-sun condition.

The study presented here is intended to be published as: S. Züfle, G. Zanotti, E. A. Katz, P. Tiwana, and B. Ruhstaller. "Reversible Photodoping of Organic Solar Cells aged by Concentrated Sunlight". *manuscript in preparation* (2017) [557].

12 LIGHT INDUCED DEGRADATION: BURN-IN

In this chapter we present a second study of photodegradation by concentrated sunlight. The devices therefore employ the prototypical polymer PCDTBT mixed with the fullerene $PC_{71}BM$. This study was performed as a short-term scientific mission in collaboration with Karlstad University and Ben-Gurion University within the COST StableNextSol project [532].

Just as in Chapter 11 we aim to investigate whether the photodegradation processes under high illumination intensities are the same as those under 1-sun condition. Should this be the case, could accelerated ageing by concentrated sunlight considerably speed up lifetime predictions for organic solar cells [550, 551].

12.1 EXPERIMENTAL

The cells comprising the active materials PCDTBT and $PC_{71}BM$ have been fabricated by Rickard Hansson at Karlstad University, Sweden. The devices aged by concentrated sunlight employ the hole transport material PEDOT:PSS, while some additional devices for the second part use evaporated MoO_3. The glass substrates with prestructured ITO were purchased from Ossila Ltd. and contain 6 devices with active areas of 4.5 mm^2. The solar cells were encapsulated using UV-curable encapsulation epoxy and glass coverslips. More details on the sample preparation can be found in: R. Hansson. "Materials and Device Engineering for Efficient and Stable Polymer Solar Cells". PhD thesis. Karlstad University, 2017 [558].

The layer structure is ITO (100 nm)/PEDOT:PSS (50 nm)/PCDTBT:$PC_{71}BM$ (1:4) (90 nm)/LiF (0.3 nm)/Al (100 nm) respectively ITO (100 nm)/MoO_3 (8 nm)/PCDTBT:$PC_{71}BM$ (90 nm)/LiF (0.3 nm)/Al (100 nm). The cells were sent to the Sede Boker Campus of Ben-Gurion University of the Negev. Here we performed photodegradation studies under different illumination conditions which are summarized in Table 12.1. Photodegradation with concentrated sunlight ($1 - 100$ suns intensity) was performed using the concentrator setup at BGU shown in Fig. 11.1 and described in the last chapter [549, 552, 553, 555]. Degradation under approximately 1 sun was performed outdoors at BGU.

For the second series of devices we have employed a sun simulator (Oriel Sol2A, model 94022A, with a 150 W Xenon lamp with AM1.5 filter) in Karlstad for photodegradation under 1 sun illumination, following the ISOS-L1 protocol [282]. Finally we also employed the *Paios* white high-power LED (Cree XP-G, integrated power 720 W/m^2) with negligible UV spectrum [300] for degradation (see Fig. A.2b). During photodegradation all cells were kept under open-circuit condition. The various experiments with different illumination sources and intensities as well as two different HTLs are summarized in Table 12.1.

IV-curves and other experiments were recorded at different times during the degradation process using *Paios* 3, which employs a white LED as light source [300]. For the cells aged with the sun simulator IV-curves were recorded with a Keithley 2636A.

HTL	ILL. SOURCE	INTENSITY (W/m^2)	TOT. ILL. DOSE (SUN·H)	INITIAL V_{oc} LOSS
PEDOT:PSS	Outdoor sunlight	1000	250	96 meV in 2 sun*h
PEDOT:PSS	Conc. sunlight 10 suns	10000	4	109 meV in 4.2 sun*h
PEDOT:PSS	Conc. sunlight 50 suns	50000	160	107 meV in 4.4 sun*h
PEDOT:PSS	Conc. sunlight 100 suns	100000	195	108 meV in 8.5 sun*h
PEDOT:PSS	Sun simulator	1000	4	72 meV in 4 sun*h
MoO_3	Sun simulator	1000	4	13 meV in 4 sun*h
PEDOT:PSS	White LED	700	0.7	58 meV in 0.7 sun*h
MoO_3	White LED	700	9	11 meV in 9 sun*h

Table 12.1: Summary of the performed studies using different illumination sources, intensities, and varying the hole transport layer. For comparison the total integrated illumination dose is specified. The last column denotes the maximum observed drop in open-circuit voltage for each experiment.

12.2 RESULTS

Figure 12.1 shows IV-curves of encapsulated ITO/PEDOT:PSS/PCDTBT:$PC_{71}BM$/LiF/Al solar cells that have been exposed to sunlight of different intensities. Independent of the illumination intensity, all the solar cells show a marked initial drop in V_{oc}. As can be seen in the plots, the V_{oc} loss is due to a shift of the entire IV-curve towards lower voltages, a shift that is observed for both the light and the dark IV-curves. Thus, the overall shape of the IV-curves is preserved and the fillfactor is only very slightly affected (see Fig. 12.2c). The initial voltage shift is also observed in the capacitance-voltage and conductance-voltage plots (Fig. 12.9f).

How the V_{oc} changes over time for the solar cells is shown in Fig. 12.2a for different illumination intensities. The burn-in loss occurs during the first sun-hours of illumination dose and reaches around 100 mV, thus leading to an efficiency loss of over 10 %. The relative size of the V_{oc} loss does not depend on the illumination intensity and after the initial drop, the V_{oc} remains stable.

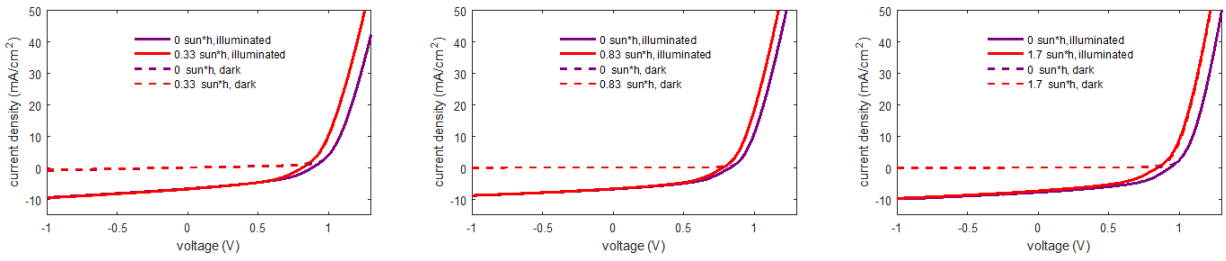

(a) IV-curve at 1 sun (b) IV-curve at 10 suns (c) IV-curve at 100 suns

Figure 12.1: Dark and light IV-curves during initial photodegradation of PEDOT:PSS based devices under different illumination intensities.

The observation that the IV-curve shifts during the burn-in period (see Fig. 12.1), implies that the burn-in is linked to the injection behaviour under forward bias, which depends on the built-in voltage and the injection barriers at the electrodes. In order to investigate whether this is related to the interlayer materials, the hole transporting layer (HTL) was changed from PEDOT:PSS to

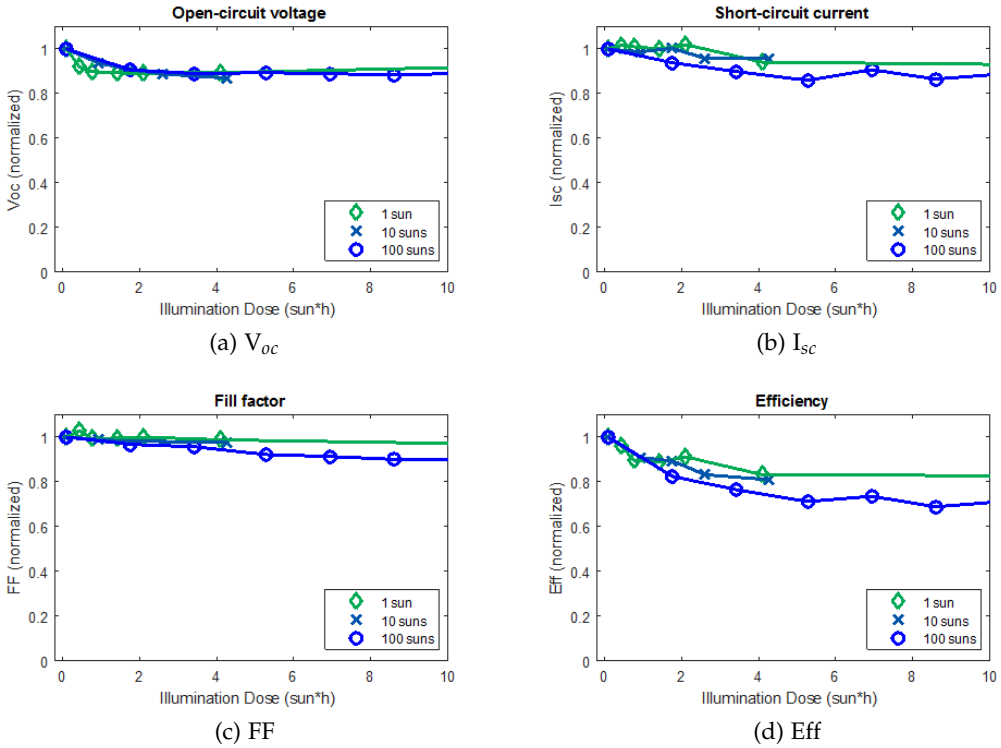

(a) V_{oc} (b) I_{sc}

(c) FF (d) Eff

Figure 12.2: Behaviour of the solar cell parameters versus integrated sun-dose for the different PEDOT:PSS based devices aged with concentrated sunlight.

MoO_3. In Fig. 12.3, IV-curves of encapsulated ITO/HTL/PCDTBT:PC_{71}BM/LiF/Al solar cells exposed to simulated sunlight at an intensity of 1 sun for different times are compared for PEDOT:PSS (Fig. 12.3a) and MoO_3 (Fig. 12.3b) as the HTL. Here a distinct difference can be seen between solar cells using PEDOT:PSS and MoO_3. While devices with PEDOT:PSS exhibit again a shift in the IV-curve along with a drop of V_{oc} during the first 30 minutes of illumination, devices with MoO_3 remain stable. Figure 12.4 shows how the solar cell parameters change over time for the two devices. We find that the initial V_{oc} losses can be significantly reduced by replacing the PEDOT:PSS HTL with MoO_3. Thus it is clear that the burn-in loss is directly linked to the PEDOT:PSS layer.

PARAMETER	PEDOT:PSS	MoO_3
J_{sc}	7.2 mA/cm^2	7.2 mA/cm^2
V_{oc}	0.81 V	0.83 V
FF	51 %	56 %
Eff	3.0 %	3.4 %

Table 12.2: Solar cell parameters of the fresh PEDOT:PSS and MoO_3 based devices.

The initial performances of the solar cells with PEDOT:PSS and MoO_3 are summarized in Table 12.2, and the open-circuit voltage loss for different illumination sources and intensities are shown in Table 12.1. Varying the sunlight concentration from one sun to 100 suns does not significantly affect the burn-in loss for solar cells with PEDOT:PSS. When changing the illumination source to

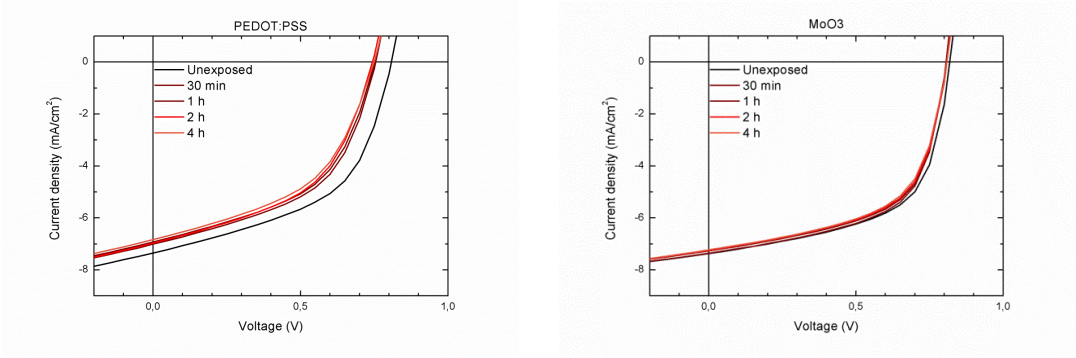

(a) PEDOT:PSS (b) MoO_3

Figure 12.3: IV-curves for a PEDOT:PSS and a MoO_3 based device during photodegradation under a solar simulator at 1 sun intensity.

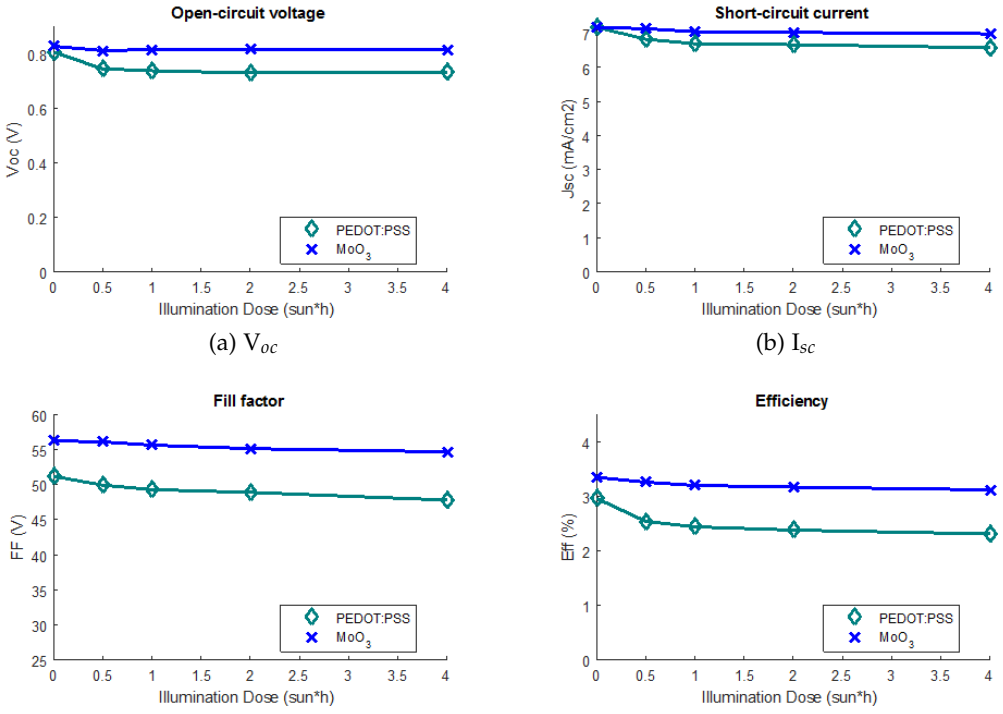

(a) V_{oc} (b) I_{sc}

(c) FF (d) Eff

Figure 12.4: Behaviour of the solar cell parameters versus integrated sun-dose comparing PEDOT:PSS and MoO_3 based devices aged under 1 sun of the sun-simulator.

a white LED whose spectrum does not contain any UV-light, a burn-in loss is still observed for devices with PEDOT:PSS, but not for devices with MoO_3.

There have previously been several reports on burn-in related V_{oc} losses in PCDTBT-based solar cells [132, 148, 292, 294, 559–561]. Heumueller et al. found an initial loss of 40 mV under white light illumination from an LED and of 120 mV using UV light [560]. The same group also observed that the V_{oc} lost during the burn-in remains lost even after replacing the top metal electrode with a fresh one, thus showing that the V_{oc} loss does not depend on the metal-organic interface [133].

How the initial burn-in loss is affected by the HTL material has previously been investigated by replacing PEDOT:PSS with metal oxides[132, 559]. Bovill et al. compared PEDOT:PSS with MoO_3 and V_2O_5 and found the PEDOT:PSS-containing solar cells to exhibit a higher stability both during and after the burn-in period [559], which is in contrast to our observations. Peters et al. on the other hand, found that substituting PEDOT:PSS with MoO_3 or V_2O_5 lead to a smaller loss in V_{oc} during the burn-in [132]. The V_{oc} loss during the burn-in period has previously been attributed by Peters et al. to a photo-induced reaction in the active layer that leads to the formation of sub-bandgap states increasing the energetic disorder in the active layer [132]. Heumueller et al. then suggested a model where the increased energetic disorder causes a broadening of the density-of-states (DOS) and results in V_{oc} losses [560].

12.3 MODELLING APPROACH

In the following we aim to model the observed effect by a drift-diffusion approach using *Setfos* 4.4. We start with a global fit of various measurements of the fresh device, such as IV-curve, capacitance-voltage, capacitance-frequency, transient photocurrent and photo-CELIV, giving us high confidence in the used modelling parameters. This fit and the associated parameters can be found in the Appendix B.3.

In the next step we try to model the device changes during photodegradation, namely the rapid voltage shift. The open-circuit voltage is defined as the difference of the quasi-Fermilevels [425], which pictures the filling of the density-of-states (DOS). This is influenced strongly by the energetics of the contact as well as the shape of the DOS. Several analytic formulas for the V_{oc} have been derived to describe the intensity and temperature dependence, one approach gives [562, 563]:

$$V_{oc} = E_g^{eff} - \frac{k_b T}{q} \cdot \ln\left(\frac{N_0 \cdot P_0}{n \cdot p}\right) \tag{12.1}$$

$$E_g^{eff} = E_{HOMO,D} - E_{LUMO,A} - \frac{\sigma_n^2}{k_B T} - \frac{\sigma_p^2}{k_B T} \tag{12.2}$$

where $E_{HOMO,D}$-$E_{LUMO,A}$ is the electronic band gap, $\sigma_{n/p}$ denotes the width of the Gaussian DOS, N_0/P_0 is the total density-of-states and n/p the number of free charge carriers. An important constraint for a valid model must not only be that it can reproduce the open-circuit voltage drop, but it must also conserve the shape of the IV-curve and the fillfactor, as was observed in the measurements (Figs. 12.1 – 12.3).

From this it becomes obvious that several effects can have a strong influence on open-circuit voltage. We will investigate four effects to decrease V_{oc}: (a) a broadening of the density-of-states, (b) an increase in the total number of states, (c) a change of the hole injection barrier, and (d) a decrease of the electronic band gap.

Following the disorder model [562] used by Heumueller et al. [560] we can indeed reproduce a V_{oc} loss by increasing the width of the DOS in the extended Gaussian disorder model (EGDM) [408] (see Section 3.1). The resulting simulated IV-curves are shown in Fig. 12.5. Substantial changes in the forward current, and a related loss in fillfactor clearly show that this model is not applicable to our own experiments. Heumueller et al. do not give a representative plot of their IV-curves before and after degradation, so we can only assume that they observed the accompanied fillfactor loss and decreased injection current, which is also featured in the

underlying modelling study by Blakesley et al. [562]. The mechanism of broadening of the DOS by creation of in-gap states (traps) can however still take place as a minor effect [132]. It could then explain the very small open-circuit voltage losses of 10 mV that have been observed for the MoO_3 devices, and would be intrinsic to the active layer.

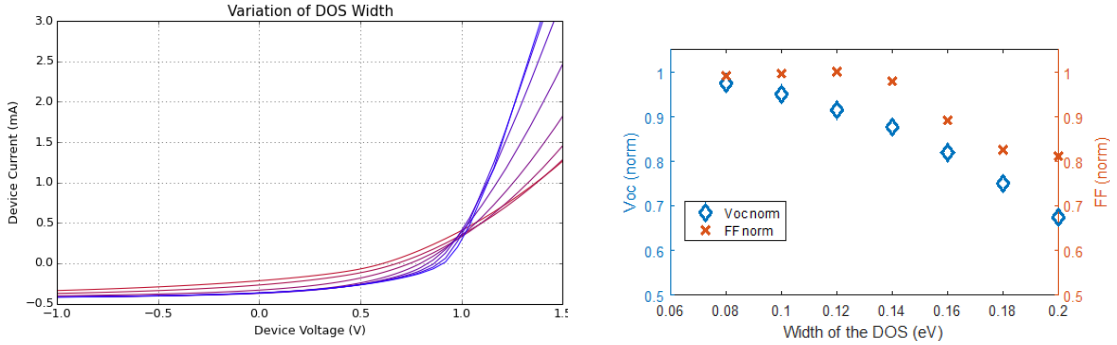

Figure 12.5: Simulation of IV-curves with increasing width of the polymer HOMO Gaussian density-of-states, using the ohmic injection model and the EGDM mobility model. The right plot shows the influence on V_{oc} and FF.

There are, however, other effects conceivable from modelling that would lead to a V_{oc} loss. From Eq. 12.1 one would expect the V_{oc} to drop if the density-of-states either increases or broadens. An increase in the total density-of-states, which could be due to light-induced trap formation, indeed shifts the curve to lower voltages, thus decreasing the V_{oc}. At the same time the shape of the curve and the fillfactor are only slightly affected, as shown in Fig. 12.6. This effect, however, should then also occur in the MoO_3 based devices.

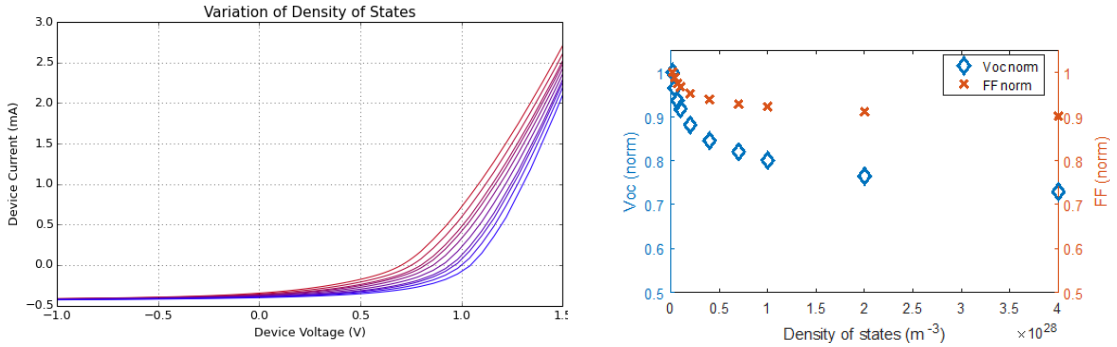

Figure 12.6: Simulation of IV-curves with increasing polymer HOMO density-of-states, using the ohmic injection model and constant mobilities. The right plot shows the influence on V_{oc} and FF.

As the observed voltage shift is linked to the use of PEDOT:PSS, and also observed in the dark-IV, it could also be due to the hole injection properties. In our model we employ an ohmic injection model including an injection barrier E_a at the interface, being the difference between the PCDTBT HOMO and the PEDOT:PSS (or MoO_3) workfunction. There are reports that the PEDOT:PSS workfunction can increase due to illumination [564–569], which would in our case lead to a decrease of the injection barrier accompanied with a better contact. We find in Fig. 12.7 that by changing the barrier from 0.2 eV (from the global fit) towards 0 eV hardly any changes are observed, as the contact is already good enough.

On the other hand it is also conceivable that some residual oxygen or ambient water is left inside the encapsulation, which has been shown to decrease to PEDOT:PSS workfunction [223, 570, 571]. In this case the contact properties would diminish, as seen in the simulations of Fig. 12.7. While for larger barriers the shape of the IV-curves is nearly unchanged, the currents are much lower than observed, so it seems that a decreasing PEDOT:PSS workfunction can not explain the observations.

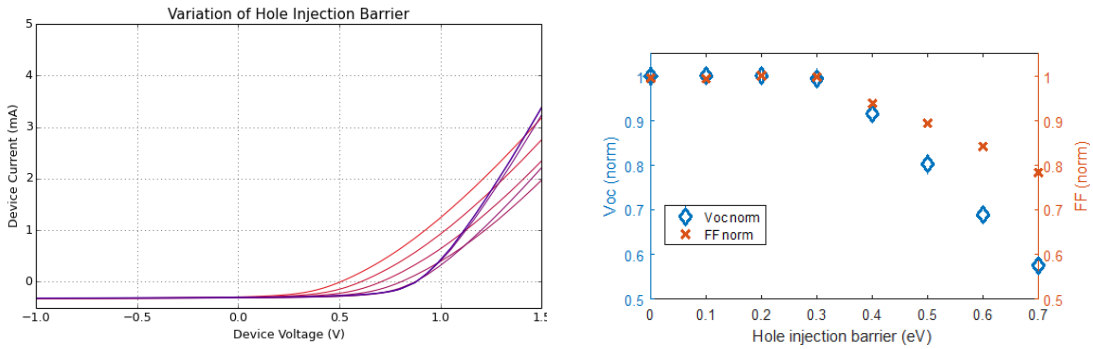

Figure 12.7: Simulation of IV-curves with varying hole injection barrier between PEDOT:PSS and PCDTBT HOMO by changing the PEDOT:PSS workfunction, using the ohmic injection model and constant mobilities. The right plot shows the influence on V_{oc} and FF.

The fourth effect influencing Eq. 3.13 would be a decrease of the electronic band gap, which however would imply considerable chemical alterations to the active layer materials (or at least the polymer). The bandgap has a linear correlation with the forward current and the open-circuit voltage, therefore the shift is reproduced as found in the experiments (see Fig. 12.8). The question remains how such a strong change in the material properties could happen, and why the effect is not observed in the MoO_3 based devices.

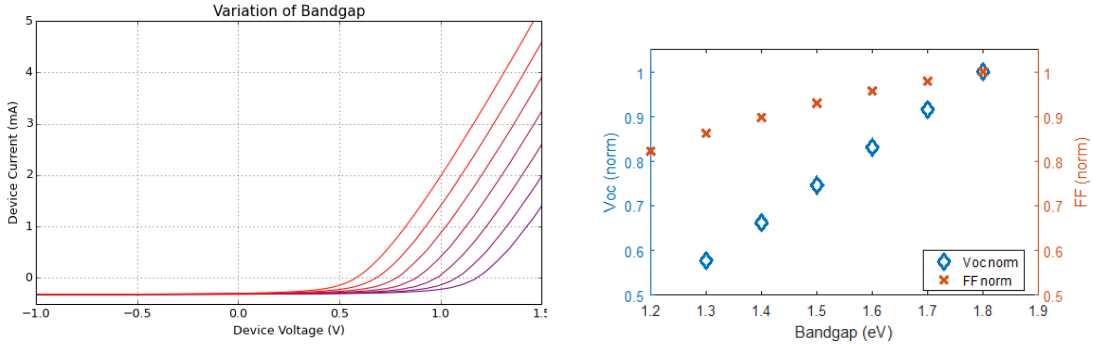

Figure 12.8: Simulation of IV-curves with varying PCDTBT bandgap by changing the PCDTBT HOMO while keeping the injection barrier constant, using the ohmic injection model and constant mobilities. The right plot shows the influence on V_{oc} and FF.

So far we have shown that conventional, bulk models can not explain the observed effects and link it to the PEDOT:PSS contact. We therefore postulate that a thin interface layer forms induced by illumination, which has energetic properties such that the quasi-Fermilevel splitting is reduced. The so-called band-bending effect has been under debate recently [572–574], and it describes the position dependent energy levels that are affected by injection barriers, accumulated charges and

the applied field, leading to thin regions near the contact interface that do not behave like the bulk material.

At this point it remains unclear if there are other factors influencing the PEDOT:PSS behaviour. The described effect has not been reported before for full solar cell devices, while PEDOT:PSS is widely used among the community. So we express the assumption that by using a different PEDOT formulation, or by different processing steps during fabrication, it may be possible to obtain a more stable PEDOT:PSS layer.

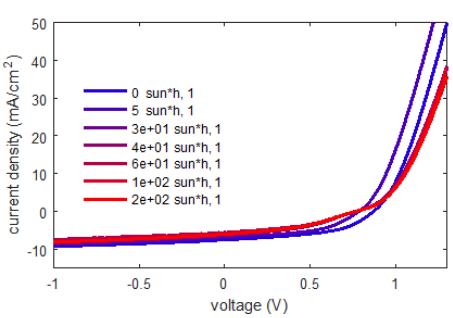

(a) IV-curve.

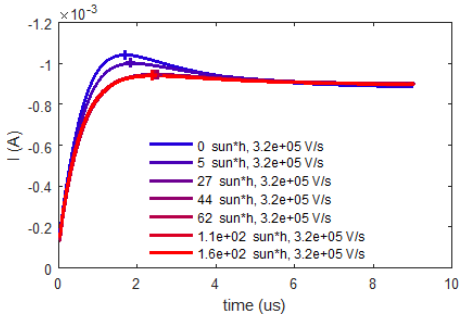

(b) Photo-CELIV current.

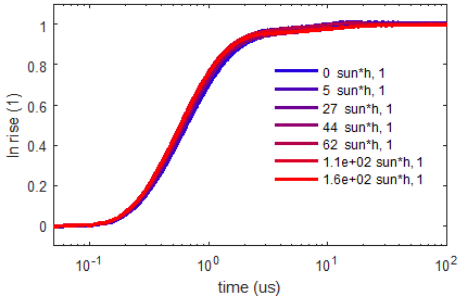

(c) TPC normalized rise.

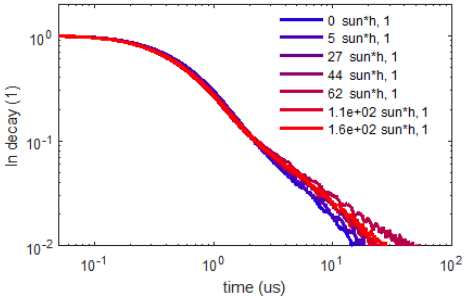

(d) TPC normalized decay.

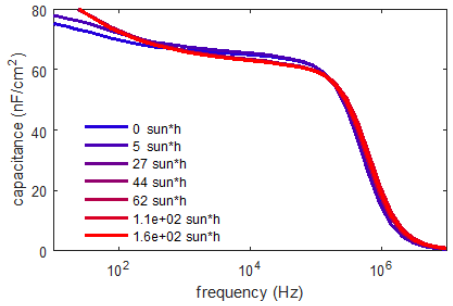

(e) Capacitance-frequency.

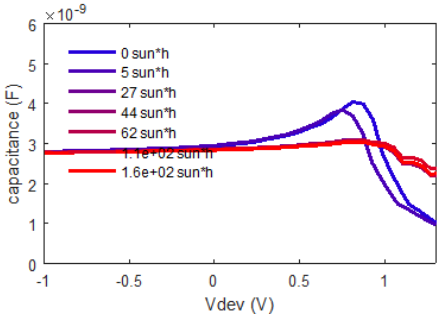

(f) Capacitance-voltage.

Figure 12.9: Various experiments during photodegradation of a PEDOT:PSS based PCDTBT:PCBM device for 2 h at 50 suns.

As we have seen, the burn-in effect occurred for all devices comprising PEDOT:PSS independent on the illumination intensity. In the following we will shortly discuss the further degradation progress. It turns out that the qualitative behaviour remains the same for the different ageing conditions. The measurements shown in Fig. 12.9 exemplarily depict the device aged under

50 suns.

While during the initial burn-in the forward current increases, at later times of degradation the injection efficiency and the forward currents decrease. This is accompanied by the introduction of an S-shape, leading to a loss in fillfactor and short-circuit current.

The decreased photocurrent is also observed as the steady-state value of the TPC signal (not shown). The rise and decay of the TPC, which are signatures of the charge carrier mobilities, do not change considerably, thus the mobilities are probably stable. There is, however, an indication of a slow decay component, visible at times above 10 μs, which may be related to traps.

The photo-CELIV current shows a rapid and complete disappearance of the extraction peak, which is at least partly related to the S-shape and therefore a sign for an extraction problem. Another process contributing to a lower CELIV peak could be an increased recombination.

Finally, the capacitance-frequency plot shows only minor changes at low frequencies. These can also be interpreted as trapping signatures.

The qualitative behaviour described above is observed for all ageing intensities from 1-100 suns. In line with Fig. 12.2 the devices are relatively stable after the burn-in phase. Therefore the changes in the other experiments at later times are only minor. There are, however, several indications that traps are generated leading to a more dispersive charge transport. Traps could also be one of the reasons for the diminished photo-CELIV peak. The second reason is the formation of an extraction barrier, which is also responsible for the observed S-shape. So far we cannot attribute this barrier to either of the contacts, yet, as the PEDOT:PSS contact/interface has been found to be susceptible to changes, and furthermore the PEDOT:PSS itself is know to change upon illumination, our assumption is that the extraction barrier is formed there.

12.4 CONCLUSIONS

We have found a strong burn-in effect during photodegradation of encapsulated PDCTBT:$PC_{71}BM$ organic solar cells that takes place under real and artificial sunlight as well as at illumination concentrations up to 100 suns. The rapid V_{oc} drop of around 100 mV during the first sun-hours is accompanied by a shift of the complete current-voltage curve towards lower voltages. The effect is related to the employed PEDOT:PSS as hole transport layer, as it is not observed when replacing this material by MoO_3. Using numerical drift-diffusion simulation we discussed possible mechanisms that can lead to a loss in open-circuit voltage. An already described broadening of the density-of-states, that is increased disorder of the active layer, shows to be unsuitable in our case, as the V_{oc} drop is accompanied by a loss in fillfactor and a change in the IV-curve shape. However an increase in the total density-of-states, as well as a decrease of the effective bandgap of PCDTBT:$PC_{71}BM$ reproduces the qualitative behaviour correctly. The question remains how this process may occur only in the PEDOT:PSS based devices. We therefore propose that a further mechanism, affecting the interface of the PEDOT:PSS to the PCDTBT:$PC_{71}BM$ blend, is responsible for the observed behaviour and leads to a decrease in the quasi-Fermilevel splitting. We speculate that this is due to photoinduced formation of a thin interlayer with different energetic properties.

As the initial efficiency drop during this burn-in phase amounts to over 10 %, it is obvious that PEDOT:PSS can strongly harm the overall stability of these devices, even in the encapsulated device. This study also underlines the importance of the injection and transport layers even for intrinsic stability studies. Here the intrinsic stability of the active material turns out to be much higher than the stability of the stack, so it can be a challenge to probe only the intrinsic degradation of the active layer.

In the PCDTBT:$PC_{71}BM$ bulk-heterojunction the photodegradation processes are independent of the used illumination intensity. The signatures of various experimental techniques show the same behaviour during ageing. So we may conclude that in this material system accelerated ageing by concentrated sunlight is a valid method to estimate the device stability.

The study presented here is intended to be published as: S. Züfle, R. Hansson, E. A. Katz, E. Moons, and B. Ruhstaller. "Burn-in degradation of PCDTBT:PC70BM organic photovoltaics: underlying mechanism and interlayer effect". *manuscript in preparation* (2017) [575].

Part IV

CONCLUSIONS

This part summarizes and further discusses the main results of this thesis. We review the original objectives and how the combined approach of experiments and simulation can help to improve the understanding of the device physics.

13 SUMMARY

This thesis investigates charge carrier transport in organic semiconductor devices. For this purpose we employ a novel approach of combining experiment and simulation and a variety of characterization techniques. We use this approach to investigate and formulate parameter extraction methods, and to analyse and determine degradation mechanisms in organic solar cells and polar OLEDs. The tools for our investigations are the measurement setup *Paios* and the modelling software *Setfos*, which are developed and commercialized by the company Fluxim AG.

13.1 COMBINATORIAL APPROACH

The measurement setup *Paios* unites a large variety of electrical characterization techniques in the dc, ac, and transient mode for solar cells and OLEDs. It allows to perform these experiments in an automated, consistent and reproducible way. There are several advantages to this approach:

- The measurement errors which are due to the measurement instrument are the same for all techniques, leading to a higher comparability.
- The automation of the measurement routines leads to unprecedented data acquisition speed.
- Performing all experiments with the same device under the same environmental conditions and without re-contacting gives a highly increased comparability and consistency of the data, as it excludes device-to-device variation and minimizes degradation in between measurements.
- The specific hardware used (*Paios*) further comes with a sophisticated graphical user interface, additional functional modules (e.g. stress-test, temperature), and the possibility to include numerical modelling by the drift-diffusion solver *Setfos* and fitting directly in the same user interface.

Most of the devices we investigated are small-area research devices fabricated in academic laboratories mainly by hand and mostly with solution-processing of the active layers. Therefore, device-to-device as well as sample-to-sample variations can be high and the reproducibility of measurements is impaired. Thus, it is difficult to obtain identical devices in the first place. This obviously can strongly influence the results, especially when investigating degradation, or for quantitative parameter determination.

This problem has lead to the current situation that solar cell efficiency values are often reported as a statistical mean over a series of nominally identical devices, that is, devices which have been produced in one batch with the same fabrication process and parameters. While this allows to estimate the reliability of the data and numbers, this strategy is not applicable to the investigation of degradation by complementary techniques. The time and effort needed to sequentially degrade and characterize a series of identical devices without an automated stress and measurement setup is very high. Furthermore, any re-contacting and transfer between different measurement equipments represents a potential error source, and uncontrolled time delays between stress and measurement may also distort the consistency of the data. Hence, for a degradation analysis that does

not focus only on one measurement technique it is much more suitable to employ one device at a time, and therefore automate the stress and measurement process as far as possible.

With the *Paios* Stress-Test Module it is possible to apply an electrical, light or thermal stress to the device and sequentially measure the whole measurement routine, making it a highly suited tool for stability analysis.

We base our work on both the combination of various electrical experiments in the steady-state, transient and impedance modes, as well as the combination of measurement with simulation. In general, the steady-state measurement of an IV-curve conceals a lot of important information, as it depicts only the equilibrium situation. Transient and modulated methods are much better suited to investigate the dynamics of charge transport in organic electronic materials.

Charge transport in all solar cells and light-emitting devices is governed by electric fields (drift) and density gradients (diffusion). While in most inorganic devices diffusion currents dominate, due to the employment of doped layers , in organic semiconductors the transport is mainly governed by drift. The drift-diffusion modelling approach is in principle suited for all semiconductor devices, and specific models for charge carrier mobility, injection, excitons and furthermore have been developed to account for the individual peculiarities of the different technologies.

The possibility to for the first time simulate all these different experiments allows to qualitatively understand the influences of the various material and device parameters on the experiments. Hereby the qualitative shape of a characterization signal can give valuable information without the need for being quantitative. Furthermore, this approach helps us to relate specific features in different experiments to each other. For example, the occurrence of an S-shaped IV-curve can, but does not need to be correlated with a current overshoot in the TPC signal, depending on the underlying mechanism. Thus, a synoptic view of several experiments allows us to identify the underlying process.

The numerical modelling furthermore is very useful to test analytic parameter extraction formulas. It turns out that they are usually not applicable for the complete parameter space, but their accuracy is limited to specific conditions and parameter regions. Being able to model the experiments, we can specify these parameter regions and the accuracy of the extracted values. From this we are able to give advise for more appropriate experimental conditions, and it is also possible to design new parameter extraction routines and analytical models.

Another way to obtain material parameter values is the full drift-diffusion modelling of the experiment combined with a fitting procedure. Hereby the experiment is simulated with the correct measurement settings, and the deviation between simulation and measurement is minimized by an algorithm which is stepwise adapting the model parameters. However, multiple local minima of the error may exist due to the multi-dimensional parameter space, and depending on the starting values different solutions may be obtained. We have shown that this ambiguity can be avoided by fitting several different experiments at the same time. This leads to a strongly changed error landscape in the multi-dimensional parameter space, and it is much more likely to find the global minimum of the error, and therefore the correct parameters.

13.2 PARAMETER EXTRACTION

In order to determine specific material parameters like the charge carrier mobility, often unipolar, single-layer devices are fabricated. In this configuration only one carrier contributes to the current, and the analysis is not complicated by a second carrier type or by bimolecular recombination. The simplification of the system usually yields higher success for parameter determination using analytic formulas. This approach comes, however, with a fundamental drawback, namely that the direct transfer of the results to a full device is often not correct.

There are several reasons for this:

- Analytic models for single-carrier devices are often only valid for and applied to thick films, while in fully functional devices the layer thicknesses are much smaller. Layers of different thicknesses need different fabrication conditions, which can lead to a different morphology and changed material properties.
- The surrounding functional layers can influence the determined as well as the effective parameters. For example the nominal barrier for carrier injection from the electrode into the active material is strongly reduced by an injection layer.
- In a bipolar device bimolecular as well as Shockley-Read-Hall recombination can strongly affect parameter analysis. The determined effective mobility can be lower than the one in a unipolar device by orders of magnitude.

On the other hand, because in bipolar devices electron and hole parameters can not be distinguished, it can still be useful to employ unipolar devices. Layer stacks comprising an insulating layer have been introduced as an alternative, as they keep the active layer processing parameters while being strictly unipolar. They are, however, non-functional devices. Yet, under specific circumstances, also regular devices show a regime where the signatures of only one carrier type are observed. This condition will probably yield the most accurate parameter estimation, as it does not require an unusual film thickness or preparation.

One class of devices that shows a unipolar regime are polar bilayer OLEDs. Due to the polarity of the ETL there is a voltage regime where holes are already injected and the layers are still empty of electrons. Thus, there is no steady-state current, but transient and impedance techniques can be performed to investigate hole transport and injection. In the voltage regime between the hole injection voltage and the built-in voltage the device can be understood as a metal-insulator-semiconductor (MIS) device, where the ETL is still insulating and the HTL is already semiconducting. In this work we have investigated these polar OLEDs and elaborated new ways to determine parameters by exploiting the MIS character.

The MIS-CELIV experiment was originally developed for "real" MIS-devices. We show for the first time that it can be employed also in polar bilayer OLEDs to determine the hole mobility in the HTL. Hereby the thickness ratio between ETL and HTL defines the available experimental voltage region for the measurements, and whether the small-charge regime or the space-charge limited case can be evaluated. We find values of the hole mobility in α-NPD of $\mu_h \approx 10^{-4}$ cm^2/Vs at room temperature, using voltages just above the hole injection voltage.

The temperature dependence of the charge mobility is a second topic that we have addressed. Assuming an exponential increase of the mobility with temperature, we employ simulation to

investigate how well the mobility activation energy can be obtained using an Arrhenius analysis. We find that a large hole injection barrier can influence the determined values. Furthermore, we show that the temperature dependent transition frequency between the two capacitance plateaus in C-f-T data can also be analysed by an Arrhenius fit, however giving an effective activation energy which depends on both the mobility activation and the injection barrier. The combination of C-f-T and MIS-CELIV therefore has the potential to allow distinguishing between the two contributions of injection and transport to the thermal activation. We find in an α-NPD/Alq_3 device that the combined activation energy of $\approx$ 0.5 eV is composed of two nearly equal contributions of the hole injection barrier and the charge mobility activation energy. Furthermore, the use of simulation allows us to better understand the limitations of the analysis methods. The main reasons for the inaccuracies found in the self-consistency study are the inhomogeneous charge density profiles which contradict with the assumptions of the analytical model.

There are other devices that show both a second capacitance plateau and a peak in the dark-CELIV signal - doped organic solar cells. While the doping is basically a loss mechanism and usually due to degradation, these devices also allow to consider only one carrier type in some measurements. The dark-CELIV peak contains only carriers of one type, therefore the extracted mobility is more reliable than the one from photo-CELIV. Using drift-diffusion simulation allows for fitting the dark-CELIV with only one mobility, and then keeping this mobility while fitting the photo-CELIV signal with the other mobility and the recombination prefactor as the only fit parameters. Furthermore, the temperature dependence of the capacitance-frequency in doped devices also yields an activation energy which depends mainly on the mobility activation.

Thus, in order to accurately determine material parameters one needs to distinguish between different processes. This can be done by simplifying the layer stack, or by exploiting the specific operating regimes of some layer stacks and by utilizing specific signatures of physical processes. Often already the distinction of electron and hole parameters is not possible, and at one point an arbitrary assignment is made. In the cases presented here the assignment of the respective carrier type is straight-forward, however.

13.3 DEGRADATION ANALYSIS

The second part of this work deals with the degradation of organic semiconductor devices by various factors such as humidity, oxygen, light or electrical current. Traditionally degradation mechanisms are studied by monitoring the gradual performance decrease of a series of devices during prolonged operation. What we propose in this thesis is to intermittently and repeatedly carry out a series of diagnostic techniques in AC, DC and transient mode on the same device. Thereby a rich and comprehensive data set is acquired that enables a systematic analysis and an understanding of the underlying mechanisms that goes beyond the standard stability lifetime measurements. The studies we have performed are in principle similar to other studies done before, which however included further, rather time-consuming, expensive and sometimes invasive, experimental methods. We show the same conclusions can be obtained by our approach in a far more elegant way.

The first study we present underlines the role of hole transport materials in the degradation of the cathode. We investigated the solar cell stack ITO/HTL/P3HT:PC_{61}BM/Al with different

solution-processed hole transporters: PEDOT:PSS, MoO_3, V_2O_5 Oxopolymer and V_2O_5 Xerogel. The devices were not encapsulated and exposed to air in the dark under three different temperature and humidity conditions.

The dominant degradation mechanism is the oxidation of the aluminium cathode triggered by an ingress of humidity, leading to the formation of a thin insulating aluminium oxide layer and thus a loss in effective area for charge extraction. The most prominent signature of this effect in the IV-curve is therefore the strong loss of short-circuit current and at the same time a stable open-circuit voltage. In transient photocurrent measurements a short-lived transient current is observed, as the active material and with it the photogeneration is still unchanged. However, the electrons cannot be extracted at the organic/insulator interface barrier, leading to a space-charge build-up and a complete loss of the driving electric field, giving a steady-state photocurrent of zero. In this fully degraded state the whole device area is oxidized and the device has become a MIS-device, which is confirmed in capacitance-voltage and MIS-CELIV measurements.

The effect is accelerated by humidity as well as temperature, and its speed is governed by the choice of the HTL. We find that PEDOT:PSS, which is hygroscopic, strongly enhances the diffusion of water into the device. In contrast, the alternative HTLs can slow down the process by a factor of up to 380.

From modelling the water concentration inside the stack we could compute the loss in effective area which is proportional to the measured short-circuit current over time. The diffusion simulation gives a squareroot-of-time dependence for diffusion from the edges, which agrees well with the measured behaviour. The 2D modelling thus confirms the proposed lateral progress of degradation, and further allows us to give an estimate of the water diffusion constant in the different hole transport materials.

Another study was performed using encapsulated devices with the structure ITO/HTL/PCDTBT:PC_{71}BM/LiF/Al where PEDOT:PSS and evaporated MoO_3 were used as hole transport layers. The encapsulation prevents water and oxygen ingress and with it the oxidation of the aluminium electrode. The devices were stressed by illumination, thus most of the degradation is expected to stem from the active material. However, in the PEDOT:PSS devices a strong initial voltage loss was observed, in contrast to the MoO_3 devices. This burn-in effect is thus related to the PEDOT:PSS/organic interface energetics. This initial instability leads to a large drop in V_{oc} of around 100 meV. At later times the main degradation mechanism is the photodegradation of the absorber layer.

We also addressed photodegradation by concentrated sunlight, thereby investigating the PCDTBT:PC_{71}BM solar cell stack as well as a second batch of samples based on a HBG1:PC_{61}BM blend. In the first case an increased illumination intensity basically just accelerates the degradation. The burn-in behaviour is always observed, and later trapping probably becomes the dominant mechanism. Therefore, in this material system concentrated light may be used to accelerate the degradation and to predict device stability lifetimes.

In the HBG1-based devices, however, a clear difference is observed for devices aged at 1 sun and devices aged with 50 or 100 suns. Under high illuminations the devices show signatures of doping building up, additionally to trap-related signatures which are observed under all intensities. We furthermore find that the photodoping part is fully reversible after storage in the dark for 30 days. Therefore, in this BHJ material, accelerated ageing by concentrated sunlight is not a valid tool to predict the cell stability.

Based on the degradation studies shown here we conclude that it is crucial to look at the complete stack when investigating stability of organic solar cells. It would have been grossly incorrect to ascribe the short-circuit current loss of uncencapsulated devices to a change in the active material. It is also wrong to relate the burn-in observed in the PCDTBT-based cells only to the PCDTBT. In both cases the role of the functional layers (hole transport layers) and the encapsulation cannot be underestimated. Thus, variations of the experiment are indispensable in order to learn about the contributions of the various layers to the overall degradation, and we suggest to:

- Compare encapsulated to non-encapsulated devices
- Vary the material(s) of the functional layer(s)
- Vary the ageing conditions temperature, humidity, current, illumination intensity

The second conclusion we can draw from the degradation experiments is not to focus only on the IV-curve parameters. Basically every degradation mechanism leads to a decrease of the device performance (PCE) over time. While recording this curve may allow to determine a lifetime, and to compare different materials or ageing conditions, it is not possible to determine the dominant ageing mechanism from this data alone.

Only by the combination of several experiments a full picture of the processes going on in the device may be obtained. While a huge range of other experimental techniques has been employed for this purpose, we have demonstrated that also the combined analysis of various electrical measurements is equally useful. Finally, the postulated degradation mechanisms can be tested by numerical modelling of the full device, and the picture can be completed.

14 OUTLOOK

We have shown that simulation-based analysis of transient electrical measurements can give deeper insight into the underlying physical processes in organic semiconductor devices. This approach also allowed us to test commonly used models and develop new analytic routines for parameter extraction.

In fact, this procedure may be applied to a large range of analytical models and parameter extraction routines:

- The CELIV formula has been demonstrated to be not always reliable, as the assumptions made are usually not correct. Also the improved equations based on more appropriate models, partly even based on (simplified) drift-diffusion modelling, turn out to be not suited to accurately determine the charge carrier mobility in relevant stack architectures. Therefore, based on our tools, a new parametrized CELIV formula dependent on ramp rate, peak position and peak height may be developed in the future.

- As we show in the Appendix C.5, also other techniques like the transient photocurrent rise may be suited to determine the mobility. Here as well a simulation-based development of a dedicated formula and the investigation of its limitations would be a very useful effort.

- The modulated photocurrent techniques IMPS/IMVS also offer new ways to gain information on mobility and recombination. As they have just become available for simulation now, they surely should be investigated in more detail.

- We find that the transient photovoltage decay commonly used to analyse the recombination behaviour is problematic. First of all the basic theory of minority carrier recombination is usually not fulfilled in organic solar cells. Secondly the influence of the measurement resistor as well as non-ideal shunting behaviour can distort the signal and render it useless. In our opinion time-delayed charge extraction methods like OTRACE-CELIV or Delaytime Charge Extraction are much better suited to really measure the recombination kinetics.

- The assessment of trap parameters - density, energetic distribution, capture rates - constitutes a huge task. Especially in the context of photodegradation trapping and dispersive transport play an important role. Therefore dedicated experiments for quantitative parameter determination need to be found and understood. Deep-level transient spectroscopy might be such a technique, as well as temperature-dependent low-frequency impedance measurements (thermal admittance spectroscopy). For this effort, however, also the simulation side may need some extensions, as currently not all combinations of mobility, injection, and trapping models are supported.

While the idea of comparing several experiments as well as comparing measurement and simulation is not new, only now we are for the first time able to pursue this idea with respect to electrical techniques, and bring it to a quantitative level. For this achievement it was necessary to have a measurement setup where complementary experiments can be performed in a short time, enabling a synoptic approach. And only due to the improved computation speeds in *Setfos* it has become possible and realistic to simulate all experiments and to perform global fitting routines.

The polar bilayer OLED stack was identified to be well-suited for specific parameter extraction routines borrowing from the theory of MIS-devices. One of our conclusions for reliable parameter determination is that for the investigation of new materials there is probably no way around fabricating dedicated devices to determine specific parameters. Now, apart from purely unipolar devices and "real" MIS structures, also devices with a polar layer implement carrier selectivity. This concept enables new layer combinations, and in principle allows to separately address both electron and hole parameters of a material.

For our experiments we employed very standard materials and layer stacks which have been available for us. This leads to various consequences: Simple stacks are easier to understand and therefore more suitable for degradation as well as parameter extraction studies. Common active layer materials such as P3HT:PCBM or α-NPD/Alq_3 are useful in order to compare the results to previous studies. They do, however, only offer limited efficiencies as well as stabilities. Therefore it is unclear whether the results obtained can be directly transferred to more efficient or very stable devices. Today's record cells probably do not suffer from the same loss and degradation mechanisms, otherwise they wouldn't be that efficient.

The hand-made and mainly solution-processed devices show only a low reproducibility. Thus fully quantitative studies do not always seem meaningful, as a different device from the same batch will behave slightly different. Therefore qualitative behaviour of different experiments versus a parameter variation are more informative. The variation may be a measurement parameter like light intensity, a device parameter like the layer thickness or the used functional material, and the progress of degradation under a given stress condition. In all these cases qualitative changes in the shapes of the various measurements are observed which are signatures for specific physical (or chemical) processes. We believe that the goal should be to find a suitable model that can explain all these observed changes qualitatively. As models always contain simplifications it is unlikely that a fully quantitative picture can be found which is based on the change of only one model parameter. Especially for stability analysis several processes happen simultaneously, and the goal should be to identify the most severe one.

The current focus in OPV stability research is on photostable materials and thermally stable morphologies. Photodegradation usually contains chemical reactions that decompose the organic material and lead to the generation of charged species (doping, radicals) or sub-bandgap states (traps). Therefore the characterization of the changes in the density-of-states would be the most important task concerning (opto-)electrical measurements and simulations. For this purpose it is probably necessary to include further experimental techniques such as thermally stimulated current spectroscopy or spectral response.

During thermal stress the morphology of a bulk-heterojunction changes. It is assumed that during a de-mixing process the fullerene tends to cluster and form larger domains while simultaneously diffusing towards one side of the film. Some of the resulting effects could be tackled with our approach. The phase-segregation will lead to a change in the recombination efficiency, and may also lead to a lower effective mobility. Furthermore fullerene accumulation on one side could be simulated as a thin fullerene-only layer at the interface, mainly leading to extraction problems.

However, more complicated situations and a more direct accounting for the changing cluster sizes is not directly possible within our drift-diffusion effective medium approach. The presented effective area model using a parallel circuit of different cells might be one way to go, by simulating various cross-sections corresponding to different polymer/fullerene mixing. On the other hand, as the electrical measurements only deliver a total current of the full device, other experiments would be needed to justify a chosen parametrization. Thus, the use of a 1D effective medium model to describe thermal stability studies still needs to be evaluated.

As for the degradation issues related to oxygen and water, we are confident that good encapsulation strategies and materials are available today, also from the OLED industry, and that this will not pose a threat to device stability in a future industrial fabrication scenario of OSCs. Furthermore, the reproducibility issues can also be well handled by upscaling and automation. Therefore, the race for organic solar cells is still on!

Part V

APPENDIX

Here we present some additional results from the simulation. The default model parameters and layer stacks are summarized, and the global fits obtained for several devices are shown. Furthermore we examine the influence of some device and measurement parameters on various experiments.

A SIMULATION PARAMETERS

In the following we describe the standard layer stack for solar cells, polar OLEDs which was employed for simulations with *Setfos*. We summarize all modelling parameters that are needed and give their default values, which have been used for qualitative simulations of parameter sensitivities or typical charge carrier profiles, as for example in Figs. 3.2 & 5.1 and in the Appendix C.

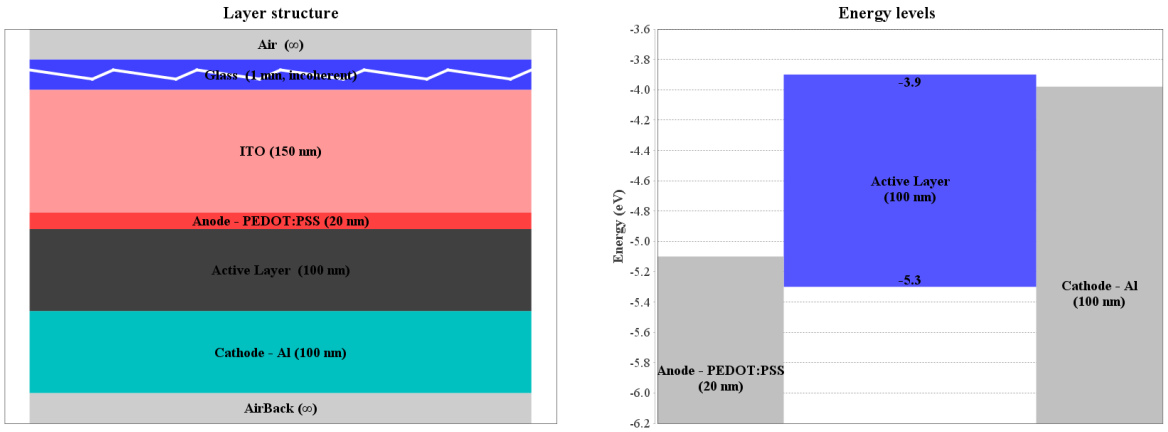

(a) Layer structure

(b) Energy levels

Figure A.1: Default layer stack and schematic energy levels used for the simulations of organic solar cells. Graphs taken from *Setfos* GUI.

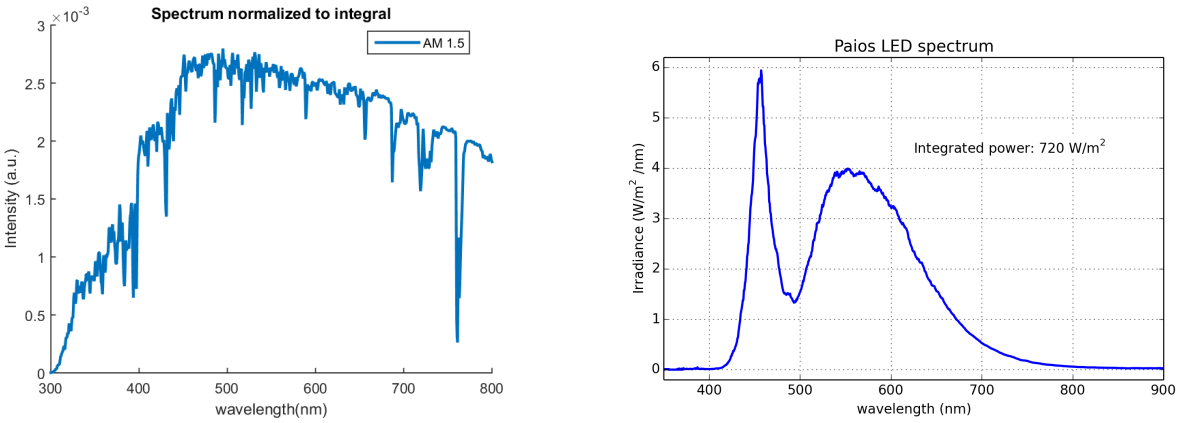

(a) Sunspectrum AM1.5g.

(b) Spectrum of the white LED [300] used in *Paios*.

Figure A.2: Illumination spectra used for solar cell simulations and *Paios* measurements.

PARAMETER	VALUE	UNIT
Thickness of the active layer	100	nm
Thickness of the Anode (usually PEDOT:PSS)	20	nm
Thickness of the Substrate (usually ITO)	150	nm
Thickness of the Cathode (usually Al)	100	nm
Device area	4.0	mm^2
Series Resistance	30	Ω
Parallel Resistance	∞	Ω
Temperature	300	K
Workfunction Cathode	4.15	eV
Workfunction Anode	5.05	eV
V_{bi}	0.85	eV
E_{HOMO}	5.3	eV
E_{LUMO}	3.9	eV
bandgap (E_{HOMO} - E_{LUMO})	1.4	eV
Energy barrier at cathode	0.25	eV
Energy barrier at anode	0.25	eV
Relative permittivity	3.5	
Total density-of-states	$1.5 \cdot 10^{27}$	m^{-3}
Electron mobility	$1.5 \cdot 10^{-4}$	cm^2/Vs
Hole mobility	$3.5 \cdot 10^{-4}$	cm^2/Vs
Recombination efficiency	0.05	

Table A.1: Default modelling parameters for solar cell simulations with *Setfos*.

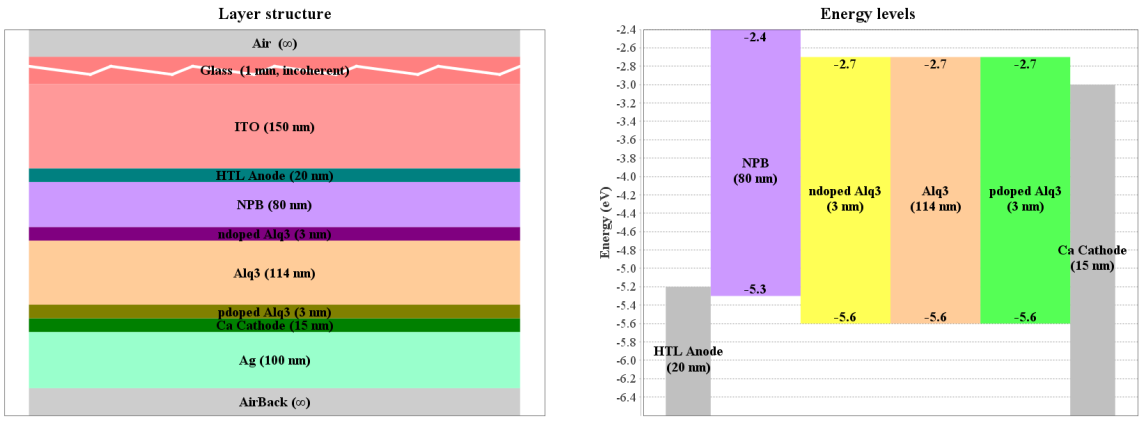

(a) Layer stack

(b) Energy levels

Figure A.3: Default layer stack and schematic energy levels used for the simulations of polar bilayer OLEDs. Graphs taken from *Setfos* GUI.

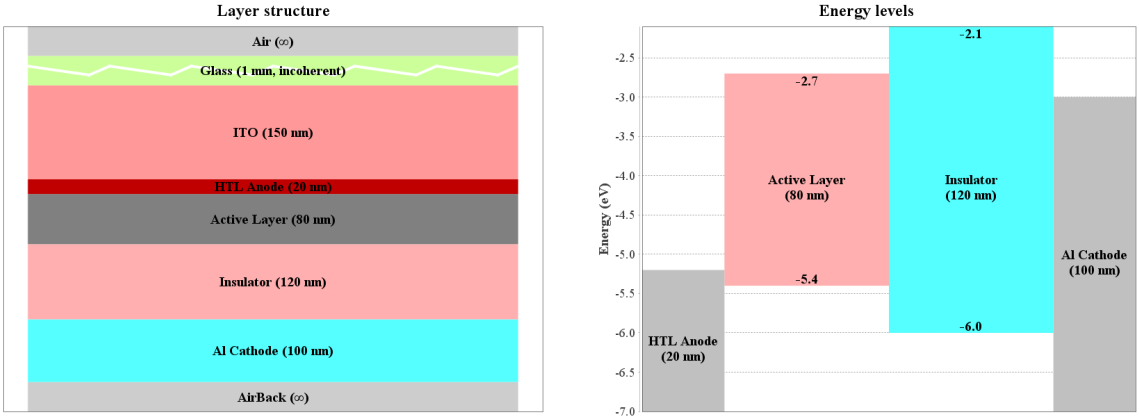

(a) Layer stack (b) Energy levels

Figure A.4: Default layer stack and schematic energy levels used for the simulations of MIS-devices. Graphs taken from *Setfos* GUI.

	POLAR OLED		MIS-DEVICE	
PARAMETER	VALUE	UNIT	VALUE	UNIT
HTL thickness	80	nm	80	nm
polar ETL / insulator thickness	60	nm	60	nm
Relative permittivity HTL	3.5		3.5	
Relative permittivity ETL/Ins	3.5		3.5	
Total density-of-states HTL	$1 \cdot 10^{27}$	m^{-3}	$1 \cdot 10^{27}$	m^{-3}
Total density-of-states ETL/Ins	$1 \cdot 10^{27}$	m^{-3}	$1 \cdot 10^{27}$	m^{-3}
Hole Mobility HTL	$1 \cdot 10^{-4}$	cm^2/Vs	$1 \cdot 10^{-4}$	cm^2/Vs
Electron Mobility HTL	$1 \cdot 10^{-7}$	cm^2/Vs	$1 \cdot 10^{-7}$	cm^2/Vs
Hole Mobility ETL / insulator	$1 \cdot 10^{-8}$	cm^2/Vs	$1 \cdot 10^{-6}$	cm^2/Vs
Electron Mobility ETL / insulator	$1 \cdot 10^{-7}$	cm^2/Vs	$1 \cdot 10^{-9}$	cm^2/Vs
Anode Workfunction	5.2	eV	5.2	eV
Cathode Workfunction	3	eV	3	eV
Built-in Voltage	2.2	V	2.2	V
HOMO HTL	5.6	eV	5.6	eV
LUMO HTL	2.4	eV	2.7	eV
HOMO ETL/Ins	5.9	eV	6.2	eV
LUMO ETL/Ins	2.7	eV	2.1	eV
Sheet charge density ETL	-1.8	mC/cm^2		
Applied Voltage	0	V	3.4	V
Temperature	300	K	300	K
Series Resistance	10	Ω	10	Ω
Parallel Resistance	∞	Ω	∞	Ω
Device area	4.0	mm^2	4.0	mm^2

Table A.2: Default modelling parameters for simulations of polar OLEDs and MIS-devices with *Setfos*.

B GLOBAL PARAMETER FITS

B.1 P3HT:$PC_{61}BM$

PARAMETER	VALUE	UNIT
Thickness of the active layer	85	nm
Device area	4.0	mm^2
Relative permittivity	2.7	
Series Resistance	95	Ω
Temperature	320	K
Total density-of-states	$1.2 \cdot 10^{27}$	m^{-3}
Electron mobility	$11.5 \cdot 10^{-5}$	cm^2/Vs
Hole mobility	$4.5 \cdot 10^{-5}$	cm^2/Vs
Recombination efficiency	$6.1 \cdot 10^{-3}$	
HOMO	5.2	eV
LUMO	4.01	eV
Workfunction Cathode	4.14	eV
Workfunction Anode	4.99	eV
E_{HOMO} - E_{LUMO}	1.19	eV
V_{bi}	0.85	eV
Energy barrier at cathode	0.13	eV
Energy barrier at anode	0.21	eV
Acceptor doping density	$1 \cdot 10^{22}$	m^{-3}
Electron trap density	$8.5 \cdot 10^{22}$	m^{-3}
Electron trap depth	0.31	eV
Electron trap capture rate	$1.2 \cdot 10^{-17}$	$m^3\ s^{-1}$

Table B.1: Simulation parameters for an ITO/PEDOT:PSS/P3HT:$PC_{61}BM$/Al device.

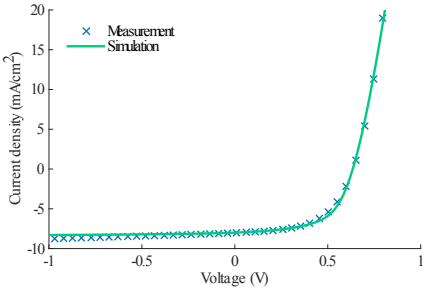

(a) Light IV-curve.

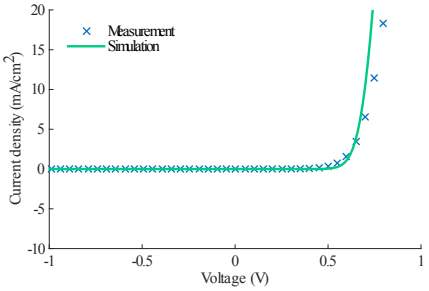

(b) Dark IV-curve.

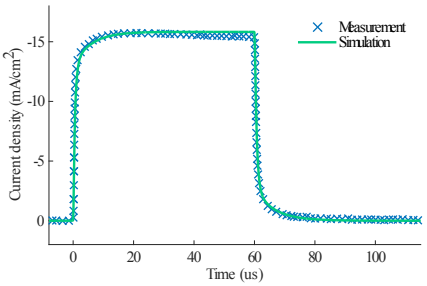

(c) Transient photocurrent response to a 60 μs light pulse.

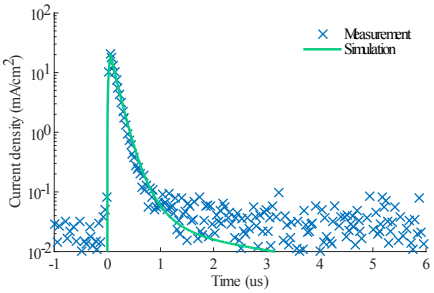

(d) Response to a small voltage step.

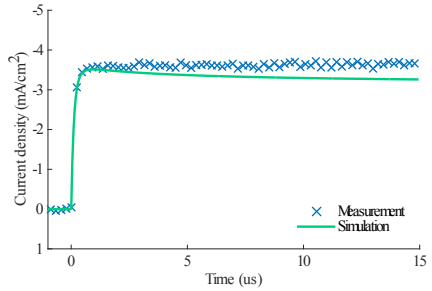

(e) Dark-CELIV current.

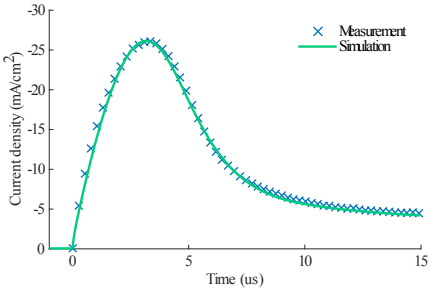

(f) Photo-CELIV current.

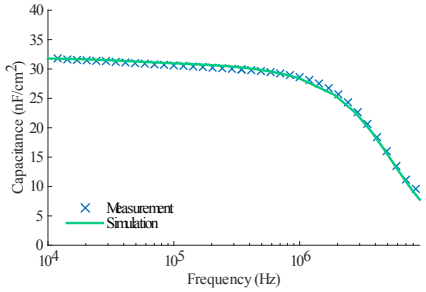

(g) Capacitance-frequency without offset voltage.

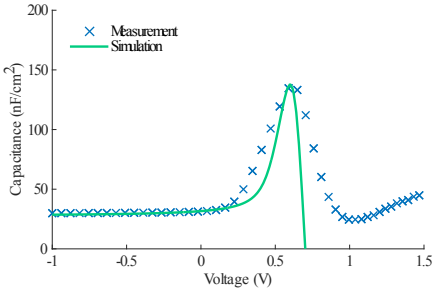

(h) Capacitance-voltage at 20 kHz.

Figure B.1: Global fit for an ITO/PEDOT:PSS/P3HT:PCBM/Al device.

B.2 HBG1:PC$_{61}$BM

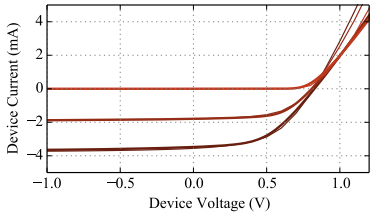

(a) IV-curves for intensity 0, 0.5, 1.

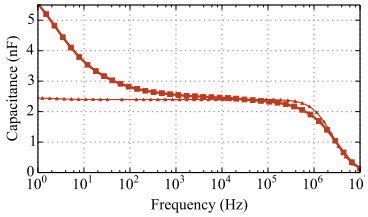

(b) Capacitance-frequency without offset voltage.

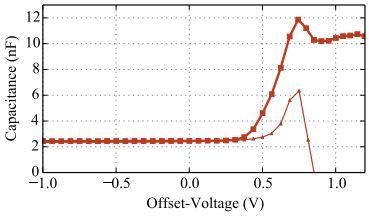

(c) Capacitance-voltage at 20 kHz.

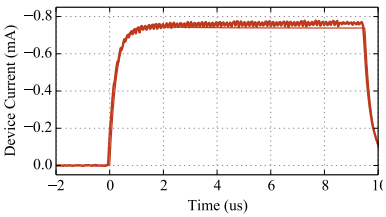

(d) Dark-CELIV current.

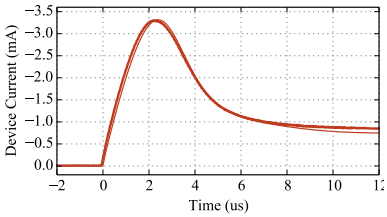

(e) Photo-CELIV current.

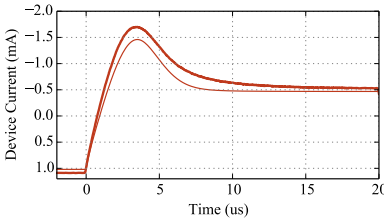

(f) Injection-CELIV current.

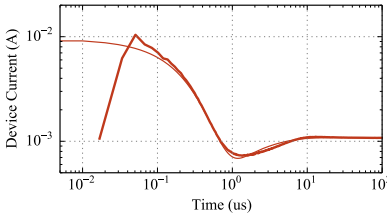

(g) Double injection transient.

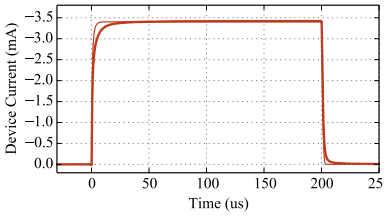

(h) Transient photocurrent.

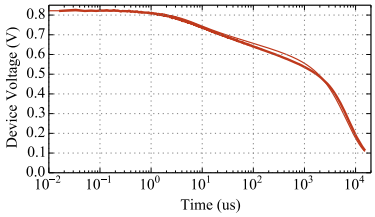

(i) Transient photovoltage decay.

Figure B.2: Global fit for an ITO/PV-E002/HBG1:PC$_{61}$BM/PEDOT:PSS/Ag device. Measurements thick lines, simulations thin lines.

PARAMETER	VALUE	UNIT
Thickness of the active layer	210	nm
Device area	16	mm^2
Series Resistance	26	Ω
Temperature	293.15	K
Intensity calibration factor	0.9	
Relative permittivity	3.48	
Total density-of-states	$1.0 \cdot 10^{27}$	m^{-3}
Electron mobility	$3.4 \cdot 10^{-4}$	cm^2/Vs
Hole mobility	$8.5 \cdot 10^{-4}$	cm^2/Vs
Recombination efficiency	0.007	
HOMO	5.35	eV
LUMO	3.95	eV
Workfunction Cathode	4.2	eV
Workfunction Anode	5.1	eV
E_{HOMO} - E_{LUMO}	1.4	eV
V_{bi}	0.9	eV
Energy barrier at cathode	0.25	eV
Energy barrier at anode	0.25	eV
Hole trap density	$4 \cdot 10^{23}$	m^{-3}
Hole trap depth	0.23	eV
Hole trap hole capture rate	$1.2 \cdot 10^{-22}$	$m^3\ s^{-1}$
Hole trap electron capture rate	$1.2 \cdot 10^{-22}$	$m^3\ s^{-1}$

Table B.2: Simulation parameters for an ITO/PV-E002/HBG1:$PC_{61}BM$/PEDOT:PSS/Ag device.

B.3 PCDTBT:PC$_{71}$BM

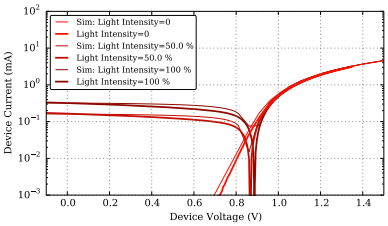

(a) Light IV-curve.

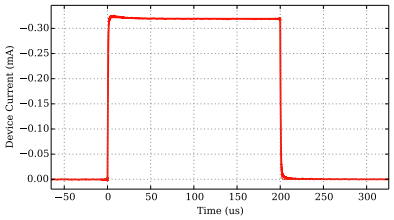

(b) Transient photocurrent.

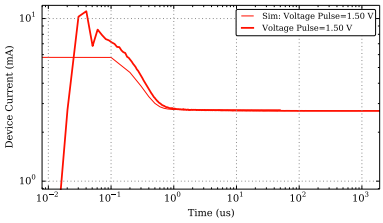

(c) Double injection transient.

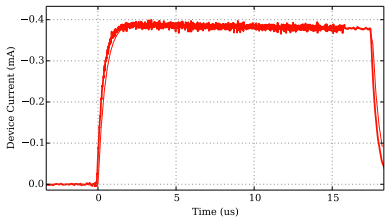

(d) Dark-CELIV current.

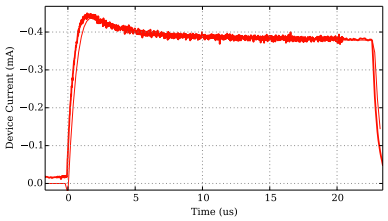

(e) Photo-CELIV current.

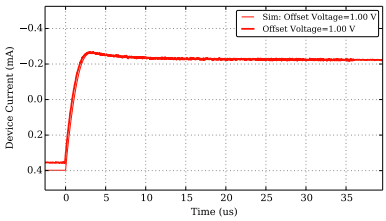

(f) Injection-CELIV current.

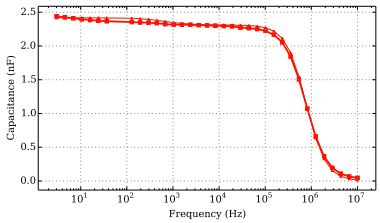

(g) Capacitance-frequency without offset voltage.

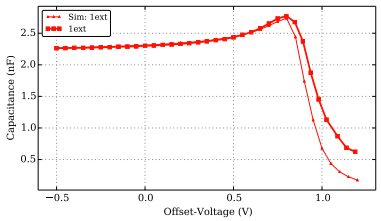

(h) Capacitance-voltage at 20 kHz.

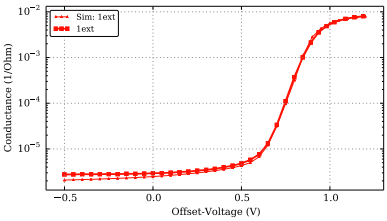

(i) Conductance-voltage at 20 kHz.

Figure B.3: Global fit for an ITO/MoO_3/PCDTBT:PC$_{71}$BM/LiF:Al device. Measurements thick lines, simulations thin lines.

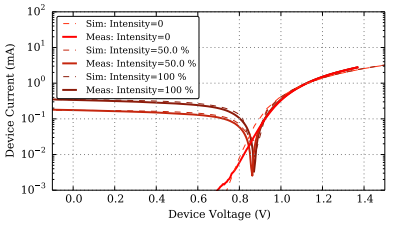

(a) Light IV-curve.

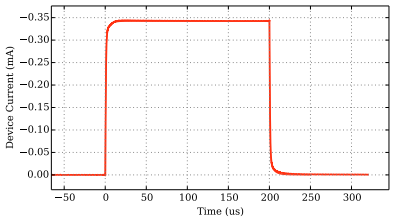

(b) Transient photocurrent.

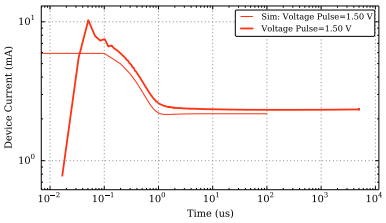

(c) Double injection transient.

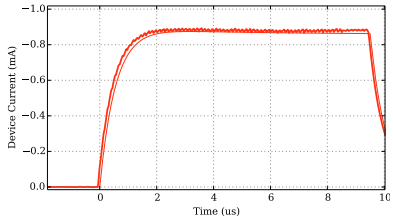

(d) Dark-CELIV current.

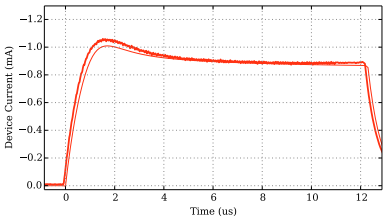

(e) Photo-CELIV current.

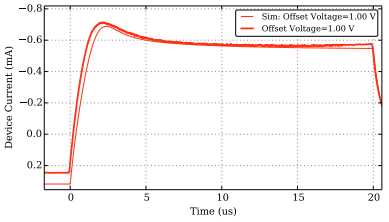

(f) Injection-CELIV current.

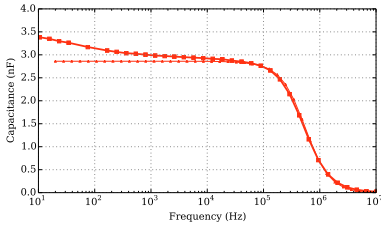

(g) Capacitance-frequency without offset voltage.

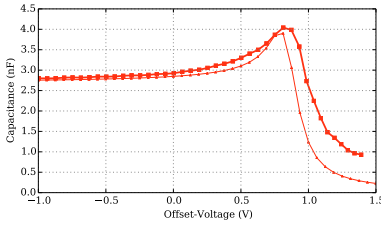

(h) Capacitance-voltage at 20 kHz.

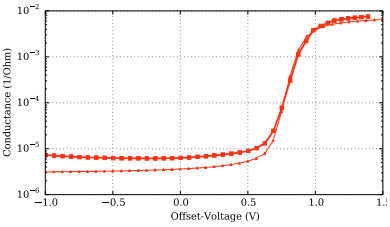

(i) Conductance-voltage at 20 kHz.

Figure B.4: Global fit for an ITO/PEDOT:PSS/PCDTBT:$PC_{71}BM$/LiF:Al device. Measurements thick lines, simulations thin lines.

	MoO_3		PEDOT:PSS	
PARAMETER	VALUE	UNIT	VALUE	UNIT
Thickness of the active layer	85	nm	85	nm
Device area	5.0	mm^2	4.5	mm^2
Relative permittivity	5.3		4.7	
Total density-of-states	$1.5 \cdot 10^{27}$	m^{-3}	$1.5 \cdot 10^{27}$	m^{-3}
Electron mobility	$1.0 \cdot 10^{-4}$	cm^2/Vs	$1.6 \cdot 10^{-3}$	cm^2/Vs
Hole mobility	$3.5 \cdot 10^{-4}$	cm^2/Vs	$8.0 \cdot 10^{-4}$	cm^2/Vs
Recombination efficiency	0.75		1.0	
HOMO	5.3	eV	5.37	eV
LUMO	3.8	eV	3.8	eV
Workfunction Cathode	3.88	eV	3.88	eV
Workfunction Anode	5.1	eV	5.22	eV
Electron trap density	$8.0 \cdot 10^{22}$	m^{-3}	$1.0 \cdot 10^{23}$	m^{-3}
Electron trap depth	0.28	eV	0.40	eV
Electron trap electron capture rate	$1 \cdot 10^{-17}$	$m^3\ s^{-1}$	$1 \cdot 10^{-17}$	$m^3\ s^{-1}$
Electron trap hole capture rate	$1 \cdot 10^{-17}$	$m^3\ s^{-1}$	$3 \cdot 10^{-16}$	$m^3\ s^{-1}$
Series Resistance	100	Ω	90	Ω

Table B.3: Simulation parameters for ITO/HTL/PCDTBT:PC$_{71}$BM/LiF:Al devices with MoO_3 and PEDOT:PSS as HTL.

B.4 α-NPD:ALQ$_3$

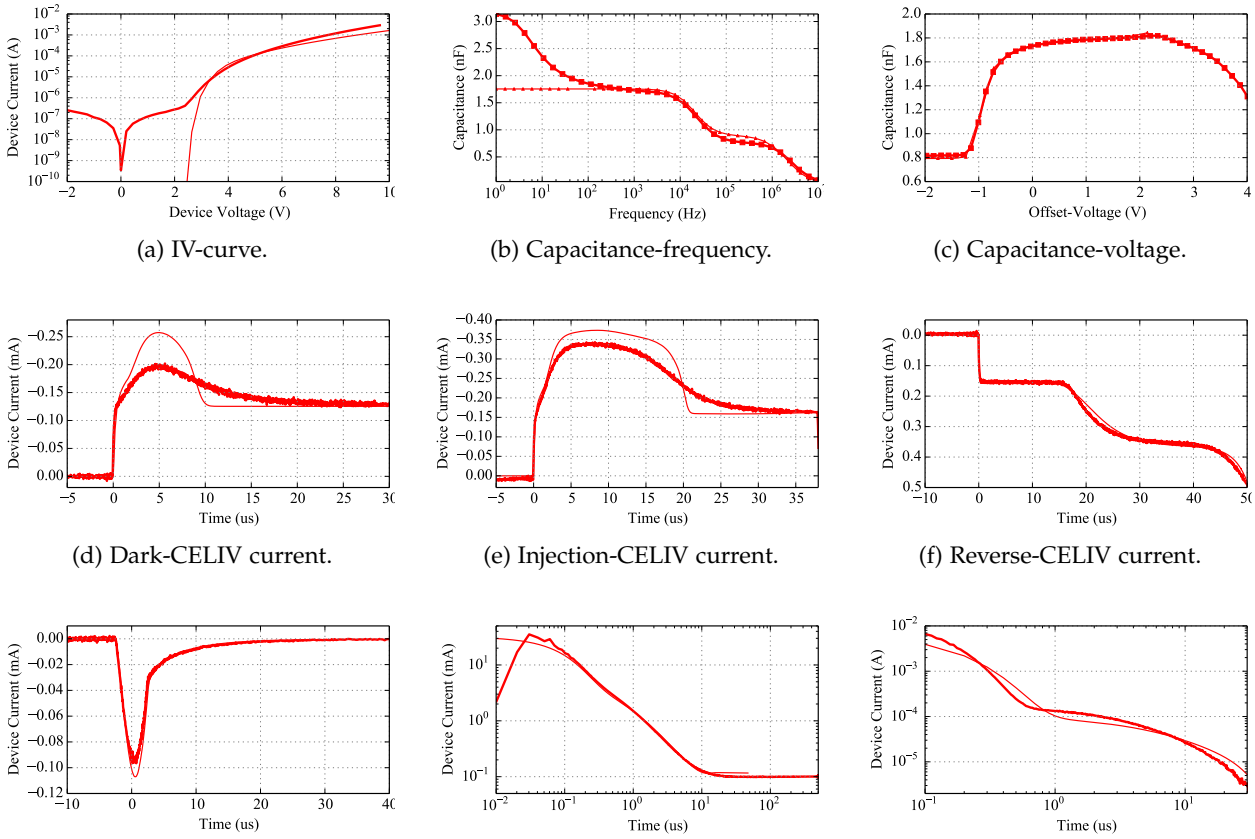

(a) IV-curve. (b) Capacitance-frequency. (c) Capacitance-voltage.

(d) Dark-CELIV current. (e) Injection-CELIV current. (f) Reverse-CELIV current.

(g) Small voltage pulse. (h) Double injection transient. (i) Deep-level transient spectroscopy.

Figure B.5: Global fit for an ITO/PEDOT:PSS/α-NPD/Alq$_3$/Ca/Al bilayer OLED. Measurements thick lines, simulations thin lines.

PARAMETER	VALUE	UNIT
Device area	3.6	mm^2
Series Resistance	80	Ω
Temperature	295	K
Workfunction Cathode	2.9	eV
Workfunction Anode	5.1	eV
V_{bi}	2.2	eV
Barrier Cathode	0.35	eV
Barrier Anode	0.41	eV

	α-NPD		ALQ_3	
PARAMETER	VALUE	UNIT	VALUE	UNIT
Thickness	80	nm	60	nm
Relative permittivity	3.5		3.5	
Total density-of-states	$2.0 \cdot 10^{27}$	m^{-3}	$1.5 \cdot 10^{27}$	m^{-3}
Zero-field electron mobility	$1.0 \cdot 10^{-7}$	cm^2/Vs	$5 \cdot 10^{-8}$	cm^2/Vs
Zero-field hole mobility	$2.5 \cdot 10^{-4}$	cm^2/Vs	$1 \cdot 10^{-9}$	cm^2/Vs
Characteristic field electrons	$2.0 \cdot 10^{6}$	V/m	$2.5 \cdot 10^{6}$	V/m
Characteristic field holes	$2.0 \cdot 10^{6}$	V/m	$2.5 \cdot 10^{6}$	V/m
Recombination efficiency	1		1	
HOMO	5.51	eV	5.81	eV
LUMO	2.3	eV	2.55	eV
Sheet charge density			−1.9	mC/m^2
Sheet charge layers thickness			3	nm

Table B.4: Simulation parameters for an ITO/PEDOT:PSS/α-NPD/Alq_3/Ca/Al OLED device.

C PARAMETER SWEEPS

This chapter shows simulation results with *Setfos* for a standard organic solar cell, using default parameters as summarized in Table A.1. We then vary one parameter in order to show its influence and sensitivity on different experiments. The obtained simulation results are meant to be used as a reference, allowing the reader to identify specific signatures and qualitative changes in the different techniques.

C.1 SERIES RESISTANCE

The series resistance, as introduced in Fig. 2.1 is mainly due to the contact resistance and the ITO lateral conductivity. It is therefore treated as an external series resistance according to the equations shown in Section 2.1.1. It influences all experiments in steady-state, transient and AC mode.

In the IV-curve the series resistance mainly leads to a lower fillfactor, and very high values also harm the short-circuit current. It is obvious from Eq. 2.2 that the open-circuit voltage is unaffected. In the high-resistance limit the IV-curve becomes a straight line and the fillfactor is 25 %. However, also intermediate resistance values of 100 Ω can already lead to a decreased efficiency.

The resistance is often deduced in equivalent circuit models as the differential resistance of the IV-curve at open-circuit. This is true for high values, however, for low values, an intrinsic resistance of the active layer and not the external value is obtained. Thus care needs to be taken when identifying the elements of the equivalent circuit.

In transients the external resistance together with the geometric capacitance lead to RC-effects, so that processes faster than the characteristic RC-time are difficult to be resolved. The RC-effects therefore slow down the response of the device to light or voltage signals.

The photo-CELIV peak shows a very strong influence on the series resistance. Due to the delay of the peak position the extracted mobility is strongly underestimated.

The DIT response shows not only the decreased steady-state forward current, but also the characteristic minimum (and maximum in unipolar devices) is delayed, again complicating parameter analysis.

The TPC response shows the reduced photocurrent in steady-state, just as observed in the IV-curves. However, additionally the rise and decay dynamics are slowed down. While the unaffected dynamics might be used to determine the transit time, with high resistance only the RC-time will be measured.

In impedance measurements the RC-time defines a cutoff frequency. For frequencies above the RC frequency the charges cannot follow the alternating voltage signal (or light signal in IMPS) any more and the device becomes conducting. The capacitance drops to zero and the high-frequency conductance is just the inverse of the series resistance. For transport analysis only frequencies

below the RC threshold may be used. This becomes especially important for materials with high mobilities.

The capacitance-voltage shows a decrease and shift of the peak position with increased resistance, which would lead to an underestimation of the built-in potential. The resistance has further an influence on the capacitance behaviour above the built-in voltage and on the negative capacitance effect.

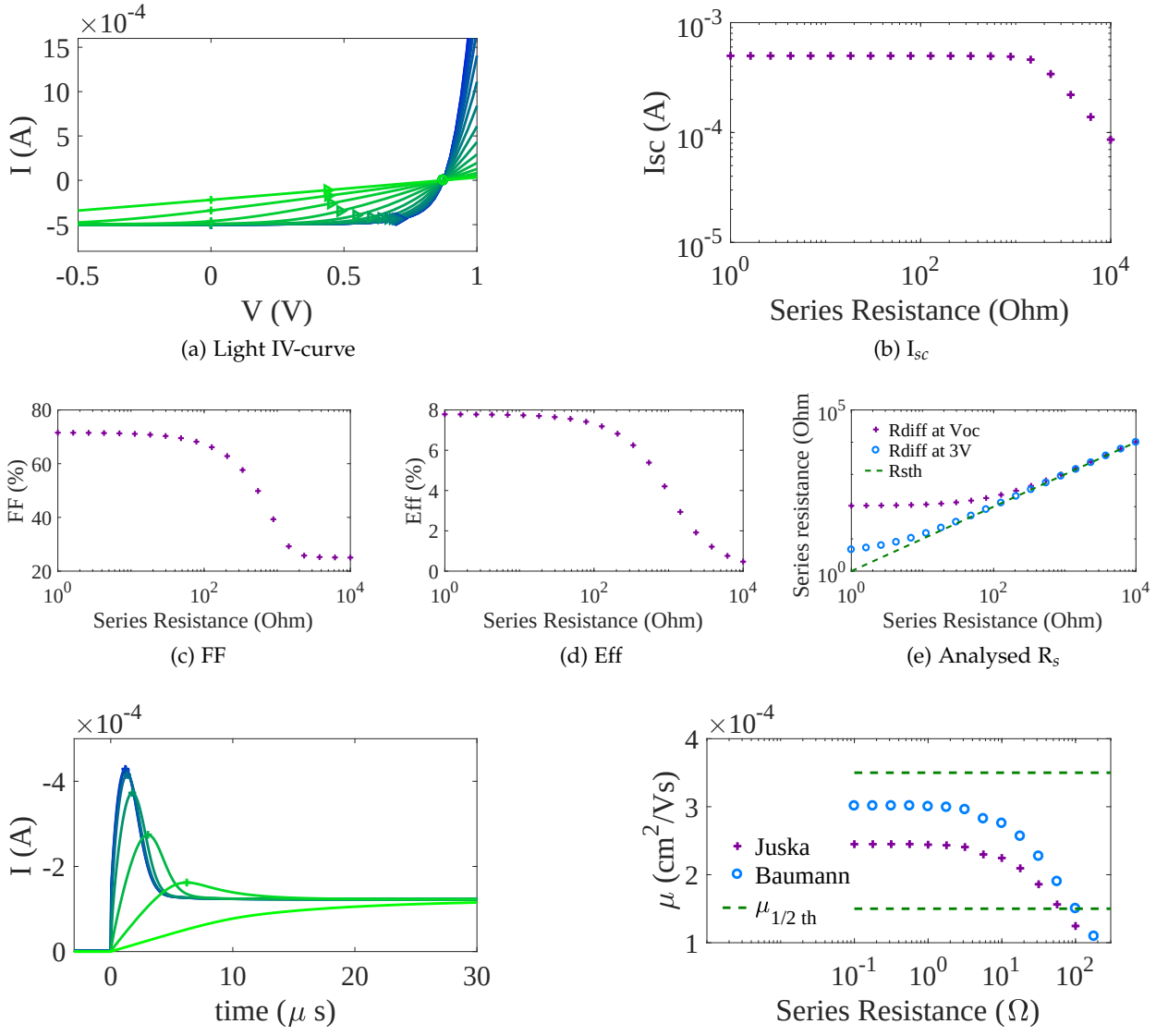

(a) Light IV-curve

(b) I_{sc}

(c) FF

(d) Eff

(e) Analysed R_s

(f) Photo-CELIV current

(g) Photo-CELIV mobility

Figure C.1: Simulations of various experiments with varied series resistance. The series resistance was varied from 1 Ω (blue curve) to 10000 Ω (green curve).

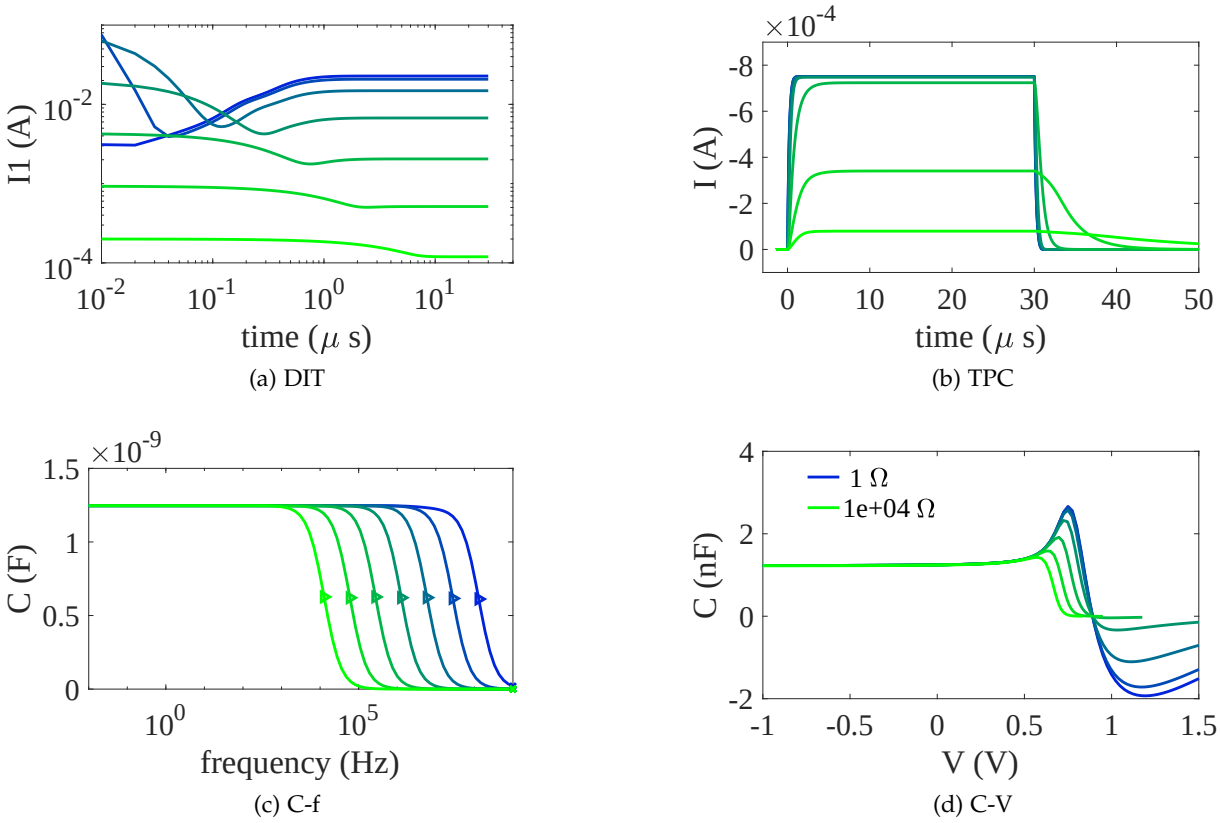

(a) DIT (b) TPC

(c) C-f (d) C-V

Figure C.2: Simulations of various experiments with varied series resistance. The series resistance was varied from 1 Ω (blue curve) to 10000 Ω (green curve).

C.2 PARALLEL RESISTANCE

The parallel resistance of an ideal solar cell is infinite. In real devices, there can however be shunts, for example due to too thin layers on top of the rough ITO electrode, leading to parallel current contributions, as discussed in Section 2.1.1.

The contribution of shunts is basically symmetric for positive and negative voltages, and adds up to the default device current (see Eq. 2.3). Therefore the device becomes nonblocking in reverse bias, while in forward only strong shunts have an effect.

In case of reverse injection due to inappropriate contact barriers the parallel current is not linear but represents a diode characteristic. The qualitative implications shown below also hold for this case.

The light IV-curve shows a strong effect of a shunt on the fillfactor, quickly leading to a linear curve. For very low parallel resistances also the open-circuit voltage is affected.

The parallel resistance in an equivalent circuit representation of the device is often determined as the differential resistance at short-circuit. This is, however, only true for very strong shunting, while for high parallel resistances they cannot be determined reliably. In real measurements the current resolution further impedes the determination of high parallel resistances.

The CELIV experiments do not show the constant displacement current any more when a shunting problem is present. The parallel current just follows the voltage ramp and adds up to the device current, thus the photo-CELIV peak can be affected. Also the plateau may be impossible to determine.

For TPV measurements the device is forced to the open-circuit condition by using a high measurement resistor ($> 1\ \mathrm{M}\Omega$). The maximum TPV lifetime that can be measured is then limited by that resistor, and corresponds to the RC time of the measurement circuit.

However, even with an ideal measurement setup the decay which is often used to investigate the recombination dynamics, is directly related to the parallel resistance of the device. Thus, the decay time constant is approximately the R_pC time, and only during the initial decay the recombination dynamics are observed. Interestingly, the rise of the open-circuit voltage is nearly unaffected.

In impedance measurements the influence on the capacitance in negligible. The parallel resistance is, however, seen well in the conductance signal and may be extracted as its low-frequency limit.

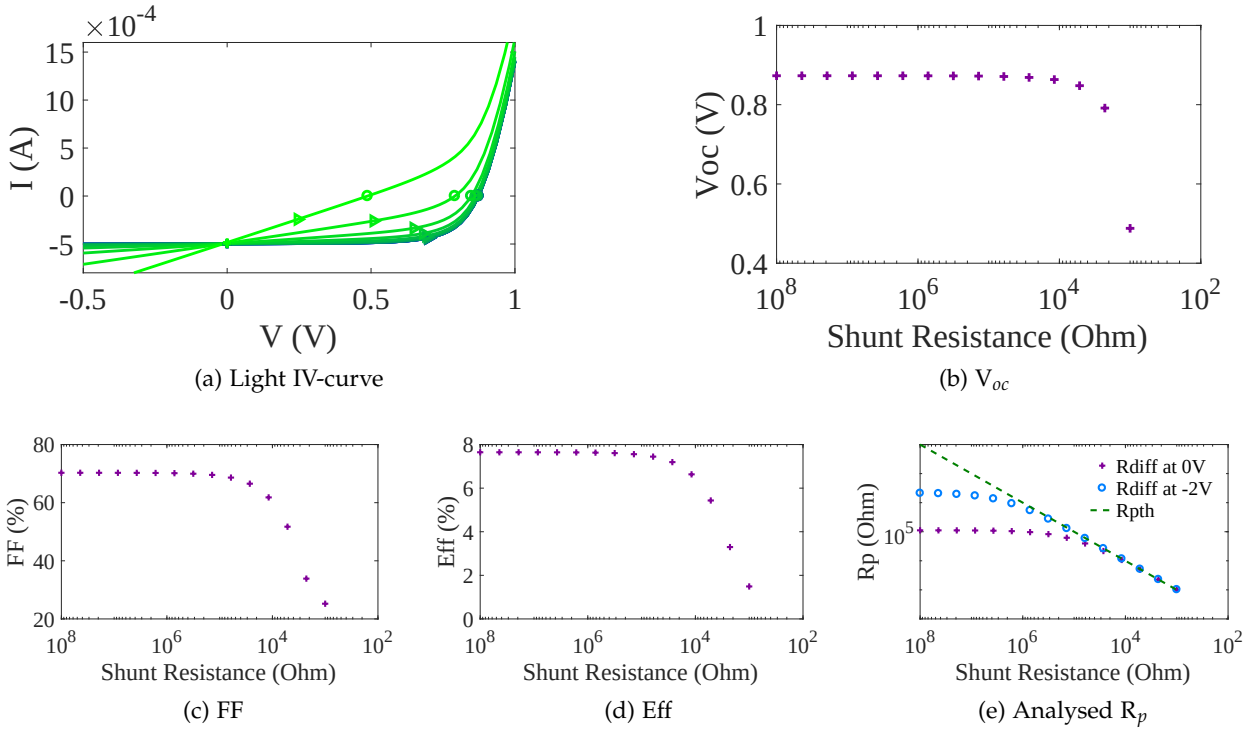

(a) Light IV-curve (b) V_{oc}

(c) FF (d) Eff (e) Analysed R_p

Figure C.3: Simulations of various experiments with varied parallel resistance. The parallel resistance was varied from 10^8 Ω (blue curve) to 10^3 Ω (green curve).

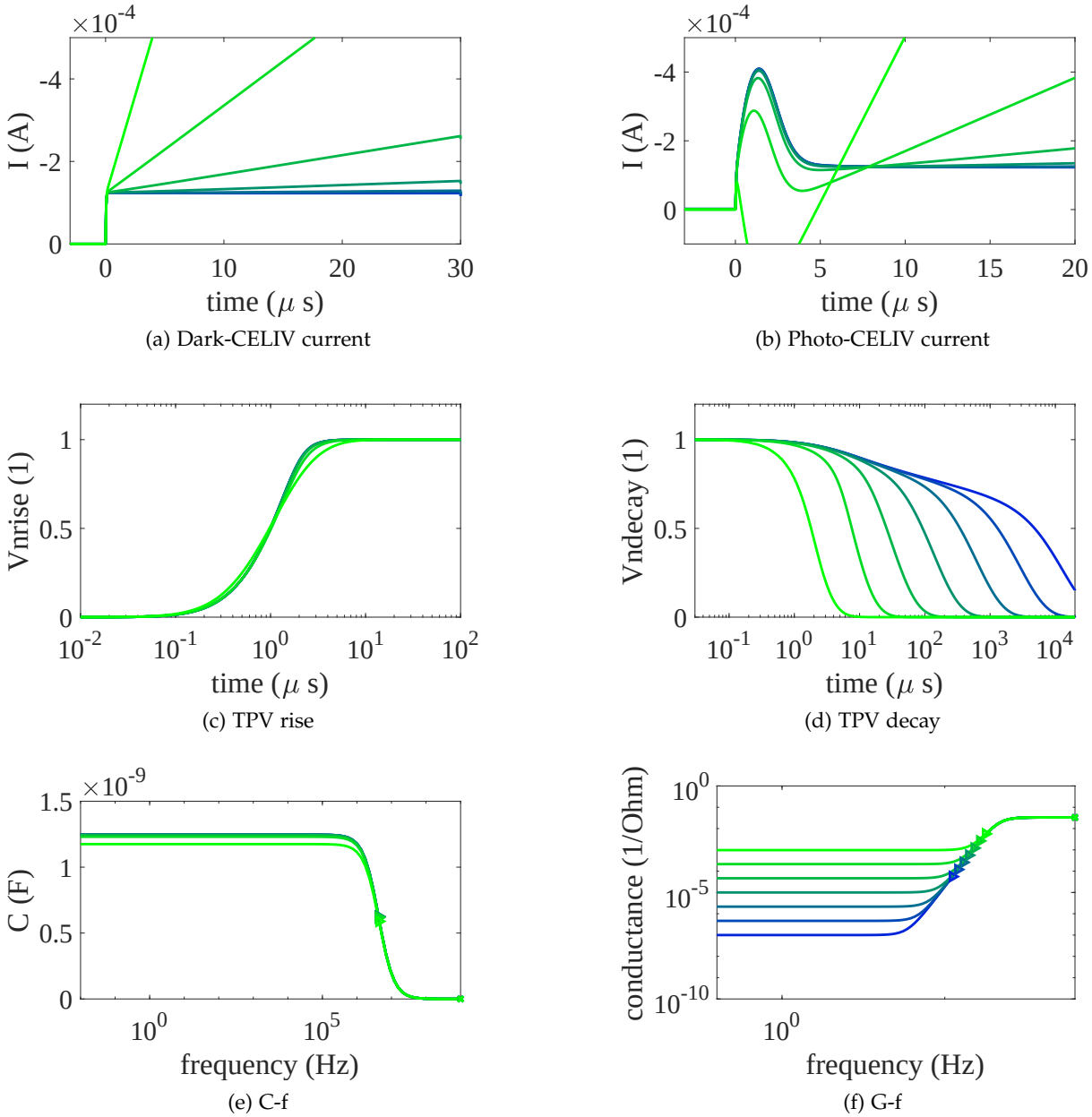

(a) Dark-CELIV current

(b) Photo-CELIV current

(c) TPV rise

(d) TPV decay

(e) C-f

(f) G-f

Figure C.4: Simulations of various experiments with varied parallel resistance. The parallel resistance was varied from 10^8 Ω (blue curve) to 10^3 Ω (green curve).

C.3 LIGHT INTENSITY

With *Paios* it is easy to sweep the incident light intensity over several orders of magnitude. This allows us to compare actual data to the qualitative simulation results shown below.

In the most simple device model (constant mobilities, no traps or doping), the short-circuit current is directly proportional to the illumination intensity. Only at very high intensities it starts to saturate due to space-charge effects and field screening. The open-circuit voltage nicely follows the expected logarithmic dependence on the light intensity. The fillfactor, however, is being strongly reduced with higher intensities as space-charge and recombination increases and the device behaves more like a resistor. This leads to the observed peak of the efficiency at an intensity below 1 sun. The actual value depends on various parameters, but the peak is always found.

The photo-CELIV peak increases with intensity, however also shows a saturation. The same is true for the extracted charge density. The reason for this is that the maximum number of charges extracted per time is limited by the device capacitance, $Q_{max} = C \cdot V$. While the peak position only slightly varies, the determined apparent mobility decreases with increasing intensity over more than one order of magnitude.

The TPV rise becomes faster with higher intensities, and also the decay accelerates. The reason for this may be that more charges for bimolecular recombination are available.

The impedance simulations do not show clear trends and are strongly dependent on other parameters such as recombination efficiency. The capacitance plateau usually increases first with increasing illumination and then decreases again. The increase is due to the space-charge leading to a lower effective thickness, while the decrease is related to recombination.

In the capacitance-voltage experiment with illumination several effects can be observed and depend on the recombination efficiency. The peak position can shift, the peak broadens and a Mott-Schottky behaviour can be sometimes observed. However, sometimes also a second peak at lower voltages is generated, and above the built-in the negative capacitance effect is influenced. Due to its sensitivity on various parameters, the CV with light experiment is complicated to understand, cowever, combined with simulation it may be a very useful technique.

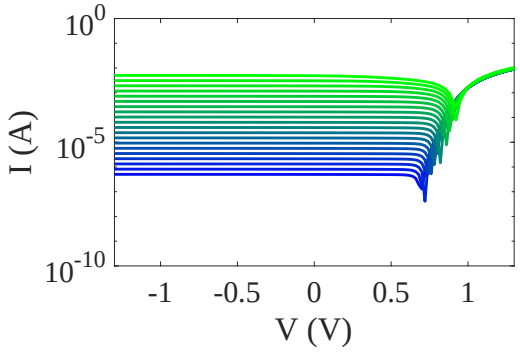

(a) Light IV-curve (logarithmic)

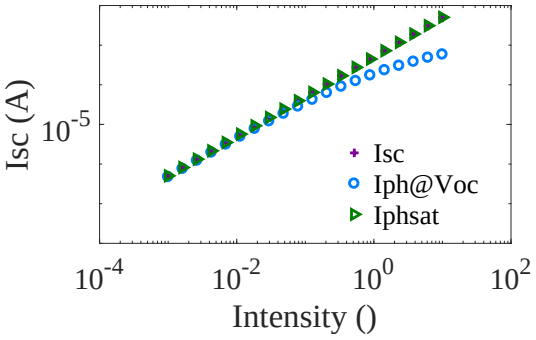

(b) I_{sc}

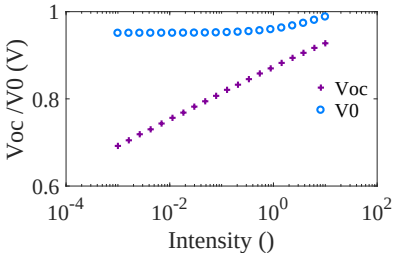

(c) V_{oc}

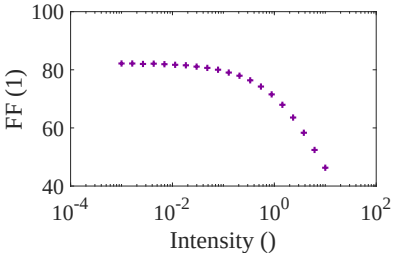

(d) FF

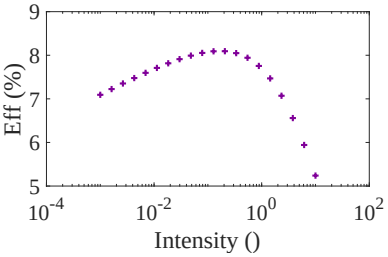

(e) Eff

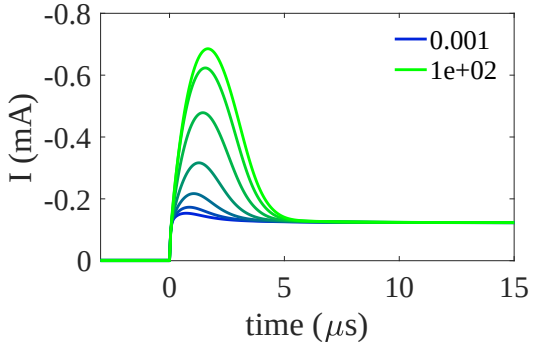

(f) Photo-CELIV current

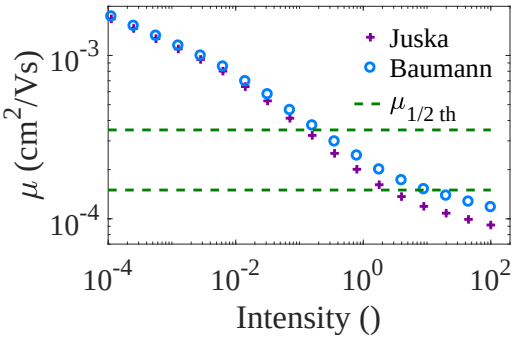

(g) Photo-CELIV mobility

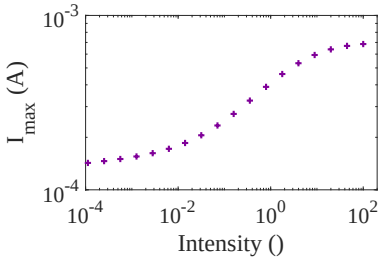

(h) Photo-CELIV current maximum

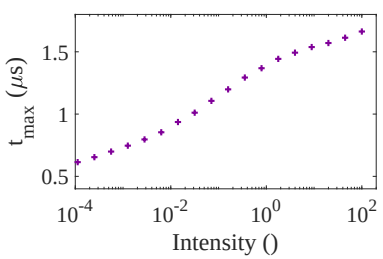

(i) Photo-CELIV t_{max}

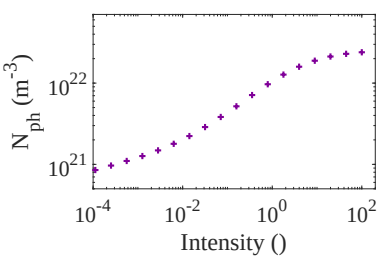

(j) Photo-CELIV charge

Figure C.5: Simulations of various experiments with varied illumination intensity. The illumination intensity varied from 10^{-3} (blue curve) to 10^{2} (green curve).

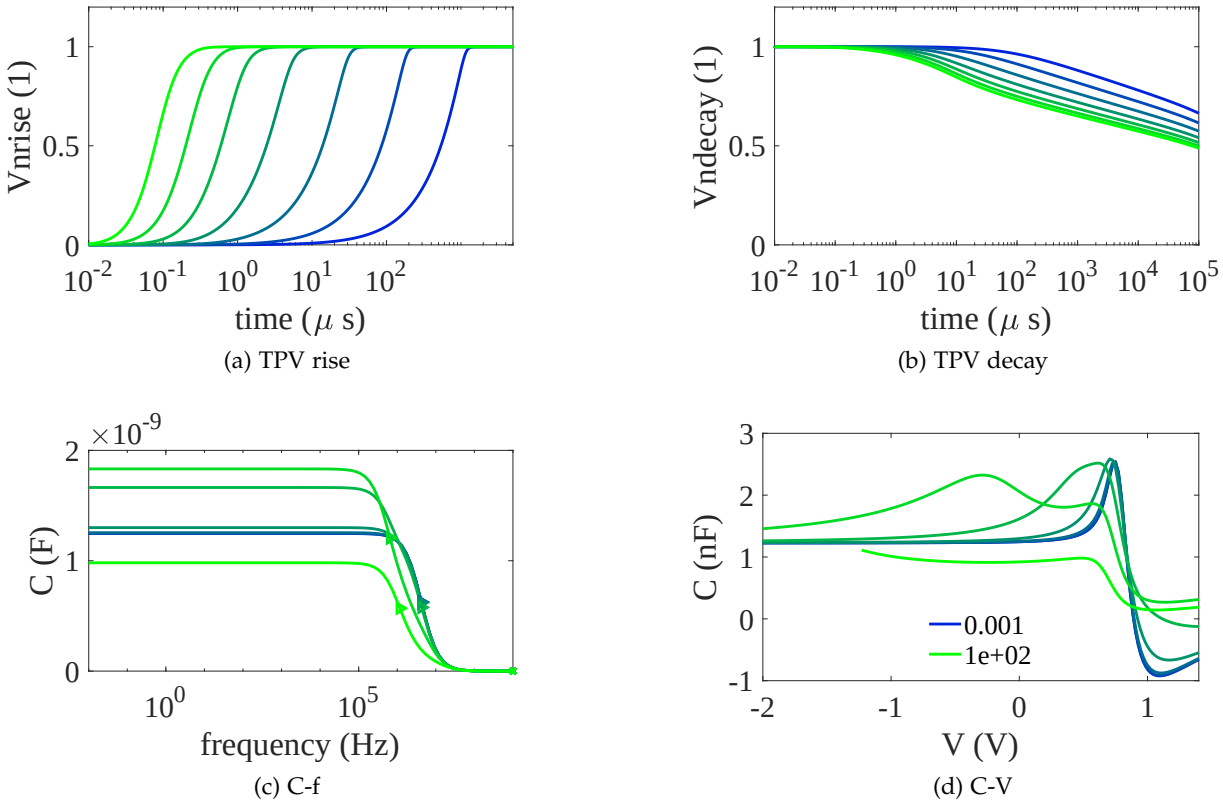

(a) TPV rise

(b) TPV decay

(c) C-f

(d) C-V

Figure C.6: Simulations of various experiments with varied illumination intensity. The illumination intensity varied from 10^{-3} (blue curve) to 10^{2} (green curve).

C.4 RECOMBINATION EFFICIENCY

For these simulation studies we only employ bimolecular recombination according to Eq. 3.15, and neglect traps and Shockley-Read-Hall recombination. The prefactor γ is en empirical parameter taking into account that in many BHJ materials the Langevin recombination efficiency is reduced. Here this prefactor was varied.

The recombination efficiency mainly affects the fillfactor of the IV-curve. Full Langevin recombination, however, also strongly reduces short-circuit current and open-circuit voltage.

In photo-CELIV the peak height is directly affected by the recombination. Obviously with CELIV only charges can be extracted that have not recombined yet. Therefore faster ramps will extract higher charge densities, and the recombination dynamics can be well investigated by time-delayed CELIV and charge extraction techniques.

The apparent mobility analysed from the peak saturates at very low and very high recombination efficiencies. For $\gamma = 1$ here the expected value is nicely observed. However, as seen above, also light intensity and ramp rate as well as the actual mobilities influence the accuracy of this value.

The TPV rise and decay dynamics are hardly affected by the recombination efficiency, which is somehow unexpected, as one would think a higher recombination prefactor would lead to a faster open-circuit voltage decay.

The capacitance-frequency at 0 V does not show any effect, as the device is empty. Here we show the C-f at forward bias with varied recombination efficiency. For decreased recombination a peak is observed and the low-frequency capacitance becomes negative.

The corresponding behaviour is observed in the CV plot above built-in. Furthermore the height of the peak decreases with increasing recombination and the peak also slightly shifts.

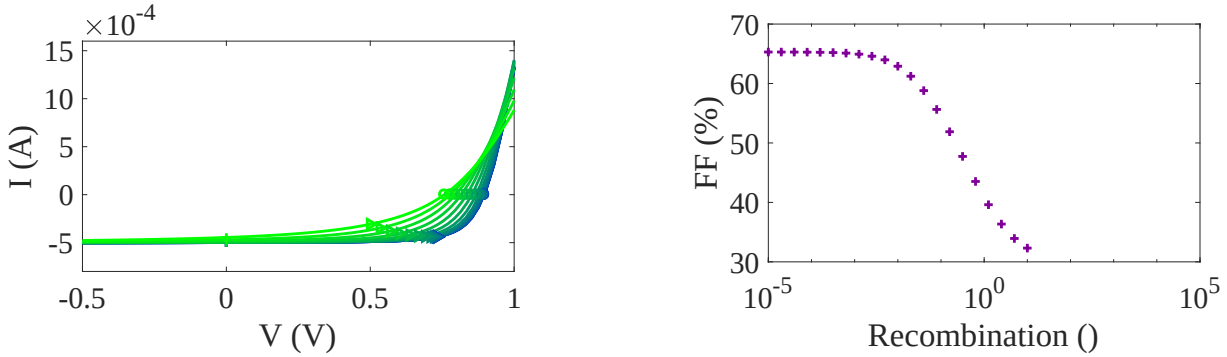

(a) Light IV-curve

(b) FF

Figure C.7: Simulations of various experiments with varied recombination efficiency. The recombination prefactor was varied from 10^{-4} (blue curve) to 1 (green curve).

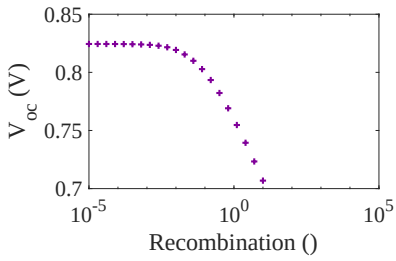

(a) V_{oc}

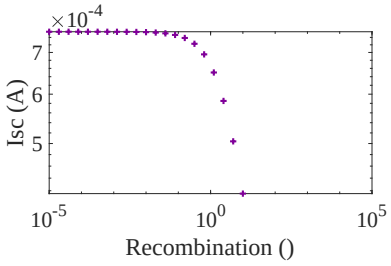

(b) I_{sc}

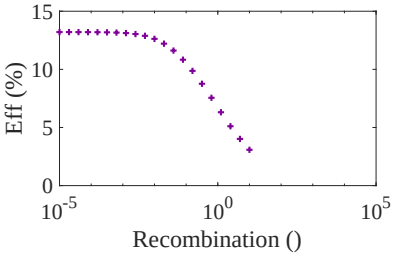

(c) Eff

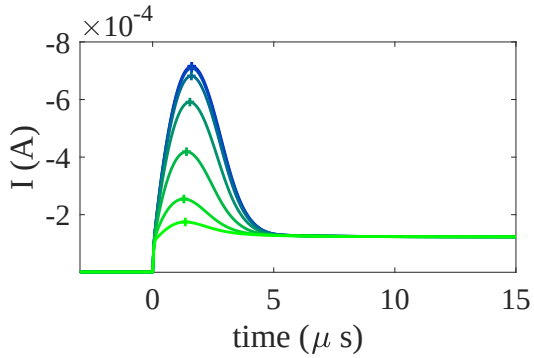

(d) Photo-CELIV current

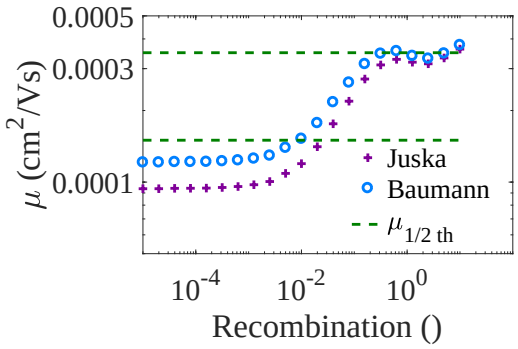

(e) Photo-CELIV mobility

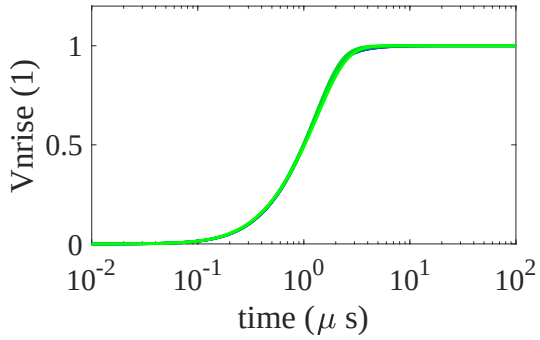

(f) TPV rise

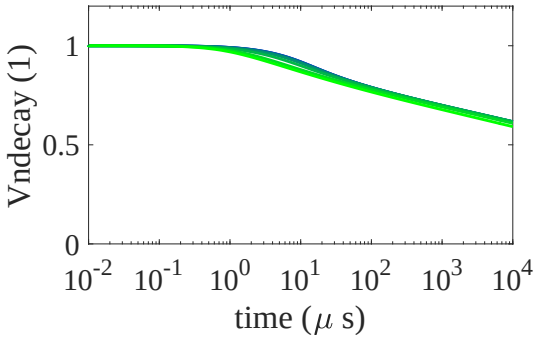

(g) TPV decay

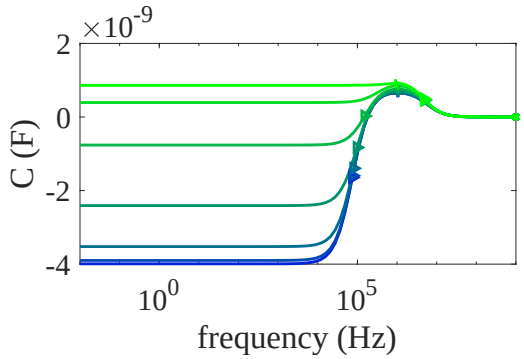

(h) C-f

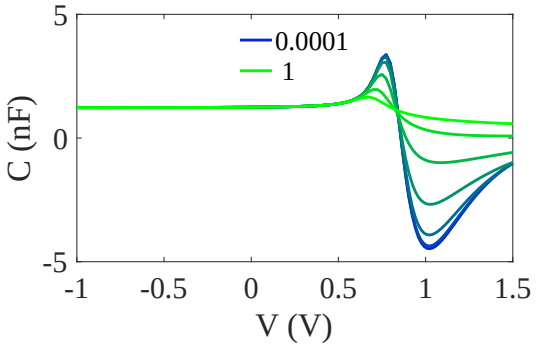

(i) C-V

Figure C.8: Simulations of various experiments with varied recombination efficiency. The recombination prefactor was varied from 10^{-4} (blue curve) to 1 (green curve).

C.5 MOBILITY

The charge carrier mobility is one of the most important parameters and influences all of the experiments. In bipolar devices two different mobilities, and also possible field-, temperature-, and density dependences complicate the determination of this parameter from experiments.

Here we choose only constant mobilities and set a ratio between electrons and holes: $\mu_e = 0.6\mu_h$. Then we sweep both mobilities at the same time with this ratio being fixed. In case of very imbalanced mobilities the simulations below can look very different.

The IV-curves are strongly affected by the mobilities, as both drift and diffusion currents directly depend on them. With increased mobilities the injection currents increase and the short-circuit current and fillfactor strongly improve, before saturating. The open-circuit voltage decreases slightly, yet the efficiency still improves with higher mobility.

The photo-CELIV technique which was developed to characterize the mobility shows a direct correlation of the peak time with mobility, and the determined values are indeed between the two input parameters. Only for high mobilities the peak becomes smaller due to enhanced recombination, and as the peak height also goes in the mobility formula, the extracted parameters tend to be too high. However, as mentioned before, such a good agreement between input and analysed value can usually not be expected, and depends on a range of parameters.

The transient photocurrent rise and decay as well as the TPV rise also show a direct relation with the input mobility, and they might be used as well to determine the mobility. Yet a high series resistance as well as overshoots and trapping effects will surely complicate such an analysis.

In the DIT the steady-state injection current is governed by the mobilities, yet also the dynamics of the injection onset and related characteristics are connected to the mobility. It is however not clear for bipolar devices whether the observed minimum or inflection point can be used for parameter extraction.

The influence of the mobilities on the capacitance-voltage is unclear. It seems that for low mobilities the injection is harmed and the peak becomes lower, whereas for very high mobilities also a slight shift of the peak is observed. Again, many other parameters also influence this plot and a clear statement is not possible.

The capacitance-frequency at forward bias shows clear signatures that could be used to calculate the mobility. This technique is indeed employed in unipolar devices to analyse mobility from the negative differential susceptance (which is a postprocessed C-f curve). However, in real measurements on bipolar devices, is it unusual to observe such a behaviour.

Finally, the IMPS imaginary part shows a peak position which is clearly linked to the mobility, and we are confident that this can indeed be used to determine a reliable value.

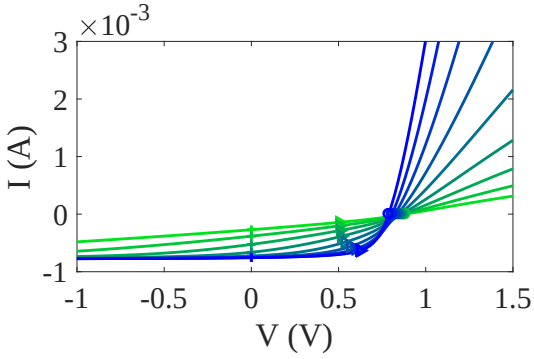

(a) Light IV-curve

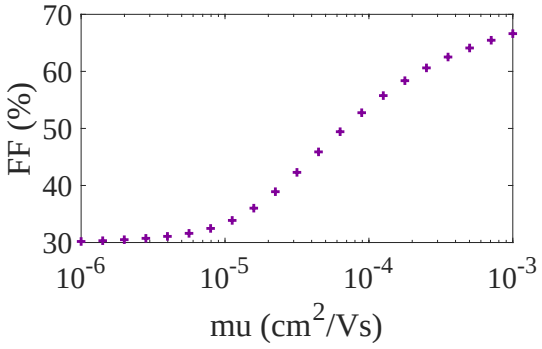

(b) FF

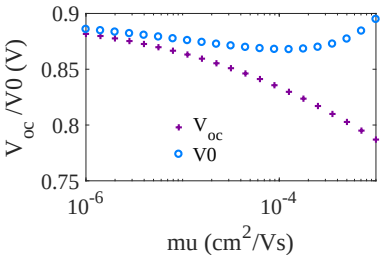

(c) V_{oc}

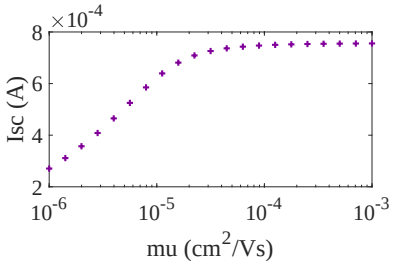

(d) I_{sc}

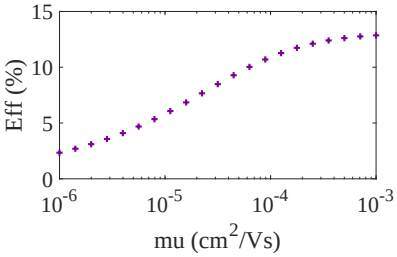

(e) Eff

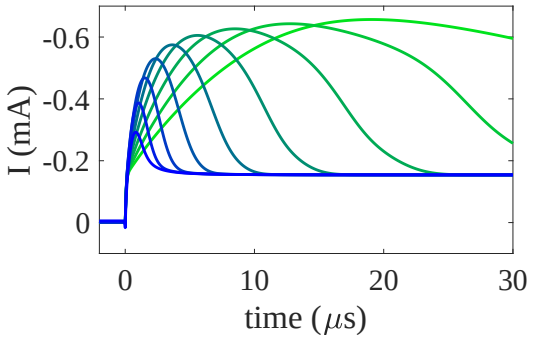

(f) Photo-CELIV current

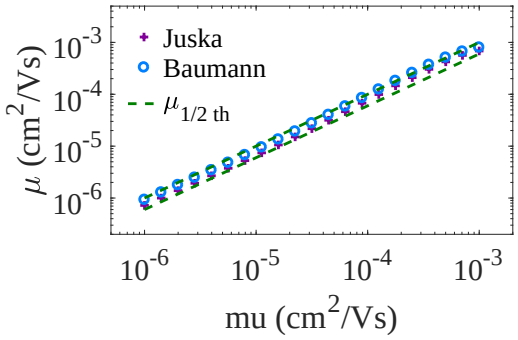

(g) Photo-CELIV mobility

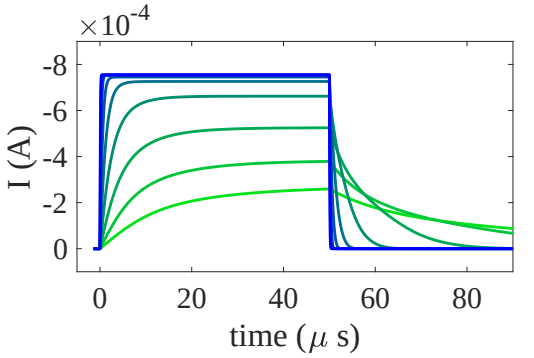

(h) TPC

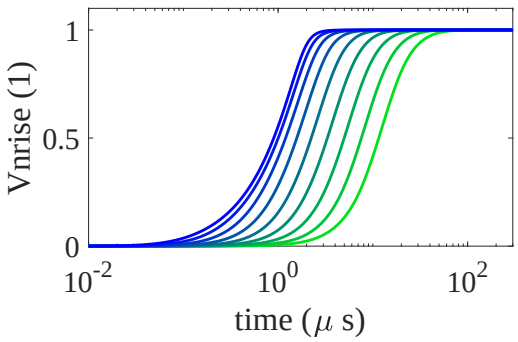

(i) TPV rise

Figure C.9: Simulations of various experiments with varied mobility. The hole mobility was varied from 10^{-6} cm^2/Vs (blue curve) to 10^{-3} cm^2/Vs (green curve).

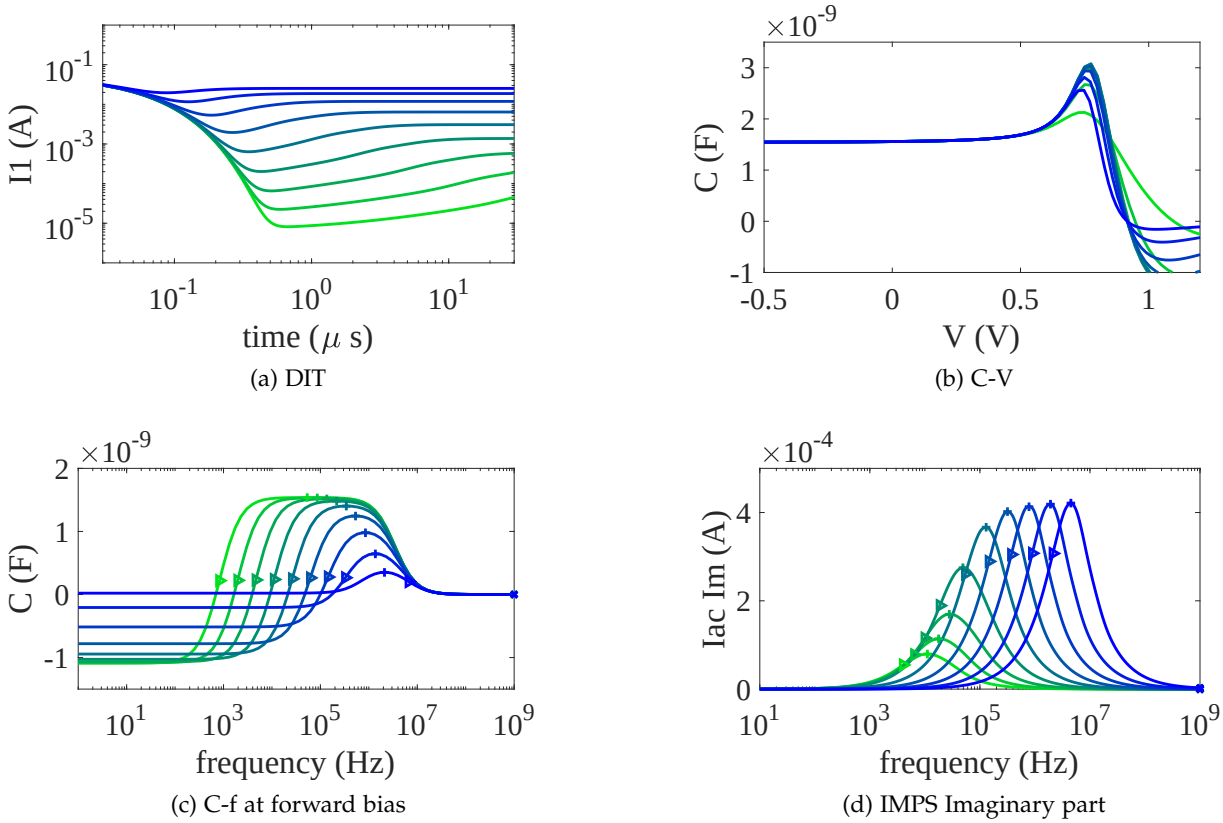

(a) DIT

(b) C-V

(c) C-f at forward bias

(d) IMPS Imaginary part

Figure C.10: Simulations of various experiments with varied mobility. The hole mobility was varied from 10^{-6} cm^2/Vs (blue curve) to 10^{-3} cm^2/Vs (green curve).

C.6 DOPING

Doping is introduced in the simulation as an immobile homogeneous charge density. Then, to ensure equilibrium and charge neutrality, mobile carriers of the opposite charge are injected. As these charges are mobile they can be moved and extracted, leading to the specific signatures of doping. As shown in Fig. 11.8 a space-charge zone is formed, where the field is nearly zero, and at the interface a depletion zone with a strong field is observed.

In the IV-curve the short-circuit current and fillfactor (and also slightly the open-circuit voltage) are reduced by increasing doping density. The photocurrent is field-dependent, as a reverse bias can increase the depletion width and thereby improve charge extraction.
In the dark IV-curve a slight increase of the current may be observed, as the field at the contact is enhanced.

The clearest signature of doping is found in the dark-CELIV current, where the induced counter-charges are extracted as a peak. In photo-CELIV they superimpose on the original photo-CELIV current, leading to a shift of the peak and a more dispersive shape. For low ramp-rates the dark-CELIV current corresponds to a purely capacitive signal and Mott-Schottky analysis can be applied.

The DLTS response is slowed down strongly, which corresponds to an increased RC time. The RC time is increased due to the capacitance which is larger as a thinner depletion zone contributes to it. This is also found in the capacitance-frequency plot.

The capacitance-voltage signal can be used for Mott-Schottky analysis, which allows to determine the doping density. There are some limits on the accuracy of the determined values, but the fact that the Mott-Schottky plot shows a straight line is always a sign for a large space charge region.

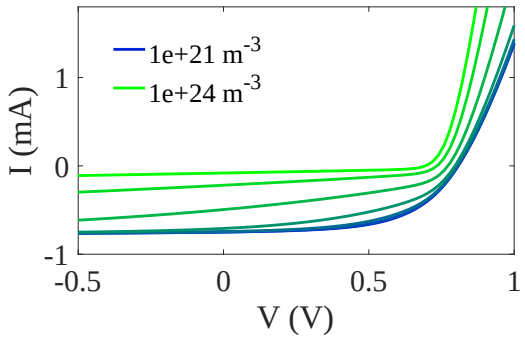

(a) Light IV-curve

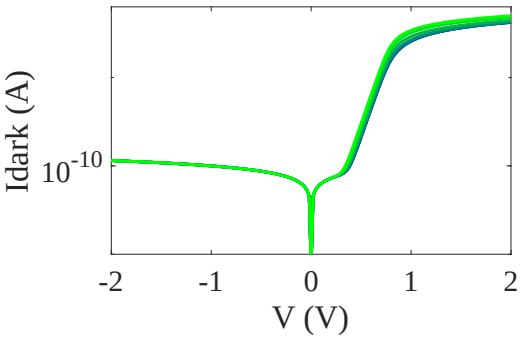

(b) Dark IV-curve

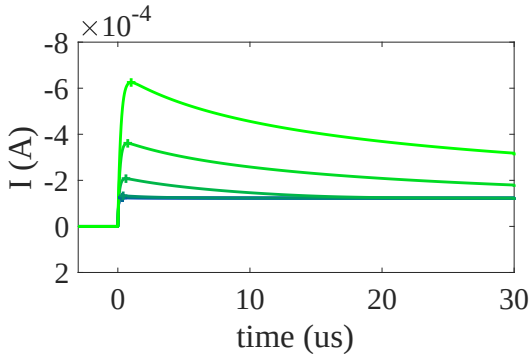

(c) Dark-CELIV current

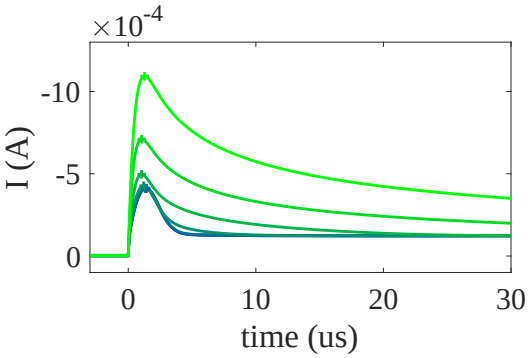

(d) Photo-CELIV current

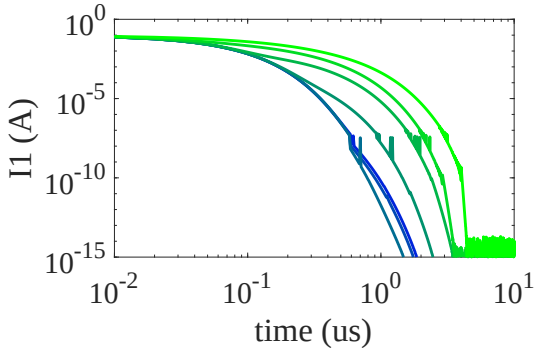

(e) DLTS

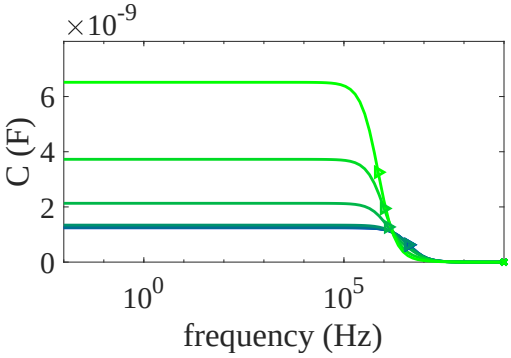

(f) C-f

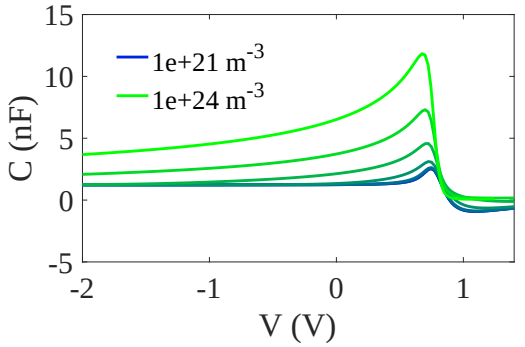

(g) CV

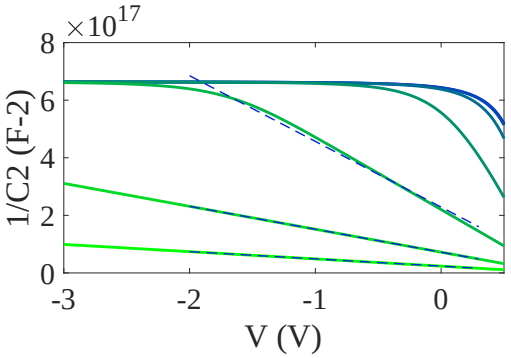

(h) Mott-Schottky plot with fit

Figure C.11: Simulations of various experiments with varied doping density. The doping density was varied from 10^{21} m^{-3} (blue curve) to 10^{24} m^{-3} (green curve).

BIBLIOGRAPHY

[1] A. Pochettino and A. Sella. "Photo-electric properties of anthracene". *Lincei Rendic* 15 (1906), pp. 171–179 (cited on p. 3).

[2] M. Volmer. "Die verschiedenen lichtelektrischen Erscheinungen am Anthracen, ihre Beziehungen zueinander, zur Fluoreszenz und Dianthracenbildung". *Annalen der Physik* 345 (1913), pp. 775–796. DOI: 10.1002/andp.19133450411 (cited on p. 3).

[3] H. Spanggaard and F. C. Krebs. "A brief history of the development of organic and polymeric photovoltaics". *Solar Energy Materials & Solar Cells* 83 (2004), pp. 125–146. DOI: 10.1016/j.solmat.2004.02.021 (cited on p. 3).

[4] H. Kallmann and M. Pope. "Photovoltaic Effect in Organic Crystals". *The Journal of Chemical Physics* 30 (1959), pp. 585–586. DOI: 10.1063/1.1729992 (cited on p. 3).

[5] D. Kearns and M. Calvin. "Photovoltaic Effect and Photoconductivity in Laminated Organic Systems". *The Journal of Chemical Physics* 29 (1958), pp. 950–951. DOI: 10.1063/1.1744619 (cited on p. 3).

[6] A Bernanose. "Electroluminescence of organic compounds". *British Journal of Applied Physics* 6 (1955), S54–S55. DOI: 10.1088/0508-3443/6/s4/319 (cited on p. 3).

[7] M. Pope, H. P. Kallmann, and P. Magnante. "Electroluminescence in Organic Crystals". *The Journal of Chemical Physics* 38 (1963), pp. 2042–2043. DOI: 10.1063/1.1733929 (cited on pp. 3, 4).

[8] C. K. Chiang, C. R. Fincher, Y. W. Park, A. J. Heeger, H. Shirakawa, E. J. Louis, S. C. Gau, and A. G. MacDiarmid. "Electrical Conductivity in Doped Polyacetylene". *Physical Review Letters* 39 (1977), pp. 1098–1101. DOI: 10.1103/PhysRevLett.39.1098 (cited on p. 3).

[9] H. Shirakawa, E. J. Louis, A. G. MacDiarmid, C. K. Chiang, and A. J. Heeger. "Synthesis of electrically conducting organic polymers: halogen derivatives of polyacetylene, (CH) x". *Journal of the Chemical Society, Chemical Communications* 24 (1977), pp. 578–580. DOI: 10.1039/c39770000578 (cited on p. 3).

[10] C. W. Tang. "Two-layer organic photovoltaic cell". *Applied Physics Letters* 48 (1986), pp. 183–185. DOI: 10.1063/1.96937 (cited on pp. 3, 7).

[11] C. W. Tang and S. A. Van Slyke. "Organic electroluminescent diodes". *Applied Physics Letters* 51 (1987), pp. 913–915. DOI: 10.1063/1.98799 (cited on pp. 3, 6, 41).

[12] F. Ebisawa, T. Kurokawa, and S. Nara. "Electrical properties of polyacetylene/polysiloxane interface". *Journal of Applied Physics* 54 (1983), pp. 3255–3259. DOI: 10.1063/1.332488 (cited on p. 3).

[13] C. Clarisse, M. Riou, M. Gauneau, and M. le Contellec. "Field-effect transistor with diphthalocyanine thin film". *Electronics Letters* 24 (1988), pp. 674–675. DOI: 10.1049/el:19880456 (cited on p. 3).

[14] G. Horowitz. "Organic Field-Effect Transistors". *Advanced Materials* 10 (1998), pp. 365–377. DOI: 10.1002/(sici)1521-4095(199803)10:5<365::aid-adma365>3.0.co;2-u (cited on pp. 3, 47).

[15] J. H. Burroughes, D. D. C. Bradley, A. R. Brown, R. N. Marks, K. Mackay, R. H. Friend, P. L. Burns, and A. B. Holmes. "Light-emitting diodes based on conjugated polymers". *Nature* 347 (1990), pp. 539–541. DOI: 10.1038/347539a0 (cited on p. 3).

[16] D. Braun and A. J. Heeger. "Visible light emission from semiconducting polymer diodes". *Applied Physics Letters* 58 (1991), pp. 1982–1984. DOI: 10.1063/1.105039 (cited on p. 3).

[17] M. Hiramoto, H. Fujiwara, and M. Yokoyama. "Three-layered organic solar cell with a photoactive interlayer of codeposited pigments". *Applied Physics Letters* 58 (1991), pp. 1062–1064. DOI: 10.1063/1.104423 (cited on p. 3).

[18] G. Yu, J. Gao, J. C. Hummelen, F. Wudl, and A. J. Heeger. "Polymer Photovoltaic Cells: Enhanced Efficiencies via a Network of Internal Donor-Acceptor Heterojunctions". *Science* 270 (1995), pp. 1789–1791. DOI: 10.1126/science.270.5243.1789 (cited on pp. 3, 7).

[19] M. Pfeiffer, A. Beyer, T. Fritz, and K. Leo. "Controlled doping of phthalocyanine layers by cosublimation with acceptor molecules: A systematic Seebeck and conductivity study". *Applied Physics Letters* 73 (1998), pp. 3202–3204. DOI: 10.1063/1.122718 (cited on p. 4).

[20] M Pfeiffer, K Leo, X Zhou, J. Huang, M Hofmann, A Werner, and J Blochwitz-Nimoth. "Doped organic semiconductors: Physics and application in light emitting diodes". *Organic Electronics* 4 (2003), pp. 89–103. DOI: 10.1016/j.orgel.2003.08.004 (cited on p. 4).

[21] T. Tsutsui, E. Aminaka, C. P. Lin, and D. U. Kim. "Extended molecular design concept of molecular materials for electroluminescence: sublimed-dye films, molecularly doped polymers and polymers with chromophores". *Philosophical Transactions of the Royal Society A* 355 (1997), pp. 801–814. DOI: 10.1098/rsta.1997.0045 (cited on pp. 4, 47).

[22] M. A. Baldo, D. F. O'Brien, M. E. Thompson, and S. R. Forrest. "Excitonic singlet-triplet ratio in a semiconducting organic thin film". *Physical Review B* 60 (1999), pp. 14422–14428. DOI: 10.1103/physrevb.60.14422 (cited on p. 4).

[23] M. A. Baldo, S. Lamansky, P. E. Burrows, M. E. Thompson, and S. R. Forrest. "Very high-efficiency green organic light-emitting devices based on electrophosphorescence". *Applied Physics Letters* 75 (1999), pp. 4–6. DOI: 10.1063/1.124258 (cited on p. 4).

[24] M. A. Baldo, D. F. O'Brien, Y. You, A. Shoustikov, S. Sibley, M. E. Thompson, and S. R. Forrest. "Highly efficient phosphorescent emission from organic electroluminescent devices". *Nature* 395 (1998), pp. 151–154. DOI: 10.1038/25954 (cited on p. 4).

[25] X. Yang, D. Neher, D. Hertel, and T. Däubler. "Highly Efficient Single-Layer Polymer Electrophosphorescent Devices". *Advanced Materials* 16 (2004), pp. 161–166. DOI: 10.1002/adma.200305621 (cited on p. 4).

[26] Y. Im, S. Y. Byun, J. H. Kim, D. R. Lee, C. S. Oh, K. S. Yook, and J. Y. Lee. "Recent Progress in High-Efficiency Blue-Light-Emitting Materials for Organic Light-Emitting Diodes". *Advanced Functional Materials* 27 (2017), p. 1603007. DOI: 10.1002/adfm.201603007 (cited on pp. 4, 6).

[27] H. Kaji, H. Suzuki, T. Fukushima, K. Shizu, K. Suzuki, S. Kubo, T. Komino, H. Oiwa, F. Suzuki, A. Wakamiya, Y. Murata, and C. Adachi. "Purely organic electroluminescent material realizing 100% conversion from electricity to light". *Nature Communications* 6 (2015), p. 8476. DOI: 10.1038/ncomms9476 (cited on p. 4).

[28] H. Uoyama, K. Goushi, K. Shizu, H. Nomura, and C. Adachi. "Highly efficient organic light-emitting diodes from delayed fluorescence". *Nature* 492 (2012), pp. 234–238. DOI: 10.1038/nature11687 (cited on p. 4).

[29] S. Hirata, Y. Sakai, K. Masui, H. Tanaka, S. Y. Lee, H. Nomura, N. Nakamura, M. Yasumatsu, H. Nakanotani, Q. Zhang, K. Shizu, H. Miyazaki, and C. Adachi. "Highly efficient blue electroluminescence based on thermally activated delayed fluorescence". *Nature Materials* 14 (2014), pp. 330–336. DOI: 10.1038/nmat4154 (cited on p. 4).

[30] S. Reineke. "Organic light-emitting diodes: Phosphorescence meets its match". *Nature Photonics* 8 (2014), pp. 269–270. DOI: 10.1038/nphoton.2014.78 (cited on p. 4).

[31] A. Endo, K. Sato, K. Yoshimura, T. Kai, A. Kawada, H. Miyazaki, and C. Adachi. "Efficient up-conversion of triplet excitons into a singlet state and its application for organic light emitting diodes". *Applied Physics Letters* 98 (2011), p. 083302. DOI: 10.1063/1.3558906 (cited on p. 4).

[32] C. W. Ko and Y. T. Tao. "Bright white organic light-emitting diode". *Applied Physics Letters* 79 (2001), pp. 4234–4236. DOI: 10.1063/1.1425454 (cited on p. 5).

[33] Y. Sun, N. C. Giebink, H. Kanno, B. Ma, M. E. Thompson, and S. R. Forrest. "Management of singlet and triplet excitons for efficient white organic light-emitting devices". *Nature* 440 (2006), pp. 908–912. DOI: 10.1038/nature04645 (cited on p. 5).

[34] M. C. Gather, A. Köhnen, and K. Meerholz. "White Organic Light-Emitting Diodes". *Advanced Materials* 23 (2010), pp. 233–248. DOI: 10.1002/adma.201002636 (cited on p. 5).

[35] S. Reineke, M. Thomschke, B. Lüssem, and K. Leo. "White organic light-emitting diodes: Status and perspective". *Reviews of Modern Physics* 85 (2013), pp. 1245–1293. DOI: 10.1103/RevModPhys.85.1245 (cited on p. 5).

[36] T. Tsujimura, K. Furukawa, H. Ii, H. Kashiwagi, M. Miyoshi, S. Mano, H. Araki, and A. Ezaki. "Commercialization of World's First all-phosphorescent OLED Product for Lighting Application". *SID Symposium Digest of Technical Papers* 43 (2012), pp. 605–609. DOI: 10.1002/j.2168-0159.2012.tb05854.x (cited on p. 5).

[37] S. Kirchmeyer. "The OE-A roadmap for organic and printed electronics: creating a guidepost to complex interlinked technologies, applications and markets". *Translational Materials Research* 3 (2016), p. 010301. DOI: 10.1088/2053-1613/3/1/010301 (cited on pp. 5, 6).

[38] J. Meyer, P. Görrn, and T. Riedl. "Transparent OLED displays". In: *Organic Light-Emitting Diodes (OLEDs)*. Ed. by A. Buckley. Elsevier, 2013. Chap. 17, pp. 512–547. ISBN: 9780857094254 (cited on p. 5).

[39] J. W. Park, D. C. Shin, and S. H. Park. "Large-area OLED lightings and their applications". *Semiconductor Science and Technology* 26 (2011), p. 034002. DOI: 10.1088/0268-1242/26/3/034002 (cited on p. 5).

[40] H. Sasabe and J. Kido. "Development of high performance OLEDs for general lighting". *Journal of Materials Chemistry C* 1 (2013), pp. 1699–1707. DOI: 10.1039/c2tc00584k (cited on p. 5).

[41] Q.-D. Ou, L. Zhou, Y.-Q. Li, S. Shen, J.-D. Chen, C. Li, Q.-K. Wang, S.-T. Lee, and J.-X. Tang. "Extremely Efficient White Organic Light-Emitting Diodes for General Lighting". *Advanced Functional Materials* 24 (2014), pp. 7249–7256. DOI: 10.1002/adfm.201402026 (cited on p. 5).

[42] T. Tsujimura. "OLED Lighting". In: *OLED Displays - Fundamentals and Applications*. John Wiley & Sons, Inc., 2012. Chap. 5, pp. 187–203. ISBN: 9781118140512 (cited on p. 5).

[43] K. Udagawa, H. Sasabe, C. Cai, and J. Kido. "Low-Driving-Voltage Blue Phosphorescent Organic Light-Emitting Devices with External Quantum Efficiency of 30%". *Advanced Materials* 26 (2014), pp. 5062–5066. DOI: 10.1002/adma.201401621 (cited on p. 5).

[44] B. Zhang, G. Tan, C.-S. Lam, B. Yao, C.-L. Ho, L. Liu, Z. Xie, W.-Y. Wong, J. Ding, and L. Wang. "High-Efficiency Single Emissive Layer White Organic Light-Emitting Diodes Based on Solution-Processed Dendritic Host and New Orange-Emitting Iridium Complex". *Advanced Materials* 24 (2012), pp. 1873–1877. DOI: 10.1002/adma.201104758 (cited on p. 5).

[45] X.-D. Zhao, Y.-Q. Li, H.-Y. Xiang, Y.-B. Zhang, J.-D. Chen, L.-H. Xu, and J.-X. Tang. "Efficient Color-Stable Inverted White Organic Light-Emitting Diodes with Outcoupling-Enhanced ZnO Layer". *ACS Applied Materials & Interfaces* 9 (2017), pp. 2767–2775. DOI: 10.1021/acsami.6b14778 (cited on p. 5).

[46] C. Chen, Y. fei Liu, Z. Chen, H. ran Wang, M. zhu Wei, C. Bao, G. Zhang, Y.-H. Gao, C.-L. Liu, W.-L. Jiang, and Y. Duan. "High efficiency warm white phosphorescent organic light emitting devices based on blue light emission from a bipolar mixed-host". *Organic Electronics* 45 (2017), pp. 273–278. DOI: 10.1016/j.orgel.2017.03.027 (cited on p. 5).

[47] P. E. Burrows, V. Bulovic, S. R. Forrest, L. S. Sapochak, D. M. McCarty, and M. E. Thompson. "Reliability and degradation of organic light emitting devices". *Applied Physics Letters* 65 (1994), pp. 2922–2924. DOI: 10.1063/1.112532 (cited on p. 5).

[48] S. A. V. Slyke, C. H. Chen, and C. W. Tang. "Organic electroluminescent devices with improved stability". *Applied Physics Letters* 69 (1996), pp. 2160–2162. DOI: 10.1063/1.117151 (cited on p. 5).

[49] P. E. Burrows, S. R. Forrest, T. X. Zhou, and L. Michalski. "Operating lifetime of phosphorescent organic light emitting devices". *Applied Physics Letters* 76 (2000), pp. 2493–2495. DOI: 10.1063/1.126386 (cited on p. 5).

[50] S. Scholz, D. Kondakov, B. Lüssem, and K. Leo. "Degradation Mechanisms and Reactions in Organic Light-Emitting Devices". *Chemical Reviews* 115 (2015), pp. 8449–8503. DOI: 10.1021/cr400704v (cited on p. 5).

[51] H. Aziz. "Degradation Mechanism of Small Molecule-Based Organic Light-Emitting Devices". *Science* 283 (1999), pp. 1900–1902. DOI: 10.1126/science.283.5409.1900 (cited on pp. 5, 6).

[52] Z. D. Popovic, H. Aziz, N.-X. Hu, A.-M. Hor, and G. Xu. "Long-term degradation mechanism of tris(8-hydroxyquinoline) aluminum-based organic light-emitting devices". *Synthetic Metals* 111-112 (2000), pp. 229–232. DOI: 10.1016/s0379-6779(99)00353-7 (cited on p. 5).

[53] Q. Wang and H. Aziz. "Degradation of Organic/Organic Interfaces in Organic Light-Emitting Devices due to Polaron-Exciton Interactions". *ACS Applied Materials & Interfaces* 5 (2013), pp. 8733–8739. DOI: 10.1021/am402537j (cited on pp. 5, 6).

[54] T. D. Schmidt, D. S. Setz, M. Flämmich, B. J. Scholz, A. Jaeger, C. Diez, D. Michaelis, N. Danz, and W. Brütting. "Degradation induced decrease of the radiative quantum efficiency in organic light-emitting diodes". *Applied Physics Letters* 101 (2012), p. 103301. DOI: 10.1063/1.4749815 (cited on p. 5).

[55] F. So and D. Kondakov. "Degradation Mechanisms in Small-Molecule and Polymer Organic Light-Emitting Diodes". *Advanced Materials* 22 (2010), pp. 3762–3777. DOI: 10.1002/adma.200902624 (cited on p. 5).

[56] D. Y. Kondakov, J. R. Sandifer, C. W. Tang, and R. H. Young. "Nonradiative recombination centers and electrical aging of organic light-emitting diodes: Direct connection between accumulation of trapped charge and luminance loss". *Journal of Applied Physics* 93 (2003), pp. 1108–1119. DOI: 10.1063/1.1531231 (cited on pp. 6, 42, 69).

[57] T.-Y. Chu, Y.-H. Lee, and O.-K. Song. "Effects of interfacial stability between electron transporting layer and cathode on the degradation process of organic light-emitting diodes". *Applied Physics Letters* 91 (2007), p. 223509. DOI: 10.1063/1.2817939 (cited on p. 6).

[58] H. Yamamoto, M. S. Weaver, H. Murata, C. Adachi, and J. J. Brown. "Understanding Extrinsic Degradation in Phosphorescent OLEDs". *SID Symposium Digest of Technical Papers* 45 (2014), pp. 758–761. DOI: 10.1002/j.2168-0159.2014.tb00199.x (cited on p. 6).

[59] S.-C. Chang, G. He, F.-C. Chen, T.-F. Guo, and Y. Yang. "Degradation mechanism of phosphorescent-dye-doped polymer light-emitting diodes". *Applied Physics Letters* 79 (2001), pp. 2088–2090. DOI: 10.1063/1.1404995 (cited on p. 6).

[60] B. W. D'Andrade, S. R. Forrest, and A. B. Chwang. "Operational stability of electrophosphorescent devices containing p and n doped transport layers". *Applied Physics Letters* 83 (2003), pp. 3858–3860. DOI: 10.1063/1.1624473 (cited on p. 6).

[61] W. Song and J. Y. Lee. "Degradation Mechanism and Lifetime Improvement Strategy for Blue Phosphorescent Organic Light-Emitting Diodes". *Advanced Optical Materials* 5 (2017), p. 1600901. DOI: 10.1002/adom.201600901 (cited on p. 6).

[62] S. R. Forrest. "Excitons and the lifetime of organic semiconductor devices". *Philosophical Transactions of the Royal Society A* 373 (2015), pp. 20140320–20140320. DOI: 10.1098/rsta.2014.0320 (cited on p. 6).

[63] Q. Wang, Z. Wu, Y. Zhao, J. Chen, and D. Ma. "Improving lifetime of phosphorescent organic light-emitting diodes by using a non-conjugated hybrid host". *Organic Electronics* 32 (2016), pp. 21–26. DOI: 10.1016/j.orgel.2016.02.006 (cited on p. 6).

[64] M. C. Gather, S. Köber, S. Heun, and K. Meerholz. "Improving the lifetime of white polymeric organic light-emitting diodes". *Journal of Applied Physics* 106 (2009), p. 024506. DOI: 10.1063/1.3176502 (cited on p. 6).

[65] D. P.-K. Tsang, T. Matsushima, and C. Adachi. "Operational stability enhancement in organic light-emitting diodes with ultrathin Liq interlayers". *Scientific Reports* 6 (2016), p. 22463. DOI: 10.1038/srep22463 (cited on p. 6).

[66] H. Fujimoto, M. Yahiro, S. Yukiwaki, K. Kusuhara, N. Nakamura, T. Suekane, H. Wei, K. Imanishi, K. Inada, and C. Adachi. "Influence of material impurities in the hole-blocking layer on the lifetime of organic light-emitting diodes". *Applied Physics Letters* 109 (2016), p. 243302. DOI: 10.1063/1.4972055 (cited on p. 6).

[67] H. Z. Siboni and H. Aziz. "The influence of the hole blocking layers on the electroluminescence stability of phosphorescent organic light emitting devices". *Organic Electronics* 12 (2011), pp. 2056–2060. DOI: 10.1016/j.orgel.2011.08.023 (cited on p. 6).

[68] B. M. Schaer, F. Nüesch, D. Berner, W. Leo, and L. Zuppiroli. "Water Vapor and Oxygen Degradation Mechanisms in Organic Light Emitting Diodes". *Advanced Functional Materials* 11 (2001), pp. 116–121. DOI: 10.1002/1616-3028(200104)11:2<116::aid-adfm116>3.3.co;2-2 (cited on pp. 6, 11).

[69] L. M. Do, E. M. Han, Y. Niidome, M. Fujihira, T. Kanno, S. Yoshida, A. Maeda, and A. J. Ikushima. "Observation of degradation processes of Al electrodes in organic electroluminescence devices by electroluminescence microscopy, atomic force microscopy, scanning electron microscopy, and Auger electron spectroscopy". *Journal of Applied Physics* 76 (1994), pp. 5118–5121. DOI: 10.1063/1.357224 (cited on p. 6).

[70] J. McElvain, H. Antoniadis, M. R. Hueschen, J. N. Miller, D. M. Roitman, J. R. Sheats, and R. L. Moon. "Formation and growth of black spots in organic light-emitting diodes". *Journal of Applied Physics* 80 (1996), pp. 6002–6007. DOI: 10.1063/1.363598 (cited on p. 6).

[71] S. F. Lim, L. Ke, W. Wang, and S. J. Chua. "Correlation between dark spot growth and pinhole size in organic light-emitting diodes". *Applied Physics Letters* 78 (2001), pp. 2116–2118. DOI: 10.1063/1.1364658 (cited on pp. 6, 95).

[72] S.-C. Luo, H.-H. Chung, E. T. Pashuck, E. P. Douglas, and P. H. Holloway. "Formation of bubbles on electrical contacts to polymer light-emitting diode devices". *Thin Solid Films* 478 (2005), pp. 326–331. DOI: 10.1016/j.tsf.2004.10.039 (cited on p. 6).

[73] L. S. Liao, J. He, X. Zhou, M. Lu, Z. H. Xiong, Z. B. Deng, X. Y. Hou, and S. T. Lee. "Bubble formation in organic light-emitting diodes". *Journal of Applied Physics* 88 (2000), pp. 2386–2390. DOI: 10.1063/1.1286009 (cited on p. 6).

[74] W. Wang, S. F. Lim, and S. J. Chua. "Bubble formation and growth in organic light-emitting diodes composed of a polymeric emitter and a calcium cathode". *Journal of Applied Physics* 91 (2002), pp. 5712–5715. DOI: 10.1063/1.1467395 (cited on p. 6).

[75] R. S. Kumar, M. Auch, E. Ou, G. Ewald, and C. S. Jin. "Low moisture permeation measurement through polymer substrates for organic light emitting devices". *Thin Solid Films* 417 (2002), pp. 120–126. DOI: 10.1016/s0040-6090(02)00584-9 (cited on p. 6).

[76] L. Wang, C. Ruan, M. Li, J. Zou, H. Tao, J. Peng, and M. Xu. "Enhanced moisture barrier performance for ALD-encapsulated OLEDs by introducing an organic protective layer". *Journal of Materials Chemistry C* 5 (2017), pp. 4017–4024. DOI: 10.1039/c7tc00903h (cited on p. 6).

[77] P. van de Weijer, P. C. Bouten, H. Fledderus, R. R. Janssen, S. H. de Winter, and H. B. Akkerman. "Mechanistic study on black and grey spot growth in OLEDs performed on laser-ablated pinholes in the cathode". *Organic Electronics* 42 (2017), pp. 59–65. DOI: 10.1016/j.orgel.2016.12.025 (cited on pp. 6, 95).

[78] E. G. Jeong, Y. C. Han, H.-G. Im, B.-S. Bae, and K. C. Choi. "Highly reliable hybrid nano-stratified moisture barrier for encapsulating flexible OLEDs". *Organic Electronics* 33 (2016), pp. 150–155. DOI: 10.1016/j.orgel.2016.03.015 (cited on p. 6).

[79] H.-L. Huang, B. Balaganesan, Y.-H. Fu, H.-Y. Lin, and T.-C. Chao. "Electron Transporting Materials for Highly Efficient and Long Lifetime Blue OLED Devices for Display and Lighting Applications". *SID Symposium Digest of Technical Papers* 47 (2016), pp. 1722–1724. DOI: 10.1002/sdtp.11037 (cited on p. 6).

[80] R. Meerheim, K. Walzer, M. Pfeiffer, and K. Leo. "Ultrastable and efficient red organic light emitting diodes with doped transport layers". *Applied Physics Letters* 89 (2006), p. 061111. DOI: 10.1063/1.2268354 (cited on p. 6).

[81] H. Fukagawa, T. Shimizu, T. Kamada, S. Yui, M. Hasegawa, K. Morii, and T. Yamamoto. "Highly efficient and stable organic light-emitting diodes with a greatly reduced amount of phosphorescent emitter". *Scientific Reports* 5 (2015), p. 9855. DOI: 10.1038/srep09855 (cited on p. 6).

[82] W. Brütting, S. Berleb, and A. G. Mückl. "Device Physics of organic light-emitting diodes based on molecular materials". *Organic Electronics* 2 (2001), pp. 1–36. DOI: 10.1016/s1566-1199(01)00009-x (cited on pp. 6, 41–43, 55, 56).

[83] S. Altazin, S. Züfle, E. Knapp, C. Kirsch, T. D. Schmidt, L. Jäger, Y. Noguchi, W. Brütting, and B. Ruhstaller. "Simulation of OLEDs with a polar electron transport layer". *Organic Electronics* 39 (2016), pp. 244–249. DOI: 10.1016/j.orgel.2016.10.014 (cited on pp. 6, 44, 49, 55, 57, 59, 72).

[84] S. R. Forrest. "The path to ubiquitous and low-cost organic electronic appliances on plastic". *Nature* 428 (2004), pp. 911–918. DOI: 10.1038/nature02498 (cited on p. 6).

[85] F. C. Krebs, N. Espinosa, M. Hösel, R. R. Søndergaard, and M. Jørgensen. "25th Anniversary Article: Rise to Power – OPV-Based Solar Parks". *Advanced Materials* 26 (2014), pp. 29–39. DOI: 10.1002/adma.201302031 (cited on p. 6).

[86] R. Søndergaard, M. Hösel, D. Angmo, T. T. Larsen-Olsen, and F. C. Krebs. "Roll-to-roll fabrication of polymer solar cells". *Materials Today* 15 (2012), pp. 36–49. DOI: 10.1016/S1369-7021(12)70019-6 (cited on p. 6).

[87] H. Kang, G. Kim, J. Kim, S. Kwon, H. Kim, and K. Lee. "Bulk-Heterojunction Organic Solar Cells: Five Core Technologies for Their Commercialization". *Advanced Materials* 28 (2016), pp. 7821–7861. DOI: 10.1002/adma.201601197 (cited on p. 6).

[88] F. C. Krebs. "Fabrication and processing of polymer solar cells: A review of printing and coating techniques". *Solar Energy Materials & Solar Cells* 93 (2009), pp. 394–412. DOI: 10.1016/j.solmat.2008.10.004 (cited on p. 6).

[89] Y. Galagan, I. G. de Vries, A. P. Langen, R. Andriessen, W. J. Verhees, S. C. Veenstra, and J. M. Kroon. "Technology development for roll-to-roll production of organic photovoltaics". *Chemical Engineering and Processing: Process Intensification* 50 (2011), pp. 454–461. DOI: 10.1016/j.cep.2010.07.012 (cited on p. 6).

[90] M. Välimäki, E. Jansson, P. Korhonen, A. Peltoniemi, and S. Rousu. "Custom-Shaped Organic Photovoltaic Modules - Freedom of Design by Printing". *Nanoscale Research Letters* 12 (2017), p. 117. DOI: 10.1186/s11671-017-1871-9 (cited on p. 6).

[91] S. Berny, N. Blouin, A. Distler, H.-J. Egelhaaf, M. Krompiec, A. Lohr, O. R. Lozman, G. E. Morse, L. Nanson, A. Pron, T. Sauermann, N. Seidler, S. Tierney, P. Tiwana, M. Wagner, and H. Wilson. "Solar Trees: First Large-Scale Demonstration of Fully Solution Coated, Semitransparent, Flexible Organic Photovoltaic Modules". *Advanced Science* 3 (2015), p. 1500342. DOI: 10.1002/advs.201500342 (cited on p. 6).

[92] T. M. Eggenhuisen, Y. Galagan, A. F.K. V. Biezemans, T. M.W. L. Slaats, W. P. Voorthuijzen, S. Kommeren, S. Shanmugam, J. P. Teunissen, A. Hadipour, W. J. H. Verhees, S. C. Veenstra, M. J. J. Coenen, J. Gilot, R. Andriessen, and W. A. Groen. "High efficiency, fully inkjet printed organic solar cells with freedom of design". *Journal of Materials Chemistry A* 3 (2015), pp. 7255–7262. DOI: 10.1039/c5ta00540j (cited on p. 6).

[93] L. Lucera, F. Machui, H. Schmidt, T. Ahmad, P. Kubis, S. Strohm, J. Hepp, A. Vetter, H.-J. Egelhaaf, and C. Brabec. "Printed semi-transparent large area organic photovoltaic modules with power conversion efficiencies of close to 5 %". *Organic Electronics* 45 (2017), pp. 209–214. DOI: 10.1016/j.orgel.2017.03.013 (cited on p. 6).

[94] G. Pace, A. Grimoldi, D. Natali, M. Sampietro, J. E. Coughlin, G. C. Bazan, and M. Caironi. "All-Organic and Fully-Printed Semitransparent Photodetectors Based on Narrow Bandgap Conjugated

Molecules". *Advanced Materials* 26 (2014), pp. 6773–6777. DOI: 10.1002/adma.201402918 (cited on p. 6).

[95] F. Guo, X. Zhu, K. Forberich, J. Krantz, T. Stubhan, M. Salinas, M. Halik, S. Spallek, B. Butz, E. Spiecker, T. Ameri, N. Li, P. Kubis, D. M. Guldi, G. J. Matt, and C. J. Brabec. "ITO-Free and Fully Solution-Processed Semitransparent Organic Solar Cells with High Fill Factors". *Advanced Energy Materials* 3 (2013), pp. 1062–1067. DOI: 10.1002/aenm.201300100 (cited on p. 6).

[96] Y. Qian, X. Zhang, L. Xie, D. Qi, B. K. Chandran, X. Chen, and W. Huang. "Stretchable Organic Semiconductor Devices". *Advanced Materials* 28 (2016), pp. 9243–9265. DOI: 10.1002/adma.201601278 (cited on p. 6).

[97] R. Steim, P. Chabrecek, U. Sonderegger, B. Kindle-Hasse, W. Siefert, T. Kroyer, P. Reinecke, T. Lanz, T. Geiger, R. Hany, and F. Nüesch. "Laminated fabric as top electrode for organic photovoltaics". *Applied Physics Letters* 106 (2015), p. 193301. DOI: 10.1063/1.4919940 (cited on p. 6).

[98] D. Lupo, W. Clemens, S. Breitung, and K. Hecker. "Market Perspectives and Road Map for Organic Electronics". In: *Organic and Printed Electronics*. Ed. by G. Nisato, D. Lupo, and S. Ganz. Pan Stanford, 2016. Chap. 14, pp. 509–536. ISBN: 9789814669740 (cited on p. 6).

[99] C. L. Cutting, M. Bag, and D. Venkataraman. "Indoor light recycling: a new home for organic photovoltaics". *Journal of Materials Chemistry C* 4 (2016), pp. 10367–10370. DOI: 10.1039/c6tc03344j (cited on p. 6).

[100] A. Tada, Y. Geng, Q. Wei, K. Hashimoto, and K. Tajima. "Tailoring organic heterojunction interfaces in bilayer polymer photovoltaic devices". *Nature Materials* 10 (2011), pp. 450–455. DOI: 10.1038/nmat3026 (cited on p. 7).

[101] N. S. Sariciftci, L. Smilowitz, A. J. Heeger, and F. Wudl. "Photoinduced Electron Transfer from a Conducting Polymer to Buckminsterfullerene". *Science* 258 (1992), pp. 1474–1476. DOI: 10.1126/science.258.5087.1474 (cited on p. 7).

[102] J. J. M. Halls, C. A. Walsh, N. C. Greenham, E. A. Marseglia, R. H. Friend, S. C. Moratti, and A. B. Holmes. "Efficient photodiodes from interpenetrating polymer networks". *Nature* 376 (1995), pp. 498–500. DOI: 10.1038/376498a0 (cited on p. 7).

[103] NREL. *Solar Cell Efficiency Chart 14.04.2017; https://www.nrel.gov/pv/*. 2017 (cited on pp. 8, 9).

[104] J.-D. Chen, C. Cui, Y.-Q. Li, L. Zhou, Q.-D. Ou, C. Li, Y. Li, and J.-X. Tang. "Single-Junction Polymer Solar Cells Exceeding 10% Power Conversion Efficiency". *Advanced Materials* 27 (2014), pp. 1035–1041. DOI: 10.1002/adma.201404535 (cited on p. 8).

[105] Z. He, B. Xiao, F. Liu, H. Wu, Y. Yang, S. Xiao, C. Wang, T. P. Russell, and Y. Cao. "Single-junction polymer solar cells with high efficiency and photovoltage". *Nature Photonics* 9 (2015), pp. 174–179. DOI: 10.1038/nphoton.2015.6 (cited on p. 8).

[106] C. Liu, C. Yi, K. Wang, Y. Yang, R. S. Bhatta, M. Tsige, S. Xiao, and X. Gong. "Single-Junction Polymer Solar Cells with Over 10% Efficiency by a Novel Two-Dimensional Donor–Acceptor Conjugated Copolymer". *ACS Applied Materials & Interfaces* 7 (2015), pp. 4928–4935. DOI: 10.1021/am509047g (cited on p. 8).

[107] Y. Liu, J. Zhao, Z. Li, C. Mu, W. Ma, H. Hu, K. Jiang, H. Lin, H. Ade, and H. Yan. "Aggregation and morphology control enables multiple cases of high-efficiency polymer solar cells". *Nature Communications* 5 (2014), p. 5293. DOI: 10.1038/ncomms6293 (cited on p. 8).

[108] Y. Yan, F. Cai, L. Yang, J. Li, Y. Zhang, F. Qin, C. Xiong, Y. Zhou, D. G. Lidzey, and T. Wang. "Light-Soaking-Free Inverted Polymer Solar Cells with an Efficiency of 10.5% by Compositional and Surface Modifications to a Low-Temperature-Processed TiO2 Electron-Transport Layer". *Advanced Materials* 29 (2016), p. 1604044. DOI: 10.1002/adma.201604044 (cited on p. 8).

[109] F. Zhao, S. Dai, Y. Wu, Q. Zhang, J. Wang, L. Jiang, Q. Ling, Z. Wei, W. Ma, W. You, C. Wang, and X. Zhan. "Single-Junction Binary-Blend Nonfullerene Polymer Solar Cells with 12.1% Efficiency". *Advanced Materials* 29 (2017), p. 1700144. DOI: 10.1002/adma.201700144 (cited on p. 8).

[110] L. Ye, W. Zhao, S. Li, S. Mukherjee, J. H. Carpenter, O. Awartani, X. Jiao, J. Hou, and H. Ade. "High-Efficiency Nonfullerene Organic Solar Cells: Critical Factors that Affect Complex Multi-Length Scale Morphology and Device Performance". *Advanced Energy Materials* 7 (2016), p. 1602000. DOI: 10.1002/aenm.201602000 (cited on p. 8).

[111] H. Bin, L. Gao, Z.-G. Zhang, Y. Yang, Y. Zhang, C. Zhang, S. Chen, L. Xue, C. Yang, M. Xiao, and Y. Li. "11.4% Efficiency non-fullerene polymer solar cells with trialkylsilyl substituted 2D-conjugated polymer as donor". *Nature Communications* 7 (2016), p. 13651. DOI: 10.1038/ncomms13651 (cited on p. 8).

[112] J. Huang, H. Wang, K. Yan, X. Zhang, H. Chen, C.-Z. Li, and J. Yu. "Highly Efficient Organic Solar Cells Consisting of Double Bulk Heterojunction Layers". *Advanced Materials* 29 (2017), p. 1606729. DOI: 10.1002/adma.201606729 (cited on p. 8).

[113] W. J. da Silva, F. K. Schneider, A. R. bin Mohd Yusoff, and J. Jang. "High performance polymer tandem solar cell". *Scientific Reports* 5 (2015), p. 18090. DOI: 10.1038/srep18090 (cited on p. 8).

[114] Heliatek. *Heliatek sets new Organic Photovoltaic world record efficiency of 13.2 %*. 2016 (cited on p. 8).

[115] M. Li, K. Gao, X. Wan, Q. Zhang, B. Kan, R. Xia, F. Liu, X. Yang, H. Feng, W. Ni, Y. Wang, J. Peng, H. Zhang, Z. Liang, H.-L. Yip, X. Peng, Y. Cao, and Y. Chen. "Solution-processed organic tandem solar cells with power conversion efficiencies > 12%". *Nature Photonics* 11 (2016), pp. 85–90. DOI: 10.1038/nphoton.2016.240 (cited on p. 8).

[116] Y. Qin, Y. Chen, Y. Cui, S. Zhang, H. Yao, J. Huang, W. Li, Z. Zheng, and J. Hou. "Achieving 12.8% Efficiency by Simultaneously Improving Open-Circuit Voltage and Short-Circuit Current Density in Tandem Organic Solar Cells". *Advanced Materials* (2017), p. 1606340. DOI: 10.1002/adma.201606340 (cited on p. 8).

[117] M. C. Scharber, D. Mühlbacher, M. Koppe, P. Denk, C. Waldauf, A. J. Heeger, and C. J. Brabec. "Design Rules for Donors in Bulk-Heterojunction Solar Cells - Towards 10 % Energy-Conversion Efficiency". *Advanced Materials* 18 (2006), pp. 789–794. DOI: 10.1002/adma.200501717 (cited on p. 8).

[118] M. C. Scharber. "On the Efficiency Limit of Conjugated Polymer:Fullerene-Based Bulk Heterojunction Solar Cells". *Advanced Materials* 28 (2016), pp. 1994–2001. DOI: 10.1002/adma.201504914 (cited on p. 8).

[119] T. Kirchartz, K. Taretto, and U. Rau. "Efficiency Limits of Organic Bulk Heterojunction Solar Cells". *The Journal of Physical Chemistry C* 113 (2009), pp. 17958–17966. DOI: 10.1021/jp906292h (cited on p. 8).

[120] N. C. Giebink, G. P. Wiederrecht, M. R. Wasielewski, and S. R. Forrest. "Thermodynamic efficiency limit of excitonic solar cells". *Physical Review B* 83 (2011), p. 195326. DOI: 10.1103/PhysRevB.83.195326 (cited on p. 8).

[121] U. Würfel, D. Neher, A. Spies, and S. Albrecht. "Impact of charge transport on current-voltage characteristics and power-conversion efficiency of organic solar cells". *Nature Communications* 6 (2015), p. 6951. DOI: 10.1038/ncomms7951 (cited on pp. 8, 47).

[122] L. J. A. Koster, S. E. Shaheen, and J. C. Hummelen. "Pathways to a New Efficiency Regime for Organic Solar Cells". *Advanced Energy Materials* 2 (2012), pp. 1246–1253. DOI: 10.1002/aenm.201200103 (cited on p. 8).

[123] K. A. Bush, A. F. Palmstrom, Z. J. Yu, M. Boccard, R. Cheacharoen, J. P. Mailoa, D. P. McMeekin, R. L. Z. Hoye, C. D. Bailie, T. Leijtens, I. M. Peters, M. C. Minichetti, N. Rolston, R. Prasanna, S. Sofia, D. Harwood, W. Ma, F. Moghadam, H. J. Snaith, T. Buonassisi, Z. C. Holman, S. F. Bent, and M. D. McGehee. "23.6%-efficient monolithic perovskite/silicon tandem solar cells with improved stability". *Nature Energy* 2 (2017), p. 17009. DOI: 10.1038/nenergy.2017.9 (cited on p. 8).

[124] T. Duong, Y. Wu, H. Shen, J. Peng, X. Fu, D. Jacobs, E.-C. Wang, T. C. Kho, K. C. Fong, M. Stocks, E. Franklin, A. Blakers, N. Zin, K. McIntosh, W. Li, Y.-B. Cheng, T. P. White, K. Weber, and K. Catchpole. "Rubidium Multication Perovskite with Optimized Bandgap for Perovskite-Silicon Tandem with

over 26 % Efficiency". *Advanced Energy Materials* (2017), p. 1700228. DOI: 10.1002/aenm.201700228 (cited on p. 8).

[125] S. S. Shin, E. J. Yeom, W. S. Yang, S. Hur, M. G. Kim, J. Im, J. Seo, J. H. Noh, and S. I. Seok. "Colloidally prepared La-doped BaSnO3 electrodes for efficient, photostable perovskite solar cells". *Science* 356 (2017), pp. 167–171. DOI: 10.1126/science.aam6620 (cited on p. 8).

[126] S. A. Gevorgyan, N. Espinosa, L. Ciammaruchi, B. Roth, F. Livi, S. Tsopanidis, S. Züfle, S. Queirós, A. Gregori, G. A. dos Reis Benatto, M. Corazza, M. V. Madsen, M. Hösel, M. J. Beliatis, T. T. Larsen-Olsen, F. Pastorelli, A. Castro, A. Mingorance, V. Lenzi, D. Fluhr, R. Roesch, M. M. D. Ramos, A. Savva, H. Hoppe, L. S. A. Marques, I. Burgués, E. Georgiou, L. Serrano-Luján, and F. C. Krebs. "Baselines for Lifetime of Organic Solar Cells". *Advanced Energy Materials* 6 (2016), p. 1600910. DOI: 10.1002/aenm.201600910 (cited on pp. 8, 10, 12–14).

[127] M. Jørgensen, K. Norrman, S. A. Gevorgyan, T. Tromholt, B. Andreasen, and F. C. Krebs. "Stability of Polymer Solar Cells". *Advanced Materials* 24 (2012), pp. 580–612. DOI: 10.1002/adma.201104187 (cited on pp. 8, 10).

[128] M. Jørgensen, K. Norrman, and F. C. Krebs. "Stability/degradation of polymer solar cells". *Solar Energy Materials & Solar Cells* 92 (2008), pp. 686–714. DOI: 10.1016/j.solmat.2008.01.005 (cited on p. 8).

[129] S. A. Gevorgyan, I. M. Heckler, E. Bundgaard, M. Corazza, M. Hösel, R. R. Søndergaard, G. A. dos Reis Benatto, M. Jørgensen, and F. C. Krebs. "Improving, characterizing and predicting the lifetime of organic photovoltaics". *Journal of Physics D: Applied Physics* 50 (2017), p. 103001. DOI: 10.1088/1361-6463/50/10/103001 (cited on p. 8).

[130] R. Roesch, T. Faber, E. von Hauff, T. M. Brown, M. Lira-Cantu, and H. Hoppe. "Procedures and Practices for Evaluating Thin-Film Solar Cell Stability". *Advanced Energy Materials* 5 (2015), p. 1501407. DOI: 10.1002/aenm.201501407 (cited on p. 8).

[131] M. Nam, M. Cha, H. H. Lee, K. Hur, K.-T. Lee, J. Yoo, I. K. Han, S. J. Kwon, and D.-H. Ko. "Long-term efficient organic photovoltaics based on quaternary bulk heterojunctions". *Nature Communications* 8 (2017), p. 14068. DOI: 10.1038/ncomms14068 (cited on pp. 8, 14).

[132] C. H. Peters, I. T. Sachs-Quintana, W. R. Mateker, T. Heumueller, J. Rivnay, R. Noriega, Z. M. Beiley, E. T. Hoke, A. Salleo, and M. D. McGehee. "The Mechanism of Burn-in Loss in a High Efficiency Polymer Solar Cell". *Advanced Materials* 24 (2012), pp. 663–668. DOI: 10.1002/adma.201103010 (cited on pp. 8, 116–118).

[133] T. Heumueller, W. R. Mateker, I. T. Sachs-Quintana, K. Vandewal, J. A. Bartelt, T. M. Burke, T. Ameri, C. J. Brabec, and M. D. McGehee. "Reducing burn-in voltage loss in polymer solar cells by increasing the polymer crystallinity". *Energy & Environmental Science* 7 (2014), pp. 2974–2980. DOI: 10.1039/C4EE01842G (cited on pp. 8, 116).

[134] N. Li, J. D. Perea, T. Kassar, M. Richter, T. Heumueller, G. J. Matt, Y. Hou, N. S. Güldal, H. Chen, S. Chen, S. Langner, M. Berlinghof, T. Unruh, and C. J. Brabec. "Abnormal strong burn-in degradation of highly efficient polymer solar cells caused by spinodal donor-acceptor demixing". *Nature Communications* 8 (2017), p. 14541. DOI: 10.1038/ncomms14541 (cited on p. 8).

[135] M. S. A. Abdou and S. Holdcroft. "Mechanisms of Photodegradation of Poly(3-alkylthiophenes) in Solution". *Macromolecules* 26 (1993), pp. 2954–2962. DOI: 10.1021/ma00063a047 (cited on p. 9).

[136] H. M. Shah, A. D. Mohite, T. Bansal, and B. W. Alphenaar. "Photovoltage bleaching in bulk heterojunction solar cells through population of the singlet exciton". *Applied Physics Letters* 97 (2010), p. 263301. DOI: 10.1063/1.3531578 (cited on p. 9).

[137] E. Palacios-Lidon, E. Escasain, E. Lopez-Elvira, A. M. Baro, and J. Colchero. "Photobleaching of MEH-PPV thin films: Correlation between optical properties and the nanoscale surface photovoltage". *Solar Energy Materials & Solar Cells* 117 (2013), pp. 15–21. DOI: 10.1016/j.solmat.2013.05.022 (cited on p. 9).

[138] A. Rivaton, S. Chambon, M. Manceau, J.-L. Gardette, N. Lemaître, and S. Guillerez. "Light-induced degradation of the active layer of polymer-based solar cells". *Polymer Degradation and Stability* 95 (2010), pp. 278–284. DOI: 10.1016/j.polymdegradstab.2009.11.021 (cited on p. 9).

[139] D. Bartesaghi, G. Ye, R. C. Chiechi, and L. J. A. Koster. "Compatibility of PTB7 and [70]PCBM as a Key Factor for the Stability of PTB7:[70]PCBM Solar Cells". *Advanced Energy Materials* 6 (2016), p. 1502338. DOI: 10.1002/aenm.201502338 (cited on p. 9).

[140] G. Williams, Q. Wang, and H. Aziz. "The Photo-Stability of Polymer Solar Cells: Contact Photo-Degradation and the Benefits of Interfacial Layers". *Advanced Functional Materials* 23 (2013), pp. 2239–2247. DOI: 10.1002/adfm.201202567 (cited on p. 9).

[141] S. K. Gupta, K. Dharmalingam, L. S. Pali, S. Rastogi, A. Singh, and A. Garg. "Degradation of organic photovoltaic devices: a review". *Nanomaterials and Energy* 2 (2013), pp. 42–58. DOI: 10.1680/nme.12.00027 (cited on p. 9).

[142] N. Wang, X. Tong, Q. Burlingame, J. Yu, and S. R. Forrest. "Photodegradation of small-molecule organic photovoltaics". *Solar Energy Materials & Solar Cells* 125 (2014), pp. 170–175. DOI: 10.1016/j.solmat.2014.03.005 (cited on p. 9).

[143] X. Wang, H.-J. Egelhaaf, H.-G. Mack, H. Azimi, C. J. Brabec, A. J. Meixner, and D. Zhang. "Morphology Related Photodegradation of Low-Band-Gap Polymer Blends". *Advanced Energy Materials* 4 (2014), p. 1400497. DOI: 10.1002/aenm.201400497 (cited on p. 9).

[144] U. Aygül, H.-J. Egelhaaf, P. Nagel, M. Merz, S. Schuppler, K. Eichele, H. Peisert, and T. Chassé. "Photodegradation of C-PCPDTBT and Si-PCPDTBT: Influence of the Bridging Atom on the Stability of a Low-Band-Gap Polymer for Solar Cell Application". *ChemPhysChem* 16 (2015), pp. 428–435. DOI: 10.1002/cphc.201402494 (cited on p. 9).

[145] U. Dettinger, H.-J. Egelhaaf, C. J. Brabec, F. Latteyer, H. Peisert, and T. Chassé. "FTIR Study of the Impact of PC[60]BM on the Photodegradation of the Low Band Gap Polymer PCPDTBT under O2Environment". *Chemistry of Materials* 27 (2015), pp. 2299–2308. DOI: 10.1021/acs.chemmater.5b00268 (cited on p. 9).

[146] H. Sato, W. S. B. Azmi, Y. Onaru, and K. Harafuji. "Degradation by ultra-violet light and its mechanism in organic solar cells". *Organic Electronics* 37 (2016), pp. 386–395. DOI: 10.1016/j.orgel.2016.07.011 (cited on p. 9).

[147] A. Tournebize, M. Seck, A. Vincze, A. Distler, H.-J. Egelhaaf, C. J. Brabec, A. Rivaton, H. Peisert, and T. Chassé. "Photodegradation of Si-PCPDTBT:PCBM active layer for organic solar cells applications: A surface and bulk investigation". *Solar Energy Materials & Solar Cells* 155 (2016), pp. 323–330. DOI: 10.1016/j.solmat.2016.06.026 (cited on p. 9).

[148] E. Voroshazi, I. Cardinaletti, T. Conard, and B. P. Rand. "Light-Induced Degradation of Polymer:Fullerene Photovoltaic Devices: An Intrinsic or Material-Dependent Failure Mechanism?" *Advanced Energy Materials* 4 (2014), p. 1400848. DOI: 10.1002/aenm.201400848 (cited on pp. 9, 116).

[149] R. Hansson, C. Lindqvist, L. K. E. Ericsson, A. Opitz, E. Wang, and E. Moons. "Photo-degradation in air of the active layer components in a thiophene–quinoxaline copolymer:fullerene solar cell". *Physical Chemistry Chemical Physics* 18 (2016), pp. 11132–11138. DOI: 10.1039/c5cp07752d (cited on p. 9).

[150] H. Hintz, H.-J. Egelhaaf, H. Peisert, and T. Chassé. "Photo-oxidation and ozonization of poly(3-hexylthiophene) thin films as studied by UV/VIS and photoelectron spectroscopy". *Polymer Degradation and Stability* 95 (2010), pp. 818–825. DOI: 10.1016/j.polymdegradstab.2010.02.004 (cited on p. 9).

[151] H. Hintz, H.-J. Egelhaaf, L. Lüer, J. Hauch, H. Peisert, and T. Chasseé. "Photodegradation of P3HT-A Systematic Study of Environmental Factors". *Chemistry of Materials* 23 (2011), pp. 145–154. DOI: 10.1021/cm102373k (cited on p. 9).

[152] Y. Aoyama, T. Yamanari, T. N. Murakami, T. Nagamori, K. Marumoto, H. Tachikawa, J. Mizukado, H. Suda, and Y. Yoshida. "Initial photooxidation mechanism leading to reactive radical formation

of polythiophene derivatives". *Polymer Journal* 47 (2014), pp. 26–30. DOI: 10.1038/pj.2014.81 (cited on p. 9).

[153] Y. Aoyama, T. Yamanari, N. Ohashi, Y. Shibata, Y. Suzuki, J. Mizukado, H. Suda, and Y. Yoshida. "Direct effect of partially photooxidized poly(3-hexylthiophene) on the device characteristics of a bulk heterojunction solar cell". *Solar Energy Materials & Solar Cells* 120 (2014), pp. 584–590. DOI: 10.1016/j.solmat.2013.09.042 (cited on p. 9).

[154] J. Müllerová, M. Kaiser, V. Nádaždy, P. Šiffalovič, and E. Majková. "Optical absorption study of P3HT:PCBM blend photo-oxidation for bulk heterojunction solar cells". *Solar Energy* 134 (2016), pp. 294–301. DOI: 10.1016/j.solener.2016.05.009 (cited on p. 9).

[155] A. Rivaton and J.-L. Gardette. "Photo-oxidation of aromatic polymers". *Die Angewandte Makromolekulare Chemie* 261-262 (1998), pp. 173–188. DOI: 10.1002/(sici)1522-9505(19981201)261-262:1<173::aid-apmc173>3.3.co;2-f (cited on p. 9).

[156] J.-F. Larché, P.-O. Bussière, S. Thérias, and J.-L. Gardette. "Photooxidation of polymers: Relating material properties to chemical changes". *Polymer Degradation and Stability* 97 (2012), pp. 25–34. DOI: 10.1016/j.polymdegradstab.2011.10.020 (cited on p. 9).

[157] S. Yamane, J. Mizukado, T. Uchimaru, Y. Suzuki, L. Chen, and H. Suda. "Photooxidation studies on indene-C60 adducts". *Solar Energy Materials & Solar Cells* 143 (2015), pp. 135–140. DOI: 10.1016/j.solmat.2015.06.045 (cited on p. 9).

[158] R. D. Pietro, D. Fazzi, T. B. Kehoe, and H. Sirringhaus. "Spectroscopic Investigation of Oxygen- and Water-Induced Electron Trapping and Charge Transport Instabilities in n-type Polymer Semiconductors". *Journal of the American Chemical Society* 134 (2012), pp. 14877–14889. DOI: 10.1021/ja304198e (cited on p. 9).

[159] R. A. Street and D. M. Davies. "Kinetics of light induced defect creation in organic solar cells". *Applied Physics Letters* 102 (2013), p. 043305. DOI: 10.1063/1.4789993 (cited on p. 9).

[160] M. R. Shijeesh, L. S. Vikas, M. K. Jayaraj, and J. Puigdollers. "Comparative study on degradation and trap density-of-states of p type and n type organic semiconductors". *Proceedings of SPIE* 9185 (2014). Ed. by Z. Bao, I. McCulloch, R. Shinar, and I. Kymissis, p. 918519. DOI: 10.1117/12.2064832 (cited on p. 9).

[161] R. A. Street, Y. Yang, B. C. Thompson, and I. McCulloch. "Capacitance Spectroscopy of Light Induced Trap States in Organic Solar Cells". *The Journal of Physical Chemistry C* 120 (2016), pp. 22169–22178. DOI: 10.1021/acs.jpcc.6b06561 (cited on p. 9).

[162] J. Schafferhans, A. Baumann, C. Deibel, and V. Dyakonov. "Trap distribution and the impact of oxygen-induced traps on the charge transport in poly(3-hexylthiophene)". *Applied Physics Letters* 93, 093303 (2008), p. 093303. DOI: 10.1063/1.2978237 (cited on p. 9).

[163] K. Kawano and C. Adachi. "Evaluating Carrier Accumulation in Degraded Bulk Heterojunction Organic Solar Cells by a Thermally Stimulated Current Technique". *Advanced Functional Materials* 19 (2009), pp. 3934–3940. DOI: 10.1002/adfm.200901573 (cited on p. 9).

[164] S. Khelifi, K. Decock, J. Lauwaert, H. Vrielinck, D. Spoltore, F. Piersimoni, J. Manca, A. Belghachi, and M. Burgelman. "Investigation of defects by admittance spectroscopy measurements in poly (3-hexylthiophene):(6,6)-phenyl C61-butyric acid methyl ester organic solar cells degraded under air exposure". *Journal of Applied Physics* 110 (2011), p. 094509. DOI: 10.1063/1.3658023 (cited on p. 9).

[165] A. L. Domanski, I. Lieberwirth, E. Sengupta, K. Landfester, H.-J. Butt, R. Berger, J. Rauh, V. Dyakonov, and C. Deibel. "Effect of Morphological Changes on Presence of Trap States in P3HT:PCBM Solar Cells Studied by Cross-Sectional Energy Filtered TEM and Thermally Stimulated Current Measurements". *The Journal of Physical Chemistry C* 117 (2013), pp. 23495–23499. DOI: 10.1021/jp406014m (cited on p. 9).

[166] V. Singh, S. Arora, P. K. Bhatnagar, M. Arora, and R. P. Tandon. "Effects of aging on the mobility and lifetime of carriers in organic bulk heterojunction solar cells". *Journal of Renewable and Sustainable Energy* 3 (2011), p. 063111. DOI: 10.1063/1.3670411 (cited on p. 9).

[167] F. Deschler, A. D. Sio, E. von Hauff, P. Kutka, T. Sauermann, H.-J. Egelhaaf, J. Hauch, and E. D. Como. "The Effect of Ageing on Exciton Dynamics, Charge Separation, and Recombination in P3HT/PCBM Photovoltaic Blends". *Advanced Functional Materials* 22 (2012), pp. 1461–1469. DOI: 10.1002/adfm.201101923 (cited on p. 9).

[168] M. Stephen, S. Karuthedath, T. Sauermann, K. Genevičius, and G. Juška. "Degradation effects on charge carrier transport in P3HT:PCBM solar cells studied by Photo-CELIV and ToF". *Proceedings of SPIE* 9184 (2014). Ed. by Z. H. Kafafi, P. A. Lane, and I. D. W. Samuel, p. 918424. DOI: 10.1117/12.2061857 (cited on p. 9).

[169] S. Karuthedath, T. Sauermann, H.-J. Egelhaaf, R. Wannemacher, C. J. Brabec, and L. Ler. "The effect of oxygen induced degradation on charge carrier dynamics in P3HT:PCBM and Si-PCPDTBT:PCBM thin films and solar cells". *Journal of Materials Chemistry A* 3 (2015), pp. 3399–3408. DOI: 10.1039/C4TA06719C (cited on p. 9).

[170] J. Schafferhans, A. Baumann, A. Wagenpfahl, C. Deibel, and V. Dyakonov. "Oxygen doping of P3HT:PCBM blends: Influence on trap states, charge carrier mobility and solar cell performance". *Organic Electronics* 11 (2010), pp. 1693–1700. DOI: 10.1016/j.orgel.2010.07.016 (cited on p. 9).

[171] A. Guerrero, P. P. Boix, L. F. Marchesi, T. Ripolles-Sanchis, E. C. Pereira, and G. Garcia-Belmonte. "Oxygen doping-induced photogeneration loss in P3HT:PCBM solar cells". *Solar Energy Materials & Solar Cells* 100 (2012), pp. 185–191. DOI: 10.1016/j.solmat.2012.01.012 (cited on p. 9).

[172] J. Steiger, S. Karg, R. Schmechel, and H. von Seggern. "Aging induced traps in organic semiconductors". *Synthetic Metals* 122 (2001), pp. 49–52. DOI: 10.1016/s0379-6779(00)01359-x (cited on pp. 9, 11).

[173] H.-H. Liao, C.-M. Yang, C.-C. Liu, S.-F. Horng, H.-F. Meng, and J.-T. Shy. "Dynamics and reversibility of oxygen doping and de-doping for conjugated polymer". *Journal of Applied Physics* 103 (2008), p. 104506. DOI: 10.1063/1.2917419 (cited on p. 9).

[174] H. Hintz, H. Peisert, H.-J. Egelhaaf, and T. Chassé. "Reversible and Irreversible Light-Induced p-Doping of P3HT by Oxygen Studied by Photoelectron Spectroscopy (XPS/UPS)". *The Journal of Physical Chemistry C* 115 (2011), pp. 13373–13376. DOI: 10.1021/jp2032737 (cited on p. 9).

[175] A. Seemann, T. Sauermann, C. Lungenschmied, O. Armbruster, S. Bauer, H.-J. Egelhaaf, and J. Hauch. "Reversible and irreversible degradation of organic solar cell performance by oxygen". *Solar Energy* 85 (2011), pp. 1238–1249. DOI: 10.1016/j.solener.2010.09.007 (cited on pp. 9, 22, 25).

[176] Y. Galagan, A. Mescheloff, S. C. Veenstra, R. Andriessen, and E. A. Katz. "Reversible degradation in ITO-containing organic photovoltaics under concentrated sunlight". *Physical Chemistry Chemical Physics* 17 (2015), pp. 3891–3897. DOI: 10.1039/C4CP05571C (cited on pp. 9, 99).

[177] O. V. Kozlov and S. A. Zapunidi. "Reversible oxygen doping of conjugated polymer and its de-doping studied by Mott-Schottky analysis". *Synthetic Metals* 169 (2013), pp. 48–54. DOI: 10.1016/j.synthmet.2013.03.005 (cited on pp. 9, 22).

[178] T. Tromholt, A. Manor, E. A. Katz, and F. C. Krebs. "Reversible degradation of inverted organic solar cells by concentrated sunlight". *Nanotechnology* 22 (2011), p. 225401. DOI: 10.1088/0957-4484/22/22/225401 (cited on pp. 9, 76, 100).

[179] M. Dusza, W. Strek, and F. Granek. "Significance of light-soaking effect in proper analysis of degradation dynamics of organic solar cells". *Journal of Photonics for Energy* 6 (2016), p. 035503. DOI: 10.1117/1.jpe.6.035503 (cited on p. 9).

[180] S. Trost, T. Becker, A. Polywka, P. Görrn, M. F. Oszajca, N. A. Luechinger, D. Rogalla, M. Weidner, P. Reckers, T. Mayer, and T. Riedl. "Avoiding Photoinduced Shunts in Organic Solar Cells by the Use of Tin Oxide (SnOx) as Electron Extraction Material Instead of ZnO". *Advanced Energy Materials* 6 (2016), p. 1600347. DOI: 10.1002/aenm.201600347 (cited on pp. 9, 76).

[181] S. Trost, A. Behrendt, T. Becker, A. Polywka, P. Görrn, and T. Riedl. "Tin Oxide (SnOx) as Universal "Light-Soaking" Free Electron Extraction Material for Organic Solar Cells". *Advanced Energy Materials* 5 (2015), p. 1500277. DOI: 10.1002/aenm.201500277 (cited on p. 9).

[182] S. Trost, K. Zilberberg, A. Behrendt, A. Polywka, P. Görrn, P. Reckers, J. Maibach, T. Mayer, and T. Riedl. "Overcoming the "Light-Soaking" Issue in Inverted Organic Solar Cells by the Use of Al:ZnO Electron Extraction Layers". *Advanced Energy Materials* 3 (2013), pp. 1437–1444. DOI: 10.1002/aenm.201300402 (cited on p. 9).

[183] M. Campoy-Quiles, T. Ferenczi, T. Agostinelli, P. G. Etchegoin, Y. Kim, T. D. Anthopoulos, P. N. Stavrinou, D. D. C. Bradley, and J. Nelson. "Morphology evolution via self-organization and lateral and vertical diffusion in polymer:fullerene solar cell blends". *Nature Materials* 7 (2008), pp. 158–164. DOI: 10.1038/nmat2102 (cited on p. 9).

[184] A. Guerrero and G. Garcia-Belmonte. "Recent Advances to Understand Morphology Stability of Organic Photovoltaics". *Nano-Micro Letters* 9 (2016), p. 10. DOI: 10.1007/s40820-016-0107-3 (cited on p. 9).

[185] I. T. Sachs-Quintana, T. Heumüller, W. R. Mateker, D. E. Orozco, R. Cheacharoen, S. Sweetnam, C. J. Brabec, and M. D. McGehee. "Electron Barrier Formation at the Organic-Back Contact Interface is the First Step in Thermal Degradation of Polymer Solar Cells". *Advanced Functional Materials* 24 (2014), pp. 3978–3985. DOI: 10.1002/adfm.201304166 (cited on p. 9).

[186] H. Cheun, J. D. Berrigan, Y. Zhou, M. Fenoll, J. Shim, C. Fuentes-Hernandez, K. H. Sandhage, and B. Kippelen. "Roles of thermally-induced vertical phase segregation and crystallization on the photovoltaic performance of bulk heterojunction inverted polymer solar cells". *Energy & Environmental Science* 4 (2011), pp. 3456–3460. DOI: 10.1039/c1ee01316e (cited on p. 9).

[187] H. C. Wong, Z. Li, C. H. Tan, H. Zhong, Z. Huang, H. Bronstein, I. McCulloch, J. T. Cabral, and J. R. Durrant. "Morphological Stability and Performance of Polymer–Fullerene Solar Cells under Thermal Stress: The Impact of Photoinduced PC60BM Oligomerization". *ACS Nano* 8 (2014), pp. 1297–1308. DOI: 10.1021/nn404687s (cited on p. 9).

[188] J. Kesters, S. Kudret, S. Bertho, N. V. den Brande, M. Defour, B. V. Mele, H. Penxten, L. Lutsen, J. Manca, D. Vanderzande, and W. Maes. "Enhanced intrinsic stability of the bulk heterojunction active layer blend of polymer solar cells by varying the polymer side chain pattern". *Organic Electronics* 15 (2014), pp. 549–562. DOI: 10.1016/j.orgel.2013.12.006 (cited on pp. 9, 10).

[189] C. Lin, E.-Y. Lin, and F.-Y. Tsai. "Enhanced Thermal Stability and Efficiency of Polymer Bulk-Heterojunction Solar Cells by Low-Temperature Drying of the Active Layer". *Advanced Functional Materials* 20 (2010), pp. 834–839. DOI: 10.1002/adfm.200901807 (cited on p. 9).

[190] S. Bertho, I. Haeldermans, A. Swinnen, J. D'Haen, L. Lutsen, J. V. Manca, and D. J. M. Vanderzande. "How stable are polymer:PCBM bulk heterojunction solar cells?" *Proceedings of SPIE* 6192 (2006). Ed. by P. L. Heremans, M. Muccini, and E. A. Meulenkamp, p. 619225. DOI: 10.1117/12.663156 (cited on p. 9).

[191] W. Greenbank, L. Hirsch, G. Wantz, and S. Chambon. "Interfacial thermal degradation in inverted organic solar cells". *Applied Physics Letters* 107 (2015), p. 263301. DOI: 10.1063/1.4938554 (cited on p. 9).

[192] F. Hermerschmidt, A. Savva, E. Georgiou, S. M. Tuladhar, J. R. Durrant, I. McCulloch, D. D. Bradley, C. J. Brabec, J. Nelson, and S. A. Choulis. "Influence of the Hole Transporting Layer on the Thermal Stability of Inverted Organic Photovoltaics Using Accelerated-Heat Lifetime Protocols". *ACS Applied Materials & Interfaces* 9 (2017), pp. 14136–14144. DOI: 10.1021/acsami.7b01183 (cited on p. 9).

[193] Z. Li, K. H. Chiu, R. S. Ashraf, S. Fearn, R. Dattani, H. C. Wong, C.-H. Tan, J. Wu, J. T. Cabral, and J. R. Durrant. "Toward Improved Lifetimes of Organic Solar Cells under Thermal Stress: Substrate-Dependent Morphological Stability of PCDTBT:PCBM Films and Devices". *Scientific Reports* 5 (2015), p. 15149. DOI: 10.1038/srep15149 (cited on p. 9).

[194] S. Bertho, B. Campo, F. Piersimoni, D. Spoltore, J. D'Haen, L. Lutsen, W. Maes, D. Vanderzande, and J. Manca. "Improved thermal stability of bulk heterojunctions based on side-chain functionalized poly(3-alkylthiophene) copolymers and PCBM". *Solar Energy Materials & Solar Cells* 110 (2013), pp. 69–76. DOI: 10.1016/j.solmat.2012.12.007 (cited on p. 9).

[195] F. Piersimoni, G. Degutis, S. Bertho, K. Vandewal, D. Spoltore, T. Vangerven, J. Drijkoningen, M. K. V. Bael, A. Hardy, J. D'Haen, W. Maes, D. Vanderzande, M. Nesladek, and J. Manca. "Influence of fullerene photodimerization on the PCBM crystallization in polymer: Fullerene bulk heterojunctions under thermal stress". *Journal of Polymer Science, Part B* 51 (2013), pp. 1209–1214. DOI: 10.1002/polb.23330 (cited on p. 9).

[196] S. Chambon, Y. Murat, G. Wantz, L. Hirsch, and P. Tardy. "Lanthanum Hexaboride As Novel Interlayer for Improving the Thermal Stability of P3HT:PCBM Organic Solar Cells". *ACS Applied Materials & Interfaces* 7 (2015), pp. 25334–25340. DOI: 10.1021/acsami.5b06475 (cited on p. 9).

[197] J. Liu, X. Zhu, J. Li, J. Shen, and G. Tu. "Enhancing the thermal stability of the bulk-heterojunction photovoltaics based on P3HT/PCBM by incorporating diblock amphipathic P3HT-PEO at D/A interface". *RSC Advances* 6 (2016), pp. 61934–61943. DOI: 10.1039/c6ra08385d (cited on p. 9).

[198] H. H. Ramanitra, S. A. Dowland, B. A. Bregadiolli, M. Salvador, H. S. Silva, D. Bégué, C. F. O. Graeff, H. Peisert, T. Chassé, S. Rajoelson, A. Osvet, C. J. Brabec, H.-J. Egelhaaf, G. E. Morse, A. Distler, and R. C. Hiorns. "Increased thermal stabilization of polymer photovoltaic cells with oligomeric PCBM". *Journal of Materials Chemistry C* 4 (2016), pp. 8121–8129. DOI: 10.1039/c6tc03290g (cited on p. 9).

[199] P. E. Keivanidis, F. Laquai, I. A. Howard, and R. H. Friend. "Room-Temperature Phase Demixing in Bulk Heterojunction Layers of Solution-Processed Organic Photodetectors: the Effect of Active Layer Ageing on the Device Electro-optical Properties". *Advanced Functional Materials* 21 (2011), pp. 1355–1363. DOI: 10.1002/adfm.201002214 (cited on p. 9).

[200] S. Engmann, V. Turkovic, H. Hoppe, and G. Gobsch. "Aging of polymer/fullerene films: Temporal development of composition profiles". *Synthetic Metals* 161 (2012), pp. 2540–2543. DOI: 10.1016/j.synthmet.2011.09.013 (cited on p. 9).

[201] A. M. Rao, P. Zhou, K.-A. Wang, G. T. Hager, J. M. Holden, Y. Wang, W.-T. Lee, X.-X. Bi, P. C. Eklund, D. S. Cornett, M. A. Duncan, and I. J. Amster. "Photoinduced Polymerization of Solid C60 Films". *Science* 259 (1993), pp. 955–957. DOI: 10.1126/science.259.5097.955 (cited on p. 9).

[202] A. Distler, T. Sauermann, H.-J. Egelhaaf, S. Rodman, D. Waller, K.-S. Cheon, M. Lee, and D. M. Guldi. "The Effect of PCBM Dimerization on the Performance of Bulk Heterojunction Solar Cells". *Advanced Energy Materials* 4 (2013), p. 1300693. DOI: 10.1002/aenm.201300693 (cited on p. 9).

[203] T. Heumueller, W. R. Mateker, A. Distler, U. F. Fritze, R. Cheacharoen, W. H. Nguyen, M. Biele, M. Salvador, M. von Delius, H.-J. Egelhaaf, and et al. "Morphological and electrical control of fullerene dimerization determines organic photovoltaic stability". *Energy & Environmental Science* 9 (2016), pp. 247–256. DOI: 10.1039/c5ee02912k (cited on p. 9).

[204] E. Bundgaard, M. Helgesen, J. E. Carlé, F. C. Krebs, and M. Jørgensen. "Advanced Functional Polymers for Increasing the Stability of Organic Photovoltaics". *Macromolecular Chemistry and Physics* 214 (2013), pp. 1546–1558. DOI: 10.1002/macp.201300076 (cited on pp. 10, 14).

[205] A. Tournebize, A. Rivaton, J.-L. Gardette, C. Lombard, B. Pépin-Donat, S. Beaupré, and M. Leclerc. "How Photoinduced Crosslinking Under Operating Conditions Can Reduce PCDTBT-Based Solar Cell Efficiency and then Stabilize It". *Advanced Energy Materials* 4 (2014), p. 1301530. DOI: 10.1002/aenm.201301530 (cited on p. 10).

[206] G. Wantz, L. Derue, O. Dautel, A. Rivaton, P. Hudhomme, and C. Dagron-Lartigau. "Stabilizing polymer-based bulk heterojunction solar cells via crosslinking". *Polymer International* 63 (2014), pp. 1346–1361. DOI: 10.1002/pi.4712 (cited on p. 10).

[207] J. Farinhas, R. Oliveira, J. Morgado, A. Charas, and J. Morgado. "Improved stability of organic solar cells by cross- linking of the electron-donor polymer". *IEEE PRIME* (2016). DOI: 10.1109/prime.2016.7519464 (cited on p. 10).

[208] J. E. Carlé, B. Andreasen, T. Tromholt, M. V. Madsen, K. Norrman, M. Jørgensen, and F. C. Krebs. "Comparative studies of photochemical cross-linking methods for stabilizing the bulk heterojunction morphology in polymer solar cells". *Journal of Materials Chemistry* 22 (2012), p. 24417. DOI: 10.1039/c2jm34284g (cited on pp. 10, 14).

[209] J. W. Rumer and I. McCulloch. "Organic photovoltaics: Crosslinking for optimal morphology and stability". *Materials Today* 18 (2015), pp. 425–435. DOI: 10.1016/j.mattod.2015.04.001 (cited on pp. 10, 14).

[210] H. S. Silva, A. Tournebize, D. Bégué, H. Peisert, T. Chassé, J.-L. Gardette, S. Therias, A. Rivaton, and R. C. Hiorns. "A universal route to improving conjugated macromolecule photostability". *RSC Advances* 4 (2014), pp. 54919–54923. DOI: 10.1039/C4RA10806J (cited on p. 10).

[211] R. R. Mohamed. "Photostabilization of polymers". *Additives for Polymers* 1991 (1991), pp. 14–15. DOI: 10.1016/0306-3747(91)90243-f (cited on p. 10).

[212] L. Ciammaruchi, F. Brunetti, and I. Visoly-Fisher. "Solvent effects on the morphology and stability of PTB7:PCBM based solar cells". *Solar Energy* 137 (2016), pp. 490–499. DOI: 10.1016/j.solener.2016.08.018 (cited on p. 10).

[213] J. Kesters, P. Verstappen, J. Raymakers, W. Vanormelingen, J. Drijkoningen, J. D'Haen, J. Manca, L. Lutsen, D. Vanderzande, and W. Maes. "Enhanced Organic Solar Cell Stability by Polymer (PCPDTBT) Side Chain Functionalization". *Chemistry of Materials* 27 (2015), pp. 1332–1341. DOI: 10.1021/cm504391k (cited on pp. 10, 14).

[214] G. E. Morse, A. Tournebize, A. Rivaton, T. Chassé, C. Taviot-Gueho, N. Blouin, O. R. Lozman, and S. Tierney. "The effect of polymer solubilizing side-chains on solar cell stability". *Physical Chemistry Chemical Physics* 17 (2015), pp. 11884–11897. DOI: 10.1039/C5CP01158B (cited on pp. 10, 14).

[215] H. J. Son, S. H. Kim, and D. H. Kim. "Critical Impact of Hole Transporting Layers and Back Electrode on the Stability of Flexible Organic Photovoltaic Module". *Advanced Energy Materials* 7 (2016), p. 1601289. DOI: 10.1002/aenm.201601289 (cited on p. 10).

[216] B. Roth, G. A. dos Reis Benatto, M. Corazza, R. R. Søndergaard, S. A. Gevorgyan, M. Jørgensen, and F. C. Krebs. "The Critical Choice of PEDOT:PSS Additives for Long Term Stability of Roll-to-Roll Processed OPVs". *Advanced Energy Materials* 5 (2015), p. 1401912. DOI: 10.1002/aenm.201401912 (cited on p. 10).

[217] A. Savva, E. Georgiou, G. Papazoglou, A. Z. Chrusou, K. Kapnisis, and S. A. Choulis. "Photovoltaic analysis of the effects of PEDOT:PSS-additives hole selective contacts on the efficiency and lifetime performance of inverted organic solar cells". *Solar Energy Materials & Solar Cells* 132 (2015), pp. 507–514. DOI: 10.1016/j.solmat.2014.10.004 (cited on p. 10).

[218] G. del Pozo, B. Arredondo, B. Romero, G. Susanna, and F. Brunetti. "Degradation of PEIE interlayer in PTB7:[70]PCBM based solar cells characterized by impedance spectroscopy". *Solar Energy* 144 (2017), pp. 105–110. DOI: 10.1016/j.solener.2017.01.003 (cited on p. 10).

[219] M. P. de Jong, L. J. van IJzendoorn, and M. J. A. de Voigt. "Stability of the interface between indium-tin-oxide and poly(3,4-ethylenedioxythiophene)/poly(styrenesulfonate) in polymer light-emitting diodes". *Applied Physics Letters* 77 (2000), pp. 2255–2257. DOI: 10.1063/1.1315344 (cited on pp. 10, 11).

[220] T. Glen, N. Scarratt, H. Yi, A. Iraqi, T. Wang, J. Kingsley, A. Buckley, D. Lidzey, and A. Donald. "Grain size dependence of degradation of aluminium/calcium cathodes in organic solar cells following exposure to humid air". *Solar Energy Materials & Solar Cells* 140 (2015), pp. 25–32. DOI: 10.1016/j.solmat.2015.03.015 (cited on pp. 10, 11).

[221] B. Ecker, J. C. Nolasco, J. Pallarés, L. F. Marsal, J. Posdorfer, J. Parisi, and E. von Hauff. "Degradation Effects Related to the Hole Transport Layer in Organic Solar Cells". *Advanced Functional Materials* 21 (2011), pp. 2705–2711. DOI: 10.1002/adfm.201100429 (cited on p. 10).

[222] E. Voroshazi, B. Verreet, A. Buri, R. Müller, D. D. Nuzzo, and P. Heremans. "Influence of cathode oxidation via the hole extraction layer in polymer:fullerene solar cells". *Organic Electronics* 12 (2011), pp. 736–744. DOI: 10.1016/j.orgel.2011.01.025 (cited on pp. 10, 11, 83, 86, 97).

[223] N. Koch, A. Vollmer, and A. Elschner. "Influence of water on the work function of conducting poly(3,4-ethylenedioxythiophene)/(poly(styrenesulfonate)". *Applied Physics Letters* 90 (2007), p. 043512. DOI: 10.1063/1.2435350 (cited on pp. 10, 119).

[224] Y.-J. Lin, F.-M. Yang, C.-Y. Huang, W.-Y. Chou, J. Chang, and Y.-C. Lien. "Increasing the work function of poly(3,4-ethylenedioxythiophene) doped with poly(4-styrenesulfonate) by ultraviolet irradiation". *Applied Physics Letters* 91 (2007), p. 092127. DOI: 10.1063/1.2777147 (cited on p. 10).

[225] Y. Meng, Z. Hu, N. Ai, Z. Jiang, J. Wang, J. Peng, and Y. Cao. "Improving the Stability of Bulk Heterojunction Solar Cells by Incorporating pH-Neutral PEDOT:PSS as the Hole Transport Layer". *ACS Applied Materials & Interfaces* 6 (2014), pp. 5122–5129. DOI: 10.1021/am500336s (cited on p. 10).

[226] W. C. H. Choy and D. Zhang. "Solution-Processed Metal Oxides as Efficient Carrier Transport Layers for Organic Photovoltaics". *Small* 12 (2015), pp. 416–431. DOI: 10.1002/smll.201502258 (cited on p. 10).

[227] F. Wang, Z. Tan, and Y. Li. "Solution-processable metal oxides/chelates as electrode buffer layers for efficient and stable polymer solar cells". *Energy & Environmental Science* 8 (2015), pp. 1059–1091. DOI: 10.1039/c4ee03802a (cited on p. 10).

[228] S. Züfle, M. T. Neukom, S. Altazin, M. Zinggeler, M. Chrapa, T. Offermans, and B. Ruhstaller. "An Effective Area Approach to Model Lateral Degradation in Organic Solar Cells". *Advanced Energy Materials* 5 (2015), p. 1500835. DOI: 10.1002/aenm.201500835 (cited on pp. 10, 14, 25, 48, 52, 63, 97).

[229] A. Garg, S. K. Gupta, J. J. Jasieniak, T. B. Singh, and S. E. Watkins. "Improved lifetimes of organic solar cells with solution-processed molybdenum oxide anode-modifying layers: Improved lifetimes of organic solar cells". *Progress in Photovoltaics: Research and Applications* 23 (2014), pp. 989–996. DOI: 10.1002/pip.2512 (cited on pp. 10, 14).

[230] Y.-H. Lou, Z.-K. Wang, D.-X. Yuan, H. Okada, and L.-S. Liao. "Interfacial degradation effects of aqueous solution-processed molybdenum trioxides on the stability of organic solar cells evaluated by a differential method". *Applied Physics Letters* 105 (2014), p. 113301. DOI: 10.1063/1.4895805 (cited on p. 10).

[231] W. J. Dong, G. H. Jung, and J.-L. Lee. "Solution-processed-MoO_3 hole extraction layer on oxygen plasma-treated indium tin oxide in organic photovoltaics". *Solar Energy Materials & Solar Cells* 116 (2013), pp. 94–101. DOI: 10.1016/j.solmat.2013.04.005 (cited on p. 10).

[232] M.-Y. Lin, C.-Y. Lee, S.-C. Shiu, I.-J. Wang, J.-Y. Sun, W.-H. Wu, Y.-H. Lin, J.-S. Huang, and C.-F. Lin. "Sol-gel processed CuOx thin film as an anode interlayer for inverted polymer solar cells". *Organic Electronics* 11 (2010), pp. 1828–1834. DOI: 10.1016/j.orgel.2010.08.009 (cited on p. 11).

[233] K. X. Steirer, J. P. Chesin, N. E. Widjonarko, J. J. Berry, A. Miedaner, D. S. Ginley, and D. C. Olson. "Solution deposited NiO thin-films as hole transport layers in organic photovoltaics". *Organic Electronics* 11 (2010), pp. 1414–1418. DOI: 10.1016/j.orgel.2010.05.008 (cited on p. 11).

[234] C. Girotto, E. Voroshazi, D. Cheyns, P. Heremans, and B. P. Rand. "Solution-Processed MoO_3 Thin Films As a Hole-Injection Layer for Organic Solar Cells". *ACS Applied Materials & Interfaces* 3 (2011), pp. 3244–3247. DOI: 10.1021/am200729k (cited on pp. 11, 14).

[235] H. Choi, B. Kim, M. J. Ko, D.-K. Lee, H. Kim, S. H. Kim, and K. Kim. "Solution processed WO_3 layer for the replacement of PEDOT:PSS layer in organic photovoltaic cells". *Organic Electronics* 13 (2012), pp. 959–968. DOI: 10.1016/j.orgel.2012.01.033 (cited on p. 11).

[236] G. Terán-Escobar, J. Pampel, J. M. Caicedo, and M. Lira-Cantú. "Low-temperature, solution-processed, layered V_2O_5 hydrate as the hole-transport layer for stable organic solar cells". *Energy & Environmental Science* 6 (2013), pp. 3088–3098. DOI: 10.1039/c3ee42204f (cited on p. 11).

[237] D. X. Long, Y. Xu, S.-J. Kang, W.-T. Park, E.-Y. Choi, Y.-C. Nah, C. Liu, and Y.-Y. Noh. "Solution processed vanadium pentoxide as charge injection layer in polymer field-effect transistor with Mo electrodes". *Organic Electronics* 17 (2015), pp. 66–76. DOI: 10.1016/j.orgel.2014.11.020 (cited on p. 11).

[238] A. Alsulami, J. Griffin, R. Alqurashi, H. Yi, A. Iraqi, D. Lidzey, and A. Buckley. "Thermally Stable Solution Processed Vanadium Oxide as a Hole Extraction Layer in Organic Solar Cells". *Materials* 9 (2016), p. 235. DOI: 10.3390/ma9040235 (cited on p. 11).

[239] F. A. S. Lima, M. J. Beliatis, B. Roth, T. R. Andersen, A. Bortoti, Y. Reyna, E. Castro, I. F. Vasconcelos, S. A. Gevorgyan, F. C. Krebs, and M. Lira-Cantu. "Flexible ITO-free organic solar cells applying aqueous solution-processed V_2O_5 hole transport layer: An outdoor stability study". *APL Materials* 4 (2016), p. 026104. DOI: 10.1063/1.4942638 (cited on p. 11).

[240] T. Yamanari, T. Taima, J. Sakai, J. Tsukamoto, and Y. Yoshida. "Effect of Buffer Layers on Stability of Polymer-Based Organic Solar Cells". *Japanese Journal of Applied Physics* 49 (2010), 01AC02. DOI: 10.1143/JJAP.49.01AC02 (cited on pp. 11, 14, 84).

[241] M. Wang, F. Xie, J. Du, Q. Tang, S. Zheng, Q. Miao, J. Chen, N. Zhao, and J. Xu. "Degradation mechanism of organic solar cells with aluminum cathode". *Solar Energy Materials & Solar Cells* 95 (2011), pp. 3303–3310. DOI: 10.1016/j.solmat.2011.07.020 (cited on pp. 11, 84, 86).

[242] M. Seeland, R. Rösch, and H. Hoppe. "Luminescence imaging of polymer solar cells: Visualization of progressing degradation". *Journal of Applied Physics* 109 (2011), p. 064513. DOI: 10.1063/1.3553864 (cited on pp. 11, 84).

[243] J. Adams, M. Salvador, L. Lucera, S. Langner, G. D. Spyropoulos, F. W. Fecher, M. M. Voigt, S. A. Dowland, A. Osvet, H.-J. Egelhaaf, and C. J. Brabec. "Water Ingress in Encapsulated Inverted Organic Solar Cells: Correlating Infrared Imaging and Photovoltaic Performance". *Advanced Energy Materials* 5 (2015), p. 1501065. DOI: 10.1002/aenm.201501065 (cited on p. 11).

[244] K. Feron, T. J. Nagle, L. J. Rozanski, B. B. Gong, and C. J. Fell. "Spatially resolved photocurrent measurements of organic solar cells: Tracking water ingress at edges and pinholes". *Solar Energy Materials & Solar Cells* 109 (2013), pp. 169–177. DOI: 10.1016/j.solmat.2012.10.027 (cited on pp. 11, 84, 95).

[245] D. Han, H. Lee, S. Jeong, J. Lee, J.-Y. Lee, and S. Yoo. "Stability enhancement of normal-geometry organic solar cells in a highly damp condition: A study on the effect of top electrodes". *Organic Electronics* 25 (2015), pp. 31–36. DOI: 10.1016/j.orgel.2015.06.008 (cited on p. 11).

[246] T. S. Glen, N. W. Scarratt, H. Yi, A. Iraqi, T. Wang, J. Kingsley, A. R. Buckley, D. G. Lidzey, and A. M. Donald. "Dependence on material choice of degradation of organic solar cells following exposure to humid air". *Journal of Polymer Science, Part B* 54 (2015), pp. 216–224. DOI: 10.1002/polb.23905 (cited on p. 11).

[247] M. O. Reese, A. J. Morfa, M. S. White, N. Kopidakis, S. E. Shaheen, G. Rumbles, and D. S. Ginley. "Short-Term Metal/Organic Interface Stability Investigations of Organic Photovoltaic Devices". *IEEE PVSC* (2008). DOI: 10.1109/pvsc.2008.4922720 (cited on p. 11).

[248] S. Savagatrup, A. D. Printz, T. F. O'Connor, A. V. Zaretski, D. Rodriquez, E. J. Sawyer, K. M. Rajan, R. I. Acosta, S. E. Root, and D. J. Lipomi. "Mechanical degradation and stability of organic solar cells: molecular and microstructural determinants". *Energy & Environmental Science* 8 (2015), pp. 55–80. DOI: 10.1039/C4EE02657H (cited on p. 11).

[249] M. Corazza, N. Rolston, R. H. Dauskardt, M. Beliatis, F. C. Krebs, and S. A. Gevorgyan. "Role of Stress Factors on the Adhesion of Interfaces in R2R Fabricated Organic Photovoltaics". *Advanced Energy Materials* 6 (2016), p. 1501927. DOI: 10.1002/aenm.201501927 (cited on p. 11).

[250] J.-H. Kim, I. Lee, T.-S. Kim, N. Rolston, B. L. Watson, and R. H. Dauskardt. "Understanding mechanical behavior and reliability of organic electronic materials". *MRS Bulletin* 42 (2017), pp. 115–123. DOI: 10.1557/mrs.2017.3 (cited on p. 11).

[251] T. Xiao, F. Fungura, M. Cai, J. W. Anderegg, J. Shinar, and R. Shinar. "Improved efficiency and stability of inverted polymer solar cells with a solution-processed BPhen interlayer and polystyrene beads". *Organic Electronics* 14 (2013), pp. 2555–2563. DOI: 10.1016/j.orgel.2013.06.019 (cited on pp. 11, 14).

[252] A. Turak. "Interfacial degradation in organic optoelectronics". *RSC Advances* 3 (2013), pp. 6188–6225. DOI: 10.1039/c2ra22770c (cited on p. 11).

[253] E. Voroshazi, I. Cardinaletti, G. Uytterhoeven, S. Li, M. Empl, T. Aernouts, and B. P. Rand. "Role of Electron- and Hole-Collecting Buffer Layers on the Stability of Inverted Polymer: Fullerene Pho-

tovoltaic Devices". *IEEE Journal of Photovoltaics* 4 (2014), pp. 265–270. DOI: 10.1109/jphotov.2013.2287913 (cited on p. 11).

[254] M. Wang, F. Xie, W. Xie, S. Zheng, N. Ke, J. Chen, and N. Zhao. "Device lifetime improvement of polymer-based bulk heterojunction solar cells by incorporating copper oxide layer at Al cathode". *Applied Physics Letters* 98 (2011), p. 183304. DOI: 10.1063/1.3580629 (cited on p. 11).

[255] S. Kundu, S. R. Gollu, R. Sharma, S. G, A. Ashok, A. Kulkarni, and D. Gupta. "Device stability of inverted and conventional bulk heterojunction solar cells with MoO_3 and ZnO nanoparticles as charge transport layers". *Organic Electronics* 14 (2013), pp. 3083–3088. DOI: 10.1016/j.orgel.2013.07.016 (cited on pp. 11, 13).

[256] X. Hao, S. Wang, T. Sakurai, S. Masuda, and K. Akimoto. "Improvement of Stability for Small Molecule Organic Solar Cells by Suppressing the Trap Mediated Recombination". *ACS Applied Materials & Interfaces* 7 (2015), pp. 18379–18386. DOI: 10.1021/acsami.5b04334 (cited on pp. 11, 13).

[257] D. Han and S. Yoo. "The stability of normal vs. inverted organic solar cells under highly damp conditions: Comparison with the same interfacial layers". *Solar Energy Materials & Solar Cells* 128 (2014), pp. 41–47. DOI: 10.1016/j.solmat.2014.04.036 (cited on pp. 11, 13).

[258] A. Sharma, G. Andersson, and D. A. Lewis. "Role of humidity on indium and tin migration in organic photovoltaic devices". *Physical Chemistry Chemical Physics* 13 (2011), pp. 4381–4387. DOI: 10.1039/c0cp02203a (cited on p. 11).

[259] M. Girtan and M. Rusu. "Role of ITO and PEDOT:PSS in stability/degradation of polymer:fullerene bulk heterojunctions solar cells". *Solar Energy Materials & Solar Cells* 94 (2010), pp. 446–450. DOI: 10.1016/j.solmat.2009.10.026 (cited on p. 11).

[260] K. He, X. Yang, H. Yan, Z. Wu, Z. Li, S. Zhong, Q. Ou, and R. Liang. "Work function changes of plasma treated indium tin oxide". *Organic Electronics* 15 (2014), pp. 1731–1737. DOI: 10.1016/j.orgel.2014.05.008 (cited on p. 11).

[261] M. Hermenau, K. Leo, and M. Riede. "Comparison of different conditions for accelerated ageing of small molecule organic solar cells". *Proceedings of SPIE* 7722 (2010). Ed. by P. L. Heremans, R. Coehoorn, and C. Adachi, 77220K. DOI: 10.1117/12.853834 (cited on p. 11).

[262] X. Wang, C. X. Zhao, G. Xu, Z.-K. Chen, and F. Zhu. "Degradation mechanisms in organic solar cells: Localized moisture encroachment and cathode reaction". *Solar Energy Materials & Solar Cells* 104 (2012), pp. 1–6. DOI: 10.1016/j.solmat.2012.04.038 (cited on pp. 11, 84, 86).

[263] M. Giannouli, V. M. Drakonakis, A. Savva, P. Eleftheriou, G. Florides, and S. A. Choulis. "Methods for Improving the Lifetime Performance of Organic Photovoltaics with Low-Costing Encapsulation". *ChemPhysChem* 16 (2015), pp. 1134–1154. DOI: 10.1002/cphc.201402749 (cited on p. 11).

[264] J. A. Hauch, P. Schilinsky, S. A. Choulis, R. Childers, M. Biele, and C. J. Brabec. "Flexible organic P3HT:PCBM bulk-heterojunction modules with more than 1 year outdoor lifetime". *Solar Energy Materials & Solar Cells* 92 (2008), pp. 727–731. DOI: 10.1016/j.solmat.2008.01.004 (cited on p. 11).

[265] J. A. Hauch, P. Schilinsky, S. A. Choulis, S. Rajoelson, and C. J. Brabec. "The impact of water vapor transmission rate on the lifetime of flexible polymer solar cells". *Applied Physics Letters* 93 (2008), p. 103306. DOI: 10.1063/1.2975185 (cited on p. 11).

[266] M. D. Kempe, A. A. Dameron, and M. O. Reese. "Evaluation of moisture ingress from the perimeter of photovoltaic modules". *Progress in Photovoltaics: Research and Applications* 22 (2013), pp. 1159–1171. DOI: 10.1002/pip.2374 (cited on pp. 11, 94).

[267] R. Roesch, K.-R. Eberhardt, S. Engmann, G. Gobsch, and H. Hoppe. "Polymer solar cells with enhanced lifetime by improved electrode stability and sealing". *Solar Energy Materials & Solar Cells* 117 (2013), pp. 59–66. DOI: 10.1016/j.solmat.2013.05.013 (cited on pp. 11, 14).

[268] J. Ahmad, K. Bazaka, L. J. Anderson, R. D. White, and M. V. Jacob. "Materials and methods for encapsulation of OPV: A review". *Renewable and Sustainable Energy Reviews* 27 (2013), pp. 104–117. DOI: 10.1016/j.rser.2013.06.027 (cited on pp. 11, 13).

[269] H. C. Weerasinghe, S. E. Watkins, N. Duffy, D. J. Jones, and A. D. Scully. "Influence of moisture out-gassing from encapsulant materials on the lifetime of organic solar cells". *Solar Energy Materials & Solar Cells* 132 (2015), pp. 485–491. DOI: 10.1016/j.solmat.2014.09.030 (cited on p. 11).

[270] D. Yu, Y.-Q. Yang, Z. Chen, Y. Tao, and Y.-F. Liu. "Recent progress on thin-film encapsulation technologies for organic electronic devices". *Optics Communications* 362 (2016), pp. 43–49. DOI: 10.1016/j.optcom.2015.08.021 (cited on p. 11).

[271] H. C. Weerasinghe, D. Vak, B. Robotham, C. J. Fell, D. Jones, and A. D. Scully. "New barrier encapsulation and lifetime assessment of printed organic photovoltaic modules". *Solar Energy Materials & Solar Cells* 155 (2016), pp. 108–116. DOI: 10.1016/j.solmat.2016.04.051 (cited on p. 11).

[272] D. M. Tanenbaum, M. Hermenau, E. Voroshazi, M. T. Lloyd, Y. Galagan, B. Zimmermann, M. Hösel, H. F. Dam, M. Jørgensen, S. A. Gevorgyan, and et al. "The ISOS-3 inter-laboratory collaboration focused on the stability of a variety of organic photovoltaic devices". *RSC Advances* 2 (2012), pp. 882–893. DOI: 10.1039/c1ra00686j (cited on p. 12).

[273] S. A. Gevorgyan, M. Corazza, M. V. Madsen, G. Bardizza, A. Pozza, H. Müllejans, J. C. Blakesley, G. F. Dibb, F. A. Castro, J. F. Trigo, and et al. "Interlaboratory indoor ageing of roll-to-roll and spin coated organic photovoltaic devices: Testing the ISOS tests". *Polymer Degradation and Stability* 109 (2014), pp. 162–170. DOI: 10.1016/j.polymdegradstab.2014.07.013 (cited on p. 12).

[274] F. C. Krebs et al. "A round robin study of flexible large-area roll-to-roll processed polymer solar cell modules". *Solar Energy Materials & Solar Cells* 93 (2009), pp. 1968–1977. DOI: 10.1016/j.solmat.2009.07.015 (cited on p. 12).

[275] G. Teran-Escobar, D. M. Tanenbaum, E. Voroshazi, M. Hermenau, K. Norrman, M. T. Lloyd, Y. Galagan, B. Zimmermann, M. Hösel, H. F. Dam, M. Jørgensen, S. Gevorgyan, S. Kudret, W. Maes, L. Lutsen, D. Vanderzande, U. Würfel, R. Andriessen, R. Rösch, H. Hoppe, A. Rivaton, G. Y. Uzunoğlu, D. Germack, B. Andreasen, M. V. Madsen, E. Bundgaard, F. C. Krebs, and M. Lira-Cantu. "On the stability of a variety of organic photovoltaic devices by IPCE and in situ IPCE analyses - the ISOS-3 inter-laboratory collaboration". *Physical Chemistry Chemical Physics* 14 (2012), pp. 11824–11845. DOI: 10.1039/c2cp40821j (cited on p. 12).

[276] S. A. Gevorgyan, M. V. Madsen, H. F. Dam, M. Jørgensen, C. J. Fell, K. F. Anderson, B. C. Duck, A. Mescheloff, E. A. Katz, A. Elschner, R. Roesch, H. Hoppe, M. Hermenau, M. Riede, and F. C. Krebs. "Interlaboratory outdoor stability studies of flexible roll-to-roll coated organic photovoltaic modules: Stability over 10,000h". *Solar Energy Materials & Solar Cells* 116 (2013), pp. 187–196. DOI: 10.1016/j.solmat.2013.04.024 (cited on pp. 12, 14).

[277] C. Owens, G. Ferguson, M. Hermenau, E. Voroshazi, Y. Galagan, B. Zimmermann, R. Rösch, D. Angmo, G. Teran-Escobar, C. Uhrich, R. Andriessen, H. Hoppe, U. Würfel, M. Lira-Cantu, F. Krebs, and D. Tanenbaum. "Comparative Indoor and Outdoor Degradation of Organic Photovoltaic Cells via Inter-laboratory Collaboration". *Polymers* 8 (2015), p. 1. DOI: 10.3390/polym8010001 (cited on p. 12).

[278] M. Lira-Cantu, D. M. Tanenbaum, K. Norrman, E. Voroshazi, M. Hermenau, M. T. Lloyd, G. Teran-Escobar, Y. Galagan, B. Zimmermann, M. Hösel, H. F. Dam, M. Jørgensen, S. Gevorgyan, L. Lutsen, D. Vanderzande, H. Hoppe, R. Rösch, U. Würfel, R. Andriessen, A. Rivaton, G. Y. Uzunoğlu, D. Germack, B. Andreasen, M. V. Madsen, E. Bundgaard, and F. C. Krebs. "Combined characterization techniques to understand the stability of a variety of organic photovoltaic devices: the ISOS-3 inter-laboratory collaboration". *Proceedings of SPIE* 8472 (2012). Ed. by N. G. Dhere and J. H. Wohlgemuth, p. 847203. DOI: 10.1117/12.929579 (cited on p. 12).

[279] R. Rösch, D. M. Tanenbaum, M. Jørgensen, M. Seeland, M. Bärenklau, M. Hermenau, E. Voroshazi, M. T. Lloyd, Y. Galagan, B. Zimmermann, U. Würfel, M. Hösel, H. F. Dam, S. A. Gevorgyan, S. Kudret, W. Maes, L. Lutsen, D. Vanderzande, R. Andriessen, G. Teran-Escobar, M. Lira-Cantu, A. Rivaton, G. Y. Uzunoğlu, D. Germack, B. Andreasen, M. V. Madsen, K. Norrman, H. Hoppe, and F. C. Krebs. "Investigation of the degradation mechanisms of a variety of organic photovoltaic

devices by combination of imaging techniques - the ISOS-3 inter-laboratory collaboration". *Energy & Environmental Science* 5 (2012), pp. 6521–6540. DOI: 10.1039/c2ee03508a (cited on p. 12).

[280] R. R. Søndergaard, T. Makris, P. Lianos, A. Manor, E. A. Katz, W. Gong, S. M. Tuladhar, J. Nelson, R. Tuomi, P. Sommeling, S. C. Veenstra, A. Rivaton, A. Dupuis, G. Teran-Escobar, M. Lira-Cantu, S. B. Sapkota, B. Zimmermann, U. Würfel, A. Matzarakis, and F. C. Krebs. "The use of polyurethane as encapsulating method for polymer solar cells - An inter laboratory study on outdoor stability in 8 countries". *Solar Energy Materials & Solar Cells* 99 (2012), pp. 292–300. DOI: 10.1016/j.solmat.2011.12.013 (cited on p. 12).

[281] D. M. Tanenbaum, M. Hermenau, E. Voroshazi, M. T. Lloyd, Y. Galagan, B. Zimmermann, M. Hösel, H. F. Dam, M. Jørgensen, S. Gevorgyan, S. Kudret, W. Maes, L. Lutsen, D. Vanderzande, U. Würfel, R. Andriessen, R. Rösch, H. Hoppe, M. Lira-Cantu, G. Teran-Escobar, A. Dupuis, P.-O. Bussière, A. Rivaton, G. Y. Uzunoglu, D. Germack, B. Andreasen, M. V. Madsen, K. Norrman, E. Bundgaard, and F. C. Krebs. "Stability and degradation of organic photovoltaics fabricated , aged , and characterized by the ISOS 3 inter-laboratory collaboration". *Proceedings of SPIE* 8477 (2012). Ed. by Z. H. Kafafi, C. J. Brabec, and P. A. Lane, p. 847704. DOI: 10.1117/12.930451 (cited on p. 12).

[282] M. O. Reese, S. A. Gevorgyan, M. Jørgensen, E. Bundgaard, S. R. Kurtz, D. S. Ginley, D. C. Olson, M. T. Lloyd, P. Morvillo, E. a. Katz, and et al. "Consensus stability testing protocols for organic photovoltaic materials and devices". *Solar Energy Materials & Solar Cells* 95 (2011), pp. 1253–1267. DOI: 10.1016/j.solmat.2011.01.036 (cited on pp. 12, 113).

[283] P. Kumar, C. Bilen, B. Vaughan, X. Zhou, P. C. Dastoor, and W. J. Belcher. "Comparing the degradation of organic photovoltaic devices under ISOS testing protocols". *Solar Energy Materials & Solar Cells* 149 (2016), pp. 179–186. DOI: 10.1016/j.solmat.2015.12.032 (cited on p. 12).

[284] J. Kettle, V. Stoichkov, D. Kumar, M. Corazza, S. Gevorgyan, and F. Krebs. "Using ISOS consensus test protocols for development of quantitative life test models in ageing of organic solar cells". *Solar Energy Materials & Solar Cells* 167 (2017), pp. 53–59. DOI: 10.1016/j.solmat.2017.04.005 (cited on p. 12).

[285] M. Corazza, F. C. Krebs, and S. A. Gevorgyan. "Lifetime of organic photovoltaics: Linking outdoor and indoor tests". *Solar Energy Materials & Solar Cells* 143 (2015), pp. 467–472. DOI: 10.1016/j.solmat.2015.07.037 (cited on p. 13).

[286] G. A. dos Reis Benatto, M. Corazza, B. Roth, F. Schütte, M. Rengenstein, S. A. Gevorgyan, and F. C. Krebs. "Inside or Outside? Linking Outdoor and Indoor Lifetime Tests of ITO-Free Organic Photovoltaic Devices for Greenhouse Applications". *Energy Technology* 5 (2016), pp. 338–344. DOI: 10.1002/ente.201600335 (cited on p. 13).

[287] N. Bristow and J. Kettle. "Outdoor performance of organic photovoltaics: Diurnal analysis, dependence on temperature, irradiance, and degradation". *Journal of Renewable and Sustainable Energy* 7 (2015), p. 013111. DOI: 10.1063/1.4906915 (cited on p. 13).

[288] K. Norrman, M. V. Madsen, S. A. Gevorgyan, and F. C. Krebs. "Degradation Patterns in Water and Oxygen of an Inverted Polymer Solar Cell". *Journal of the American Chemical Society* 132 (2010), pp. 16883–16892. DOI: 10.1021/ja106299g (cited on p. 13).

[289] P. van de Weijer, P. C. Bouten, S. Unnikrishnan, H. B. Akkerman, J. J. Michels, and T. M. van Mol. "High-performance thin-film encapsulation for organic light-emitting diodes". *Organic Electronics* 44 (2017), pp. 94–98. DOI: 10.1016/j.orgel.2017.02.009 (cited on p. 13).

[290] M.-F. Xu, L.-S. Cui, X.-Z. Zhu, C.-H. Gao, X.-B. Shi, Z.-M. Jin, Z.-K. Wang, and L.-S. Liao. "Aqueous solution-processed MoO3 as an effective interfacial layer in polymer/fullerene based organic solar cells". *Organic Electronics* 14 (2013), pp. 657–664. DOI: 10.1016/j.orgel.2012.12.016 (cited on p. 14).

[291] M. Kielar, O. Dhez, G. Pecastaings, A. Curutchet, and L. Hirsch. "Long-Term Stable Organic Photodetectors with Ultra Low Dark Currents for High Detectivity Applications". *Scientific Reports* 6 (2016), p. 39201. DOI: 10.1038/srep39201 (cited on p. 14).

[292] Y. Zhang, E. Bovill, J. Kingsley, A. R. Buckley, H. Yi, A. Iraqi, T. Wang, and D. G. Lidzey. "PCDTBT based solar cells: one year of operation under real-world conditions". *Scientific Reports* 6 (2016), p. 21632. DOI: 10.1038/srep21632 (cited on pp. 14, 116).

[293] D. Angmo, P. M. Sommeling, R. Gupta, M. Hösel, S. A. Gevorgyan, J. M. Kroon, G. U. Kulkarni, and F. C. Krebs. "Outdoor Operational Stability of Indium-Free Flexible Polymer Solar Modules Over 1 Year Studied in India, Holland, and Denmark". *Advanced Engineering Materials* 16 (2014), pp. 976–987. DOI: 10.1002/adem.201400002 (cited on p. 14).

[294] J. Kong, S. Song, M. Yoo, G. Y. Lee, O. Kwon, J. K. Park, H. Back, G. Kim, S. H. Lee, H. Suh, and K. Lee. "Long-term stable polymer solar cells with significantly reduced burn-in loss". *Nature Communications* 5 (2014), p. 5688. DOI: 10.1038/ncomms6688 (cited on pp. 14, 116).

[295] D. Angmo and F. C. Krebs. "Over 2 Years of Outdoor Operational and Storage Stability of ITO-Free, Fully Roll-to-Roll Fabricated Polymer Solar Cell Modules". *Energy Technology* 3 (2015), pp. 774–783. DOI: 10.1002/ente.201500086 (cited on p. 14).

[296] A. Karpinski, S. Berson, H. Terrisse, M. M.-L. Granvalet, S. Guillerez, L. Brohan, and M. Richard-Plouet. "Anatase colloidal solutions suitable for inkjet printing: Enhancing lifetime of hybrid organic solar cells". *Solar Energy Materials & Solar Cells* 116 (2013), pp. 27–33. DOI: 10.1016/j.solmat.2013.04.006 (cited on p. 14).

[297] C. H. Peters, I. T. Sachs-Quintana, J. P. Kastrop, S. Beaupré, M. Leclerc, and M. D. McGehee. "High Efficiency Polymer Solar Cells with Long Operating Lifetimes". *Advanced Energy Materials* 1 (2011), pp. 491–494. DOI: 10.1002/aenm.201100138 (cited on p. 14).

[298] *Platform for All-In-One characterisation of Solar Cells, Fluxim AG, www.fluxim.com*. 2017 (cited on p. 15).

[299] *Setfos 4.4, Fluxim AG, www.fluxim.com*. 2017 (cited on pp. 15, 32, 59).

[300] Cree. *Power LED white XP-G*. (Cited on pp. 17, 113, 137).

[301] J. C. Maxwell. *A Treatise on Electricity and Magnetism*. Dover Publications Inc., 1873. 560 pp. ISBN: 0486606368 (cited on p. 18).

[302] M. Neukom, N. Reinke, and B. Ruhstaller. "Charge extraction with linearly increasing voltage: A numerical model for parameter extraction". *Solar Energy* 85 (2011), pp. 1250–1256. DOI: 10.1016/j.solener.2011.02.028 (cited on pp. 19, 25, 27, 48).

[303] M. T. Neukom. "Charge Carrier Dynamics of Methylammonium Lead-Iodide Perovskite Solar Cells". *Masters Thesis* (2016). arXiv: 1611.06425v1 [cond-mat.mtrl-sci] (cited on p. 20).

[304] P. W. M. Blom, V. D. Mihailetchi, L. J. A. Koster, and D. E. Markov. "Device Physics of Polymer:Fullerene Bulk Heterojunction Solar Cells". *Advanced Materials* 19 (2007), pp. 1551–1566. DOI: 10.1002/adma.200601093 (cited on p. 21).

[305] L. J. A. Koster, V. D. Mihailetchi, R. Ramaker, and P. W. M. Blom. "Light intensity dependence of open-circuit voltage of polymer:fullerene solar cells". *Applied Physics Letters* 86 (2005), p. 123509. DOI: 10.1063/1.1889240 (cited on pp. 21, 31).

[306] A. Foertig, J. Rauh, V. Dyakonov, and C. Deibel. "Shockley equation parameters of P3HT:PCBM solar cells determined by transient techniques". *Physical Review B* 86 (2012), p. 115302. DOI: 10.1103/PhysRevB.86.115302 (cited on pp. 21, 24).

[307] D. Rauh, A. Wagenpfahl, C. Deibel, and V. Dyakonov. "Relation of open circuit voltage to charge carrier density in organic bulk heterojunction solar cells". *Applied Physics Letters* 98, 133301 (2011), p. 133301. DOI: http://dx.doi.org/10.1063/1.3566979 (cited on p. 21).

[308] A. Maurano, R. Hamilton, C. G. Shuttle, A. M. Ballantyne, J. Nelson, B. O'Regan, W. Zhang, I. McCulloch, H. Azimi, M. Morana, C. J. Brabec, and J. R. Durrant. "Recombination Dynamics as a Key Determinant of Open Circuit Voltage in Organic Bulk Heterojunction Solar Cells: A Comparison of Four Different Donor Polymers". *Advanced Materials* 22 (2010), pp. 4987–4992. DOI: 10.1002/adma.201002360 (cited on p. 21).

[309] K. Vandewal, K. Tvingstedt, A. Gadisa, O. Inganäs, and J. V. Manca. "On the origin of the open-circuit voltage of polymer-fullerene solar cells". *Nature Materials* 8 (2009), pp. 904–909. DOI: 10.1038/nmat2548 (cited on p. 21).

[310] T. Kirchartz, F. Deledalle, P. S. Tuladhar, J. R. Durrant, and J. Nelson. "On the Differences between Dark and Light Ideality Factor in Polymer:Fullerene Solar Cells". *The Journal of Physical Chemistry Letters* 4 (2013), pp. 2371–2376. DOI: 10.1021/jz4012146 (cited on p. 21).

[311] L. J. A. Koster, V. D. Mihailetchi, H. Xie, and P. W. M. Blom. "Origin of the light intensity dependence of the short-circuit current of polymer/fullerene solar cells". *Applied Physics Letters* 87, 203502 (2005), p. 203502. DOI: http://dx.doi.org/10.1063/1.2130396 (cited on p. 21).

[312] J. Greulich, M. Glatthaar, and S. Rein. "Fill factor analysis of solar cells - current-voltage curves". *Progress in Photovoltaics: Research and Applications* 18 (2010), pp. 511–515. DOI: 10.1002/pip.979 (cited on p. 21).

[313] M. A. Lampert. "Volume-controlled current injection in insulators". *Reports on Progress in Physics* 27 (1964), pp. 329–367. DOI: 10.1088/0034-4885/27/1/307 (cited on p. 21).

[314] M. A. Lampert. "Simplified Theory of Space-Charge-Limited Currents in an Insulator with Traps". *Physical Review* 103 (1956), pp. 1648–1656. DOI: 10.1103/physrev.103.1648 (cited on p. 21).

[315] M. Abkowitz, J. S. Facci, and M. Stolka. "Time-resolved space charge-limited injection in a trap-free glassy polymer". *Chemical Physics* 177 (1993), pp. 783–792. DOI: 10.1016/0301-0104(93)85041-6 (cited on p. 21).

[316] S. Knox, H. Jones, and T. Esward. "Device history dependent effects in dark injection transient current measurements of charge mobility in organic light-emitting diodes". *Proceedings of SPIE* 7722 (2010). Ed. by P. L. Heremans, R. Coehoorn, and C. Adachi, p. 772218. DOI: 10.1117/12.854217 (cited on p. 21).

[317] I. Jurić and E. Tutiš. "Dark injection transient spectroscopy and density of states in amorphous organics". *Organic Electronics* 15 (2014), pp. 226–239. DOI: 10.1016/j.orgel.2013.11.014 (cited on p. 21).

[318] P. N. Murgatroyd. "Theory of space-charge-limited current enhanced by Frenkel effect". *Journal of Physics D: Applied Physics* 3 (1970), pp. 151–156. DOI: 10.1088/0022-3727/3/2/308 (cited on p. 22).

[319] J. Scherbel, P. H. Nguyen, G. Paasch, W. Brütting, and M. Schwoerer. "Temperature dependent broadband impedance spectroscopy on poly-(p-phenylene-vinylene) light-emitting diodes". *Journal of Applied Physics* 83 (1998), pp. 5045–5055. DOI: 10.1063/1.367321 (cited on pp. 22, 56).

[320] M. Glatthaar, M. Riede, N. Keegan, K. Sylvester-Hvid, B. Zimmermann, M. Niggemann, A. Hinsch, and A. Gombert. "Efficiency limiting factors of organic bulk heterojunction solar cells identified by electrical impedance spectroscopy". *Solar Energy Materials & Solar Cells* 91 (2007), pp. 390–393. DOI: 10.1016/j.solmat.2006.10.020 (cited on p. 22).

[321] G. Garcia-Belmonte, A. Munar, E. M. Barea, J. Bisquert, I. Ugarte, and R. Pacios. "Charge carrier mobility and lifetime of organic bulk heterojunctions analyzed by impedance spectroscopy". *Organic Electronics* 9 (2008), pp. 847–851. DOI: http://dx.doi.org/10.1016/j.orgel.2008.06.007 (cited on p. 22).

[322] J. Bisquert, G. Garcia-Belmonte, J. M. Montero, and H. J. Bolink. "Charge injection in organic light emitting diodes governed by interfacial states". *Proceedings of SPIE* 6192 (2006). Ed. by P. L. Heremans, M. Muccini, and E. A. Meulenkamp, p. 619210. DOI: 10.1117/12.661454 (cited on p. 22).

[323] M. Knipper, J. Parisi, K. Coakley, C. Waldauf, C. J. Brabec, and V. Dyakonov. "Impedance Spectroscopy on Polymer-Fullerene Solar Cells". *Zeitschrift für Naturforschung A* 62 (2007), p. 490. DOI: 10.1515/zna-2007-0904 (cited on p. 22).

[324] A. T. Mallajosyula, S. S. K. Iyer, and B. Mazhari. "Charge transport in polythiophene:fullerene:nanotube bulk heterojunction photovoltaic devices investigated by impedance spectroscopy". *Current Applied Physics* 13 (2013), pp. 677–683. DOI: 10.1016/j.cap.2012.11.007 (cited on p. 22).

[325] G. Perrier, R. de Bettignies, S. Berson, N. Lemaître, and S. Guillerez. "Impedance spectrometry of optimized standard and inverted P3HT-PCBM organic solar cells". *Solar Energy Materials & Solar Cells* 101 (2012), pp. 210–216. DOI: http://dx.doi.org/10.1016/j.solmat.2012.01.013 (cited on p. 22).

[326] S. Nowy, W. Ren, A. Elschner, W. Lövenich, and W. Brütting. "Impedance spectroscopy as a probe for the degradation of organic light-emitting diodes". *Journal of Applied Physics* 107 (2010), p. 054501. DOI: 10.1063/1.3294642 (cited on pp. 22, 56, 57).

[327] J. Bisquert. "A variable series resistance mechanism to explain the negative capacitance observed in impedance spectroscopy measurements of nanostructured solar cells". *Physical Chemistry Chemical Physics* 13 (2011), pp. 4679–4685. DOI: 10.1039/c0cp02555k (cited on p. 22).

[328] I. Mora-Seró, G. Garcia-Belmonte, P. P. Boix, M. A. Vázquez, and J. Bisquert. "Impedance spectroscopy characterisation of highly efficient silicon solar cells under different light illumination intensities". *Energy & Environmental Science* 2 (2009), pp. 678–686. DOI: 10.1039/b812468j (cited on p. 22).

[329] Á. Pitarch, G. Garcia-Belmonte, I. Mora-Seró, and J. Bisquert. "Electrochemical impedance spectra for the complete equivalent circuit of diffusion and reaction under steady-state recombination current". *Physical Chemistry Chemical Physics* 6 (2004), pp. 2983–2988. DOI: 10.1039/b401234h (cited on p. 22).

[330] E. Knapp and B. Ruhstaller. "Numerical impedance analysis for organic semiconductors with exponential distribution of localized states". *Applied Physics Letters* 99 (2011), p. 093304. DOI: 10.1063/1.3633109 (cited on p. 22).

[331] E. Knapp and B. Ruhstaller. "The role of shallow traps in dynamic characterization of organic semiconductor devices". *Journal of Applied Physics* 112 (2012), p. 024519. DOI: 10.1063/1.4739303 (cited on pp. 22, 27, 36).

[332] J. V. Li, A. M. Nardes, Z. Liang, S. E. Shaheen, B. A. Gregg, and D. H. Levi. "Simultaneous measurement of carrier density and mobility of organic semiconductors using capacitance techniques". *Organic Electronics* 12 (2011), pp. 1879–1885. DOI: 10.1016/j.orgel.2011.08.002 (cited on p. 22).

[333] S. L. M. van Mensfoort and R. Coehoorn. "Determination of Injection Barriers in Organic Semiconductor Devices from Capacitance Measurements". *Physical Review Letters* 100 (2008), p. 086802. DOI: 10.1103/PhysRevLett.100.086802 (cited on pp. 22, 65).

[334] M. Mingebach, C. Deibel, and V. Dyakonov. "Built-in potential and validity of the Mott-Schottky analysis in organic bulk heterojunction solar cells". *Physical Review B* 84 (2011), p. 153201. DOI: 10.1103/PhysRevB.84.153201 (cited on p. 23).

[335] A. S. Kavasoglu, N. Kavasoglu, and S. Oktik. "Simulation for capacitance correction from Nyquist plot of complex impedance-voltage characteristics". *Solid-State Electronics* 52 (2008), pp. 990–996. DOI: 10.1016/j.sse.2008.02.004 (cited on p. 23).

[336] G. Paasch and S. Scheinert. "Simulation and modeling of C-V curves of OLEDs with trap states for the holes". *Synthetic Metals* 122 (2001), pp. 145–147. DOI: http://dx.doi.org/10.1016/S0379-6779(00)01332-1 (cited on p. 23).

[337] T. Kirchartz, W. Gong, S. A. Hawks, T. Agostinelli, R. C. I. MacKenzie, Y. Yang, and J. Nelson. "Sensitivity of the Mott-Schottky Analysis in Organic Solar Cells". *The Journal of Physical Chemistry C* 116 (2012), pp. 7672–7680. DOI: 10.1021/jp300397f. eprint: http://pubs.acs.org/doi/pdf/10.1021/jp300397f (cited on pp. 23, 109).

[338] G. Jarosz. "On doubts about Mott-Schottky plot of organic planar heterojunction in photovoltaic cell". *Journal of Non-Crystalline Solids* 354 (2008), pp. 4338–4340. DOI: 10.1016/j.jnoncrysol.2008.06.077 (cited on p. 23).

[339] J. T. Heath, J. D. Cohen, and W. N. Shafarman. "Bulk and metastable defects in CuIn1-xGaxSe2 thin films using drive-level capacitance profiling". *Journal of Applied Physics* 95 (2004), pp. 1000–1010. DOI: 10.1063/1.1633982 (cited on p. 23).

[340] M. Neukom, S. Züfle, and B. Ruhstaller. "Reliable extraction of organic solar cell parameters by combining steady-state and transient techniques". *Organic Electronics* 13 (2012), pp. 2910–2916. DOI: 10.1016/j.orgel.2012.09.008 (cited on pp. 23, 38, 52, 63).

[341] M. V. der Auweraer, F. C. D. Schryver, P. M. Borsenberger, and H. Bässler. "Disorder in Charge Transport in doped polymers". *Advanced Materials* 6 (1994), pp. 199–213. DOI: 10.1002/adma.19940060304 (cited on p. 23).

[342] C. Soci, D. Moses, Q.-H. Xu, and A. J. Heeger. "Charge-carrier relaxation dynamics in highly ordered poly(p-phenylene vinylene): Effects of carrier bimolecular recombination and trapping". *Physical Review B* 72 (2005), p. 245204. DOI: 10.1103/PhysRevB.72.245204 (cited on p. 23).

[343] A. Pivrikas, G. Juška, K. Arlauskas, M. Scharber, A. Mozer, N. Sariciftci, H. Stubb, and R. Österbacka. "Charge carrier transport and recombination in bulk-heterojunction solar-cells". *Proceedings of SPIE* 5938 (2005). Ed. by Z. H. Kafafi and P. A. Lane, 59380N. DOI: 10.1117/12.614864 (cited on pp. 23, 47, 48).

[344] I. Hwang, C. R. McNeill, and N. C. Greenham. "Drift-diffusion modeling of photocurrent transients in bulk heterojunction solar cells". *Journal of Applied Physics* 106 (2009), p. 094506. DOI: 10.1063/1.3247547 (cited on p. 23).

[345] I Hwang and N. C. Greenham. "Modeling photocurrent transients in organic solar cells". *Nanotechnology* 19 (2008), p. 424012. DOI: 10.1088/0957-4484/19/42/424012 (cited on p. 23).

[346] L. C. C. Elliott, J. I. Basham, K. P. Pernstich, P. R. Shrestha, L. J. Richter, D. M. DeLongchamp, and D. J. Gundlach. "Probing Charge Recombination Dynamics in Organic Photovoltaic Devices under Open-Circuit Conditions". *Advanced Energy Materials* 4 (2014), p. 1400356. DOI: 10.1002/aenm.201400356 (cited on p. 24).

[347] A. Foertig, A. Baumann, D. Rauh, V. Dyakonov, and C. Deibel. "Charge carrier concentration and temperature dependent recombination in polymer-fullerene solar cells". *Applied Physics Letters* 95 (2009), p. 052104. DOI: 10.1063/1.3202389 (cited on p. 24).

[348] R. Hamilton, C. G. Shuttle, B. O'Regan, T. C. Hammant, J. Nelson, and J. R. Durrant. "Recombination in Annealed and Nonannealed Polythiophene/Fullerene Solar Cells: Transient Photovoltage Studies versus Numerical Modeling". *Journal of Physical Chemistry Letters* 1 (2010), pp. 1432–1436. DOI: 10.1021/jz1001506 (cited on p. 24).

[349] Y. Yao, X. Sun, B. Ding, D.-L. Li, X. Hou, and C.-Q. Wu. "A combined theoretical and experimental investigation on the transient photovoltage in organic photovoltaic cells". *Applied Physics Letters* 96 (2010), p. 203306. DOI: 10.1063/1.3431289 (cited on p. 24).

[350] D. Credgington, F. C. Jamieson, B. Walker, T.-Q. Nguyen, and J. R. Durrant. "Quantifi cation of Geminate and Non-Geminate Recombination Losses within a Solution-Processed Small-Molecule Bulk Heterojunction Solar Cell". *Advanced Materials* 24 (2012), pp. 2135–2141. DOI: 10.1002/adma.201104738 (cited on p. 24).

[351] G. Juška, K. Arlauskas, M. Viliūnas, and J. Kočka. "Extraction Current Transients: New Method of Study of Charge Transport in Microcrystalline Silicon". *Physical Review Letters* 84 (21 2000), pp. 4946–4949. DOI: 10.1103/PhysRevLett.84.4946 (cited on pp. 24, 25, 47, 57).

[352] G. Juška, K. Arlauskas, M. Viliūnas, K. Genevicius, R. Österbacka, and H. Stubb. "Charge transport in p-conjugated polymers from extraction current transients". *Physical Review B* 62 (2000), R16235–R16238. DOI: 10.1103/PhysRevB.62.R16235 (cited on pp. 25, 26, 47, 48).

[353] G. Juška, N. Nekrašas, and K. Genevicius. "Investigation of charge carriers transport from extraction current transients of injected charge carriers". *Journal of Non-Crystalline Solids* 358 (2012), pp. 748–750. DOI: 10.1016/j.jnoncrysol.2011.12.016 (cited on pp. 25, 48, 50–52, 57, 58, 62, 64).

[354] A. Armin, M. Velusamy, P. L. Burn, P. Meredith, and A. Pivrikas. "Injected charge extraction by linearly increasing voltage for bimolecular recombination studies in organic solar cells". *Applied Physics Letters* 101 (2012), p. 083306. DOI: 10.1063/1.4747330 (cited on p. 25).

[355] S. J. Baik, M. Neukom, L. Fang, K. S. Lim, T. van der Hofstad, T. Lanz, and B. Ruhstaller. "Fast And Direct Characterization Of Thin Film Si Solar Cells Using Celiv". In: *EUPVSEC*. 27th European Photovoltaic Solar Energy Conference and Exhibition. Vol. 3DV.1.30. 2012, pp. 2532–2534. DOI: 10.4229/27thEUPVSEC2012-3DV.1.30 (cited on p. 25).

[356] G. Juška, N. Nekrašas, V. Valentinavičius, P. Meredith, and A. Pivrikas. "Extraction of photogenerated charge carriers by linearly increasing voltage in the case of Langevin recombination". *Physical Review B* 84 (2011), p. 155202. DOI: 10.1103/PhysRevB.84.155202 (cited on pp. 25, 26).

[357] S. Kraner. "Measurement of charge carrier mobility and charge carrier concentration of organic photovoltaic diodes under in situ light soaking conditions and varying temperatures". MA thesis. Linz, 2011 (cited on p. 25).

[358] A. Pivrikas, M. Ullah, C. Simbrunner, H. Sitter, H. Neugebauer, and N. S. Sariciftci. "Comparative study of bulk and interface transport in disordered fullerene films". *physica status solidi (b)* 248 (2011), pp. 2656–2659. DOI: 10.1002/pssb.201100061 (cited on p. 25).

[359] A. J. Mozer, G. Dennler, N. S. Sariciftci, M. Westerling, A. Pivrikas, R. Österbacka, and G. Juška. "Time-dependent mobility and recombination of the photoinduced charge carriers in conjugated polymer/fullerene bulk heterojunction solar cells". *Physical Review B* 72 (2005), p. 035217. DOI: 10.1103/PhysRevB.72.035217 (cited on p. 25).

[360] J. Lorrmann, B. H. Badada, O. Inganäs, V. Dyakonov, and C. Deibel. "Charge carrier extraction by linearly increasing voltage: Analytic framework and ambipolar transients". *Journal of Applied Physics* 108 (2010), p. 113705. DOI: 10.1063/1.3516392 (cited on pp. 25, 48).

[361] J. Peng, X. Chen, Y. Chen, O. J. Sandberg, R. Österbacka, and Z. Liang. "Transient Extraction of Holes and Electrons Separately Unveils the Transport Dynamics in Organic Photovoltaics". *Advanced Electronic Materials* 2 (2016), p. 1500333. DOI: 10.1002/aelm.201500333 (cited on p. 25).

[362] A. Armin, G. Juska, M. Ullah, M. Velusamy, P. L. Burn, P. Meredith, and A. Pivrikas. "Balanced Carrier Mobilities: Not a Necessary Condition for High-Efficiency Thin Organic Solar Cells as Determined by MIS-CELIV". *Advanced Energy Materials* 4 (2014), p. 1300954. DOI: 10.1002/aenm.201300954 (cited on pp. 25, 47, 48, 51, 57).

[363] A. Armin, G. Juska, B. W. Philippa, P. L. Burn, P. Meredith, R. D. White, and A. Pivrikas. "Doping-Induced Screening of the Built-in-Field in Organic Solar Cells: Effect on Charge Transport and Recombination". *Advanced Energy Materials* 3 (2012), pp. 321–327. DOI: 10.1002/aenm.201200581 (cited on p. 25).

[364] A. J. Mozer, N. S. Sariciftci, L. Lutsen, D. Vanderzande, R. Österbacka, M. Westerling, and G. Juška. "Charge transport and recombination in bulk heterojunction solar cells studied by the photoinduced charge extraction in linearly increasing voltage technique". *Applied Physics Letters* 86 (2005), p. 112104. DOI: 10.1063/1.1882753 (cited on p. 25).

[365] G. Dennler, A. Mozer, G. Juška, A. Pivrikas, R. Österbacka, A. Fuchsbauer, and N. Sariciftci. "Charge carrier mobility and lifetime versus composition of conjugated polymer/fullerene bulk-heterojunction solar cells". *Organic Electronics* 7 (2006), pp. 229–234. DOI: 10.1016/j.orgel.2006.02.004 (cited on p. 25).

[366] G. Juška, N. Nekrašas, K. Genevičius, J. Stuchlik, and J. Kočka. "Relaxation of photoexited charge carrier concentration and mobility in μc-Si:H". *Thin Solid Films* 451-452 (2004), pp. 290–293. DOI: 10.1016/j.tsf.2003.11.053 (cited on p. 25).

[367] A. Pivrikas, G. Juška, R. Österbacka, M. Westerling, M. Viliūnas, K. Arlauskas, and H. Stubb. "Langevin recombination and space-charge-perturbed current transients in regiorandom poly(3-hexylthiophene)". *Physical Review B* 71 (2005), p. 125205. DOI: 10.1103/PhysRevB.71.125205 (cited on p. 25).

[368] S. Bange, M. Schubert, and D. Neher. "Charge mobility determination by current extraction under linear increasing voltages: Case of nonequilibrium charges and field-dependent mobilities". *Physical Review B* 81 (2010), p. 035209. DOI: 10.1103/physrevb.81.035209 (cited on pp. 25, 48).

[369] A. Baumann, J. Lorrmann, D. Rauh, C. Deibel, and V. Dyakonov. "A New Approach for Probing the Mobility and Lifetime of Photogenerated Charge Carriers in Organic Solar Cells Under Real Operating Conditions". *Advanced Materials* 24 (2012), pp. 4381–4386. DOI: 10.1002/adma.201200874 (cited on p. 25).

[370] S. Albrecht, J. R. Tumbleston, S. Janietz, I. Dumsch, S. Allard, U. Scherf, H. Ade, and D. Neher. "Quantifying Charge Extraction in Organic Solar Cells: The Case of Fluorinated PCPDTBT". *The Journal of Physical Chemistry Letters* 5 (2014), pp. 1131–1138. DOI: 10.1021/jz500457b (cited on p. 25).

[371] C. Deibel. "Charge carrier dissociation and recombination in polymer solar cells". *physica status solidi (a)* 12 (2009), pp. 2731–2736. DOI: 10.1002/pssa.200925282 (cited on pp. 25, 48).

[372] S. A. Hawks, B. Y. Finck, and B. J. Schwartz. "Theory of Current Transients in Planar Semiconductor Devices: Insights and Applications to Organic Solar Cells". *Physical Review Applied* 3 (2015), p. 044014. DOI: 10.1103/physrevapplied.3.044014 (cited on pp. 25, 48).

[373] R. Österbacka, A. Pivrikas, G. Juška, K. Genevičius, K. Arlauskas, and H. Stubb. "Mobility and density relaxation of photogenerated charge carriers in organic materials". *Current Applied Physics* 4 (2004), pp. 534–538. DOI: 10.1016/j.cap.2004.01.013 (cited on p. 27).

[374] C. G. Shuttle, A. Maurano, R. Hamilton, B. O'Regan, J. C. de Mello, and J. R. Durrant. "Charge extraction analysis of charge carrier densities in a polythiophene/fullerene solar cell: Analysis of the origin of the device dark current". *Applied Physics Letters* 93 (2008), p. 183501. DOI: 10.1063/1.3006316 (cited on p. 27).

[375] P. R. F. Barnes, K. Miettunen, X. Li, A. Y. Anderson, T. Bessho, M. Gratzel, and B. C. O'Regan. "Interpretation of Optoelectronic Transient and Charge Extraction Measurements in Dye-Sensitized Solar Cells". *Advanced Materials* 25 (2013), pp. 1881–1922. DOI: 10.1002/adma.201201372 (cited on p. 27).

[376] C. G. Shuttle, R. Hamilton, B. C. O'Regan, J. Nelson, and J. R. Durrant. "Charge-density-based analysis of the current-voltage response of polythiophene/fullerene photovoltaic devices". *Proceedings of the National Academy of Sciences* 107 (2010), pp. 16448–16452. DOI: 10.1073/pnas.1004363107 (cited on p. 27).

[377] T. M. Clarke, C. Lungenschmied, J. Peet, N. Drolet, and A. J. Mozer. "A Comparison of Five Experimental Techniques to Measure Charge Carrier Lifetime in Polymer/Fullerene Solar Cells". *Advanced Energy Materials* 5 (2014), p. 1401345. DOI: 10.1002/aenm.201401345 (cited on p. 27).

[378] H. K. Lee, K. K. Chan, and S. So. "Role of electron blocking and trapping layers in transport characterization of a photovoltaic polymer poly(3-hexylthiophene)". *Organic Electronics* 13 (2012), pp. 541–544. DOI: 10.1016/j.orgel.2011.12.023 (cited on p. 27).

[379] A. Campbell, D. Bradley, and H. Antoniadis. "Trap-free, space-charge-limited currents in a polyfluorene copolymer using pretreated indium tin oxide as a hole injecting contact". *Synthetic Metals* 122 (2001), pp. 161–163. DOI: http://dx.doi.org/10.1016/S0379-6779(00)01336-9 (cited on p. 27).

[380] T. Esward, S. Knox, H. Jones, P. Brewer, C. Murphy, L. Wright, and J. Williams. "A metrology perspective on the dark injection transient current method for charge mobility determination in organic semiconductors". *Journal of Applied Physics* 109 (2011), p. 093707. DOI: http://dx.doi.org/10.1063/1.3580256 (cited on p. 27).

[381] D. M. Goldie. "Transient space-charge-limited current pulse shapes in molecularly doped polymers". *Journal of Physics D: Applied Physics* 32 (1999), pp. 3058–3067. DOI: 10.1088/0022-3727/32/23/312 (cited on p. 27).

[382] M. Z. Szymanski, I. Kulszewicz-Bajer, J. Faure-Vincent, and D. Djurado. "Comparison of simulations to experiment for a detailed analysis of space-charge-limited transient current measurements in organic semiconductors". *Physical Review B* 85 (2012), p. 195205. DOI: 10.1103/PhysRevB.85.195205 (cited on p. 27).

[383] M. Z. Szymanski, I. Kulszewicz-Bajer, J. Faure-Vincent, and D. Djurado. "Transport properties of triarylamine based dendrimers studied by space charge limited current transients". *Optical Materials* 34 (2012), pp. 1630–1634. DOI: http://dx.doi.org/10.1016/j.optmat.2012.03.036 (cited on p. 27).

[384] M. Z. Szymanski, B. Luszczynska, J.-M. Verilhac, P. Reiss, and D. Djurado. "Simplified transient space-charge-limited current measurements of mobility using transimpedance amplifier". *Organic Electronics* 14 (2013), pp. 230–235. DOI: 10.1016/j.orgel.2012.11.006 (cited on p. 27).

[385] D. Bozyigit, M. Jakob, O. Yarema, and V. Wood. "Deep Level Transient Spectroscopy (DLTS) on Colloidal-Synthesized Nanocrystal Solids". *ACS Applied Materials & Interfaces* 5 (2013), pp. 2915–2919. DOI: 10.1021/am400326t (cited on p. 28).

[386] S. Neugebauer, J. Rauh, C. Deibel, and V. Dyakonov. "Investigation of electronic trap states in organic photovoltaic materials by current-based deep level transient spectroscopy". *Applied Physics Letters* 100 (2012), p. 263304. DOI: 10.1063/1.4731637 (cited on p. 28).

[387] O. Gaudin, R. B. Jackman, T.-P. Nguyen, and P. L. Rendu. "Determination of traps in poly(p-phenylene vinylene) light emitting diodes by charge-based deep level transient spectroscopy". *Journal of Applied Physics* 90 (2001), pp. 4196–4204. DOI: 10.1063/1.1403669 (cited on p. 28).

[388] Gamry. *Dye Solar Cells - IMPS/IMVS Measurements. http://www.gamry.com/application-notes/physechem/dye-solar-cells-imps-imvs/* (cited on pp. 28, 29).

[389] K. Adhitya, A. Alsulami, A. Buckley, R. C. Tozer, and M. Grell. "Intensity-Modulated Spectroscopy on Loaded Organic Photovoltaic Cells". *IEEE Journal of Photovoltaics* 5 (2015), pp. 1414–1421. DOI: 10.1109/JPHOTOV.2015.2447838 (cited on p. 28).

[390] Y. Gao, A. J. Wise, A. K. Thomas, and J. K. Grey. "Spectroscopic and Intensity Modulated Photocurrent Imaging of Polymer/Fullerene Solar Cells". *ACS Applied Materials & Interfaces* 8 (2016), pp. 285–293. DOI: 10.1021/acsami.5b08724 (cited on p. 28).

[391] Y. T. Set, E. Birgersson, and J. Luther. "Predictive Mechanistic Model for the Electrical Impedance and Intensity-Modulated Photocurrent and Photovoltage Spectroscopic Responses of an Organic Bulk Heterojunction Solar Cell". *Physical Review Applied* 5 (2016), p. 054002. DOI: 10.1103/physrevapplied.5.054002 (cited on p. 28).

[392] M. Bag and K. S. Narayan. "Universality in the intensity-modulated photocurrent in bulk-heterojunction polymer solar cells". *Physical Review B* 82 (2010), p. 075308. DOI: 10.1103/PhysRevB.82.075308 (cited on p. 28).

[393] A. Pockett, G. E. Eperon, T. Peltola, H. J. Snaith, A. Walker, L. M. Peter, and P. J. Cameron. "Characterization of Planar Lead Halide Perovskite Solar Cells by Impedance Spectroscopy, Open-Circuit Photovoltage Decay, and Intensity-Modulated Photovoltage/Photocurrent Spectroscopy". *The Journal of Physical Chemistry C* 119 (2015), pp. 3456–3465. DOI: 10.1021/jp510837q (cited on p. 28).

[394] G. Schlichthörl, N. G. Park, and A. J. Frank. "Evaluation of the Charge-Collection Efficiency of Dye-Sensitized Nanocrystalline TiO 2-Solar Cells". *The Journal of Physical Chemistry B* 103 (1999), pp. 782–791. DOI: 10.1021/jp9831177 (cited on pp. 28, 29).

[395] Y. T. Set, M. D. Heinemann, E. Birgersson, and J. Luther. "On the Origin of the Quadrant I Semicircle in Intensity-Modulated Photocurrent Spectra of P3HT:PCBM Bulk Heterojunction Solar Cells: Evidence of Degradation-Related Trap-Assisted Recombination". *The Journal of Physical Chemistry C* 117 (2013), pp. 7993–8000. DOI: 10.1021/jp310841v (cited on p. 28).

[396] T. Kirchartz and J. Nelson. "Device Modelling of Organic Bulk Heterojunction Solar Cells". *Topics in Current Chemistry* 352 (2013). Ed. by D. Beljonne and J. Cornil, pp. 279–324. DOI: 10.1007/128_2013_473 (cited on p. 31).

[397] P. Kordt, J. J. M. van der Holst, M. A. Helwi, W. Kowalsky, F. May, A. Badinski, C. Lennartz, and D. Andrienko. "Modeling of Organic Light Emitting Diodes: From Molecular to Device Properties". *Advanced Functional Materials* 25 (2015), pp. 1955–1971. DOI: 10.1002/adfm.201403004 (cited on p. 31).

[398] Wolfgang Tress. *Organic Solar Cells*. Springer International Publishing, 2014. ISBN: 9783319100968 (cited on p. 31).

[399] P. K. Watkins, A. B. Walker, and G. L. B. Verschoor. "Dynamical Monte Carlo Modelling of Organic Solar Cells: The Dependence of Internal Quantum Efficiency on Morphology". *Nano Letters* 5 (2005), pp. 1814–1818. DOI: 10.1021/nl051098o (cited on p. 31).

[400] J. Nelson, J. J. Kwiatkowski, J. Kirkpatrick, and J. M. Frost. "Modeling Charge Transport in Organic Photovoltaic Materials". *Accounts of Chemical Research* 42 (2009), pp. 1768–1778. DOI: 10.1021/ar900119f (cited on p. 31).

[401] J. J. M. van der Holst, F. W. A. van Oost, R. Coehoorn, and P. A. Bobbert. "Monte Carlo study of charge transport in organic sandwich-type single-carrier devices: Effects of Coulomb interactions". *Physical Review B* 83 (2011), p. 085206. DOI: 10.1103/PhysRevB.83.085206 (cited on p. 31).

[402] T. Christen and M. Seeger. "Simulation of unipolar space charge controlled electric fields". *Journal of Electrostatics* 65 (2007), pp. 11–20. DOI: 10.1016/j.elstat.2006.05.004 (cited on p. 31).

[403] J. J. M. van der Holst, M. A. Uijttewaal, B. Ramachandhran, R. Coehoorn, P. A. Bobbert, G. A. de Wijs, and R. A. de Groot. "Modeling and analysis of the three-dimensional current density in sandwich-type single-carrier devices of disordered organic semiconductors". *Physical Review B* 79 (2009), p. 085203. DOI: 10.1103/PhysRevB.79.085203 (cited on p. 31).

[404] S. L. M. van Mensfoort, J. Billen, M. Carvelli, S. I. E. Vulto, R. A. J. Janssen, and R. Coehoorn. "Predictive modeling of the current density and radiative recombination in blue polymer-based light-emitting diodes". *Journal of Applied Physics* 109 (2011), p. 064502. DOI: 10.1063/1.3553412 (cited on p. 31).

[405] A. Miller and E. Abrahams. "Impurity Conduction at Low Concentrations". *Physical Review* 120 (1960), pp. 745–755. DOI: 10.1103/PhysRev.120.745 (cited on p. 31).

[406] H. Bässler, G. Schönherr, M. Abkowitz, and D. M. Pai. "Hopping transport in prototypical organic glasses". *Physical Review B* 26 (1982), pp. 3105–3113. DOI: 10.1103/PhysRevB.26.3105 (cited on p. 31).

[407] H. Bässler. "Charge Transport in Disordered Organic Photoconductors a Monte Carlo Simulation Study". *physica status solidi (b)* 175 (1993), pp. 15–56. DOI: 10.1002/pssb.2221750102 (cited on pp. 31, 64).

[408] W. F. Pasveer, J. Cottaar, C. Tanase, R. Coehoorn, P. A. Bobbert, P. W. M. Blom, D. M. de Leeuw, and M. A. J. Michels. "Unified Description of Charge-Carrier Mobilities in Disordered Semiconducting Polymers". *Physical Review Letters* 94 (2005), p. 206601. DOI: 10.1103/PhysRevLett.94.206601 (cited on pp. 31, 37, 117).

[409] S. L. M. van Mensfoort and R. Coehoorn. "Effect of Gaussian disorder on the voltage dependence of the current density in sandwich-type devices based on organic semiconductors". *Physical Review B* 78 (2008), p. 085207. DOI: 10.1103/PhysRevB.78.085207 (cited on p. 31).

[410] W. Shockley and H. J. Queisser. "Detailed Balance Limit of Efficiency of pn Junction Solar Cells". *Journal of Applied Physics* 32 (1961), pp. 510–519. DOI: 10.1063/1.1736034 (cited on p. 31).

[411] J. Bisquert and R. A. Marcus. "Device Modeling of Dye-Sensitized Solar Cells". *Topics in Current Chemistry* 352 (2013), pp. 325–395. DOI: 10.1007/128_2013_471 (cited on p. 31).

[412] F. D. Castro, A. Laudani, F. R. Fulginei, and A. Salvini. "An in-depth analysis of the modelling of organic solar cells using multiple-diode circuits". *Solar Energy* 135 (2016), pp. 590–597. DOI: 10.1016/j.solener.2016.06.033 (cited on p. 31).

[413] B. Ruhstaller, T. Flatz, D. Rezzonico, M. Moos, N. Reinke, E. Huber, R. Haeusermann, and B. Perucco. "Comprehensive simulation of light-emitting and light-harvesting organic devices". *Proceedings of SPIE* 7051 (2008). Ed. by F. So and C. Adachi, 70510J. DOI: 10.1117/12.802447 (cited on p. 32).

[414] B. Ruhstaller, E. Knapp, B. Perucco, N. Reinke, D. Rezzonico, and F. Müller. "Advanced Numerical Simulation of Organic Light-Emitting Devices". In: *Optoelectronic Devices and Properties*. Ed. by O. Sergiyenko. InTech, 2011. Chap. 21, pp. 433–458. ISBN: 9789533072043 (cited on p. 32).

[415] R. Häusermann, E. Knapp, M. Moos, N. A. Reinke, T. Flatz, and B. Ruhstaller. "Coupled optoelectronic simulation of organic bulk-heterojunction solar cells: Parameter extraction and sensitivity analysis". *Journal of Applied Physics* 106 (2009), p. 104507. DOI: 10.1063/1.3259367 (cited on pp. 32, 48).

[416] E. Knapp, R. Häusermann, H. U. Schwarzenbach, and B. Ruhstaller. "Numerical simulation of charge transport in disordered organic semiconductor devices". *Journal of Applied Physics* 108 (2010), p. 054504. DOI: 10.1063/1.3475505 (cited on pp. 32, 37).

[417] J. C. Scott, S. Karg, and S. A. Carter. "Bipolar charge and current distributions in organic light-emitting diodes". *Journal of Applied Physics* 82 (1997), pp. 1454–1460. DOI: 10.1063/1.365923 (cited on pp. 32, 47).

[418] P. S. Davids, I. H. Campbell, and D. L. Smith. "Device model for single carrier organic diodes". *Journal of Applied Physics* 82 (1997), pp. 6319–6325. DOI: 10.1063/1.366522 (cited on p. 32).

[419] B. Ruhstaller, S. A. Carter, S. Barth, H. Riel, W. Riess, and J. C. Scott. "Transient and steady-state behavior of space charges in multilayer organic light-emitting diodes". *Journal of Applied Physics* 89 (2001), pp. 4575–4586. DOI: 10.1063/1.1352027 (cited on p. 32).

[420] J. Staudigel, M. Stößel, F. Steuber, and J. Simmerer. "A quantitative numerical model of multilayer vapor-deposited organic light emitting diodes". *Journal of Applied Physics* 86 (1999), pp. 3895–3910. DOI: 10.1063/1.371306 (cited on pp. 32, 36).

[421] A. B. Walker, A Kambili, and S. J. Martin. "Electrical transport modelling in organic electroluminescent devices". *Journal of Physics: Condensed Matter* 14 (2002), pp. 9825–9876. DOI: 10.1088/0953-8984/14/42/303 (cited on p. 32).

[422] L. J. A. Koster, E. C. P. Smits, V. D. Mihailetchi, and P. W. M. Blom. "Device model for the operation of polymer/fullerene bulk heterojunction solar cells". *Physical Review B* 72 (2005), p. 085205. DOI: 10.1103/PhysRevB.72.085205 (cited on p. 32).

[423] Y. Roichman, Y. Preezant, and N. Tessler. "Analysis and modeling of organic devices". *physica status solidi (a)* 201 (2004), pp. 1246–1262. DOI: 10.1002/pssa.200404342 (cited on p. 32).

[424] B. Ruhstaller, T. Beierlein, H. Riel, S. Karg, J. C. Scott, and W. Riess. "Simulating electronic and optical processes in multilayer organic light-emitting devices". *IEEE Journal of Selected Topics in Quantum Electronics* 9 (2003), pp. 723–731. DOI: 10.1109/JSTQE.2003.818852 (cited on p. 32).

[425] S. Sze and K. K. Ng. *Physics of Semiconductor Devices*. 3rd ed. Hoboken, N.J: John Wiley & Sons, Inc., 2006. ISBN: 9780471143239 (cited on pp. 34, 36, 109, 117).

[426] C. Crowell and S. Sze. "Current transport in metal-semiconductor barriers". *Solid-State Electronics* 9 (1966), pp. 1035–1048. DOI: 10.1016/0038-1101(66)90127-4 (cited on p. 36).

[427] W. Schottky. "Halbleitertheorie der Sperrschicht". *Die Naturwissenschaften* 26 (1938), pp. 843–843. DOI: 10.1007/bf01774216 (cited on p. 36).

[428] M. P. Langevin. "Recombinaison et mobilite des ions dans les gaz". *Annales de Chimie et de Physique* 28 (1903), pp. 433–450. DOI: 10.1051/jphystap:019050040032201 (cited on p. 36).

[429] L. Onsager. "Initial Recombination of Ions". *Physical Review* 54 (1938), pp. 554–557. DOI: 10.1103/PhysRev.54.554 (cited on p. 36).

[430] A. Pivrikas, G. Juška, A. J. Mozer, M. Scharber, K. Arlauskas, N. S. Sariciftci, H. Stubb, and R. Österbacka. "Bimolecular Recombination Coefficient as a Sensitive Testing Parameter for Low-Mobility Solar-Cell Materials". *Physical Review Letters* 94 (2005), p. 176806. DOI: 10.1103/PhysRevLett.94.176806 (cited on p. 36).

[431] C. Deibel, A. Wagenpfahl, and V. Dyakonov. "Origin of reduced polaron recombination in organic semiconductor devices". *Physical Review B* 80 (2009), p. 075203. DOI: 10.1103/PhysRevB.80.075203 (cited on p. 36).

[432] A. J. Mozer and T. M. Clarke. "Reduced Bimolecular Recombination in Conjugated Polymer Donor/-Fullerene Acceptor Bulk Heterojunction Solar Cells". *Australian Journal of Chemistry* 65 (2012), pp. 442–447. DOI: 10.1071/CH12028 (cited on p. 36).

[433] W. Shockley and W. T. Read. "Statistics of the Recombinations of Holes and Electrons". *Physical Review B* 87 (1952), pp. 835–842. DOI: 10.1103/physrev.87.835 (cited on p. 36).

[434] R. N. Hall. "Electron-Hole Recombination in Germanium". *Physical Review* 87 (1952), pp. 387–387. DOI: 10.1103/PhysRev.87.387 (cited on p. 36).

[435] R. J. de Vries, S. L. M. van Mensfoort, V. Shabro, S. I. E. Vulto, R. A. J. Janssen, and R. Coehoorn. "Analysis of hole transport in a polyfluorene-based copolymer- evidence for the absence of correlated disorder". *Applied Physics Letters* 94 (2009), p. 163307. DOI: 10.1063/1.3119317 (cited on p. 37).

[436] Y. He, S. Gong, R. Hattori, and J. Kanicki. "High performance organic polymer light-emitting heterostructure devices". *Applied Physics Letters* 74 (1999), pp. 2265–2267. DOI: 10.1063/1.123862 (cited on p. 41).

[437] Y. He and J. Kanicki. "High-efficiency organic polymer light-emitting heterostructure devices on flexible plastic substrates". *Applied Physics Letters* 76 (2000), pp. 661–663. DOI: 10.1063/1.125854 (cited on p. 41).

[438] C. A. Zuniga, S. Barlow, and S. R. Marder. "Approaches to Solution-Processed Multilayer Organic Light-Emitting Diodes Based on Cross-Linking". *Chemistry of Materials* 23 (2011), pp. 658–681. DOI: 10.1021/cm102401k (cited on p. 41).

[439] Y. Noguchi, Y. Miyazaki, Y. Tanaka, N. Sato, Y. Nakayama, T. D. Schmidt, W. Brütting, and H. Ishii. "Charge accumulation at organic semiconductor interfaces due to a permanent dipole moment and its orientational order in bilayer devices". *Journal of Applied Physics* 111 (2012), p. 114508. DOI: 10.1063/1.4724349 (cited on pp. 41, 42, 55).

[440] A. Rajagopal, C. I. Wu, and A. Kahn. "Energy level offset at organic semiconductor heterojunctions". *Journal of Applied Physics* 83 (1998), pp. 2649–2655. DOI: 10.1063/1.367027 (cited on pp. 41, 65).

[441] H. Ishii and K. Seki. "Energy level alignment at organic/metal interfaces studied by UV photoemission: breakdown of traditional assumption of a common vacuum level at the interface". *IEEE Transactions on Electron Devices* 44 (1997), pp. 1295–1301. DOI: 10.1109/16.605471 (cited on p. 41).

[442] S. Berleb, W. Brütting, and G. Paasch. "Interfacial charges and electric field distribution in organic hetero-layer light-emitting devices". *Organic Electronics* 1 (2000), pp. 41–47. DOI: 10.1016/s1566-1199(00)00007-0 (cited on pp. 41–43, 55, 71).

[443] E. Ito, Y. Washizu, N. Hayashi, H. Ishii, N. Matsuie, K. Tsuboi, Y. Ouchi, Y. Harima, K. Yamashita, and K. Seki. "Spontaneous buildup of giant surface potential by vacuum deposition of Alq[sub 3] and its removal by visible light irradiation". *Journal of Applied Physics* 92 (2002), pp. 7306–7310. DOI: 10.1063/1.1518759 (cited on pp. 41, 42, 67).

[444] L. Jäger, T. D. Schmidt, and W. Brütting. "Manipulation and control of the interfacial polarization in organic light-emitting diodes by dipolar doping". *AIP Advances* 6 (2016), p. 095220. DOI: 10.1063/1.4963796 (cited on pp. 41, 42, 52, 64).

[445] N. Kajimoto, T. Manaka, and M. Iwamoto. "Decay process of a large surface potential of Alq3 films by heating". *Journal of Applied Physics* 100 (2006), p. 053707. DOI: 10.1063/1.2338137 (cited on pp. 41, 67).

[446] K. Yoshizaki, T. Manaka, and M. Iwamoto. "Large surface potential of Alq3 film and its decay". *Journal of Applied Physics* 97 (2005), p. 023703. DOI: 10.1063/1.1835543 (cited on pp. 41, 67).

[447] T. D. Schmidt, L. Jäger, Y. Noguchi, H. Ishii, and W. Brütting. "Analyzing degradation effects of organic light-emitting diodes via transient optical and electrical measurements". *Journal of Applied Physics* 117 (2015), p. 215502. DOI: 10.1063/1.4921829 (cited on pp. 41, 49, 67, 69).

[448] Y. Noguchi, N. Sato, Y. Tanaka, Y. Nakayama, and H. Ishii. "Threshold voltage shift and formation of charge traps induced by light irradiation during the fabrication of organic light-emitting diodes". *Applied Physics Letters* 92 (2008), p. 203306. DOI: 10.1063/1.2936084 (cited on pp. 42, 67).

[449] M. Kröger, S. Hamwi, J. Meyer, T. Dobbertin, T. Riedl, W. Kowalsky, and H.-H. Johannes. "Temperature-independent field-induced charge separation at doped organic/organic interfaces: Ex-

perimental modeling of electrical properties". *Physical Review B* 75 (2007), p. 235321. DOI: 10.1103/PhysRevB.75.235321 (cited on p. 42).

[450] Y. Okabayashi, E. Ito, T. Isoshima, and M. Hara. "Positive Giant Surface Potential of Tris(8-hydroxyquinolinolato) Aluminum (Alq3) Film Evaporated onto Backside of Alq3 Film Showing Negative Giant Surface Potential". *Applied Physics Express* 5 (2012), p. 055601. DOI: 10.1143/APEX.5.055601 (cited on p. 42).

[451] Y. Noguchi, H. Lim, T. Isoshima, E. Ito, M. Hara, W. Won Chin, J. Wook Han, H. Kinjo, Y. Ozawa, Y. Nakayama, and H. Ishii. "Influence of the direction of spontaneous orientation polarization on the charge injection properties of organic light-emitting diodes". *Applied Physics Letters* 102 (2013), p. 203306. DOI: 10.1063/1.4807797 (cited on pp. 42, 52).

[452] T. Isoshima, Y. Okabayashi, E. Ito, M. Hara, W. W. Chin, and J. W. Han. "Negative giant surface potential of vacuum-evaporated tris(7-propyl-8-hydroxyquinolinolato) aluminum(III) [Al(7-Prq)3] film". *Organic Electronics* 14 (2013), pp. 1988–1991. DOI: 10.1016/j.orgel.2013.04.032 (cited on p. 42).

[453] S. Egusa, A. Miura, N. Gemma, and M. Azuma. "Carrier Injection Characteristics of Organic Electroluminescent Devices". *Japanese Journal of Applied Physics* 33 (1994), pp. 2741–2745. DOI: 10.1143/jjap.33.2741 (cited on p. 43).

[454] E. Knapp and B. Ruhstaller. "Analysis of negative capacitance and self-heating in organic semiconductor devices". *Journal of Applied Physics* 117 (2015), p. 135501. DOI: 10.1063/1.4916981 (cited on pp. 45, 55).

[455] H. Okumoto and T. Tsutsui. "A source of negative capacitance in organic electronic devices observed by impedance spectroscopy: Self-heating effects". *Applied Physics Express* 7 (2014), p. 061601. DOI: 10.7567/APEX.7.061601 (cited on p. 45).

[456] M. Regnat, S. Züfle, K. Pernstich, and B. Ruhstaller. "The importance of changes in the emission zone for the efficiency roll-off in OLEDs". *manuscript in preparation* (2017) (cited on p. 47).

[457] M. Kuik, G.-J.A. H. Wetzelaer, H. T. Nicolai, N. I. Craciun, D. M. D. Leeuw, and P. W. M. Blom. "25th Anniversary Article: Charge Transport and Recombination in Polymer Light-Emitting Diodes". *Advanced Materials* 26 (2014), pp. 512–531. DOI: 10.1002/adma.201303393 (cited on p. 47).

[458] W. Tress, A. Petrich, M. Hummert, M. Hein, K. Leo, and M. Riede. "Imbalanced mobilities causing S-shaped IV curves in planar heterojunction organic solar cells". *Applied Physics Letters* 98 (2011), p. 063301. DOI: 10.1063/1.3553764 (cited on p. 47).

[459] J. D. Kotlarski and P. W. M. Blom. "Impact of unbalanced charge transport on the efficiency of normal and inverted solar cells". *Applied Physics Letters* 100 (2012), p. 013306. DOI: 10.1063/1.3663860 (cited on p. 47).

[460] M. Stolterfoht, A. Armin, S. Shoaee, I. Kassal, P. Burn, and P. Meredith. "Slower carriers limit charge generation in organic semiconductor light-harvesting systems". *Nature Communications* 7 (2016), p. 11944. DOI: 10.1038/ncomms11944 (cited on p. 47).

[461] M. M. Mandoc, L. J. A. Koster, and P. W. M. Blom. "Optimum charge carrier mobility in organic solar cells". *Applied Physics Letters* 90 (2007), p. 133504. DOI: 10.1063/1.2711534 (cited on p. 47).

[462] C. Deibel, A. Wagenpfahl, and V. Dyakonov. "Influence of charge carrier mobility on the performance of organic solar cells". *physica status solidi (RRL) - Rapid Research Letters* 2 (2008), pp. 175–177. DOI: 10.1002/pssr.200802110 (cited on p. 47).

[463] P. W. M. Blom, M. J. M. de Jong, and M. G. van Munster. "Electric-field and temperature dependence of the hole mobility in poly(p-phenylene vinylene)". *Physical Review B* 55 (1997), R656–R659. DOI: 10.1103/PhysRevB.55.R656 (cited on pp. 47, 58).

[464] K. S. Haber and A. C. Albrecht. "Time-of-Flight technique for Mobility measurement in the Condensed Phase". *The Journal of Physical Chemistry* 88 (1984), pp. 6025–6030. DOI: 10.1021/j150668a057 (cited on p. 47).

[465] M. Abkowitz and D. M. Pai. "Comparison of the drift mobility measured under transient and steady-state conditions in a prototypical hopping system". *Philosophical Magazine B* 53 (1986), pp. 193–216. DOI: 10.1080/13642818608240642 (cited on p. 47).

[466] H. C. F. Martens, H. B. Brom, and P. W. M. Blom. "Frequency-dependent electrical response of holes in poly (p -phenylene vinylene)". *Physical Review B* 60 (1999), R8489–R8492. DOI: 10.1103/physrevb.60.r8489 (cited on p. 47).

[467] K. K. Tsung and S. K. So. "Advantages of admittance spectroscopy over time-of-flight technique for studying dispersive charge transport in an organic semiconductor". *Journal of Applied Physics* 106 (2009), p. 083710. DOI: 10.1063/1.3251409 (cited on p. 47).

[468] P. A. Torpey. "Double-carrier injection and recombination in insulators, including diffusion effects". *Journal of Applied Physics* 56 (1984), pp. 2284–2294. DOI: 10.1063/1.334262 (cited on p. 47).

[469] D. Poplavskyy, W. Su, and F. So. "Bipolar charge transport, injection, and trapping studies in a model green-emitting polyfluorene copolymer". *Journal of Applied Physics* 98 (2005), p. 014501. DOI: 10.1063/1.1941482 (cited on p. 47).

[470] A. Pivrikas, N. S. Sariciftci, G. Juška, and R. Österbacka. "A Review of Charge Transport and Recombination in Polymer/Fullerene Organic Solar Cells". *Progress in Photovoltaics: Research and Applications* 15 (2007), pp. 677–696. DOI: 10.1002/pip.791 (cited on p. 47).

[471] K. Genevicius, R. Österbacka, G. Juska, K. Arlauskas, and H. Stubb. "Charge transport in p-conjugated polymers from extraction current transients". *Thin Solid Films* 403-404 (2002), pp. 415–418. DOI: 10.1016/s0040-6090(01)01583-8 (cited on p. 47).

[472] S. Jenatsch, R. Hany, A. C. Véron, M. Neukom, S. Züfle, A. Borgschulte, B. Ruhstaller, and F. Nüesch. "Influence of Molybdenum Oxide Interface Solvent Sensitivity on Charge Trapping in Bilayer Cyanine Solar Cells". *The Journal of Physical Chemistry C* 118 (2014), pp. 17036–17045. DOI: 10.1021/jp5005314 (cited on p. 48).

[473] M. Nyman, O. Sandberg, J. F. M. Hardigree, S. Kola, H. E. Katz, and R. Österbacka. "Voltage dependent displacement current as a tool to measure the vacuum level shift caused by self-assembled monolayers on aluminum oxide". *Applied Physics Letters* 103 (2013), p. 243502. DOI: 10.1063/1.4844875 (cited on p. 48).

[474] J. Važgėla, K. Genevičius, and G. Juška. "i-CELIV technique for investigation of charge carriers transport properties". *Chemical Physics* 478 (2016), pp. 126–129. DOI: 10.1016/j.chemphys.2016.04.005 (cited on pp. 51, 58, 62, 64).

[475] E. Knapp and B. Ruhstaller. "Analysis of self-heating and trapping in organic semiconductor devices". *Proceedings of SPIE* 9566 (2015). Ed. by F. So, C. Adachi, and J.-J. Kim, p. 95660X. DOI: 10.1117/12.2185712 (cited on p. 55).

[476] Z. Kohári, E. Kollár, L. Pohl, and A. Poppe. "Nonlinear electro-thermal modeling and field-simulation of OLEDs for lighting applications II: Luminosity and failure analysis". *Microelectronics Journal* 44 (2013), pp. 1011–1018. DOI: 10.1016/j.mejo.2012.05.015 (cited on p. 55).

[477] J. Park, J. Lee, and Y.-Y. Noh. "Optical and thermal properties of large-area OLED lightings with metallic grids". *Organic Electronics* 13 (2012), pp. 184–194. DOI: 10.1016/j.orgel.2011.10.024 (cited on p. 55).

[478] American Society for Testing Materials. *ASTM G173-03(2012), Standard Tables for Reference Solar Spectral Irradiances: Direct Normal and Hemispherical on 37° Tilted Surface*. 2012. DOI: 10.1520/G0173-03R12 (cited on pp. 55, 99).

[479] Q. Burlingame, G. Zanotti, L. Ciammaruchi, E. A. Katz, and S. R. Forrest. "Outdoor operation of small-molecule organic photovoltaics". *Organic Electronics* 41 (2017), pp. 274–279. DOI: 10.1016/j.orgel.2016.11.015 (cited on pp. 55, 102).

[480] S. Züfle, S. Altazin, A. Hofmann, L. Jäger, M. T. Neukom, T. D. Schmidt, W. Brütting, and B. Ruhstaller. "The use of charge extraction by linearly increasing voltage in polar organic light-emitting

diodes". *Journal of Applied Physics* 121 (2017), p. 175501. DOI: 10.1063/1.4982903 (cited on pp. 55, 57–59, 64, 72).

[481] O. Armbruster, C. Lungenschmied, and S. Bauer. "Investigation of trap states and mobility in organic semiconductor devices by dielectric spectroscopy: Oxygen-doped P3HT:PCBM solar cells". *Physical Review B* 86 (2012), p. 235201. DOI: 10.1103/PhysRevB.86.235201 (cited on p. 56).

[482] T. Kobayashi, Z. J. L. Kao, and T. Nakada. "Temperature dependent current-voltage and admittance spectroscopy on heat-light soaking effects of Cu(In,Ga)Se2 solar cells with ALD-Zn(O,S) and CBD-ZnS(O,OH) buffer layers". *Solar Energy Materials & Solar Cells* 143 (2015), pp. 159–167. DOI: 10.1016/j.solmat.2015.06.044 (cited on p. 56).

[483] J. Ahn, T. W. Kim, and W. J. Lee. "Temperature-dependent dielectric relaxation in ITO/Alq3/Al organic light-emitting diodes". *Journal of Ceramic Processing Research* 13 (2012), pp. 163–165 (cited on p. 56).

[484] F. Reis, D. Mencaraglia, S. O. Saad, I. Séguy, M. Oukachmih, P. Jolinat, and P. Destruel. "Characterization of ITO/CuPc/AI and ITO/ZnPc/Al structures using optical and capacitance spectroscopy". *Synthetic Metals* 138 (2003), pp. 33–37. DOI: 10.1016/S0379-6779(02)01284-5 (cited on p. 56).

[485] S. Berleb. "Raumladungsbegrenzte Ströme und Hoppingtransport in organischen Leuchtdioden aus Tris(8-hydroxyquinolin)-Aluminium (Alq3)". PhD thesis. University of Bayreuth, 2001 (cited on p. 56).

[486] S. Nowy. "Understanding losses in OLEDs: optical device simulation and electrical characterization using impedance spectroscopy". PhD thesis. University of Augsburg, 2010 (cited on p. 56).

[487] S. Nowy, W. Ren, J. Wagner, J. A. Weber, and W. Brütting. "Impedance spectroscopy of organic hetero-layer OLEDs as a probe for charge carrier injection and device degradation". *Proceedings of SPIE* 7415 (2009). Ed. by F. So and C. Adachi, 74150G. DOI: 10.1117/12.824856 (cited on p. 56).

[488] W. D. Gill. "Drift mobilities in amorphous charge-transfer complexes of trinitrofluorenone and poly-n-vinylcarbazole". *Journal of Applied Physics* 43 (1972), pp. 5033–5040. DOI: 10.1063/1.1661065 (cited on p. 58).

[489] L. Bozano, S. A. Carter, J. C. Scott, G. G. Malliaras, and P. J. Brock. "Temperature-and field-dependent electron and hole mobilities in polymer light-emitting diodes". *Applied Physics Letters* 74 (1999), pp. 1132–1134. DOI: 10.1063/1.123959 (cited on p. 58).

[490] P. Servati, A. Nathan, and G. A. J. Amaratunga. "Generalized transport-band field-effect mobility in disordered organic and inorganic semiconductors". *Physical Review B* 74 (2006), p. 245210. DOI: 10.1103/physrevb.74.245210 (cited on p. 58).

[491] S. Altazin, R. Clerc, R. Gwoziecki, D. Boudinet, G. Ghibaudo, G. Pananakakis, I. Chartier, and R. Coppard. "Analytical modeling of the contact resistance in top gate/bottom contacts organic thin film transistors". *Organic Electronics* 12 (2011), pp. 897–902. DOI: 10.1016/j.orgel.2011.03.007 (cited on p. 63).

[492] T. van Woudenbergh. "Charge Injection Into Organic Semiconductors". PhD thesis. University of Groningen, 2005 (cited on pp. 64, 65).

[493] V. Arkhipov, E. Emelianova, G. Adriaenssens, and H Bässler. "Equilibrium carrier mobility in disordered organic semiconductors". *Journal of Non-Crystalline Solids* 299-302 (2002), pp. 1047–1051. DOI: 10.1016/s0022-3093(01)01071-7 (cited on p. 64).

[494] R. Rohloff, N. B. Kotadiya, N. I. Crăciun, P. W. M. Blom, and G. A. H. Wetzelaer. "Electron and hole transport in the organic small molecule α-NPD". *Applied Physics Letters* 110 (2017), p. 073301. DOI: 10.1063/1.4976205 (cited on p. 64).

[495] K. L. Tong, S. W. Tsang, K. K. Tsung, S. C. Tse, and S. K. So. "Hole transport in molecularly doped naphthyl diamine". *Journal of Applied Physics* 102 (2007), p. 093705. DOI: 10.1063/1.2804109 (cited on p. 64).

[496] T. Y. Chu and O. K. Song. "Apparent thickness dependence of mobility in organic thin films analyzed by Gaussian disorder model". *Journal of Applied Physics* 104 (2008), p. 023711. DOI: 10.1063/1.2959825 (cited on p. 64).

[497] W. F. Pasveer, P. A. Bobbert, and M. A. J. Michels. "Temperature and field dependence of the mobility in 1D for a Gaussian density of states". *physica status solidi (c)* 1 (2004), pp. 164–167. DOI: 10.1002/pssc.200303631 (cited on p. 64).

[498] S. Novikov and A. Vannikov. "Field dependence of charge mobility in polymer matrices.Monte Carlo simulation of the escape of a charge carrier from a dipole trap". *Chemical Physics* 169 (1993), pp. 21–33. DOI: 10.1016/0301-0104(93)80037-a (cited on p. 64).

[499] R. Coehoorn, W. F. Pasveer, P. A. Bobbert, and M. A. J. Michels. "Charge-carrier concentration dependence of the hopping mobility in organic materials with Gaussian disorder". *Physical Review B* 72 (2005), p. 155206. DOI: 10.1103/PhysRevB.72.155206 (cited on p. 64).

[500] S. van Mensfoort. "Effects of disorder on the charge transport and recombination in organic light-emitting diodes". PhD thesis. Technical University Eindhoven, 2009 (cited on p. 64).

[501] N. I. Craciun, J. Wildeman, and P. W. M. Blom. "Universal Arrhenius Temperature Activated Charge Transport in Diodes from Disordered Organic Semiconductors". *Physical Review Letters* 100 (2008), p. 056601. DOI: 10.1103/PhysRevLett.100.056601 (cited on p. 64).

[502] G. G. Malliaras and J. C. Scott. "Numerical simulations of the electrical characteristics and the efficiencies of single-layer organic light emitting diodes". *Journal of Applied Physics* 85 (1999), pp. 7426–7432. DOI: 10.1063/1.369373 (cited on p. 64).

[503] G. G. Malliaras and J. C. Scott. "The roles of injection and mobility in organic light emitting diodes". *Journal of Applied Physics* 83 (1998), pp. 5399–5403. DOI: 10.1063/1.367369 (cited on p. 64).

[504] W. Brütting, S. Berleb, and A. Mückl. "Space-charge limited conduction with a field and temperature dependent mobility in Alq light-emitting devices". *Synthetic Metals* 122 (2001), pp. 99–104. DOI: 10.1016/s0379-6779(00)01342-4 (cited on p. 64).

[505] P. Borsenberger, E. Magin, and J. Shi. "Charge transport in vapor deposited molecular glasses". *Physica B: Condensed Matter* 217 (1996), pp. 212–220. DOI: 10.1016/0921-4526(95)00627-3 (cited on p. 64).

[506] T. Okachi, T. Nagase, T. Kobayashi, and H. Naito. "Influence of injection barrier on the determination of charge-carrier mobility in organic light-emitting diodes by impedance spectroscopy". *Thin Solid Films* 517 (2008), pp. 1331–1334. DOI: 10.1016/j.tsf.2008.09.020 (cited on p. 64).

[507] I. G. Hill and A. Kahn. "Energy level alignment at interfaces of organic semiconductor heterostructures". *Journal of Applied Physics* 84 (1998), pp. 5583–5586. DOI: 10.1063/1.368864 (cited on p. 64).

[508] I. G. Hill, D. Milliron, J. Schwartz, and A. Kahn. "Organic semiconductor interfaces: electronic structure and transport properties". *Applied Surface Science* 166 (2000), pp. 354–362. DOI: 10.1016/s0169-4332(00)00449-9 (cited on p. 64).

[509] H. Ishii, K. Sugiyama, E. Ito, and K. Seki. "Energy Level Alignment and Interfacial Electronic Structures at Organic/Metal and Organic/Organic Interfaces". *Advanced Materials* 11 (1999), pp. 605–625. DOI: 10.1002/(SICI)1521-4095(199906)11:8<605::AID-ADMA605>3.0.CO;2-Q (cited on p. 64).

[510] J. Hwang, A. Wan, and A. Kahn. "Energetics of metal–organic interfaces: New experiments and assessment of the field". *Materials Science and Engineering: R* 64 (2009), pp. 1–31. DOI: 10.1016/j.mser.2008.12.001 (cited on p. 65).

[511] N. Koch, A. Kahn, J. Ghijsen, J.-J. Pireaux, J. Schwartz, R. L. Johnson, and A. Elschner. "Conjugated organic molecules on metal versus polymer electrodes: Demonstration of a key energy level alignment mechanism". *Applied Physics Letters* 82 (2003), pp. 70–72. DOI: 10.1063/1.1532102 (cited on p. 65).

[512] S. L. M. van Mensfoort, V. Shabro, R. J. de Vries, R. A. J. Janssen, and R. Coehoorn. "Hole transport in the organic small molecule material α-NPD: Evidence for the presence of correlated disorder". *Journal of Applied Physics* 107 (2010), p. 113710. DOI: 10.1063/1.3407561 (cited on p. 65).

[513] J. D. Anderson, E. M. McDonald, P. A. Lee, M. L. Anderson, E. L. Ritchie, H. K. Hall, T. Hopkins, E. A. Mash, J. Wang, A. Padias, S. Thayumanavan, S. Barlow, S. R. Marder, G. E. Jabbour, S. Shaheen, B. Kippelen, N. Peyghambarian, R. M. Wightman, and N. R. Armstrong. "Electrochemistry and Electrogenerated Chemiluminescence Processes of the Components of Aluminum Quinolate/-Triarylamine, and Related Organic Light-Emitting Diodes". *Journal of the American Chemical Society* 120 (1998), pp. 9646–9655. DOI: 10.1021/ja980707+ (cited on p. 65).

[514] P. I. Djurovich, E. I. Mayo, S. R. Forrest, and M. E. Thompson. "Measurement of the lowest unoccupied molecular orbital energies of molecular organic semiconductors". *Organic Electronics* 10 (2009), pp. 515–520. DOI: 10.1016/j.orgel.2008.12.011 (cited on p. 65).

[515] Y. Gao. "Surface analytical studies of interfaces in organic semiconductor devices". *Materials Science and Engineering: R* 68 (2010), pp. 39–87. DOI: 10.1016/j.mser.2010.01.001 (cited on p. 65).

[516] T. Chassé, C.-I. Wu, I. G. Hill, and A. Kahn. "Band alignment at organic-inorganic semiconductor interfaces: α-NPD and CuPc on InP(110)". *Journal of Applied Physics* 85 (1999), pp. 6589–6592. DOI: 10.1063/1.370165 (cited on p. 65).

[517] Z. Wang, Y. Lou, S. Naka, and H. Okada. "Temperature dependence of carrier injection in small molecular organic light emitting device with a mixed single layer". *Chemical Physics Letters* 501 (2010), pp. 75–79. DOI: 10.1016/j.cplett.2010.10.056 (cited on p. 65).

[518] K. Sugi, H. Ishii, Y. Kimura, M. Niwano, E. Ito, Y. Washizu, N. Hayashi, Y. Ouchi, and K. Seki. "Characterization of light-erasable giant surface potential built up in evaporated Alq3 thin films". *Thin Solid Films* 464-465 (2004), pp. 412–415. DOI: 10.1016/j.tsf.2004.06.035 (cited on p. 67).

[519] Z.-Q. Xu, F.-Z. Sun, J. Li, S.-T. Lee, Y.-Q. Li, and J.-X. Tang. "Irradiation-induced molecular dipole reorientation in inverted polymer solar cell using small molecular electron collection layer". *Applied Physics Letters* 99 (2011), p. 203301. DOI: 10.1063/1.3663548 (cited on p. 67).

[520] M. Minagawa and N. Takahashi. "Lifetime improvement mechanism in organic light-emitting diodes with mixed materials at a heterojunction interface". *Japanese Journal of Applied Physics* 55 (2016), 02BB08. DOI: 10.7567/jjap.55.02bb08 (cited on p. 67).

[521] T. Miyamae, N. Takada, T. Yoshioka, S. Miyaguchi, H. Ohata, and T. Tsutsui. "Rearrangement of the molecular orientation of Alq3 in organic light-emitting diodes under constant current aging investigated using sum frequency generation spectroscopy". *Chemical Physics Letters* 616-617 (2014), pp. 86–90. DOI: 10.1016/j.cplett.2014.10.027 (cited on p. 67).

[522] D. Y. Kondakov. "Direct observation of deep electron traps in aged organic light emitting diodes". *Journal of Applied Physics* 97 (2005), p. 024503. DOI: 10.1063/1.1835567 (cited on p. 69).

[523] D. Y. Kondakov and R. H. Young. "Variable sensitivity of organic light-emitting diodes to operation-induced chemical degradation: Nature of the antagonistic relationship between lifetime and efficiency". *Journal of Applied Physics* 108 (2010), p. 074513. DOI: 10.1063/1.3483251 (cited on p. 69).

[524] D. Y. Kondakov. "Role of chemical reactions of arylamine hole transport materials in operational degradation of organic light-emitting diodes". *Journal of Applied Physics* 104 (2008), p. 084520. DOI: 10.1063/1.3006890 (cited on p. 69).

[525] N. C. Giebink, B. W. D'Andrade, M. S. Weaver, J. J. Brown, and S. R. Forrest. "Direct evidence for degradation of polaron excited states in organic light emitting diodes". *Journal of Applied Physics* 105 (2009), p. 124514. DOI: 10.1063/1.3151689 (cited on p. 69).

[526] J. Steiger, S. Karg, and H. von Seggern. "Electronic traps in OLED transport layers: influence of doping and accelerated aging". *Proceedings of SPIE* 4105 (2001). Ed. by Z. H. Kafafi, pp. 256–264. DOI: 10.1117/12.416902 (cited on p. 69).

[527] H. Aziz and Z. D. Popovic. "Degradation Phenomena in Small-Molecule Organic Light-Emitting Devices". *Chemistry of Materials* 16 (2004), pp. 4522–4532. DOI: 10.1021/cm040081o (cited on p. 69).

[528] S. Züfle, S. Altazin, A. Hofmann, L. Jäger, M. T. Neukom, W. Brütting, and B. Ruhstaller. "Determination of charge transport activation energy and injection barrier in organic semiconductor devices". *Journal of Applied Physics* 122 (2017), p. 115502. DOI: 10.1063/1.4992041 (cited on p. 72).

[529] H. Hoppe, M. Seeland, and B. Muhsin. "Optimal geometric design of monolithic thin-film solar modules: Architecture of polymer solar cells". *Solar Energy Materials & Solar Cells* 97 (2012), pp. 119–126. DOI: 10.1016/j.solmat.2011.09.037 (cited on p. 75).

[530] M. Seeland and H. Hoppe. "Comparison of distributed vs. lumped series resistance modeling of thin-film solar cells and modules: Influence on the geometry-dependent efficiency". *physica status solidi (a)* 212 (2015), pp. 1991–2000. DOI: 10.1002/pssa.201431886 (cited on p. 75).

[531] A. Manor, E. A. Katz, T. Tromholt, and F. C. Krebs. "Electrical and Photo-Induced Degradation of ZnO Layers in Organic Photovoltaics". *Advanced Energy Materials* 1 (2011), pp. 836–843. DOI: 10.1002/aenm.201100227 (cited on pp. 76, 100).

[532] T. Aernouts, F. Brunetti, J. de la Fuente, N. Espinosa, A. Urbina, M. Fonrodona, M. Lira-Cantu, Y. Galagan, H. Hoppe, E. Katz, M. Ramos, M. Riede, K. Vandewal, S. Veenstra, and E. von Hauff. "EU COST Action MP1307 - Unravelling the degradation mechanisms of emerging solar cell technologies". *Proceedings of MELECON* (2016). DOI: 10.1109/melcon.2016.7495310 (cited on pp. 80, 113).

[533] B. Wegler, O. Schmidt, B. Hensel, O. Schmidt, and B. Hensel. "Influence of PEDOT : PSS on the effectiveness of barrier layers prepared by atomic layer deposition in organic light emitting diodes Influence of PEDOT : PSS on the effectiveness of barrier layers prepared by atomic layer deposition in organic light emitting diodes". *Journal of Vacuum Science & Technology A* 33 (2015), 01A147. DOI: 10.1116/1.4904500 (cited on p. 83).

[534] T. Offermans, J. Schleuniger, and G. Nisato. "Inkjet Printing of Polymer Solar Cells". *Proceedings of LOPE-C* (2010), pp. 99–102 (cited on p. 83).

[535] Seoul Semiconductor. *Power LED white W724Co* (cited on p. 83).

[536] K. Kawano, R. Pacios, D. Poplavskyy, J. Nelson, D. D. Bradley, and J. R. Durrant. "Degradation of organic solar cells due to air exposure". *Solar Energy Materials & Solar Cells* 90 (2006), pp. 3520–3530. DOI: 10.1016/j.solmat.2006.06.041 (cited on p. 84).

[537] B. Conings, S. Bertho, K. Vandewal, A. Senes, J. D'Haen, J. Manca, and R. A. J. Janssen. "Modeling the temperature induced degradation kinetics of the short circuit current in organic bulk heterojunction solar cells". *Applied Physics Letters* 96 (2010), p. 163301. DOI: 10.1063/1.3391669 (cited on p. 84).

[538] M. Porro, C. de Falco, M. Verri, G. Lanzani, and R. Sacco. "Multiscale simulation of organic heterojunction light harvesting devices". *COMPEL: The International Journal for Computation and Mathematics in Electrical and Electronic Engineering* 33 (2014), pp. 1107–1122. DOI: 10.1108/COMPEL-12-2012-0365 (cited on p. 86).

[539] M. Ullah, D. M. Taylor, R. Schwödiauer, H. Sitter, S. Bauer, N. S. Sariciftci, and T. B. Singh. "Electrical response of highly ordered organic thin film metal-insulator-semiconductor devices". *Journal of Applied Physics* 106 (2009), p. 114505. DOI: 10.1063/1.3267045 (cited on p. 86).

[540] H. Klumbies, M. Karl, M. Hermenau, R. Rösch, M. Seeland, H. Hoppe, L. Müller-Meskamp, and K. Leo. "Water ingress into and climate dependent lifetime of organic photovoltaic cells investigated by calcium corrosion tests". *Solar Energy Materials & Solar Cells* 120 (2014), pp. 685–690. DOI: 10.1016/j.solmat.2013.10.023 (cited on p. 86).

[541] A. Fick. "Ueber Diffusion". *Annalen der Physik und Chemie* 170 (1855), pp. 59–86. DOI: 10.1002/andp.18551700105 (cited on p. 94).

[542] A. Fick. "On liquid diffusion". *The London, Edinburgh, and Dublin Philosophical Magazine and Journal of Science* 10 (1855), pp. 30–39. DOI: 10.1080/14786445508641925 (cited on p. 94).

[543] J. Crank. *The mathematics of diffusion*. 2. ed., reprint. Oxford: Clarendon Press, 1976. ISBN: 9780198533443 (cited on p. 94).

[544] H. Carslaw and J. Jaeger. *Conduction of heat in solids*. Oxford University Press, 1959. ISBN: 0198533446 (cited on p. 94).

[545] S. Harris. "Microscopic theory for the diffusive evolution of an isoconcentration surface". *Physical Review A* 42 (6 1990), pp. 3504–3506. DOI: 10.1103/PhysRevA.42.3504 (cited on p. 94).

[546] L. Ke, S. F. Lim, and S. J. Chua. "Organic Light-Emitting Device Dark Spot Growth Behavior Analysis by Diffusion Reaction Theory". *Journal of Polymer Science, Part B* 39 (2001), pp. 1697–1703. DOI: 10.1002/polb.1141.abs (cited on p. 95).

[547] S. F. Lim, W. Wang, and S. J. Chua. "Degradation of organic light-emitting devices due to formation and growth of dark spots". *Materials Science and Engineering: B* 85 (2001), pp. 154–159. DOI: 10.1016/s0921-5107(01)00599-2 (cited on p. 95).

[548] D. Fluhr, S. Züfle, B. Muhsin, R. Öttking, M. Seeland, R. Rösch, U. Schubert, B. Ruhstaller, S. Krischok, and H. Hoppe. "Unified description of electrode corrosion dynamics in organic solar cells". *submitted* (2017) (cited on p. 97).

[549] E. A. Katz, A. Manor, A. Mescheloff, T. Tromholt, and F. C. Krebs. "Accelerated stability testing of organic photovoltaics using concentrated sunlight". *IEEE PVSC* (2012), pp. 3249–3252. DOI: 10.1109/pvsc.2012.6318270 (cited on pp. 99, 113).

[550] S. Schuller, P. Schilinsky, J. Hauch, and C. Brabec. "Determination of the degradation constant of bulk heterojunction solar cells by accelerated lifetime measurements". *Applied Physics A: Solids and Surfaces* 79 (2004), pp. 37–40. DOI: 10.1007/s00339-003-2499-4 (cited on pp. 99, 113).

[551] O. Haillant, D. Dumbleton, and A. Zielnik. "An Arrhenius approach to estimating organic photovoltaic module weathering acceleration factors". *Solar Energy Materials & Solar Cells* 95 (2011), pp. 1889–1895. DOI: 10.1016/j.solmat.2011.02.013 (cited on pp. 99, 113).

[552] E. A. Katz, J. M. Gordon, W. Tassew, and D. Feuermann. "Photovoltaic characterization of concentrator solar cells by localized irradiation". *Journal of Applied Physics* 100 (2006), p. 044514. DOI: 10.1063/1.2266161 (cited on pp. 99, 100, 113).

[553] I. Visoly-Fisher, A. Mescheloff, M. Gabay, C. Bounioux, L. Zeiri, M. Sansotera, A. Goryachev, A. Braun, Y. Galagan, and E. Katz. "Concentrated sunlight for accelerated stability testing of organic photovoltaic materials: towards decoupling light intensity and temperature". *Solar Energy Materials & Solar Cells* 134 (2015), pp. 99–107. DOI: 10.1016/j.solmat.2014.11.033 (cited on pp. 99, 102, 113).

[554] D. Faiman, S. Jacob, and A. Karnieli. "Concerning the relationship between clear-sky, global and direct-beam, solar spectra". *Progress in Photovoltaics: Research and Applications* 10 (2002), pp. 527–532. DOI: 10.1002/pip.451 (cited on p. 99).

[555] J. M. Gordon, E. A. Katz, D. Feuermann, and M. Huleihil. "Toward ultrahigh-flux photovoltaic concentration". *Applied Physics Letters* 84 (2004), pp. 3642–3644. DOI: 10.1063/1.1723690 (cited on pp. 99, 113).

[556] G. F. A. Dibb, M.-A. Muth, T. Kirchartz, S. Engmann, H. Hoppe, G. Gobsch, M. Thelakkat, N. Blouin, S. Tierney, M. Carrasco-Orozco, and et al. "Influence of doping on charge carrier collection in normal and inverted geometry polymer:fullerene solar cells". *Scientific Reports* 3 (2013), p. 3335. DOI: 10.1038/srep03335 (cited on p. 110).

[557] S. Züfle, G. Zanotti, E. A. Katz, P. Tiwana, and B. Ruhstaller. "Reversible Photodoping of Organic Solar Cells aged by Concentrated Sunlight". *manuscript in preparation* (2017) (cited on p. 112).

[558] R. Hansson. "Materials and Device Engineering for Efficient and Stable Polymer Solar Cells". PhD thesis. Karlstad University, 2017 (cited on p. 113).

[559] E. Bovill, N. Scarratt, J. Griffin, H. Yi, A. Iraqi, A. R. Buckley, J. W. Kingsley, and D. G. Lidzey. "The role of the hole-extraction layer in determining the operational stability of a polycarbazole:fullerene bulk-heterojunction photovoltaic device". *Applied Physics Letters* 106 (2015), p. 073301. DOI: 10.1063/1.4909530 (cited on pp. 116, 117).

[560] T. Heumueller, T. M. Burke, W. R. Mateker, I. T. Sachs-Quintana, K. Vandewal, C. J. Brabec, and M. D. McGehee. "Disorder-Induced Open-Circuit Voltage Losses in Organic Solar Cells During Photoinduced Burn-In". *Advanced Energy Materials* 5 (2015), p. 1500111. DOI: 10.1002/aenm.201500111 (cited on pp. 116, 117).

[561] D. H. Wang, J. K. Kim, J. H. Seo, O. O. Park, and J. H. Park. "Stability comparison: A PCDTBT/PC71BM bulk-heterojunction versus a P3HT/PC71BM bulk-heterojunction". *Solar Energy Materials & Solar Cells* 101 (2012), pp. 249–255. DOI: 10.1016/j.solmat.2012.02.005 (cited on p. 116).

[562] Blakesley. "Relationship between energetic disorder and open-circuit voltage in bulk heterojunction organic solar cells". *Physical Review B* 84 (2011), p. 075210. DOI: 10.1103/PhysRevB.84.075210 (cited on pp. 117, 118).

[563] G. Garcia-Belmonte. "Temperature dependence of open-circuit voltage in organic solar cells from generation-recombination kinetic balance". *Solar Energy Materials & Solar Cells* 94 (2010), pp. 2166–2169. DOI: 10.1016/j.solmat.2010.07.006 (cited on p. 117).

[564] A. Benor, S. ya Takizawa, C. Pérez-Bolívar, and P. Anzenbacher. "Efficiency improvement of fluorescent OLEDs by tuning the working function of PEDOT:PSS using UV–ozone exposure". *Organic Electronics* 11 (2010), pp. 938–945. DOI: 10.1016/j.orgel.2010.02.014 (cited on p. 118).

[565] H. K. Lee, J.-K. Kim, and O. O. Park. "Effects of UV light-irradiated buffer layer on the performance of polymer solar cells". *Organic Electronics* 10 (2009), pp. 1641–1644. DOI: 10.1016/j.orgel.2009.09.010 (cited on p. 118).

[566] A. Moujoud, S. H. Oh, J. J. Hye, and H. J. Kim. "Improvement in stability of poly(3-hexylthiophene-2,5-diyl)/[6,6]-phenyl-C61-butyric acid methyl ester bulk heterojunction solar cell by using UV light irradiation". *Solar Energy Materials & Solar Cells* 95 (2011), pp. 1037–1041. DOI: 10.1016/j.solmat.2010.08.019 (cited on p. 118).

[567] C. Tengstedt, A. Kanciurzewska, M. P. de Jong, S. Braun, W. R. Salaneck, and M. Fahlman. "Ultraviolet light-ozone treatment of poly(3,4-ethylenedioxy-thiophene)-based materials resulting in increased work functions". *Thin Solid Films* 515 (2006), pp. 2085–2090. DOI: 10.1016/j.tsf.2006.07.005 (cited on p. 118).

[568] Y. J. Xing, M. F. Qian, J. F. Qin, and G. M. Zhang. "Field emission study of change in work function of poly(3,4-ethylenedioxythiophene):poly(styrenesulfonate) film". *Journal of Vacuum Science & Technology B* 32 (2014), 02B101. DOI: 10.1116/1.4827635 (cited on p. 118).

[569] Y.-J. Xing, M.-F. Qian, D.-Z. Guo, and G.-M. Zhang. "Increased work function in PEDOT:PSS film under ultraviolet irradiation". *Chinese Physics B* 23 (2014), p. 038504. DOI: 10.1088/1674-1056/23/3/038504 (cited on p. 118).

[570] J. Huang, P. Miller, J. Wilson, A. de Mello, J. de Mello, and D. Bradley. "Investigation of the Effects of Doping and Post-Deposition Treatments on the Conductivity, Morphology, and Work Function of Poly(3,4-ethylenedioxythiophene)/Poly(styrene sulfonate) Films". *Advanced Functional Materials* 15 (2005), pp. 290–296. DOI: 10.1002/adfm.200400073 (cited on p. 119).

[571] J. Wagner, M. Gruber, A. Wilke, Y. Tanaka, K. Topczak, A. Steindamm, U. Hörmann, A. Opitz, Y. Nakayama, H. Ishii, J. Pflaum, N. Koch, and W. Brütting. "Identification of different origins for s-shaped current voltage characteristics in planar heterojunction organic solar cells". *Journal of Applied Physics* 111 (2012), p. 054509. DOI: 10.1063/1.3692050 (cited on p. 119).

[572] I. Lange, J. C. Blakesley, J. Frisch, A. Vollmer, N. Koch, and D. Neher. "Band Bending in Conjugated Polymer Layers". *Physical Review Letters* 106 (2011), p. 216402. DOI: 10.1103/physrevlett.106.216402 (cited on p. 119).

[573] M. Oehzelt, K. Akaike, N. Koch, and G. Heimel. "Energy-level alignment at organic heterointerfaces". *Science Advances* 1 (2015), e1501127–e1501127. DOI: 10.1126/sciadv.1501127 (cited on p. 119).

[574] M. Oehzelt, N. Koch, and G. Heimel. "Organic semiconductor density of states controls the energy level alignment at electrode interfaces". *Nature Communications* 5 (2014), p. 4174. DOI: 10.1038/ncomms5174 (cited on p. 119).

[575] S. Züfle, R. Hansson, E. A. Katz, E. Moons, and B. Ruhstaller. "Burn-in degradation of PCDTBT:PC70BM organic photovoltaics: underlying mechanism and interlayer effect". *manuscript in preparation* (2017) (cited on p. 122).

[576] *This document was typeset using the typographical look-and-feel* `classicthesis` *developed by André Miede, which is available at https://bitbucket.org/amiede/classicthesis/.*

[577] *The author further acknowledges Martin Neukom for providing an adapted version of* `classicthesis`.

ACKNOWLEDGEMENTS

This thesis would not have been possible without the expertise, support, advice, patience and tolerance of many people, to whom I would like to express my deepest gratitude.

First of all I would like to thank my supervisors Prof. Uli Lemmer and Prof. Beat Ruhstaller for giving me the opportunity of this PhD project. I thank Uli for his readiness to supervise this work as an external dissertation, for his time, advice and trust. Thank you also to Prof. Sebastian Randel for agreeing to be a co-examiner of this work.

I am very grateful to Beat for providing and organizing the funding for my PhD project, and for his supervision in the daily work. His confidence in my skills, trust and optimism have been essential to make this thesis. I am grateful to him also for sharing many contacts and for giving me the opportunity to participate in several conferences and workshops. Furthermore I want to thank Beat for the good and open working atmosphere and conditions in the OEPHO and Fluxim teams, which inspire and motivate everyone and make the daily work fun and fulfilling.

All my efforts would not have been successful without the colleagues in the Organic Electronics and Photovoltaics group at the ICP and without the Fluxim team. I could always rely on their support, and I was integrated and felt as a valuable member of the group. As for my work the tools *Paios* and *Setfos* were essential, I benefited a lot from the direct contact with the developers. Many of the results would not have been possible without this support, and I enjoyed very much being a "premium user" and a beta-tester. It is also a very rewarding feeling to see some of my suggestions and own additions to these tools are realized in commercial products and help customers in their research. Thus, being a physicist working with engineers on applications that are really used and needed is a very fulfilling job.

Without being able to mention everyone I would like to specially thank Martin Neukom for his support, commitment and friendship. I am always impressed how he manages his workload and about his ingenuity and creativity. Thank you also to Stéphane Altazin for always being available for scientific assistance and for bringing up many new ideas. The rest of the *Paios* team is acknowledged for their assistance, and a special thanks to Adrian Gentsch and Matthias Diethelm for taking over many responsibilities during the final stage of my thesis. I further want to mention Lieven Penninck, Alexandre Stous, and Jordi Sastre from the Fluxim team who I closely collaborated with.

From the ICP team I would like to thank Markus Regnat, Kurt Pernstich, Paolo Losio and Jonas Dunst for their support and advise on the experimental side, for giving me space in the glovebox and time with the measurement equipment.

Due to the manifold contacts of Beat I was able to collaborate with many groups, and to obtain research samples for my studies. I want to acknowledge Ton Offermans from CSEM in Basel, and I thank Priti Tiwana from Merck in Southampton for the fruitful collaboration. We also had several experiments with devices from Belectric/OPVIUS provided by Tobias Sauermann. Furthermore I would like to thank Alexander Colsmann from KIT and and his colleagues Dominik Landerer, Christian Sprau and Bernd Ebenhoch for providing devices and for interesting discussions.

The work on OLEDs has been mainly funded through the DFG/SNSF project CARDYN which is performed together with the group of Prof. Wolfgang Brütting at Augsburg University. I would like to acknowledge Wolfgang, Tobias Schmidt, Lars Jäger and Alexander Hofmann for a very successful collaboration, for providing samples and for the nice project meetings.

I am especially grateful for the chance of being involved in the COST StableNextSol project, which allowed me to establish many contacts and participate in various experiments. In this context I want to acknowledge the effort by Mónica Lira-Cantú, Harald Hoppe and Yulia Galagan, who organize the huge consortium and the joint experiments. The greatest impact for me had the two-week short-term scientific mission in Israel that I was enabled to do by funding from the COST action. My great thanks go to my host Prof. Eugene Katz and colleagues at BGU Gloria Zanotti and Will Brooks. I am also very grateful that Prof. Ellen Moons from Karlstad University and her student Rickard Hansson as well as Priti Tiwana from Merck UK were willing to provide samples for this study.

As I did not have my own devices to measure, it is invaluable to me that I could collaborate with so many groups and experts in device fabrication, that enabled the large set of measurements which have been performed in this work. The second critical ingredient was the infrastructure given at ZHAW and Fluxim concerning both the measurement (*Paios*, cryostat, glovebox, EQE) and the computational (*Setfos*, Matlab, Mathematica) equipment.

Last but not least, I also want to thank Christian and my family who have always supported me in my plans and whom I neglected in the past months. I am really thankful to have them always by my side.